Controlling the Electrospinning of Nanofibrous Polymer Scaffolds for Neuronal Tissue Engineering

By

Teodor-Matei Cirstea

A thesis submitted for the degree of Doctor of Philosophy

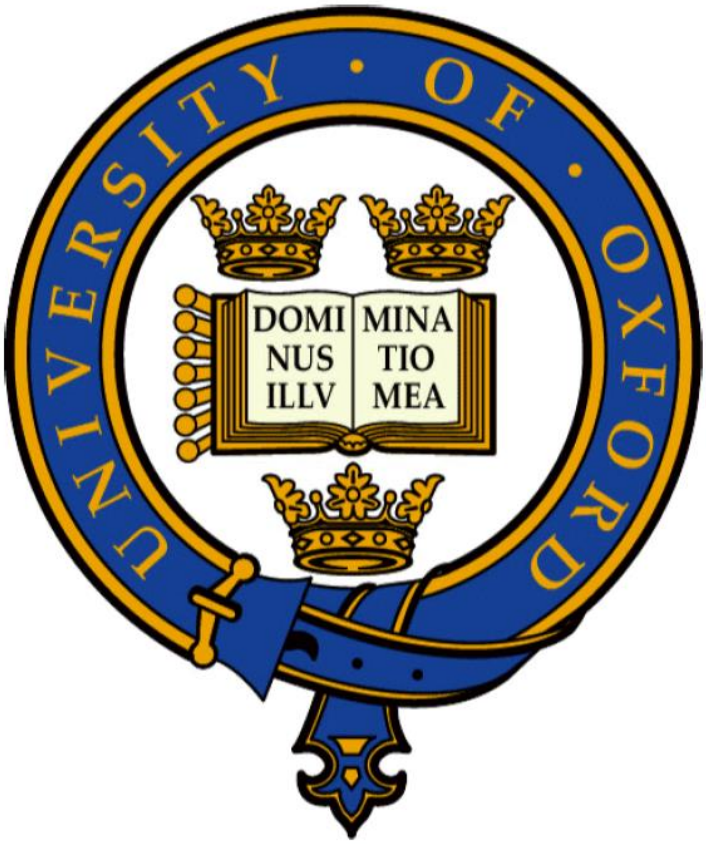

St. Cross College

University of Oxford

Abstract

The use of nanofibrous scaffolds for tissue engineering applications is emerging as an important area of research in the field of regenerative medicine. Due to their close morphological similarity to the extra-cellular matrix (ECM) these types of scaffolds could be ideal candidates for synthetic, ECM-like substitutes. The main aim of this thesis is to understand and tailor the physical and morphological properties of nanofibrous scaffolds through control of the processing conditions and the incorporation of multi-walled carbon nanotubes and finally their application as substrates for neuronal cell growth.

Nanofibrous scaffolds from polycaprolactone, poly(methyl methacrylate) and gelatin were produced using a self-made electrospinning kit. Advanced experimental design was employed to understand the impact of the processing parameters on the morphology of these scaffolds. The crystalline structure of polycaprolactone scaffolds was measured as a function of the fibre morphology and the processing conditions. It was found that the mechanical properties were strongly dependant on both of these factors which allows for the production of scaffolds with similar fibre structures but markedly different mechanical properties. Carbon nanotubes were successfully incorporated into polycaprolactone and gelatin nanofibres to form composite scaffolds. The targeted functionalization – polycaprolactone was chemically grafted onto carbon nanotubes to macht the polycaprolactone matrix – of carbon nanotubes to the polymer matrix was found to be superior to a more common approach to nanotube functionalization in its reinforcement properties on the electrospun scaffolds. Finally the performance of polycaprolactone scaffolds with bespoke fibre morphologies and different levels of carbon nanotube reinforcements as substrates for human neuronal cell growth was explored in a pilot study. Initial results indicate that the addition of carbon nanotubes greatly enhance neuronal cell growth on scaffolds as determined by an increased cell proliferation and neuronal cell cell differentiation.

"*Whereas the man of action binds his life to reason and its concepts so that he will not be swept away and lost, the scientific investigator builds his hut right next to the tower of science so that he will be able to work on it and to find shelter for himself beneath those bulwarks which presently exist. And he requires shelter, for there are frightful powers which continuously break in upon him, powers which oppose scientific 'truth' with completely different kinds of 'truths' which bear on their shields the most varied sorts of emblems."*

Friedrich Nietzsche - On Truth and Lie in an Extra-Moral Sense (1873)

Acknowledgments

The work described in this thesis was carried out in the Department of Materials Science at the University of Oxford under the supervision of Prof. Pete Dobson and Prof. Andrew Watt.

I would not have been able to even attempt to complete this work without the unwavering support and love from my mother, my father and my sister. I am forever indebted and grateful for all that they have done.

Furthermore I want to express my gratitude to Prof. Pete Dobson for believing in me and helping me despite the difficulty of working with me through the hard times I experienced. I also want to thank Prof. Andrew Watt for taking a leap of faith and taking me in, in spite of the differences in the areas of expertise.

Additionally I want to thank the following people for their help:

Dr. Julian George for helping me expand my research into new territories and helping me with the cell work.

My colleagues in both the Grobert and the Watt group for their feedback and stimulating conversations.

And finally John, Jamie, Philipp, Tatiana, Sebouh, Abi, Tess, Marea, Tobias, Alyssa, Ash, Juliane, Kat, Sheel, Peter, Marzia, Victoria, Kim, Meryn, Bronwyn, Rosa, Giles, Marco, Aron, Jonas, Felix and Dayne for without them my journey so far would have been decidedly different and certainly a worse one!

Table of Contents

Abstract 1

Acknowledgments 3

i. List of Abbreviations 9

ii. List of Figures 10

iii. List of Tables 15

iv. List of Equations 16

1. Introduction 17

1.1. Regenerative Medicine 17

1.2. Tissue Engineering 18

1.2.1. Examples of Tissue Engineering 19

1.2.2. Cell/Matrix Interactions 21

1.2.3. Advantages of Nanofibrous Scaffolds 22

1.3. Electrospinning 23

1.3.1. Basic Principles of Electrospinning 23

1.3.2. Electrospinning Parameters 25

1.3.3. Uses of Electrospinning 26

1.3.4. Recent Advances in Electrospinning 26

1.3.5. Challenges of Electrospinning in Tissue Engineering 28

1.3.6. Comparison to the Extra Cellular Matrix 29

1.3.7. Comparison of Synthetic and Organic Polymers 29

1.3.8. “Design Objectives” for Electrospun Scaffolds in Tissue Engineering 31

1.4. The Use of Composite Nanofibres 32

1.4.1. Hydroxyapatite 32

1.5. The Use of Carbon Nanotubes in Tissues Engineering 32
1.5.1. A Brief History of Carbon Nanotubes 32
1.5.2. The Properties of Carbon Nanotubes....33
1.5.3. Examples of Carbon Nanotubes for Regenerative Medicine 34
1.5.3.1. Cell tracking and labelling....34
1.5.3.2. Sensing Cellular Behaviour....34
1.5.3.3. Augmenting Cellular Behaviour 35
1.5.3.4. Matrix Enhancement....35
1.5.4. Challenges for Carbon Nanotubes in Tissue Engineering 39
1.6. Conclusions and Thesis Roadmap....39
2. Methods 41
2.1. Electrospinning Set-Up....41
2.2. Estimation of Impact of Humidity 41
2.3. Scanning Electron Microscopy 42
2.4. Diameter Distributions....42
2.5. Transmission Electron Microscopy....43
2.6. X-Ray Diffraction....43
2.7. Viscosity Measurements 43
2.8. Mechanical Testing 46
2.9. Differential Scanning calorimetry Measurements....46
2.10. X-ray Photoelectron Spectroscopy....47
2.11. Scaffold Porosity Measurements 47
3. The Use of Experimental Design in Electrospinning 48
3.1. Introduction 48

3.2. Methods and Materials 49
3.2.1. PCL Study 49
3.2.1.1. Electrospinning 49
3.2.1.2. Design of Experiments 49
3.2.1.3. Statistical Analysis 50
3.2.2. PMMA 50
3.2.2.1. Electrospinning 50
3.2.2.2. Design of Experiments 50
3.2.2.3. Statistical Analysis 51
3.2.3. Morphological Analysis 51
3.3. Results and Discussion 51
3.3.1. PCL 51
3.3.2. Summary of PCL Study 65
3.3.3. PMMA Parameter Study 66
3.4. Conclusion 75
4. The Crystalline Properties of Electrospun PCL Fibres 77
4.1. Introduction 77
4.2. Methods 78
4.2.1. Electrospinning 78
4.3. Mechanical Testing of Whole Scaffolds 78
4.4. Results and Discussion 80
4.5. Conclusion 89
5. Reinforcement of PCL Nanofibres with Carbon Nanotubes 91
5.1. Introduction 91

5.2. Materials and Method 92
5.2.1. CNT Synthesis 92
5.2.2. CNT Functionalization 92
5.2.3. FT-IR Spectroscopy 93
5.2.4. Incorporation of CNTs into PCL Nanofibres 93
5.2.5. Streaming Potential Measurements 93
5.3. Results and Discussion 94
5.4. Conclusion 110
6. Electrospinning of Gelatin and CNT/Gelatin Nanofibres 111
6.1. Introduction 111
6.2. Materials and Method 111
6.2.1. Electrospinning of Pure Gelatin Nanofibres 111
6.2.2. Incorporation of Carbon Nanotubes into Gelatin Nanofibres 112
6.3. Results and Discussion 112
6.4. Conclusion 125
7. Neuronal Cell Growth on Electrospun PCL Scaffolds 127
7.1. Introduction 127
7.2. Materials and Method 128
7.2.1. Electrospinning 128
7.2.2. Cell Line 129
7.2.3. Sterilisation and Coating 129
7.2.4. Seeding 130
7.2.5. Fixation 130
7.2.6. Staining 130

7.2.7. Image Acquisition 131
7.2.8. Image Analysis 131
7.2.9. Control Samples 131
7.3. Results and Discussion 131
7.4. Conclusion 143
8. Conclusion 145
8.1. Understanding of the Electrospinning Process and Nanofibrous Structures 145
8.2. Multi-Walled Carbon Nanotubes as Reinforcement Material in Nanofibres 146
8.3. Electrospun Scaffolds for Neuronal Tissue Engineering 147
9. Future Work 148
9.1. Mechanical Testing 148
9.2. Electric Conductivity of CNT Containing Scaffolds 148
9.3. Gelatin Molecular Weight Reduction 149
9.4. Cell Study 149
10. Appendix 151
10.1. Residual Solvent Analysis of PCL Scaffolds 151
10.2. Electrospinning of Type 1 Collagen and Degradation Analysis 152
10.3. Residual Solvent Analysis of Collagen Scaffolds 156
10.4. SEM Imaging of PCL Scaffold Cross-Section 157
11. Bibliography 159

i. List of Abbreviations

AL	Alumiium
BSA	Bovine serum albumin
CA	Cellulose acetate
CNT	Carbon Nanotube
CVD	Chemical Vapour Deposition
DCC	N,N'-Dicyclohexylcarbodiimide
DMF	Dimethylformamide
DoE	Design of Experiments
DSC	Differential scanning calorimetry
DWCNT	Double-Walled Carbon Nanotube
ECM	Extra-Cellular Matrix
EDA	Ethylenediamine
ES	Electrospinning
FIB	Focused ion beam
FTIR	Fourier transform infrared spectroscopy
GDP	Gross Domestic Product
GHG	Greenhouse Gas
GPC	Gel permeation chromatography
HA	Hydroxylapatite
HCl	Hydrochloric acid
HFIP	1,1,1,3,3,3-Hexafluoro-2-propanol
iPSC	Induced pluripotent stem cell
KCl	Potassium chloride
MWCNT	Multi-Walled Carbon Nanotube
NIR	Near-Infrared
OECD	Organisation for Economic Cooperation and Development
PAH	Polyanhydrides
PAN	Polyacrylonitrile
PANi	Polyaniline
PBS	Phosphate-buffered saline
PBT	Polybutylene terephthalate
PCL	Polycaprolactone
PE	Polyethylene
PEG	Polyethylene glycol
PEO	Poly(ethylene oxide)
PET	Polyethylene terephthalate
PHBV	Poly(3-hydroxybutyrate-co-3-hydroxyvalerate)
PI	Polyimide
PLA	Polylactic acid
PLGA	Poly(lactic-co-glycolic acid)
PLLA	Polylactic acid
PMMA	Poly(methyl methacrylate)
PS	Polystyrene
PSS	Polystyrene sulfonate

PTT	Polytrimethylene terephthalate
PU	Polyurethane
PVA	Polyvinyl alcohol
PVDF	Polyvinylidene fluoride
SEM	Scanning electron microscope
SWCNT	Single-Walled Carbon Nanotube
TE	Tissue Engineering
TEM	Transmission electron microscope
UTS	Ultimate Tensile Strength
XPS	X-ray photoelectron spectroscopy
XRD	X-ray Diffraction

ii. List of Figures

Figure 1: Schematic of the principle of tissue engineering[8]: A sample of the target tissue is extracted from the patient (A) and screened for phenotype, as well as cultivated in a bioreactor (B). The cells are then seeded on a porous scaffold in conjunction with growth factors in order to increase proliferation (C). The seeded scaffolds are placed in bioreactors for an additional increase in cell number (D). In a last step, the re-grown tissue is medically implanted back into the patient (E).Taken from George (2004)[8]..... 19

Figure 2: An in vitro grown trachea, made from stem cells from the patient on a nanocomposite scaffold. Taken from Harvard Bioscience Inc.[31] 20

Figure 3 Comparison of the environmental impact of different kinds of meat in contrast to culture meat (normalised for beef).Taken from Tuomisto (2011)[33]. GHG stands for greenhouse gas. 21

Figure 4 Simple overview of different achievable scaffold morphologies with current technology and the type of cell binding found with those morphologies. Taken from George (2004)[8]..... 22

Figure 5: Schematic of a Basic ES set-up. Taken from Norris et al. (2000)[63]. 23

Figure 6 Detailed illustration of the formation of fibres and the jet behaviour during ES. Taken from Joanna Gatford - The New Zealand Institute for Plant and Food Research Ltd[70]. 25

Figure 7: Various forms of electrospun fibres. A) Electrospun tubes. B) 3D scaffold and C) Continous yarn[103]. 27

Figure 8 Different, interconnected tubes made by the use of different collectors. A) Schematic of the fabrication process. Hollow tubes are used as templates that can be removed after fibre deposition. B) Final structure resulting from the above schematic. C) Various other shapes of interconnected tubes that could be produced with that technique. (Scale bar = 5 mm).Taken from Zhang et al. (2008[104]..... 27

Figure 9: Aligned electrospun meshes. A) A4 sized membrane. B) 1m wide and 3m long membrane. Taken from Teo et al. (2011)[103]. 28

Figure 10 Conductivity of PVA fibres as a function of the MWCNT content. Taken from Wang et al. (2006)[151]. 37

Figure 11: Osteoblast function measured by AlamarBlue absorbance after 7 days seeding with varying DC currents applied. TCP = Tissue Culture Plate, R0 = Neat, random PCL fibres, A0 = Neat, aligned PCL fibres, R1 – R5 PCL = Random PCL fibres with increasing MWCNT content, A1 – A5 = Aligned PCL fibres with increasing MWCNT content. Taken from Shao et al. (2011)[220]. 38

Figure 12: Top: Overview of the morphology of scaffolds made from 6 wt% solutions at a humidity of 32% (left) and 55% - 65% (right) Bottom: Comparison of the average fibre diameter between the dry and the humid state. All error bars are given as one standard deviation. 42

Figure 13: : A one order of magnitude change in the viscosity of a 4 wt% PCL/HFIP solution is observed over a period of 13 minutes which can be attributed to solvent evaporation..... 44

Figure 14: A: Stability of a 5 wt% PCL and 3 wt% PCL solution over times. The results show no change in viscosity at a constant shear-rate of 100^{-1} s. B: Transient shear viscosity of various solutions that were used for electrospinning..... 45

Figure 15 Zero shear viscosity as a function of PCL content in the solution. The red line represents a linear fit with R^2 ~0.99..... 45

Figure 16: Schematic of the modified deposition technique for the tensile testing samples. The cross-sectional area of the test samples will depend on the experimental parameters, such as time, flow-rate and polymer concentration. 46

Figure 17: Overview of various types of PCL scaffolds produced. Scaffolds that exhibited the smallest fibre diameters (A), a standard midpoint sample (B). the largest average fibre diameter found (C), scaffolds with the smallest standard deviation of the fibre distribution (D) and the largest standard deviation found (E). All scale bars are 3 µm..... 55

Figure 18: Overview of the correlations within the investigated parameters. R^2-values for the linear fits are: Top: 0.52, Middle: 0.05, Bottom: 0.09..... 57

Figure 19: Overview of the impacts of the five significant parameters on the average fibre diameter. 58

Figure 20: Overview of the impacts of the four significant parameters on the standard distribution of fibre diameters..... 59

Figure 21: Overview of the impacts of the five significant parameters on the area of deposition of the scaffolds. 60

Figure 22: Comparison of the influence of the needle inner diameter on the mean fibre diameter, standard deviation of fibre diameters and area of deposition of the scaffolds for the PCL experimental series. 65

Figure 23: Overview of various types of PMMA scaffolds produced. Scaffolds that exhibited the smallest fibre diameters (A), a standard midpoint sample (B). the largest average fibre diameter found (C), scaffolds with the smallest standard deviation of the fibre distribution (D) and the largest standard deviation found (E). All scale bars are 5 µm. *68*

Figure 24: Overview of the individual influence of the processing parameters on the average fibre diameter, the standard deviation of diameters and the area of deposition of PMMA scaffolds. *71*

Figure 25: Molecular structure of polycaprolactone. *77*

Figure 26: Relationship between the average fibre diameters with respect to a change in either concentration or feed rate. *80*

Figure 27: Relationship between the degree of crystallinity as measured by DSC and XRD with respect to a change in the concentration or the feed rate. *81*

Figure 28: Comparison of the relationship with the (110) and (200) crystallite size as measured by XRD with a change in concentration or feed rate. *83*

Figure 29: DSC thermograms taken of PCL scaffolds made with a 5 wt% solution at 0.55 mL/h (top), a 3 wt% solution at 0.55 mL/h (middle) and 5 wt% solution at 0.1 mL/h (bottom). *84*

Figure 30: Relationship of the modulus, UTS and strain at break of the PCL scaffolds with respect to a change in concentration or solution feed rate. *86*

Figure 31: Overview of the modulus, UTS and strain at break for PCL scaffolds with respect to the average fibre diameter of the scaffold. *87*

Figure 32: Comparison of two stress-strain curves of PCL scaffolds with similar average diameters. The scaffold with a higher degree of crystallinity and smaller crystallite sizes (blue) has a significantly higher modulus, UTS and strain at break than the scaffold with a similar diameter (orange) but a lower degree of crystallinity and larger average crystallite sizes. *88*

Figure 33: A: Comparison of FT-IR spectra for pure CNTs (black, -OH functionalized CNTs (red) and amino-functionalized CNTs (red). B: Comparison of FT-IT spectra for electrospun pure PCL scaffolds (red) and PCL-grafted CNTs containing PCL scaffolds (black). *96*

Figure 34: Comparison of XPS spectra of pure CNTs (black) and –OH functionalized CNTs (red). The peaks for carbon and oxygen are highlighted. *97*

Figure 35: Comparison of the change in average fibre diameter with respect to CNT content in PCL scaffolds. Top: -OH functionalized CNTs. Bottom: PCl-grafted CNTs. *98*

Figure 36: Examples of diameter distributions of fibre distributions found for –OH functionalized CNT containing scaffolds (left) and PCL-grafted CNT containing scffolds (right) with outlier box plots. *99*

Figure 37: Change in the two modes of the fibre distributions for –OH functionalized CNT containing scaffolds with CNT content. *99*

Figure 38: TEM images of CNT containing PCL fibres. Top: Cluster of –OH functionalized CNTs. Middle and bottom: Aligned PCL-grafted CNTs in PCL fibres. *101*

Figure 39: Overview of UTS, modulus and strain at break of –OH functionalized CNT containing PCL scaffolds. *102*

Figure 40: Overview of UTS, modulus and strain at break of PCL-grafted CNT containing PCL scaffolds. *103*

Figure 41: Comparison of the ratios for the increase in UTS (left) and modulus (right) of the literature. The ratios were created by taking the largest increase found with respect to pure PCL scaffolds. *105*

Figure 42: Change in degree of crystallinity (left) and crystallite size (right) with PCL-grafted CNT loading as measured by XRD. *106*

Figure 43: DSC thermograms for PCL scaffolds with different PCL-grafted CNT loadings. *107*

Figure 44: Close-up of a DSC thermogram of a PCL scaffold containing 5 wt% of PCL-grafted CNTs. Two distinct melting peaks are visible. *108*

Figure 45: Change in zeta potential of PCL scaffolds made from different solution concentrations and a CNT containing scaffolds with solution pH. *109*

Figure 46: SEM images of electrospun gelatin scaffolds made from solutions with different ages and different gelatin solution concentrations. All scale bars are 30 µm. *114*

Figure 47: Overview of the change in average fibre diameter with gelatin solution concentrations and solution age. *115*

Figure 48: Change in solution viscosity with both gelatin concentration and solution age. *116*

Figure 49: Comparison of the change in UTS, modulus and strain at break of electrospun gelatin scaffolds with gelatin solution concentration. *118*

Figure 50: SEM images of electrospun gelatin scaffolds containing 1 wt% (left), 2.5 wt% (middle) and 5 wt% (right) PCL-grafted CNTs. All scale bars are 9 µm. *119*

Figure 51: TEM images of PCL-grafted CNTs incorporated into gelatin nanofibres. *121*

Figure 52: Change in average fibre diameter in electrospun gelatin scaffolds with increased PCL-grafted CNT loading. *122*

Figure 53: Overview of UTS, modulus and strain at break of electrospun gelatin scaffolds with a change in PCL-grafted CNT content. *123*

Figure 54: Comparison of stress-strain curves for a pure electrospun gelatin scaffold (red) and a PCL-grafted CNT containing gelatin scaffold. *124*

Figure 55: Comparison of the average fibre diameter of the different types of scaffolds used for the cell study. *132*

Figure 56: Fluorescence microscopy image of neurons grown on a flat substrate after 7 days of cell growth. *133*

Figure 57: Fluorescence microscopy images of cells from the first batch grown for 7 days on the different scaffolds used. Top left: 3 wt% PCL. Top center: 5 wt% PCL. Top right: 7 wt% PCL. Bottom left: 1 wt% CNTs. Bottom right: 5 wt% CNTs. *134*

Figure 58: Fluorescence microscopy images of cells from the second batch grown for 7 days on the different scaffolds used. Top left: 3 wt% PCL. Top center: 5 wt% PCL. Top right: 7 wt% PCL. Bottom left: 1 wt% CNTs. Bottom right: 5 wt% CNTs. *135*

Figure 59: Comparison of the average cell count found on the different types of scaffolds and the control substrate after 7 days of cell growth. *136*

Figure 60: Comparison of the dendritic density found on the different types of scaffolds and the control substrate after 7 days of cell growth. *138*

Figure 61: Comparison of the average dendrite length found on the different types of scaffolds and the control substrate after 7 days of cell growth. *140*

Figure 62: Composite fluorescence microscopy image of neurons grown on a 5 wt% PCL-grafted CNT containing PCL scaffold exhibiting good interconnectivity and long dendrite outgrowth. *142*

Figure 63: FT-IR spectra of pure PCL (top), HFIP (middle) and an electrospun PCL scaffold (bottom). *151*

Figure 64: Low and high magnification SEM images of 3 wt% collagen (A and B respectively), 4 wt% collagen (C and D respectively) and 5 wt% collagen (E and F respectively). Scale bars are 50 µm for the left column and 5 µm for the right column of images. *153*

Figure 65. Change in average fibre diameter of electrospun collagen scaffolds as a function of collagen solution concentration. *154*

Figure 66: Low and high magnification SEM images of seven day old electrospun 3 wt% collagen (A and B respectively), 4 wt% collagen (C and D respectively) and 5wt% collagen (E and F respectively) solutions. Scale bars are 50 µm for the left column and 5 µm for the right column of images. *155*

Figure 67: Comparison of FT-IR spectra for pure collagen powder (top), HFIP (middle) and an electrospun collagen scaffold (bottom). Five prominent peaks found in HFIP are marked with red lines. 156

Figure 68: SEM images of the process of creating a cross-section in a FIB-SEM. Top: First cut perpendicular to the surface. Middle: Expansion of the area in front of the cut. Bottom: Tilted image of the created cross-section. 158

iii. List of Tables

Table 1: Overview of the mechanical properties of various human tissues. 30

Table 2: Comparison of the mechanical properties of Collagen scaffolds with PVA scaffolds. 30

Table 3: Overview of design objectives for neuronal tissue. 31

Table 4: Overview of scaffold porosity of a standard PCL and PMMA membrane. 47

Table 5: Overview of all the experimental runs and their parameters used for the PCL experimental series. Each run is repeated once except for the midpoint which is repeated eight times. 53

Table 6: Overview of the r^2 values of the models constructed for the average fibre diameter, the standard deviation of the fibre diameters and the area of deposition of the PCL scaffolds. 61

Table 7: Overview of the randomly chosen processing parameters used for the test experiments. 62

Table 8: Comparison of the predicted and measured values for the average fibre diameter, standard deviation of fibre diameters and area of deposition of the PCL scaffolds for the validation experiments. 63

Table 9: Overview of the processing parameters and experimental set-up for the PMMA experimental series. . 66

Table 10: Overview of the r^2 values of the models constructed for the average fibre diameter, the standard deviation of the fibre diameters and the area of deposition of the PMMA scaffolds. 72

Table 11: Overview of the randomly chosen processing parameters for the test experimental series. 73

Table 12: Comparison of the predicted and measured values for the average fibre diameter, standard deviation of fibre diameters and area of deposition of the PMMA scaffolds for the validation experiments. 74

Table 13: Overview of the processing parameters for the electrospinning of PCL scaffolds from the two experimental series. 78

Table 14: Overview of the processing conditions used for PCL scaffolds containing –OH functionalized and PCL-grafted CNTs. 93

Table 15: Overview of the processing parameters used for the scaffolds used for the streaming potential measurements. 94

Table 16: Overview of solution and processing parameters for the electrospinning of gelatin scaffolds. 112

Table 17: Overview of solution and processing parameters for the electrospinning of PCL-grafted CNT containing gelatin scaffolds. 112

Table 18: Overview of the processing and solution parameters used for the electrospinning of the cell study scaffolds. 129

Table 19: Overview of processing parameters for the electrospinning of collagen nanofibres. 152

iv. List of Equations

Equation 1: τ = mean size of ordered crystallite domains, K = dimensionless shape factor, λ = x-ray wavelength, β = FWHM of the line broadening, θ = Bragg angle. 43

Equation 2: X_c = Weight fraction extent of crystallinity, ΔH_f = enthalpy of fusion measured at melting point, $\Delta H°_f$ = enthalpy of fusion of the totally crystalline polymer. 47

Equation 3: Example polynomial that could be used for a statistical experimental design. In this case three main parameters, x_1, x_2 and x_3 together with their second-order interactions would be investigated by solving for a, b, c, d, e and f. 48

Equation 4: Overview of the polynomial constructed for the PCL experimental series. All first and second order interactions are being investigated, whereas only some of the third- order interactions are considered. x_1, x_2, x_3 and x_4 are voltage, distance, feed rate and concentration respectively and y is either fibre diameter, area-of-deposition or standard deviation. 50

Equation 5: Polynomial constructed for the PMMA experimental series. Only the main parameters and their potential non-linearity are considered for this model. 51

Equation 6: Calculation of the zeta potential where, dl/dp = slope of streaming current vs. differential pressure, η = electrolyte viscosity, ε_0 = permittivity, ε = dielectric coefficient of electrolyte, L/A cross section of the streaming channel. 94

Equation 7: Equation used for the estimation of reinforcement from a rule of mixture. E_c = Composite property, f = volume fraction of CNTs, E_f = CNT property (modulus or yield strength, E_m = bulk matrix property. 104

1. Introduction

We are living in a society that is experiencing both a demographic shift to a higher median age[1] and an ever increasing life expectancy[2]. These developments pose significant challenges as health care costs are exploding across developed countries[a] [3]. The scientific and medical communities strive to develop improved or new methods of treatment and approaches to guarantee our standard of living for future generations. Aging-associated, neurodegenerative diseases, such as Dementia, Alzheimer`s Disease, Parkinson's etc., will become more prominent [4] and there will be a greater need to understand, treat and possibly cure these diseases. Current *in vitro* neurological models are "crude" (Abbott et al. 2000) and there is a need to develop models that are closer to human *in vivo* conditions[5] in order to fight these diseases[6]. Additionally the need for donor tissue in organ transplants already greatly exceeds the availability which is likely to worsen in the future[7].

Our bodies have the remarkable ability to heal themselves. This mechanism is greatly inhibited by diseases and injuries, such as the aforementioned. The use of prostheses, such as, "*mechanical heart valves, intra-ocular lenses and metal, plastic and ceramic orthopaedic implants*" (George, J 2004)[8] only delivers a limited regain of the original tissues' functionality. A more promising approach would be to use the regenerative abilities of the human body and enhance them. This thesis considers the formation of artificial extra-cellular matrix substitutes to investigate their application for neuronal cell regeneration.

1.1. Regenerative Medicine

"*Regenerative medicine replaces or regenerates human cells, tissue or organs, to restore or establish normal function*" (Mason and Dunnill 2008)[9] . It is an emerging, interdisciplinary field of research that utilizes a large variety of different techniques[10], such as "*gene therapy, stem cell transplantation, tissue engineering and the reprogramming of cell and tissue types*" (Greenwood et al. 2006)[11] to enhance human well-being. Until it is possible to replicate or surpass the functionality and complexity of

[a] The health care costs as a part of the GDP across OECD countries has been rising continuously for the past 20 years beyond inflation[415].

biological tissues with artificial systems the use of regenerative medicine appears to be the best choice to improve and maintain the health of our society in conjunction with traditional health care.

1.2. Tissue Engineering

Tissue engineering is "*an interdisciplinary field that applies the principles of engineering and life sciences toward the development of biological substitutes that restore, maintain, or improve tissue function or a whole organ*" (Langer & Vacanti, 1993)[12]. Tissue engineering harnesses the regenerative abilities of natural tissue by using healthy cells from the tissue that is to be repaired[8]. These cells are seeded unto specially tailored scaffolds, comprised of either artificial[13–17], natural materials[18–22] or both[23–26]. The tissue is then cultivated *in vitro* and then implanted in the patient (Figure 1)

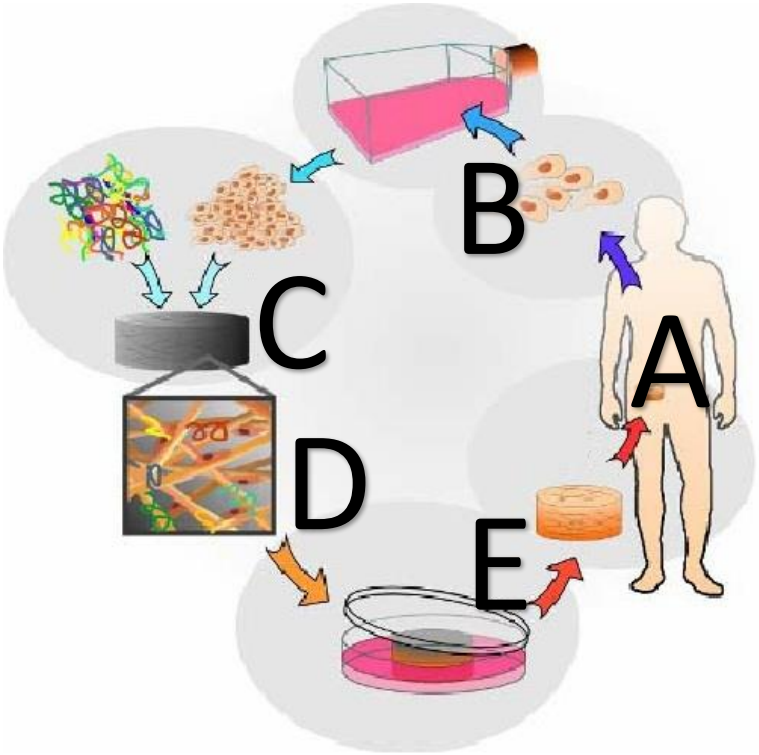

Figure 1: Schematic of the principle of tissue engineering[8]: A sample of the target tissue is extracted from the patient (A) and screened for phenotype, as well as cultivated in a bioreactor (B). The cells are then seeded on a porous scaffold in conjunction with growth factors in order to increase proliferation (C). The seeded scaffolds are placed in bioreactors for an additional increase in cell number (D). In a last step, the re-grown tissue is medically implanted back into the patient (E).Taken from George (2004)[8]

1.2.1. Examples of Tissue Engineering

Almost all of the tissues in the human body can be used for tissue engineering. Examples *in vitro* grown tissues include skin, bone, cartilage, tendon, blood vessels, teeth, heart valves and muscles, bladder, liver, neural tissues, kidney and a trachea (Figure 2)[9,10,27–30].



Figure 2: An in vitro grown trachea, made from stem cells from the patient on a nanocomposite scaffold. Taken from Harvard Bioscience Inc.[31]

Another interesting use of tissue engineering is the production of *in vitro* cultured meat[32]. It would not only eliminate the ethical problems with factory farming but also be considerably more environmentally friendly[33] (Figure 3). If the mass production of "lab meat" is successful and embraced by consumers it could very well represent a viable option to combat food shortages. [34] .

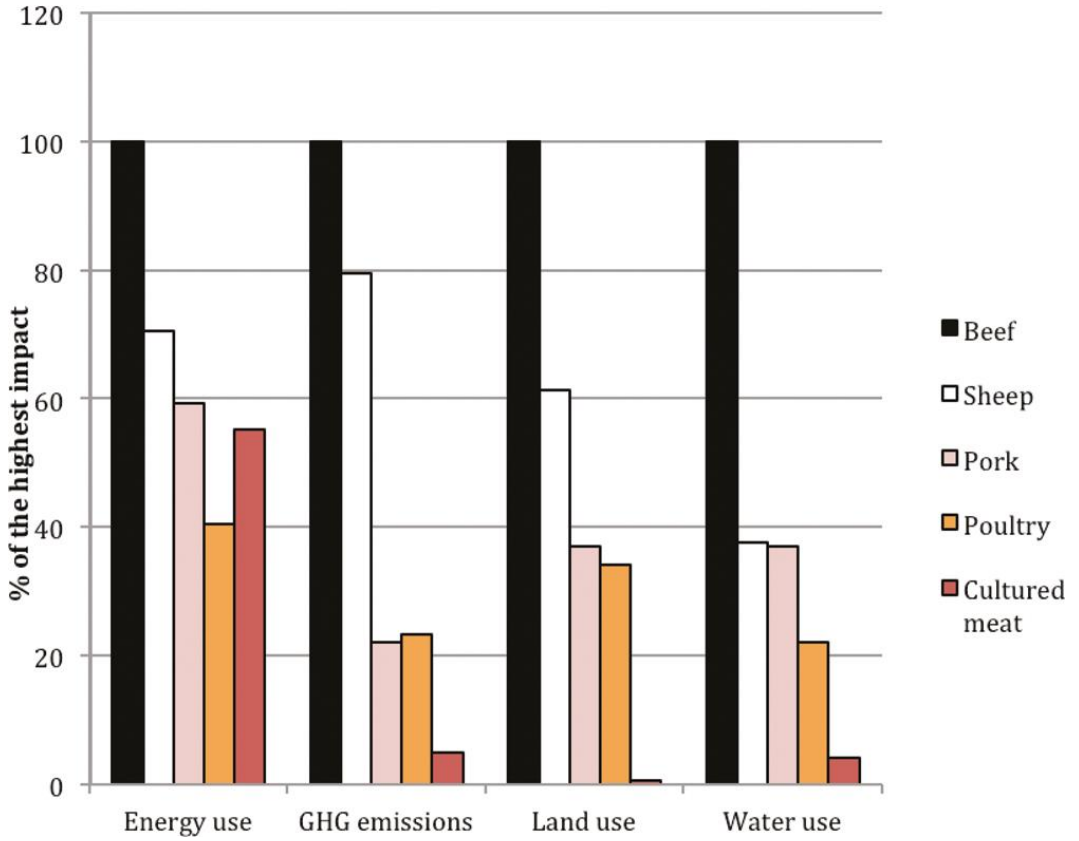

Figure 3 Comparison of the environmental impact of different kinds of meat in contrast to culture meat (normalised for beef).Taken from Tuomisto (2011)[33]. GHG stands for greenhouse gas.

1.2.2. Cell/Matrix Interactions

One of the most important factors in facilitating and tailoring scaffolds for tissue engineering (TE) is a thorough understanding of the interactions between the cells and the surrounding matrix. *In vivo*, the extracellular matrix (ECM) not only provides mechanical support to cells, but also acts as a "conductor" for the cell behaviour[35–39]. The aim for a suitable human-made scaffold must be to match the level of sophistication and utility found in nature. Recent developments in the fabrication of scaffolds offer the possibility to reach that level of complexity[40–46]. *In vivo*, cells are in a delicate balance with their surrounding environment, constantly maintaining the ECM through the expression of the correct types and ratios of proteins and glycosaminoglycans[16,47]. *Vice-versa*, the cell behaviour is regulated through the availability of binding sites on the ECM – with the correct densities, conformation and presentations to the receptor in the cell membranes[8] – that are imperative to cell function. In fact the ECM is a necessary requirement of multi-cellular life[48]. The most primitive form of the ECM can be found in the green algae *Volvox*, a member of the Chlorophyte genus, which is believed to be the first life form to develop a ECM[49]. It can be concluded that - in order for TE to be successful - it is imperative to match

the morphology, mechanical properties and surface chemistry of the scaffold to the target´s *in vivo* cellular surrounding.

1.2.3. Advantages of Nanofibrous Scaffolds

It is evident that any technique chosen to create an ECM-like substitute should be able to produce a porous, ideally fibrous structure. A simple overview of commonly used scaffold structures is shown in Figure 4:

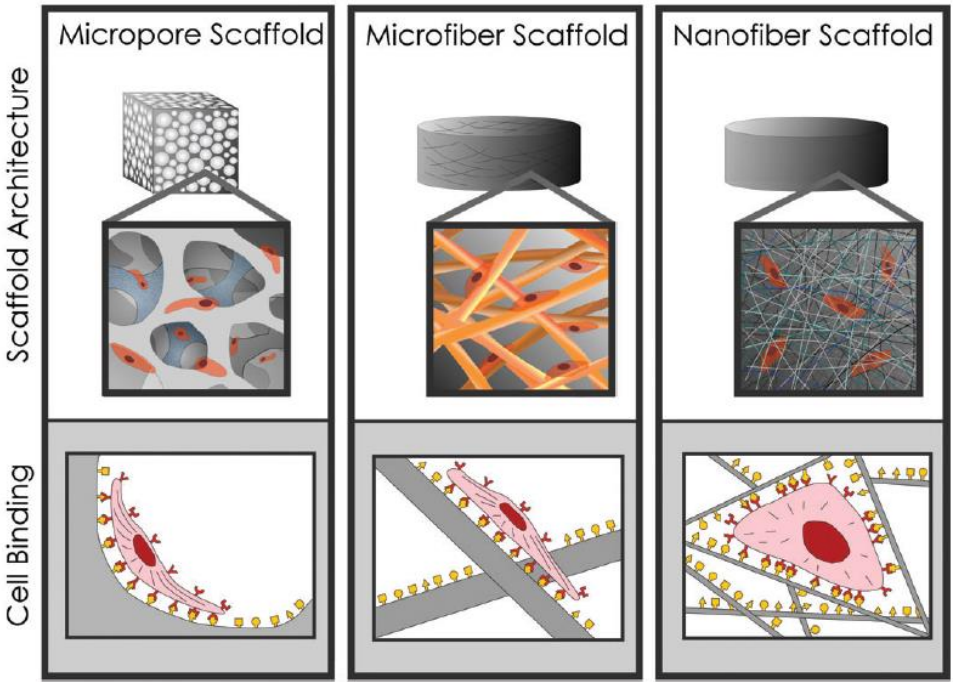

Figure 4 Simple overview of different achievable scaffold morphologies with current technology and the type of cell binding found with those morphologies. Taken from George (2004)[8].

As can be seen from Figure 4 the micropore and microfiber scaffolds – although possibly having the right surface chemistry and mechanical properties – provide only a limited surface area for cell-matrix interactions akin to a plain flat 2D substrate.

The ECM consists of nanofibrils in the range of 10 nm to 300 nm with a complicated surface structure[39]. While the cellular response to micro-topological features has been well established[50], there is limited understanding with regards to nano-features, such as ridges, steps, grooves, pillars and pits[51–57]. It is apparent that in order to create a more complex tissue, one has to be able to manipulate the scaffolds at these lengths scales. A nanofibre scaffold has a much closer resemblance to the ECM and offers a much larger surface area on which the cells can attach.

1.3. Electrospinning

Electrospinning is a fibre-producing technique in which a liquid polymer solution is drawn though a needle by electrohydrodynamic atomisation resulting in nanometre sized polymer fibres[58]. The first descriptions of the electrospinning (ES) process through patents date back as far as 1902[59] (although scientists have been using electrostatic forces to deform liquids for centuries[60]). The first steps towards a description of ES can be traced back to William Gilbert (1544 – 1603) – who discovered that a water droplet was drawn up in a conical shape in the proximity of a piece of rubbed amber[61] – and Jean-Antoine Nollet (1700 – 1770) – who demonstrated that a water jet would disintegrate when a charge was applied to it[62] – but it took another 300 year until the aforementioned patent, as there was no feasible way to achieve the high voltages necessary for ES in those times. The commercial use of ES however was limited to filtration products until 1990.

1.3.1. Basic Principles of Electrospinning

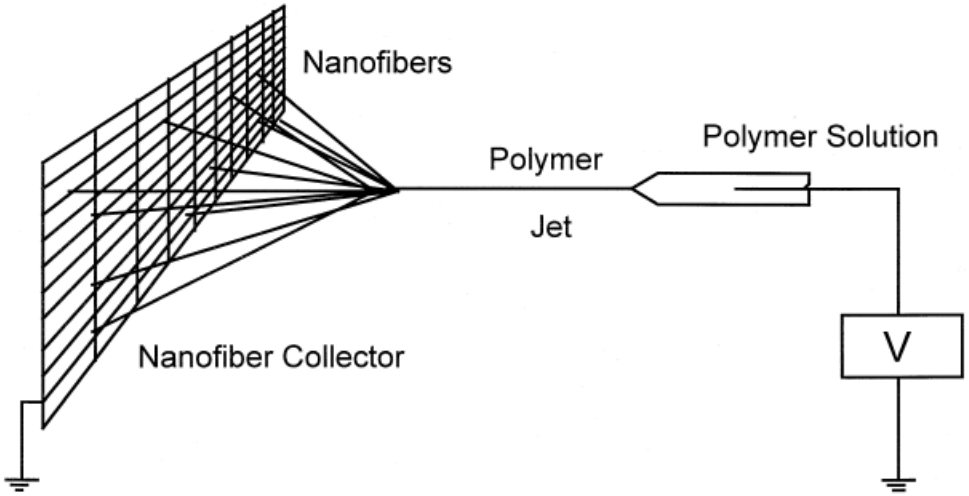

Figure 5: Schematic of a Basic ES set-up. Taken from Norris et al. (2000)[63].

The ES processing method utilizes a strong electric field generated by a high voltage power supply between a polymer containing fluid and a grounded conducting collector (Figure 5). The high voltage creates an unstable, electrically charged jet which ejects from a nozzle, and undergoes very large stretching. During flight and at the arrival on the conducting collector the solvent evaporates and the polymer solidifies, creating polymeric fibres. These fibres have a diameter scale in the nanometre regime[64], with fibre diameters as low as ~9 nm[65] up to several µm[66]. With the use of factorial

experimental designs[67] it is possible to establish the statistical significance of the processing parameters involved. This leads to a great control over the fibre properties with the possibility to precisely regulate the desired fibre morphology[68]. The ES process is initiated by the strong electrical force – generated by the high voltage power supply – that acts on the free ionic charges in and on the surface of the polymer/solvent mixture[60]. In contrast to other spinning methods[60] during ES, only the axial – as well as the non-axial – force exerted by the electric field drives the fibre formation. The movement of the ionic charges in the electric field within the solution exert a force to the polymer liquid. Once a critical threshold value for the strength of the electrical field is reached a so called "Taylor cone"[69] is formed. A stable jet of the solution ejects from the nozzle. After a short distance travelled, the balance between the axial and non-axial forces inverts due to a reduction in diameter. The jet becomes unstable because of the same number of charges now act on less material due to the evaporation and stretching of the solution. The path of the jet becomes highly chaotic until it reaches the target (Figure 6)[69].

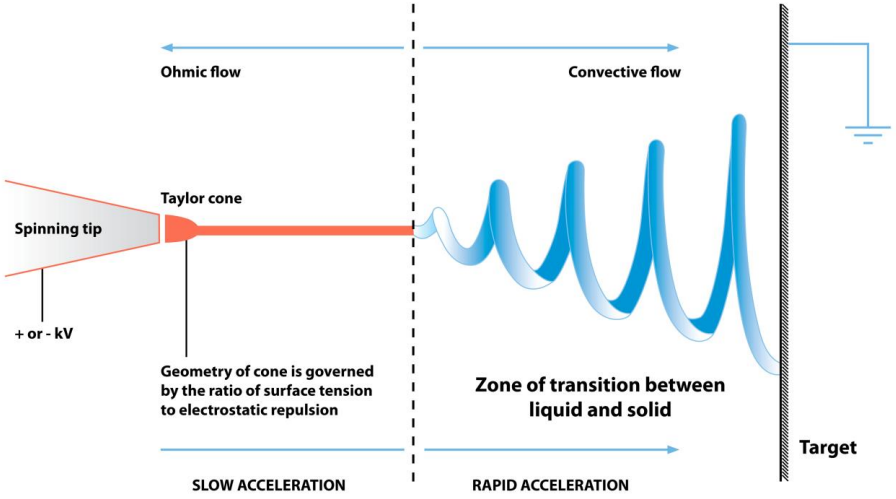

Figure 6 Detailed illustration of the formation of fibres and the jet behaviour during ES. Taken from Joanna Gatford - The New Zealand Institute for Plant and Food Research Ltd[70].

The theoretical understanding of ES complicated. On one hand the forces involved are understood and well-described. However, albeit the first description of electrospinning dates more than 100 years ago, there is no full mathematical account available that would allow *ab initio* predictions of fibre properties[71]. Nevertheless there are several empirical and semi-empirical[69,72–76] models that are able to describe some properties of the ES process. This lack of an applicable model makes ES both a very empirical branch of materials science and a very active field of research, as demonstrated by the current number of publications[b] .

The simplicity of the processing and low costs of the ES technique make it an attractive candidate for the production of scaffolds for TE.

1.3.2. Electrospinning Parameters

Despite the aforementioned difficulty in a complete theoretical description of all the electrospinning parameters there exists a good empirical understanding of how various processing parameters impact the spinning process[77]. These parameters can usually be broken down into three different categories: Solution parameters, such as solution viscosity, molecular weight of polymer, solution conductivity and surface tension. Processing parameters, such as voltage, spinning distance, spinning time, polarity, etc. And finally environmental parameters, such as, humidity, temperature, air flows etc. While some

[b] Self-conducted literature survey using Web of Knowledge and Scopus.

parameters seem to affect the properties of the electrospun scaffolds in similar ways across different polymer/solvent systems others are not. Hence for the use of a new polymer/solvent system it is often difficult to predict how a specific parameter will impact things like average fibre diameter or porosity. A more detailed discussion can be found in Chapter 3.

1.3.3. Uses of Electrospinning

Electrospun scaffolds are already an established product for the use in TE. There are several companies (Donaldson Company Inc., The Electrospinning Company Ltd., Hills Inc., Nanoforce Technology Ltd.) that sell commercial electrospun scaffolds for the use in research and medical applications, such as skin grafting[78]. Substrates made by ES are used in several studies for bone, skin, heart and neuronal models[30,79–81] due to their similarity to the ECM. Nonetheless ES has found application in areas well beyond TE. Electrospun nanofibres show promising potential in areas such as, drug delivery[82–87], biosensors[88–90], bioreactors[91], particle removal filters[92–95], organic waste removal[96], as active filter in HAZMAT suits[80] and membranes for super capacitors[97–101] and novel, high-performance batteries[102].

1.3.4. Recent Advances in Electrospinning

The advent of nanotechnology in the past two decades has reignited research effort in the field of ES. The combined commercial and scientific interest yielded major advances in the field exemplified by more specialised alterations to the basic ES set-up (Figure 5). The greater part of the technical innovations can be attributed to changes in the way the nanofibres are collected or the way the solution is delivered. The main aim with varying collector geometries is to achieve fibre alignment in specific

directions, or to cover a predesigned shape in nanofibres. Examples of some of the different macroscopic structures that can be obtained are shown in Figure 7.

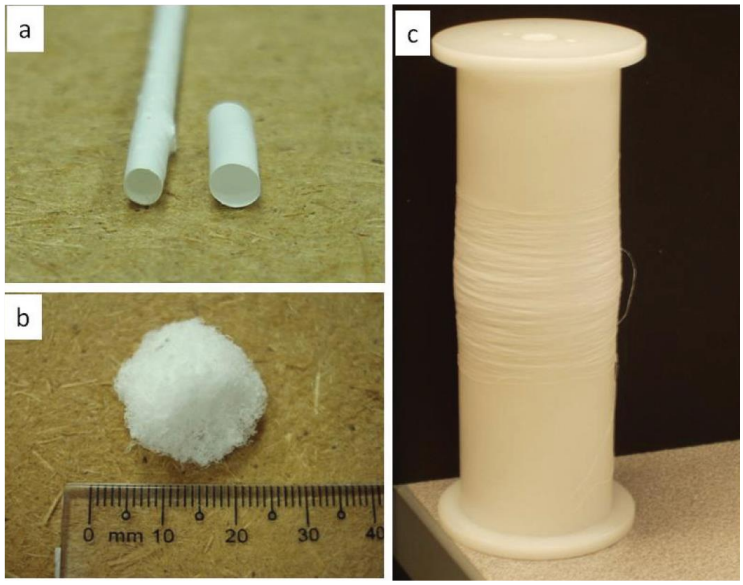

Figure 7: Various forms of electrospun fibres. A) Electrospun tubes. B) 3D scaffold and C) Continous yarn[103].

Using a combination of differently shaped electrodes with several ES runs it is possible to create even more complicated shapes, such as interconnected tubes (Figure 8). Taken from Teo et al. (2011)[104].

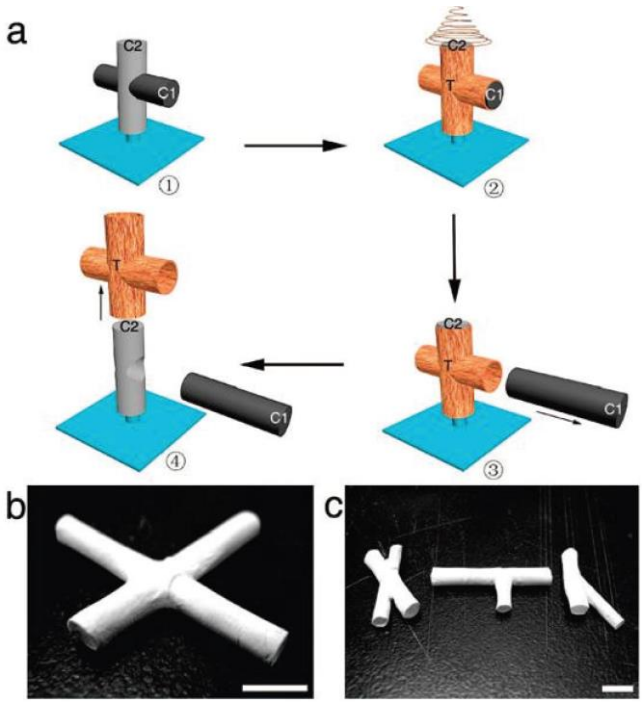

Figure 8 Different, interconnected tubes made by the use of different collectors. A) Schematic of the fabrication process. Hollow tubes are used as templates that can be removed after fibre deposition. B) Final structure resulting from the above schematic. C) Various other shapes of interconnected tubes that could be produced with that technique. (Scale bar = 5 mm).Taken from Zhang et al. (2008[104].

Recently advances in the mass production of nanofibres via ES have been achieved. New yarn-producing techniques with high production capabilities ranging from 0.234 m min-^{1} [105] to 3 m min-^{1} [106], 10 m min-^{1} [107], 12 m min-^{1} [108], 30 m min^{-1} [109], 45 m min-^{1} [110], 54 m min -^{1} [111], 63 m min-^{1} [111], 258 m min-^{1} [112] to an astonishing 894 m min-^{1} [112] are currently being explored and open up possibilities to expand the use of ES nanofibres. Concurrently techniques for large areas of deposition are becoming more viable (Figure 9).

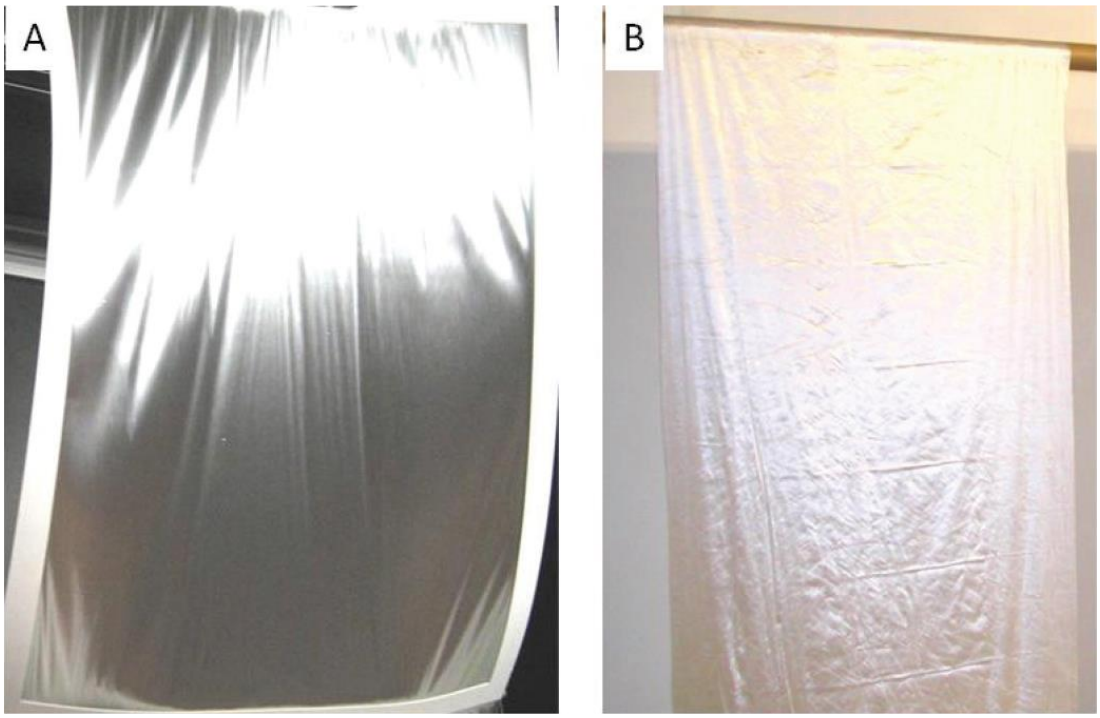

Figure 9: Aligned electrospun meshes. A) A4 sized membrane. B) 1m wide and 3m long membrane. Taken from Teo et al. (2011)[103].

As more processing variations are being explored and become available to use it can be expected that the research intensity in the field of ES is going to continue in growth and more products and studies containing electrospun nanofibrous scaffolds will emerge.

1.3.5. Challenges of Electrospinning in Tissue Engineering

ES is a fibre producing technique that allows the formation of polymer and ceramic nanofibres [113,114] with great control over properties[68] and morphology[81] while offering acceptable production rates at low production costs[80]. These factors make it a good candidate as a processing method for TE scaffolds. Nevertheless, there are still a lot of challenges to overcome to reach a level of complexity analogous to the biological scaffold, the ECM.

1.3.6. Comparison to the Extra Cellular Matrix

The ECM is a highly specialised and functionalised mix of Proteoglycans, Heparan sulphate, Chondroitin sulphate, Keratan sulphate, Hyaluronic acid, different kinds of Collagen, Elastin and various other proteins with specialised purposes[37,48]. The specific, local composition of these proteins will determine the role of that particular tissue as well as the mechanical properties. Determining the exact composition for different kinds of tissue in itself is a non-trivial task[48] and hence replicating it is even more difficult. It is possible to electrospin bi- [97,115,116], tri- [117] and even four [118]-component system. However there is currently no technique available that allows local variation of this composition without interrupting the fabrication or post processing.

Additionally, not only the composition but also the position and morphology of the ECM is essential to ensure proper functionality. Even though it is possible to create aligned fibres and control the structure of the fibres during ES, it is not yet possible to precisely control the deposition area[c]. A very promising approach was taken by Hellmann et. al. (2009)[119]. A precision displacement unit was used and only operated in the stable jet regime (Fig. 6). The resulting fibre diameters were >500 nm and the deposition speeds were very low. The path width of the spun fibres could be lowered to <100 µm, which represents a large improvement over conventional ES. The most important milestone for the establishment of ES as a technique for TE is the development of a high precision, multi-component set-up. Given the current state of the literature on ES it is certainly a possibility that this technique can evolve into a cheap, up scalable rapid-prototyping fabrication method for lab grown tissue.

1.3.7. Comparison of Synthetic and Organic Polymers

It is not only the chemical environment that dictates the cell behaviour. The mechanical properties, such as Young's Modulus and tensile strength also play an important role in cell expression and proliferation[120]. Therefore it is important that the mechanical properties of the electrospun scaffold

[c] Typical deposition areas for conventional ES are in the range of several cm² [111,119,416,417]

match those of the target tissue. An overview of typical values for the tensile strength and Youngs' modulus for different kinds of tissues is given in Table 1.

Tissue Type	Tensile Strength (MPa)	Youngs' Modulus (GPa)
Cancellous Bone[121]	N/a	0.02 – 0.5
Cortrial Bone[121]	60 – 160	3 – 30
Cartilage[122]	3.7 – 10.5	0.7 – 15.3 (MPa)
Ligament[122]	13 – 46	0.065 – 0.541
Tendon[122]	24 – 112	0.143 – 2.31

Table 1: Overview of the mechanical properties of various human tissues.

Another important factor for the biocompatibility of the scaffolds used is the cytotoxicity of the polymers utilized. The pure polymer and its possible degradation products must be compatible with the surrounding tissue and biodegradable in the human body. Using natural polymers such as Collagen [19,29], Chitosan[123], Gelatine[124], Alginate[20], Fibrinogen[26], Cellulose acetate[24,96,125,126] and silk[18,127–129] have the obvious advantage of being biocompatible. However there are processing difficulties associated with protein denaturation[130] when using biological polymers. Artificial, degradable polymers need to be carefully tested before used *in vivo*. Their degradation products may be harmful and cause inflammatory reactions. The advantage of artificial, degradable polymers, such as PLGA[131–135], PCL[85,124,136–139], PLLA[17,107,110,140–142], PU[95,143–146], PEO[23,63,119,147–149], PVA[106,115,116,147,150–152], lie in the ease of the processing and the ability to tailor the mechanical properties for the application required[153]. Artificial polymers can be spun into fibres with higher tensile strengths and moduli (Table 2) thus could be more suitable for structural tissues, or as blends, together with a natural polymer.

Polymer	Tensile Strength	Youngs' Modulus
Collagen [19,154]	0.15 MPa	52.3 MPa
PVA [150]	6 MPa	175 MPa

Table 2: Comparison of the mechanical properties of Collagen scaffolds with PVA scaffolds.

1.3.8. "Design Objectives" for Electrospun Scaffolds in Tissue Engineering

When considering the design objectives for any device used in tissue engineering it is important to tailor the properties of the device to its use as well as the target tissue. In the case for electrospun scaffolds a compromise has to be struck between what is achievable and what is feasible. Depending on whether the scaffold will be used in an *in-vitro* or and *in-vivo* environment there are additional design criteria on the scaffolds. In this work various types of electrospun scaffolds are made, characterized and then utilized as substrates for the *in-vivo* growth of neurocytes. Table 3 shows an overview of some design benchmarks for such a substrate based on the properties of the ECM of the brain:

Fibre Diameter	~100 nm – 1000 nm [155]
Stiffness	~ 2 kPa[156,157]
Porosity	~15% - 30%[158] (NOT decellularized!)
Electrical Conductivity	~0.344 Sm^{-1} to 2.225 Sm^{-1} [159]

Table 3: Overview of design objectives for neuronal tissue.

To the best of the author´s knowledge, there is no comprehensive and definite account of the physical properties of the ECM of the brain. In order to accurately measure the physical properties it is necessary to fully decellularize brain tissue. With current methods, this is not possible without aggressive detergents that might alter the physical properties and still leave residues of cells behind[155]. The value above given for the porosity for example is for the extracellular space in the brain, which includes cells. An estimate for the porosity without any cells present is in the range of 65% - 80%[158]. The range of fibre diameters shown in table 3 is easily accessible through electrospinning.

In addition to the target properties that are being aimed for when producing such scaffolds, one has also to bear in mind the practical use of them. Even scaffolds for *in-vitro* use need to withstand the experimental protocol and sterilization procedures, which make it difficult to handle scaffolds with weak mechanical properties. Recently it has been shown that high-porosity scaffolds are desirable, even if their porosity is larger than the target tissue, as it allows for a more effective cell infiltration[160].

1.4. The Use of Composite Nanofibres

Due to the aforementioned low tensile strengths of pure polymer nanofibres compared to some of the more structural tissues found in the human body (Table 1.) it is desirable to further increase and tune the mechanical properties of electrospun fibres. One such way would be the incorporation of filler materials to create a composite incorporating Hydroxyapatite or Carbon Nanotubes.

1.4.1. Hydroxyapatite

Hydroxyapatite ($Ca_5(PO_4)3(OH)$) is a natural occurring mineral that can be found in the human body and is one of the main components of bones[161]. Due to its biocompatibility it is commonly used in TE applications[17,131,132,140–142] as well as prosthetics[162,163]. Recently it has been used in ES as a filler material in bone replacement studie [131,140,142]. The studies show an increase in cell proliferation in comparison to neat substrates without Hydroxyapatite (HA)[131,142]. A recent animal model study successfully used electrospun PLLA fibres with HA to repair damaged sterna bones more effectively and faster than the natural regeneration rate[141]. The addition of HA is necessary for the growth of bone tissue as it is a structural component of the bone.

1.5. The Use of Carbon Nanotubes in Tissues Engineering

A carbon nanotube (CNT) is a rolled-up sheet of graphene[164,165] (Two dimensional sheet of hexagonally arranged carbon). If the tube consists of a single graphene layer it is called a single-walled carbon nanotube (SWCNT); if it is made up of two layers it is referred to as a double-walled carbon nanotube (DWCNT). And finally, a CNT consisting of more than two layers is called a multi-walled carbon nanotube (MWCNT).

1.5.1. A Brief History of Carbon Nanotubes

Sumio Ijima is often credited with the discovery of CNTs[166]. However there are accounts in the scientific literature – Dating back as far as 1952 – that clearly show CNTs prior to Ijimas' work[167–169]. Ijima was the first person to accurately describe the structure and brought CNTs into the focus of the scientific community, yielding a plethora of publications on that subject. There are two predominant synthesis techniques used for the production of CNTs. The first one utilized is the so called arc-discharge method.

Ijima used that method based on the process utilized for making fullerenes[170]. The arc-discharge method consists of passing a strong electric arc between two graphite rods and collecting and purifying the resulting soot. This method produces high-quality CNTs in low quantities[171,172]. The majority of CNTs nowadays are produced via the chemical vapour deposition (CVD) technique first used in 1993[173]. Most CNT-producing companies utilize the CVD method (Such as: NanoLab, Arkema, Nanocyl, Nanothinx, Hyperion Catalysts, Mitsui, Showa Denko etc...). Chemical vapour deposition produces CNTs by passing a carbon precursor into a reaction chamber at elevated temperatures. The precursor decomposes and forms CNTs in the presence of catalysts. The quality of CVD produced CNTs is generally believed to be inferior to the arc-discharge method[174]. Since the rediscovery of CNTs by Ijima a wide range of different structures have been synthesised that are collectively called CNTs[173,175–178].

1.5.2. The Properties of Carbon Nanotubes

The major reasons for the aforementioned research efforts are the extraordinary properties of CNTs. They have diameters ranging from 0.3 nm[179] to ~100 nm with lengths from several nm to mm, yielding aspect ratios of up to 10^6. The physical and chemical properties of CNTs depend on the synthesis technique used.

The mechanical properties of arc-discharge CNTs are exceptionally high. They exhibit a Youngs' modulus of ~1.28 TPa[180] or 0.27 – 0.95 TPa[181], depending on the method used for measurement. The strength of these CNTs lie in the range of 11 – 63 GPa[181]. CVD grown CNTs display moduli in the range between 12 – 50 GPa – i.e. 20 times smaller than for arc-CNTs – [182] and strengths of around ~3.6 GPa[180].

The electrical properties of CNTs are strongly correlated with their internal structure similar to their mechanical properties. The electrical properties of SWCNTs have attracted great attention. Their electric properties are depending on their chirality and diameter, and can be either metallic or semiconducting[183]. They exhibit very low resistivities, in the range of 0.3 to 1 μΩm[184] and single-electron conductance[185] with minimal Joule heating, allowing them to carry large currents of up to 100 MA/cm² [186]. Carrier mobilities exceeding those of any known semiconductor, in the range of about 10^5 cm²/Vs, were observed in semiconducting SWCNTs[187]. The electric properties of MWCNTs are more difficult to

summarise, as they are strongly dependent on the synthesis technique used. Ballistic transport properties were shown to be exhibited by high-quality arc-MWCNTs, with "*extremely high stable current densities, J > 10^7 amperes per square centimetre*" Frank et al (1998)[188]. Ebbesen et al. (1996)[189] measured the resistance of several arc-MWCNTs and found that they differ by several orders of magnitude, indicating a strong correlation between structure and their properties. The resistance varied between $2 * 10^2$ - $2.4 * 10^8$ Ω and the corresponding resistivities, assuming a hollow conductor with an inner diameter of 2 nm, was 0.8 – 5.1 * 10^{-6} Ωcm[189]. The conductivity of CVD-grown CNTs usually lies in the range of $5.4*10^4$ S/m – $2.61*10^5$ S/m[d]. The thermal conductivity of individual MWCNTs was measured to be at around 3000 $Wm^{-1}K^{-1}$ [190]. The surface of CNTs can also be modified chemically to change the hydrophobicity of the CNTs and to add functional groups[191]. This can be utilized to disperse the CNTs in different kinds of solvents. These properties make CNTs a very attractive material for the use in TE applications.

1.5.3. Examples of Carbon Nanotubes for Regenerative Medicine

Since the rediscovery by Ijima in 1991, CNTs were used for several different applications in regenerative medicine. There are four areas where CNTs are being employed to enhance functionality:

1.5.3.1. Cell tracking and labelling

Nucleic-acid encapsulated SWCNTs were used for optical *in-vivo* labelling of mural 3T3 cells and mural myoblast stem cell[192]. It was found that their employment did not affect the cell proliferation, they remained active for over three months and did not exhibit photobleaching, making them a promising material for use in optical labelling. Additionally ultra-short SWCNTs loaded with gadolinium displayed proton relaxivities ~40 to ~90 times higher than standard clinical contrast agents[193], potentially replacing other standard MRI contrast agents.

1.5.3.2. Sensing Cellular Behaviour

"*The ability to monitor cellular physiology such as ion transport, enzyme/cofactor interactions, protein and metabolite secretion and cellular behaviour such as matrix adhesion could help design better*

[d] Private correspondence with Zabeada Aslam (Department of Materials, Oxford).

engineered tissues." (Harrison, Atala, 2007)[194]. The electrical properties of CNTs become increasingly sensitive to surrounding electrical charges when a bias is applied across them[195]. This can be utilized through the functionalisation of the surface with chemical groups to make them selective for specific chemicals. A number of examples exist in the literature. Tan et al. (2005)[196] used a MWCNT-containing biosensor to accurately measure the cholesterol concentration in human blood samples while the sensors exhibited a "*high sensitivity, good repeatability and reproducibility, rapid response, good selectivity, and long-term stability*". Other examples of the use of CNTs for biosensors include platinum coated MWCNTs for the sensing of thiols[197] and the detection of putrescine with a MWCNT/glass biosensor[198].

1.5.3.3. Augmenting Cellular Behaviour

CNTs can be utilized to deliver designated substances to tissues. This would be specifically useful for TE applications where growth factors need to be transported to the tissue. Another major area is drug delivery. Due to the possibility of functionalising the surface of CNTs they can be used to deliver chemotherapeutic agents for cancer treatment. CNTs were shown to penetrate the cell membrane in several studies[199,200] and have thus attracted a lot of attention for the above-mentioned drug-delivery applications. In one study paclitaxil (a commonly used cancer chemotherapy drug) was linked to the end groups of PEG (Polyethylene glycol) functionalised SWCNTs[201]. The SWCNT approach resulted in a 10-fold higher drug accumulation on tumour sites compared to the standard clinical procedure resulting in the inhibition for the 4T1 tumour model which is known to be resistant to paclitaxil treatment[202]. In another study SWCNTs functionalised with folic acid and PEG were used for the hyperthermic treatment of cancer[203]. SWCNTs successfully bound to cancer cells and were not found inside normal, healthy cells. After exposure to NIR radiation with a 808 nm laser the cancer cells were killed while healthy cells were unaffected.

1.5.3.4. Matrix Enhancement

The aforementioned mechanical properties of CNTs make them an ideal candidate for the reinforcement of TE scaffolds. There are plenty of examples of the use of CNTs for matrix enhancement[194,204] however this review will focus on the use of CNTs in electrospun scaffolds. The first documented incorporation of CNTs in electrospun nanofibres dates back to the year 2000 by Schreuder-Gibson et al.[205] at a

symposium at the 197th ECS meeting. In this military-driven study, CNTs were dispersed in blends of polyurethane and polyaniline. The dispersion of the CNTs within the fibres was imperfect as the authors noted but they still managed to increase the conductivity of the fibres which was the main goal of that work. The first journal article was published in 2003 by Seoul et al.[206]. The authors successfully dispersed SWCNTs in PVDF [Poly(vinylidene fluoride)] which resulted in a five-order of magnitude increase in conductivity in comparison to neat PVDF fibre mats. Since then a large variety of different kinds of CNT/polymer systems have been explored. The list of polymers used includes:

CA/PAN[207], Cellulose[125,126], Chitosan/PVA[123], Nylon 6[208], Nylon 6,6[209,210], PAH[211], PAN[207,212], PANI[148,149,213], PBT[214], PCL[137,139], PE[215], PEO[147–149], PET[216,217], PHBV[218], PI[219], PLA[220,221], PLGA[132,133,222], PMMA[223–226], PS[146,227], PSS[211,228], PTT[229,230], PVA[147,150–152,231], PVDF[206,232,233] and Silk Fibrosin[127,129,234].

The mechanical and electrical properties properties of the as-spun scaffolds are sometimes investigated and it is generally agreed on the beneficial influence of CNTs.

The relationship of the electrical conductivity and the CNT concentration is much clearer in comparison to the mechanical properties. As the CNT concentration is increased, the electrical conductivity of the electrospun scaffolds increases drastically. The increase in conductivity saturates once the electrical percolation limit is reached[235]. If the polymer used is non-conductive the increase can be over several orders of magnitude (Figure 10). As a point of comparison the conductivity of rat neuronal ECM taken from Gleixner et al. (2006)[236] was added to the graph to give an reference as to what level of conductivity would be desirable for electrospun scaffolds for neuronal tissue engineering.

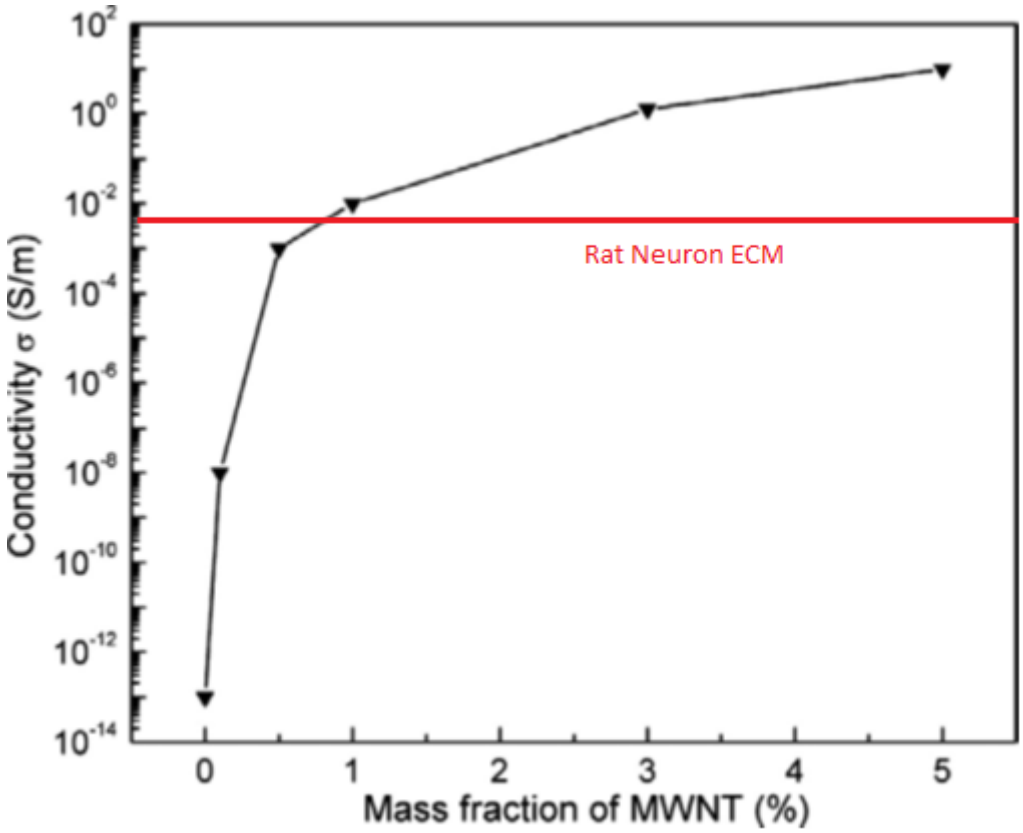

Figure 10 Conductivity of PVA fibres as a function of the MWCNT content. Taken from Wang et al. (2006)[151].

There are several accounts available on the beneficial impact of the incorporation of CNTs on cell growth and proliferation, dating back as early as 2007[142]. Albeit there is a limited amount of literature at hand it is still possible to draw conclusions on the viability of the incorporation of CNTs in electrospun scaffolds. In an early study Mei et al. (2007) found that the addition of CNTs to a PLLA/HA scaffold significantly improved the cell proliferation and number of periodontal ligament cell compared to a neat PLLA/HA scaffold and a commercially available control group[142]. In a different study, Meng et al. (2009)[237] utilized a CNT/PU scaffold to investigate the growth of fibroblast cells. "*The scaffold with the nanofibrous architecture and MWNTs component significantly enhances the cell adhesion, proliferation, migration and aggregation, and secretion*" (Meng et al. 2009) in comparison to the neat fibres without the addition of CNTs. In a more recent investigation Meng et al. (2010)[144] were able to show that electrospun CNT/PCL scaffolds not only possess good biocompatibility features but also outperform neat PCL scaffolds and commercially available glass substrates in terms of anticoagulant properties (i.e. Hemoglobin concentration of a blood-containing solution is higher than for non-CNT scaffolds when the scaffold is immersed in the solution.). Shao et al. (2011)[220] were able to utilize the increased electrical conductivity that results from the inclusion of CNTs for the proliferation and

function of Osteoblasts. It was found that while there was no difference between a standard tissue culture plate and electrospun PCL scaffolds in terms of Osteoblast proliferation at standard conditions the application of a small DC current significantly stimulated growth of the cells on the CNT containing scaffolds (Figure 11), possibly due to the preferential adsorption of select proteins with electrical stimulation.

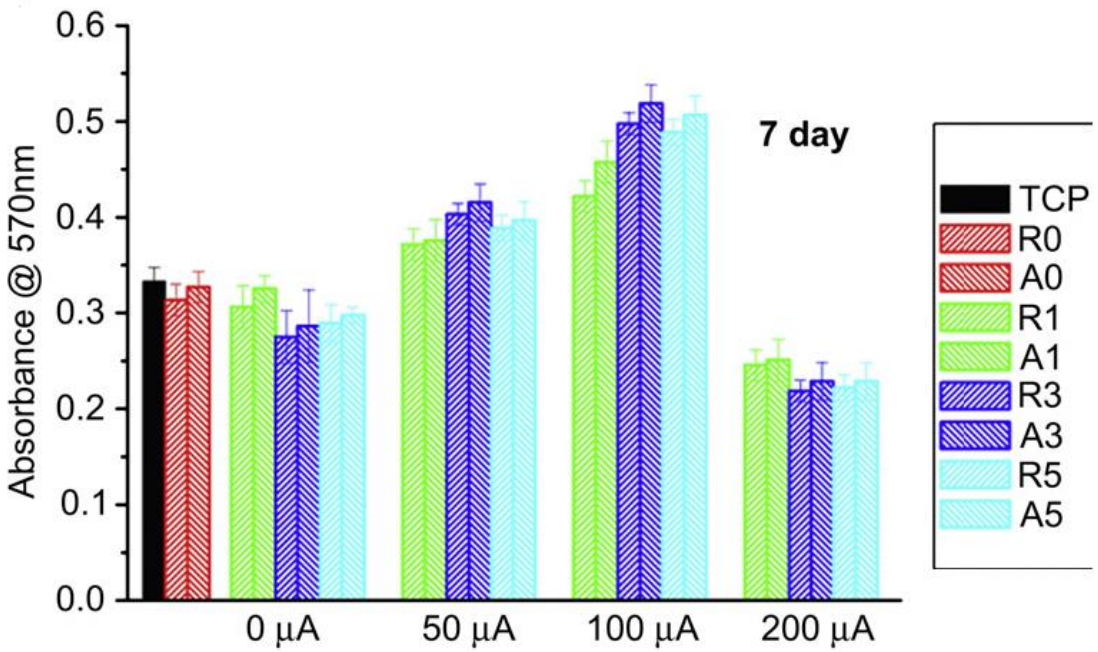

Figure 11: Osteoblast function measured by AlamarBlue absorbance after 7 days seeding with varying DC currents applied. TCP = Tissue Culture Plate, R0 = Neat, random PCL fibres, A0 = Neat, aligned PCL fibres, R1 – R5 PCL = Random PCL fibres with increasing MWCNT content, A1 – A5 = Aligned PCL fibres with increasing MWCNT content. Taken from Shao et al. (2011)[220].

In the aforementioned studies the beneficial effect of the added CNTs was due to topological changes and mechanical reinforcement of the matrix. Shao et al. (2011) demonstrated that the electrical enhancement of the scaffold can be exploited to increase the biocompatibility of the scaffolds, adding an additional dimension for the optimization of TE scaffolds. It has been shown that nanotopographical features can have a great impact on cell proliferation and differentiation[238,239]. The exact relationship and triggers for cells are however not well understood at the moment and a topic of ongoing research. Nevertheless the incorporation of CNTs does change the surface structure of electrospun fibres as will be shown in this thesis and has been demonstrated in the literature. Wu et al. (2016) successfully incorporated MWCNTs into electrospun PVDF fibres[240]. High resolution TEM images in their work shows comparisons between neat fibres and CNT-containing fibres which exhibit a rougher surface

structure. Additionally Calin et al. (2015) used AFM measurements to show a significant increase in the average surface roughness of electrospun PA-6 fibres with an increase in CNT concentration[241]. These results suggest that the incorporation of CNTs in electrospun fibres enhance nanotopographical features which are believed to be beneficial for cell growth.

1.5.4. Challenges for Carbon Nanotubes in Tissue Engineering

It becomes evident from the abovementioned uses of CNTs in TE that there is great potential for CNT/Polymer systems to improve scaffold properties and biocompatibility. There are however still challenges that prevent the widespread use of CNTs in TE applications. The main factor that is impeding the use of CNT/Polymer scaffolds is the cytotoxicity of neat CNTs, which is not well-understood as of the time of writing[242–246]. There is no scientific consensus as there are conflicting results in the literature on that topic. There are studies showing the biocompatibility of pure CNTs for different TE applications[29,194,204] as well as work suggesting that CNTs can accumulate in the body and are potentially harmful[244]. Until there is a better understanding of the safety of CNTs there can be no clinical use of CNT containing bio-scaffolds. The major problem is the large variety of CNTs available. There is no standardized production method and characterisation protocol used. Additionally the utilization of metal catalysts for large-scale synthesis results in large fractions of metal residues in the as-produced CNTs[247]. These metal particles could be harmful and make the as-produced CNTs toxic when not removed prior to application. The challenge at hand is the vast majority of different CNT-containing materials accessible coupled with the unavailability of a standardisation of the CNTs that yields very different results with regards to the toxicity of CNTs.

1.6. Conclusions and Thesis Roadmap

The motivation behind the research in tissue engineering is to be able to repair or replace damaged tissues and to create viable alternatives to existing animal test models for the development of medical treatments. There are many potential ways to create functional tissues using artificial or natural materials as scaffolds for cells. Electrospinning has emerged as a promising technique to produce ECM-like scaffolds for tissue engineering applications due to its simplicity and low-cost. It is imperative for the successful application of such scaffolds in tissue engineering to acquire a good understanding between

the processing conditions and the physical and morphological properties of those scaffolds as a result of the processing conditions. The plan of this thesis is as follows:

Chapter 3: To establish an in-depth relationship between the processing parameters and the morphology of electrospun PCL fibres. Different statistical approaches to experimental design are used and compared for PCL and PMMA nanofibres with regards to their respective predictive capabilities.

Chapter 4: To investigate the crystalline structure of PCL fibres and its effect on the mechanical properties. Different techniques are used to measure the degree of crystallinity and correlations between the internal crystalline morphology and the mechanical properties of the scaffolds are given.

Chapter 5: To demonstrate the beneficial impact of added CNTs on the physical properties of PCL scaffolds. Two types of CNTs – one with a conventional –OH functionalization and one with a targeted chemical functionalization – are incorporated into PCL nanofibres and the morphological and mechanical effect of the CNTs are measured and compared.

Chapter 6: To examine the electrospinning of gelatin nanofibres with and without added CNTs with regards to their morphology and mechanical properties. In addition to the solution concentration of gelatin, the age of the solution is also taken as a processing parameter and is found to have a significant effect on the morphology of nanofibrous gelatin scaffolds.

Chapter 7: To explore the performance of tailored, electrospun PCL scaffolds with different morphologies and CNT contents as scaffolds for neuronal tissue engineering. Human neuronal stem cells are seeded onto scaffolds and their proliferation and differentiation are examined as a function of the type of scaffold.

2. Methods

2.1. Electrospinning Set-Up

The electrospinning set-up consists of a high-voltage power supply (Genvolt 73030 30kV, negative output) and a precision syringe pump (KD Scientific Legato 200). The PCL/HFIP solutions were loaded into 1.0 mL syringes (Hamilton Company) fitted with Luer-lock needles. The syringes were mounted onto the syringe pump. A rectangular aluminium target (10 cm x 10 cm) was used as the collector. The tip of the needle was earthed and the desired high voltage potential was applied to the collector via an alligator clip. The spinning time was 5 minutes for all experiments unless otherwise stated.

2.2. Estimation of Impact of Humidity

The electrospinning set-up used does not allow for control of temperature or humidity due to its design as a portable kit within a fume hood. The temperature was found to be fairly stable throughout the year (±5°C) and hence assumed to have very little influence. The humidity however was found to vary with the seasons and the weather. Some work in the literature has commented on the effect of humidity on the morphology electrospun polyethylene oxide (PEO) in aqueous solutions[248]. The effect of the humidity was assumed to be negligible prior to this investigation as no aqueous solutions were used. A PCL scaffold was electrospun from a solution with a concentration of 6 wt% at a humidity of 32%, in contrast to the spinning that was carried out for the other experiments where the humidity was in the range of 55% - 65%. No large difference in the morphology or the diameter distributions was found (Figure 12).

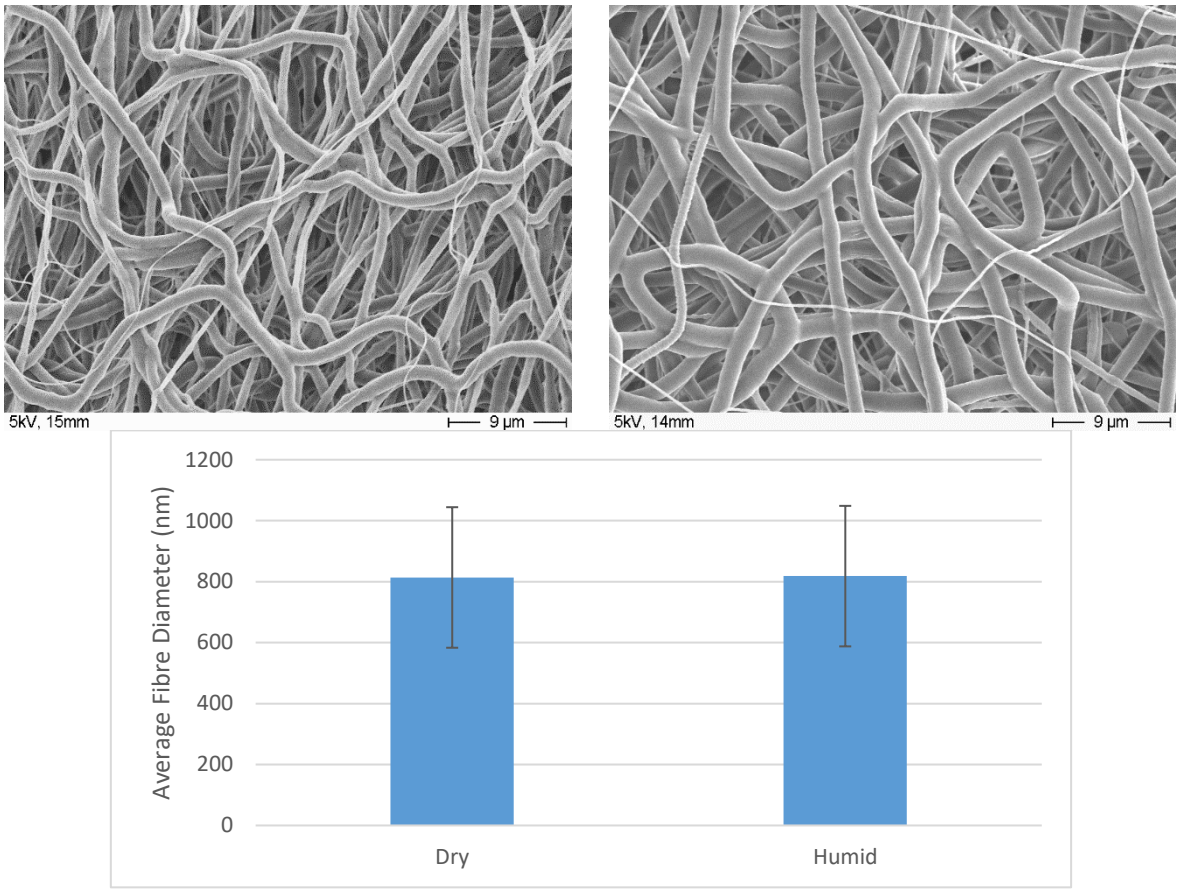

Figure 12: Top: Overview of the morphology of scaffolds made from 6 wt% solutions at a humidity of 32% (left) and 55% - 65% (right) Bottom: Comparison of the average fibre diameter between the dry and the humid state. All error bars are given as one standard deviation.

These results suggest that the humidity (within the range tested) has no measurable effect on the average fibre diameter. Because of the inability to control the humidity during electrospinning this means that its influence can be ignored for all future experiments.

2.3. Scanning Electron Microscopy

For the image acquisition the samples were platinum coated (Coater) and imaged in a JEOL 840F SEM (Jeol) using a 5 kV accelerating voltage.

2.4. Diameter Distributions

Diameter distributions were obtained using image analysis from SEM images of nanofibres. Image J (NIST) was used to measure diameters manually and a minimum of 120 fibres were measured per sample. For each scaffold five images in random positions on the scaffold were used.

2.5. Transmission Electron Microscopy

Samples for transmission electron microscopy (TEM) were prepared by attaching a copper, lacey-carbon, TEM grid at the centre of the aluminium target. The spinning time was reduced to ~45s in order to avoid full coverage of the TEM grid and ensure electron transparency. The sample was carefully removed and imaged in a JEOL 2000FX (JEOL) with a 200kV accelerating voltage.

2.6. X-Ray Diffraction

X-ray diffraction (XRD) was performed by Dr. Philip Holdway on a Siemens D5000 X-Ray Diffractometer. Rectangular samples were cut from the centre of the area-of-deposition and fixed onto the sample holders using an x-ray transparent silicone grease. The crystallite size was estimated using the Scherrer equation (Equation 1) after a mathematical k-alpha 2 stripping was performed on the XRD spectra.

$$\tau = \frac{K\lambda}{\beta \cos\theta}$$

Equation 1: τ = mean size of ordered crystallite domains, K = dimensionless shape factor, λ = x-ray wavelength, β = FWHM of the line broadening, θ = Bragg angle.

2.7. Viscosity Measurements

Viscosity measurements were carried out on an Anton Paar 301 oscillatory and rotational rheometer in a cone-plate geometry with plate diameter of 25 mm and a conic angle of ~2° at 25°C. A custom-made solvent trap was used due to the low-boiling point of HFIP. In short a steel disc with an inner diameter of 35 mm was placed around the sample and Decane (98%, Sigma-Aldrich) was used to cover the sample and prevent solvent evaporation during measurements.

A solvent trap was used as the low boiling point of the HFIP resulted in significant evaporation during the initial measurements and thus an apparent change in viscosity with time that can be attributed to an increase in polymer concentration (Figure 13).

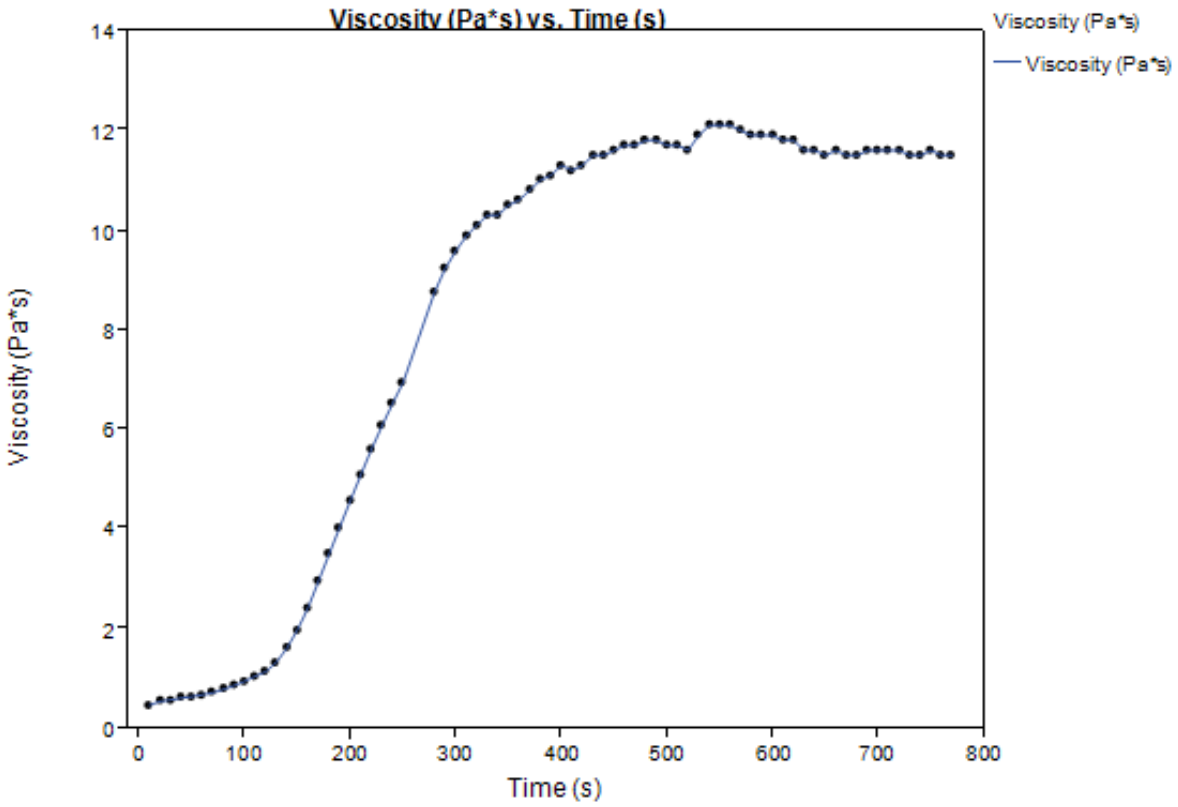

Figure 13: : A one order of magnitude change in the viscosity of a 4 wt% PCL/HFIP solution is observed over a period of 13 minutes which can be attributed to solvent evaporation

It was confirmed in a separate measurement that the use of Decane in the solvent trap does not influence the measured values for the polymer solutions. This is due to the very low viscosity of Decane of ~920 µcP which is several orders of magnitude lower than the obtained values for the PCL/HFIP system.

The transient shear measurements of PCL/HFIP solutions with 3 wt%, 4 wt%, 5 wt% were measured (Fig. 3 B). From the data it is evident that the solutions follow a Newtonian behaviour up to higher shear rates. The solutions with higher polymer concentrations exhibit a higher zero-shear viscosity (Figure 14 A and Figure 15) which is to be expected for simple linear polymers in the low concentration regime. All solutions showed signs of shear thinning at higher shear rates. The onset of the shear thinning occurred at lower shear rates with an increase in polymer concentration (Figure 14 B), a behaviour that has been documented in the literature and is to be expected.

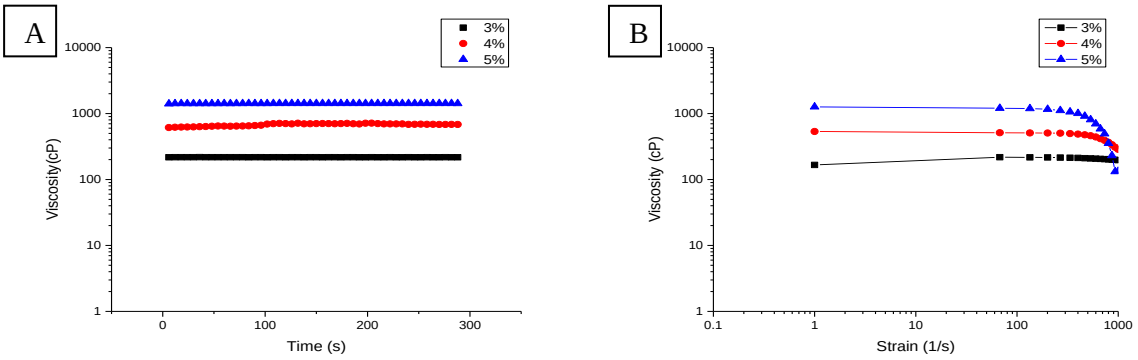

Figure 14: A: Stability of a 5 wt% PCL and 3 wt% PCL solution over times. The results show no change in viscosity at a constant shear-rate of 100^{-1} s. B: Transient shear viscosity of various solutions that were used for electrospinning.

From the zero shear viscosity it is possible to investigate the entanglement and dilution regime of the solution. (Figure 15).The slope of the linear fit of the solution viscosity with polymer concentration suggests that the critical concentration of chain entanglement was reached for all concentrations used. It is generally believed that chain entanglement is crucial for defect-free electrospinning.[249] It is understood that the solution properties – especially the viscosity – have a very large impact on the morphology and general spinabillity.

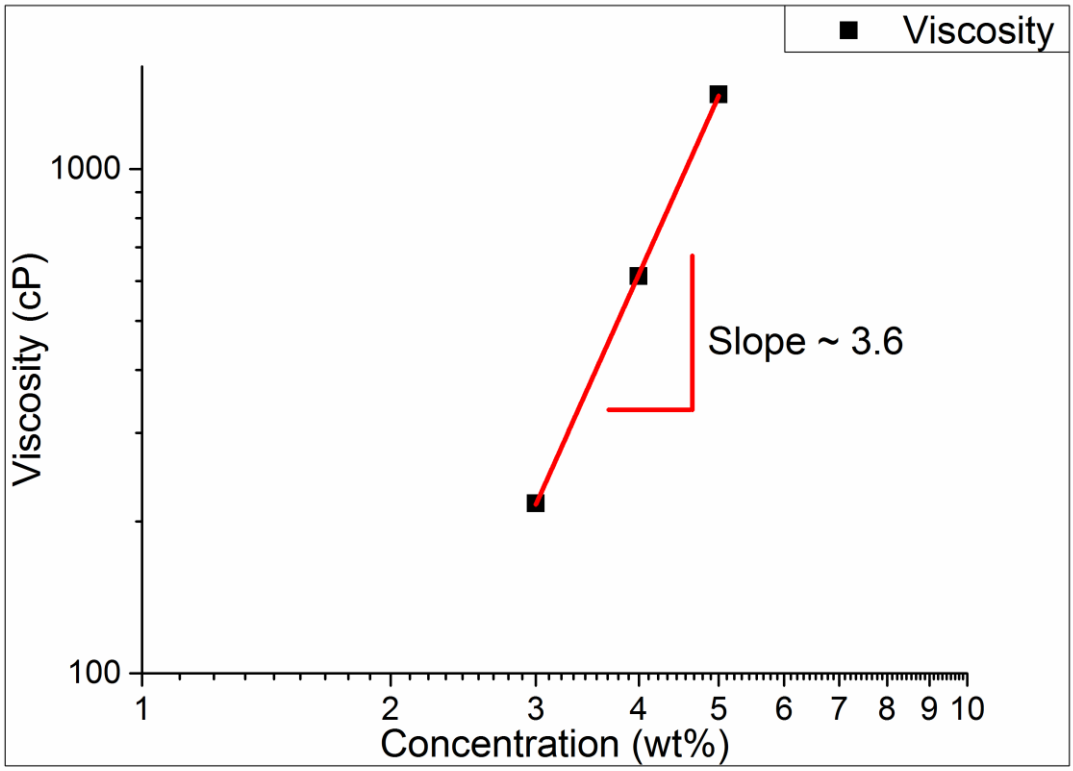

Figure 15 Zero shear viscosity as a function of PCL content in the solution. The red line represents a linear fit with R^2 ~0.99.

2.8. Mechanical Testing

Samples were electrospun according to the experimental protocol on a rectangular aluminium target with a small aluminium strip on top (Figure 16). The strip was then removed while the overhanging scaffold was cut with a razor blade. A dog-bone shaped sample was then cut onto the scaffold using a template. The cross-sectional area of the sample was determined using a high precision micrometer. The sample was then transferred to a Linkam TST350 Tensile Testing stage. Tensile testing was performed at 25°C at a strain rate of 10 µm/s. The ultimate tensile strength (UTS) was defined as the peak of the stress-strain graph. The Young´s modulus was calculated using the slope of the stress-strain curve in the elastic region.

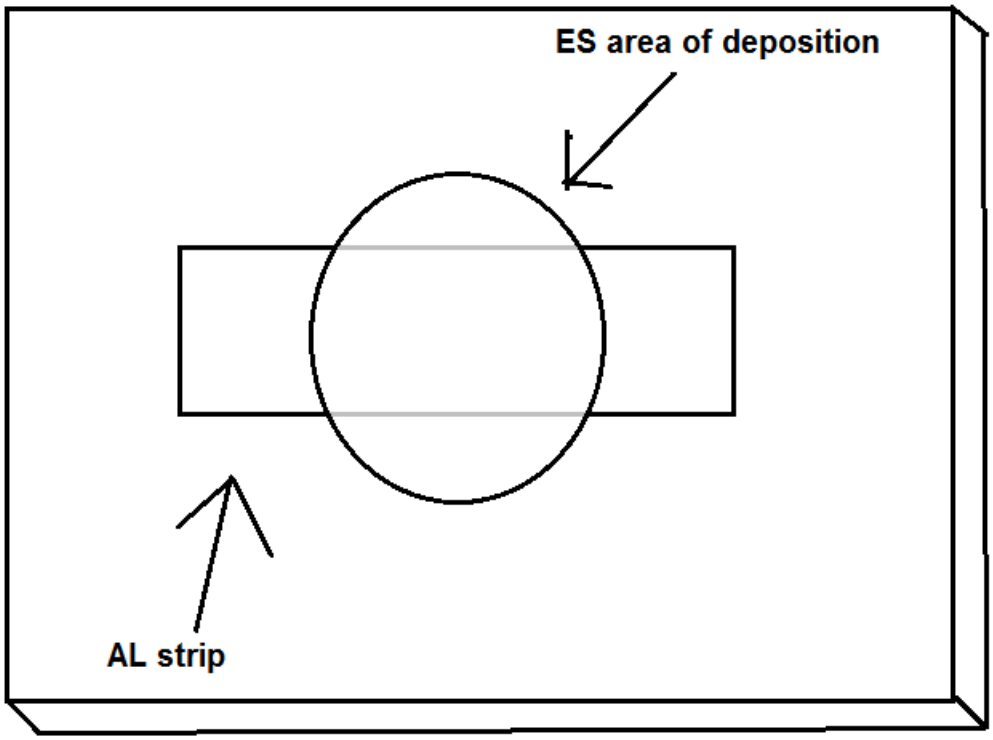

Figure 16: Schematic of the modified deposition technique for the tensile testing samples. The cross-sectional area of the test samples will depend on the experimental parameters, such as time, flow-rate and polymer concentration.

2.9. Differential Scanning calorimetry Measurements

The degree of crystallinity as measured by DSC was estimated by assuming that the melting enthalpy per unit mass of pure crystalline PCL was equivalent to that of a 100% crystalline PCL sample (139.5 J/g[250]) and then calculated using the formula:

$$X_c = \frac{\Delta H_f}{\Delta H_f^\circ}$$

Equation 2: X_c = Weight fraction extent of crystallinity, ΔH_f = enthalpy of fusion measured at melting point, ΔH°_f = enthalpy of fusion of the totally crystalline polymer.

The melting point was determined by the position of the peak of the melting endotherm. The samples used for DSC were the same samples as used in XRD after the scanning was complete to avoid batch to batch variations. Samples with varying PCL concentrations were electrospun according to the above-mentioned protocol on a rectangular aluminium target.

2.10. X-ray Photoelectron Spectroscopy

XPS analysis was carried out by Dr. Hugh Bishop. Samples supported on carbon pads on stubs were introduced into the instrument via a turbo molecular pumped entry lock. The entry lock was pumped for about 15 minutes before the sample was introduced into the analysis chamber. XPS was performed in an ion pumped VG Microtech CLAM 4 MCD analyser system. 200 Watt unmonochromated Mg X-ray excitation was used. The CLAM 4 has variable slits for small area analysis. The largest slit (5 mm) was used in this case with no apertures selected. The analyser was operated at constant pass energy of 100 eV for wide scans and 20eV for detailed scans setting the C1s peak at BE 284.8 eV to overcome any sample charging. Data was obtained using SPECTRA version 8 operating system. Data processing was performed using CASAXPS.

2.11. Scaffold Porosity Measurements

The scaffold porosity was measured by cutting a 1 cm by 1 cm rectangle out of a midpoint samples of PCL and PMMA from [3.2.1] and [3.2.2] respectively. The thickness of these scaffolds was measured using a high precision micrometer and the resulting density was compared to the bulk density of each material. Each measurement was carried out in triplicates. Additionally the expected E modulus of these scaffolds is given as a comparison, assuming a bluk material. The values can be found in table 3:

Sample	Porosity (%)	Modulus (MPa)
PCL	89% ± 4%	~40
PMMA	92% ± 6%	~235

Table 4: Overview of scaffold porosity of a standard PCL and PMMA membrane.

3. The Use of Experimental Design in Electrospinning

3.1. Introduction

Electrospinning is one of the simplest and easiest-to-use processing techniques to produce continuous, one-dimensional, fibre scaffolds[251]. Despite the facility of the production method to use a variety of polymers[64] and to create a large range of morphologies and structures[252,253] there are many processing parameters to consider when trying to understand the electrospinning process[71]. To date most electrospinning studies have used simple approaches to optimise fibre production through one-way analyses. Statistical approaches to experimental design have been shown to minimise the number of experimental runs required to understand the impact of processing parameters on physicochemical and morphological properties[254,255]. Specific experimental designs such as factorial designs or response surface methodologies[256] have been successfully employed in order to understand correlations between various electrospinning parameters and fibre morphology and the physical properties of the overall scaffold[68,257–261].

The approach in experimental design is to assume that each dependent variable – in this case the processing parameters – can be treated as a factor in a multivariate polynomial. The constant terms in the polynomial can then be calculated by solving a set of simultaneous equations based on the dataset available and thus represent the magnitude of the impact that each processing variable has on the measured quantity (Equation 3).

$$y = ax_1 + bx_2 + cx_3 + dx_1x_2 + ex_1x_3 + fx_2x_3$$

Equation 3: Example polynomial that could be used for a statistical experimental design. In this case three main parameters, x_1, x_2 and x_3 together with their second-order interactions would be investigated by solving for a, b, c, d, e and f.

This approach allows for the investigation of interactions between parameters as well as the inclusion of squared terms or, even higher exponents, which the standard one-parameter-at-a-time approach doesn't provide.

This chapter investigates the performance of an in-house made electrospinning rig to produce nanofibrous scaffolds. The impact of processing parameters on the average fibre diameter, the range of fibre diameters produced and finally the overall size of electrospun scaffolds are evaluated. Additionally,

with the use of polycaprolactone (PCL), the potential of a more advanced experimental design is demonstrated and compared to a more conventional approach using Poly(methyl methacrylate) (PMMA). The results displayed in this chapter demonstrate the usefulness of statistical methods in the design of experiments and showcase how such methods can be employed to understand the impact of processing parameters on a final product. Furthermore it can be shown that mathematical models based on the experimental design can be utilized to predict and tailor morphological properties of samples.

3.2. Methods and Materials

3.2.1. PCL Study

3.2.1.1. Electrospinning

Electrospinning was carried out using the equipment described in [2.1]. Polycaprolactone (PCL, M_w 70000 – 90000) was dissolved in 1,1,1,3,3,3-Hexafluoro-2-propanol (HFIP, 99%) in the required concentrations according to the design of the experiment. All solutions were magnetically stirred overnight at 1000 RPM before electrospinning.

3.2.1.2. Design of Experiments

A two-level central composite design[255] with one replication and four centre runs was chosen in order to investigate the influence of voltage, distance, feed rate and PCL concentration, leading to 56 experimental runs in total. Prior to the parametric investigation, a series of experiments was carried out to determine the boundary conditions. It was found that electrospinning was optimal between voltages of 20kV – 30kV, needle to collector distances of 12 cm – 18 cm, feed rates between 0.1 ml/hour – 1 ml/hour and concentrations between 3 wt% - 5 wt%. These values represent the boundary conditions of the electrospinning rig with regards to the PCL/HFIP system. The design was specifically chosen to incorporate eight centre runs in order to better assess the variance of the set-up for identical experimental settings. In this case all 1st and 2nd order interactions are analysed, four 3rd order and, since there are only four variables, one 4th order interaction is considered. Equation 4 gives an overview of the polynomial that was constructed.

$$y = a + bx_1 + cx_2 + dx_3 + ex_4 + fx_1x_2 + gx_1x_3 + hx_1x_4 + ix_2x_3 + jx_2x_4 + kx_3x_4 + lx_1^2 + mx_2^2 + nx_3^2 + ox_4^2 + \mathrm{p}x_1x_2x_3 + \mathrm{q}x_1x_2x_4 + \mathrm{r}x_1x_3x_4 + \mathrm{s}x_2x_3x_4 + \mathrm{t}x_1x_2x_3x_4$$

Equation 4: Overview of the polynomial constructed for the PCL experimental series. All first and second order interactions are being investigated, whereas only some of the third- order interactions are considered. x_1, x_2, x_3 and x_4 are voltage, distance, feed rate and concentration respectively and y is either fibre diameter, area-of-deposition or standard deviation.

3.2.1.3. Statistical Analysis

Using the above-mentioned polynomial system a standard least square regression was performed on the dataset in order to evaluate the impact of the individual parameters. The specific design used allows for the investigation of 1st, 2nd, 3rd and 4th order interactions, as well as the inclusion of squared terms in the model in order to determine non-linearity of the responses. A factor was deemed statistically significant if its impact was at least four times larger than its standard error.

3.2.2. PMMA

3.2.2.1. Electrospinning

Poly(methyl methacrylate) (PMMA, average M_w ~350,000 by GPC) was dissolved in 1,1,1,3,3,3-Hexafluoro-2-propanol (HFIP, 99%) in concentrations of 3 wt%, 4 wt% and 5 wt%. All solutions were magnetically stirred overnight at 1000 RPM before electrospinning.

3.2.2.2. Design of Experiments

An alternative approach to the design of experiments was taken with the PMMA study in order to compare a standard experimental design to the two-level central composite design used for the PCL series. Advanced experimental design has been employed to investigate the electrospinning of PMMA nanofibres in the literature. Chen et al. (2009) utilized a Box-Behnken design[254] to explore the influence of processing parameters on the fibre diameter of electrospun PMMA nanofibres[259]. Khanlou et al. (2014) carried out a similar study using a central composite design similar to the above-mentioned study in this chapter to investigate the impact of processing parameters on the fibre diameter of electrospun PMMA scaffolds[258]. PMMA was chosen as the material to compare different experimental design strategies because of the existing in-depth analyses of the potential of design of experiments. In this study each parameter was investigated independently of the others, i.e. a midpoint was chosen and every

parameter was changed individually without changing others. This is referred to as one-parameter at a time approach. Due to the nature of this design it was possible to incorporate the effect of needle size as well. Preliminary experiments were carried out to investigate the boundary conditions of the parameters. It was found that electrospinning is optimal between voltages of 15kV – 25 kV, feed rates between 0.1 mL/h and 1 mL/h and needle to collector distances of 12 cm – 18 cm. The needle inner diameter size was varied, as previously mentioned with PCL, from 0.4 mm to 0.8 mm. Each experimental run was repeated three times.

3.2.2.3. Statistical Analysis

A standard least square regression was performed on the dataset in order to evaluate the impact of the individual parameters. In contrast to the central composite design this specific experimental design only allows to analyse 1st order parameters and their squared terms (Equation 5). A factor was deemed statistically significant if its impact was at least four times larger than its standard error.

$$y = a + bx_1 + cx_2 + dx_3 + ex_4 + fx_5 + gx_1^2 + hx_2^2 + ix_3^2 + jx_4^2 + kx_5^2$$

Equation 5: Polynomial constructed for the PMMA experimental series. Only the main parameters and their potential non-linearity are considered for this model.

3.2.3. Morphological Analysis

The average fibre diameter of samples as well as the standard deviation of distributions was measured using the methodology described in [2.4]. The area of deposition was measured by using image analysis of photographs of collected scaffolds using a standard digital camera.

3.3. Results and Discussion

3.3.1. PCL

Polycaprolactone is a synthetic, biodegradable polymer that attracted a lot of attention, particularly in tissue engineering application[262]. There has been a recent surge in its use in tissue engineering[263] and it is a Food and Drug Administration approved polymer that has been used commercially in slow drug release delivery devices and as a structure material in implant devices since the 1980s (some examples are Capronor®, SynBiosys® and Monocryl®). One particularly attractive property of PCL is its long degradation time in-vivo which can be between 2-4 years[264,265]. The aim of this sub-chapter is to establish

a robust model for the processing of electrospun PCL scaffolds and thus gain a good understanding on the underlying physical principles that govern that process. The knowledge gained will then be used in subsequent chapter to make and tailor scaffolds for specific purposes.

In the experimental series each parameter is assigned a low and high value – determined by initial trial experiments – and a midpoint, consisting of the halfway values of each parameters between the low and the high value. Each standard experimental run is repeated once and the midpoint is repeated eight times in order to assess reproducibility and variance in the processing. An overview of the experimental runs is found in Table 5.

Sample No.	Voltage (kV)	Distance (cm)	Feed Rate (mL/h)	Concentration (wt%)
1	20	12	0.1	3
2	30	12	0.1	3
3	20	18	0.1	3
4	30	18	0.1	3
5	25	15	0.55	3
6	20	12	1	3
7	30	12	1	3
8	20	18	1	3
9	30	18	1	3
10	25	15	0.1	4
11	25	12	0.55	4
12	20	15	0.55	4
Midpoint	25	15	0.55	4
13	30	15	0.55	4
14	25	18	0.55	4
15	25	15	1	4
16	20	12	0.1	5
17	30	12	0.1	5
18	20	18	0.1	5
19	30	18	0.1	5
20	25	15	0.55	5
21	20	12	1	5
22	30	12	1	5
23	20	18	1	5
24	30	18	1	5

Table 5: Overview of all the experimental runs and their parameters used for the PCL experimental series. Each run is repeated once except for the midpoint which is repeated eight times.

Prior to the parametric investigation it was shown that there is no interaction with the solvent used and the PCL post spinning [10.1]. Within the all the experimental runs the average fibre diameter is found to vary from 141 nm up to 1368 nm, with the midpoints exhibiting an average fibre diameter of 390 nm ±46 nm showing good reproducibility within runs at standard conditions. The standard deviation of the fibre distributions ranges from 45 nm to 562 nm with an average deviation of 242 nm ±45 nm for the midpoint runs. Similarly, the area of deposition is found to vary from 3.7 cm^2 to 31.7 cm^2. Relatively

large variations are seen even within the same experimental runs ranging from almost a doubling of the surface area in some cases to very small variations. The midpoint runs exhibits a mean value of 11.6 cm^2 ±1.9 cm^2 suggesting an acceptable reproducibility. Figure 17 shows an overview of representative images of samples with highest and lowest values for the investigated morphological properties and a standard midpoint sample.

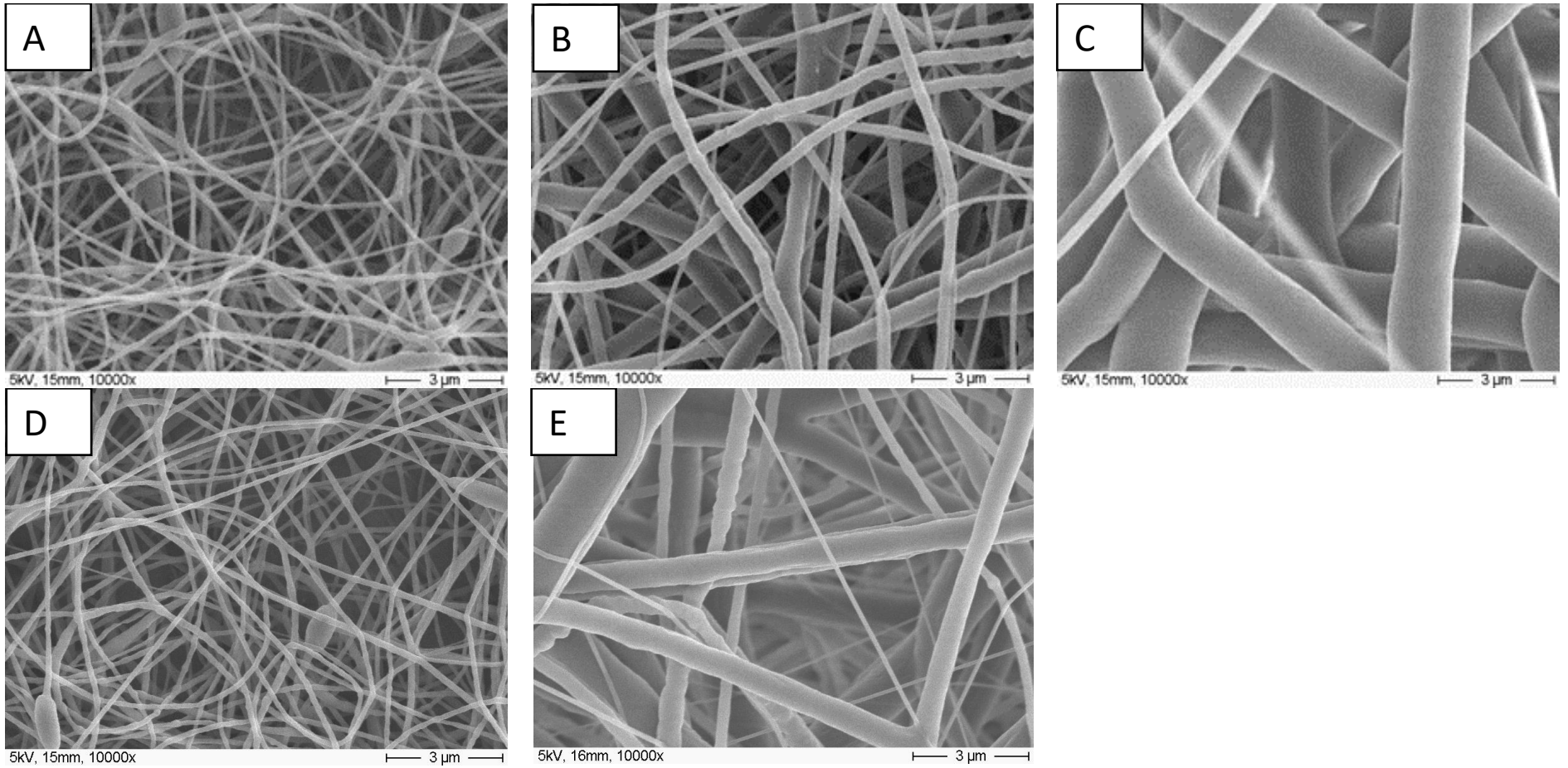

Figure 17: Overview of various types of PCL scaffolds produced. Scaffolds that exhibited the smallest fibre diameters (A), a standard midpoint sample (B). the largest average fibre diameter found (C), scaffolds with the smallest standard deviation of the fibre distribution (D) and the largest standard deviation found (E). All scale bars are 3 µm.

The range of values for the average fibre diameters encountered here are well within the scope of what has been reported elsewhere[85,109,266–269]. A change of about one order of magnitude could be achieved by only changing the few processing parameters used, displaying the great versatility of the electrospinning process. Similar to the average fibre diameter, the standard deviation of the fibre distributions changes greatly (~one order of magnitude) allowing production of scaffolds with very narrow or wide fibre distributions. The fibre diameter distribution can be an important parameter depending on the intended use of the scaffolds. Understanding how to control the fibre width distribution (narrow vs. wide) can be beneficial in order to tailor the scaffolds to a desired application. In terms of tissue engineering applications it is currently not well understood what influence standard deviation of the fibre distributions has. One of the later goals of this thesis is to understand the impact of the average fibre diameter on cell growth and proliferation. This would make a narrow fibre distribution more desirable as to remove confounding effects from extreme outliers (very large or very small fibres). The area of deposition is a factor that has received very little attention in the literature and seems to be very material and set-up dependent[270–274]. To date there is no systematic study that aims to investigate the effect of processing parameters on the change in area of deposition. In order to produce consistent and as-desired electrospun scaffolds it is important to know and understand the area of deposition for a given set of parameters, especially when producing scaffolds in larger volumes. In this work it was found that the area of deposition can vary drastically and shows a large variability within the same experimental runs. A fit of the three investigated parameters with each other was carried out to establish any possible correlations amongst them. As can be seen from Figure 18 there seems to be no correlation between the area of deposition and the average fibre diameter. This is an indication that the parameters that govern the size of the area of deposition are different from those that have the biggest impact on the other two. According to these results it should thus be possible to individually vary the area of deposition and the fibre diameter giving the possibility to create scaffold on large areas with either small or large fibres. A moderate, positive correlation was found between the standard deviation of the fibre distribution and their average fibre diameter. As the fibre diameter increases the spread of fibre sizes increases simultaneously.

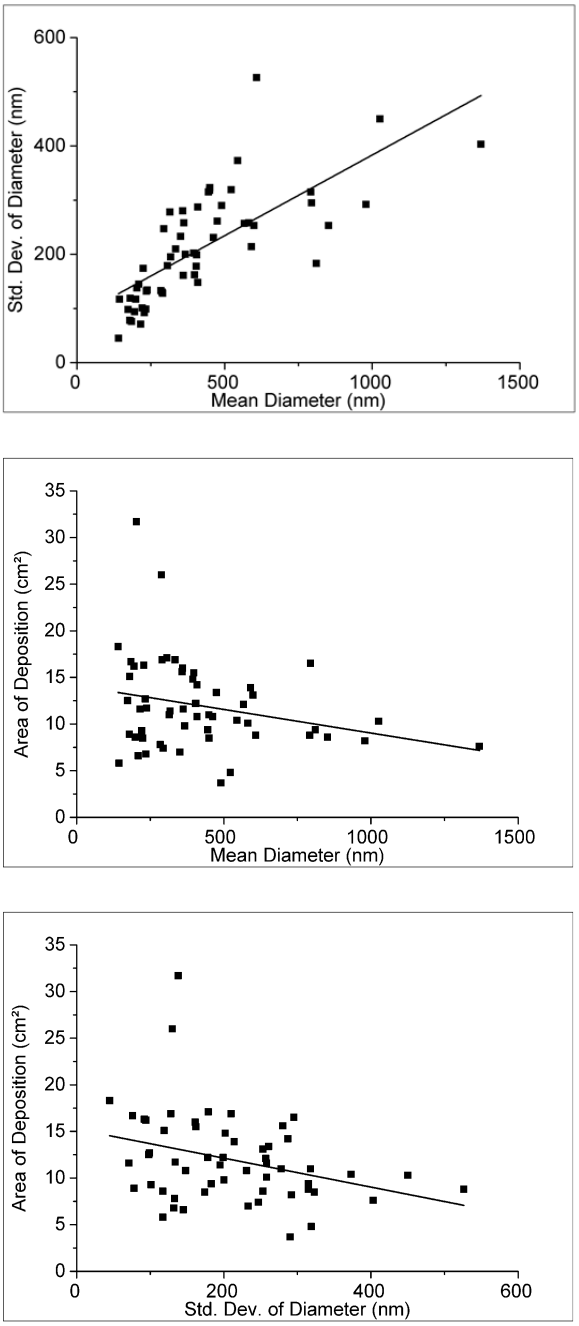

Figure 18: Overview of the correlations within the investigated parameters. R^2-values for the linear fits are: Top: 0.52, Middle: 0.05, Bottom: 0.09

A standard least square regressions was performed to model the dependence of three morphological factors with the four processing parameters used. This method assumes a simple linear model between the factors investigated and calculates a mathematical equation based on the 56 experimental runs, essentially solving a set of simultaneous equations. The independent variables are then evaluated based on their statistical significance and represent the impact of their respective parameters. The impact is determined by the average change in the response between the high and the low value of the boundary

conditions. Factors whose impacts were larger than four times their standard error were considered statistically significant. The standard error is not the same for all parameters as the precision with which they are estimated varies. For example a single parameter, such as voltage, has 18 instances in its low (20 kV) and high (30kV) state whereas a combination of two parameters, such as voltage * distance, has only 8 instances in a combined low (20 kV and 12 cm) and high state (30 kV and 18 cm) and thus yields a different standard error with a lower precision. The experimental design chosen is a combination of a fully factorial two-level design, with added centre points to estimate quadratic interactions. However a fully saturated design to evaluate fourth-order relationships between all parameters would require 3^4 = 81 runs (162 with replicate runs) which would not have been feasible. Therefore the standard error for the fourth-order expression is significantly larger than compared to the other parameters.

An overview of the statistically significant parameters governing the fibre diameter is given in Figure 19. Five significant parameters were found: The concentration, the feed rate, the second order interaction between flow rate and concentration, the voltage and the second order interaction between voltage and concentration.

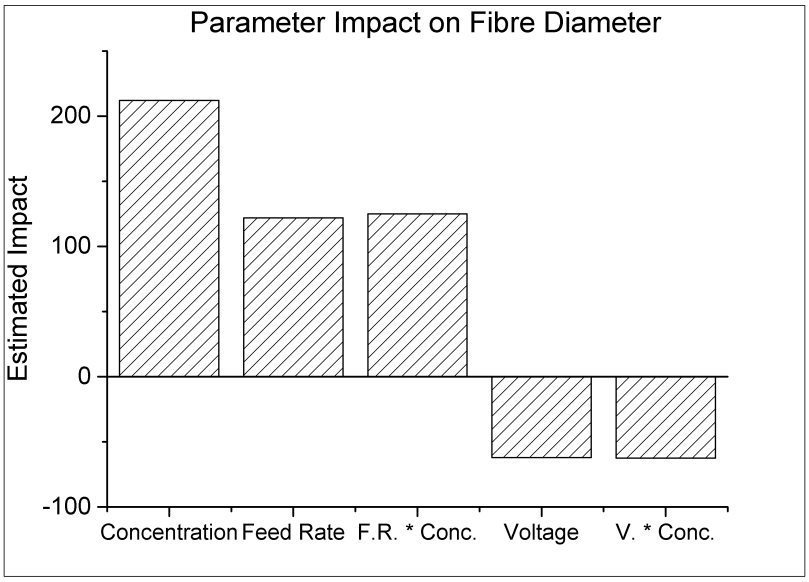

Figure 19: Overview of the impacts of the five significant parameters on the average fibre diameter.

The positive correlation of solution concentration and feed rate with the average fibre diameter has been well documented in the literature empirically[71] as well as theoretically[275], while ambiguous results exist in the literature for the influence of the voltage[64]. For the investigated system the concentration has the

largest impact on the average fibre diameter, followed by the feed rate. It can be seen that the interaction between the feed rate and the concentration has a positive correlation with the fibre diameter. This means that an increase in both feed rate and concentrations produces fibres that are larger than what would be expected from a simple linear addition of their individual impacts. The applied voltage shows a negative correlation with the mean fibre size, which has been observed previously for electrospun PCL fibres[276]. The second-order interaction between the solution concentration and the voltage also exhibits a negative correlation with the fibre diameter. An increase in the applied voltage during electrospinning in this system leads to a greater fibre stretching and thus thinner fibres. The synergistic effect of the voltage and concentration can be explained by the same physical process. An increase in the solution concentration leads to a larger charge density in the electrospinning jet and thus the applied voltage will exert a stronger force during fibre stretching.

The standard deviation of the average fibre diameter is an important measure for the uniformity of the fibres within a given scaffold. The concentration was found to be the most significant factor influencing the uniformity of the fibres, with an increase in concentration leading to an increase in the spread of fibre diameters (Figure 20).

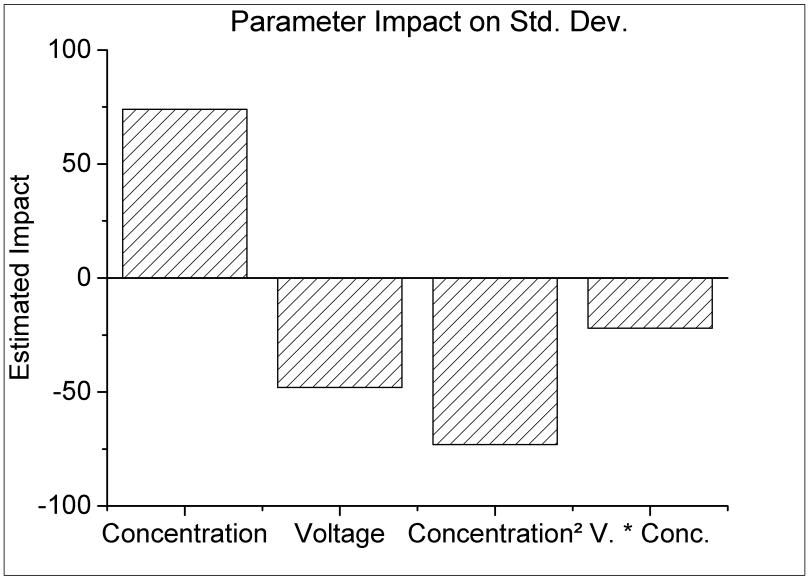

Figure 20: Overview of the impacts of the four significant parameters on the standard distribution of fibre diameters.

An increase in voltage was found to have a decreasing effect on the spread of the fibres' diameters. The high, negative impact of the squared term of the concentration indicates that, in this work, the solution concentration had a non-linear impact on the standard deviation following an inverted parabola shape. The feed rate had no significant impact on the standard deviation of the fibres' diameters, in contrast to its effect on the average fibre size. It would thus be possible to slightly vary the diameter without affecting the spread in fibre diameters via a control of the feed rate and it further explains the only moderate nature of the correlation between these two morphological properties. Existing work on the influence of processing parameters on the standard deviation of nanofibres is sparse. The work by Beachley and Wen (2009) reports contradicting results on the influence of voltage on the fibre uniformity and a non-significant impact of the concentration[276].

The voltage and the feed rate were the two most significant parameters influencing the area of deposition both positively. The concentration was found to have a negative impact on the area of deposition (Figure 21).

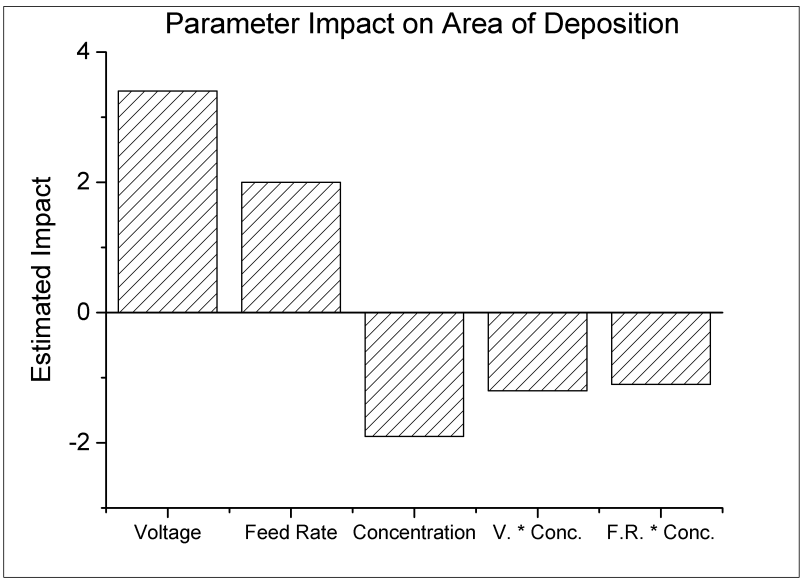

Figure 21: Overview of the impacts of the five significant parameters on the area of deposition of the scaffolds.

Both the voltage and the feed rate had a significant, negative 2nd-order interaction with the concentration, meaning that the positive impact of those was diminished with an increased concentration. There are very few accounts in the literature on the impact of processing parameters on the area of deposition.

Zheng et al. (2013) observed that an increase in voltage had a slight, negative effect on the deposition area of scaffolds made from PEO/H_2O solutions[270]. The voltage displays the opposite effect in this study which has to be explained by the difference in the polymer/solvent system used. Zargham et al. (2012) report a similar behaviour with regards to the feed rate as described in this work. Between flowrates of 0.1 mL/h to 1mL/h the area of deposition of electrospun nylon 6 fibres increases slightly[271]. An increase in the flowrate leads to an increase in the bending instabilities, which in turn then leads to a more pronounced and chaotic flight path of the polymer jet during electrospinning and thus an increase in the deposition area[69]. Both Hsu et al. (2004) and Mit-uppatham et al. (2004) found the solution concentration to have a negative influence on the area of deposition of PCL and nylon-6 fibres respectively. A higher polymer solution concentration results in a larger solution viscosity [2.7]. This results in a greater resistance of the electrospinning jet to the electric field and delays the onset of the bending instabilities[277,278], thus reducing the area of deposition.

Based on the evaluated impacts of all the factors, mathematical models for each dependent variable were constructed using Equation 4. Table 6 shows an overview of the R^2 values of the models with respect to the dataset collected with all the experimental runs. The presented R^2 values represent the accuracy of the models to predict the experimental data that was used to construct them. The model for the average diameter is the most precise, while the model for the area of deposition shows the largest margin of error.

Precision of the Established Models		
Average Diameter	Standard Deviation	Area of Deposition
R^2 = ~0.89	R^2 = ~0.74	R^2 = ~0.68

Table 6: Overview of the r^2 values of the models constructed for the average fibre diameter, the standard deviation of the fibre diameters and the area of deposition of the PCL scaffolds.

These results show that the use of the central-composite-design were successfully employed to evaluate the impact of the processing conditions on the three selected metrics, average fibre diameter, standard deviation of the fibre diameters and the area of deposition.

The high R^2 value for the average fibre diameter suggests a good validity of the model and a high expected agreement with predicted and experimentally obtained values. The results for the impact of the concentration and the feed rate on the mean diameter are well in agreement with the literature. The positive reinforcement effect of the combination of feed rate and concentration is to be expected. The voltage was found to reduce the mean fibre diameter in this study. It is noteworthy that the 2nd order interaction of voltage and concentration results in a reduction of mean diameter. These results suggest that the model developed for the average fibre diameter represents a good way of describing the influence of the investigated parameters. Confounding environmental parameters, such as humidity, temperature and air turbulences appear to be negligible. The R^2 value for the standard deviation is lower than for the fibre size. A lower R^2 value suggest the influence of additional parameters that were overlooked or a more chaotic and less reproducible nature to the spread in fibre sizes. To the best of my knowledge this is the first work that systematically analysed the dependency of the standard deviation and hence the spread in fibre diameters found in electrospun scaffolds. The R^2 value of 0.68 is sufficiently high to accept the general validity of the model but low enough to suggest some unexplained correlations. This indicates that there may be factors contributing to the area of deposition that had an influence and were not controlled for. In order to test the ability of the above-established models, a set of three experiments with random parameters within the boundary conditions were designed (Table 7). Each run was repeated three times.

Experimental Run	Voltage	Distance	Feed Rate	Concentration
1	25	12	0.1	5
2	20	18	0.3	4
3	22.5	16.5	0.7	3

Table 7: Overview of the randomly chosen processing parameters used for the test experiments.

An exceptional agreement was found with the measured values and the predicted values from the models. All measured values are well within one standard deviation of the predicted ones except the area of deposition in the third run (Table 8).

Experimental Run	Predicted Value	Measured Value
Fibre Diameter		
1	339 nm ± 117 nm	332 nm ± 45 nm
2	445 nm ± 107 nm	445 nm ± 38 nm
3	234 nm ± 87 nm	205 nm ± 13 nm
Standard Deviation		
1	160 nm ± 74 nm	173 nm ± 54 nm
2	346 nm ± 68 nm	313 nm ± 41 nm
3	125 nm ± 55 nm	113 nm ± 9 nm
Area of Deposition		
1	7.5 cm^2 ±3.9 cm^2	7.65 cm^2± 2.6 cm^2
2	11.5 cm^2 ±3.6 cm^2	13.8 cm^2 ± 6.4 cm^2
3	11.9 cm^2 ±2.9 cm^2	15.9 cm^2 ± 4 cm^2

Table 8: Comparison of the predicted and measured values for the average fibre diameter, standard deviation of fibre diameters and area of deposition of the PCL scaffolds for the validation experiments.

Given the accuracy of the developed models (Table 8) it is evident that a good control over the morphological properties of PCL electrospun scaffolds is readily achievable. This removes the need to check individual scaffolds prior to their physiochemical characterisation with various techniques, especially since the determination of fibre diameter is a semi-destructive method as the samples need to be coated and cut to specific dimensions to fit in the microscope. It opens up the possibility for a fast and facile way of producing large numbers of scaffolds with known properties for further characterisation or cell growth. The investigated parameters in this section only represent a small number of all the possible independent variables that might affect the electrospinning of nanofibrous scaffolds, nevertheless the accuracy of the developed mathematical models suggest that all major parameters were accounted for.

A parameter commonly investigated with its regards to electrospun scaffold production is the influence of the needle diameter. Due to the design criteria of the central-composite-design the inclusions of the needle inner diameter into the experimental design would have significantly increased the number of experimental runs. Accounts in the literature are either conflicting with regards to its influence on the morphology of electrospun scaffolds or found that the needle inner diameter has a negligible impact[279–281]. Thus it was decided to investigate that separately from the above analysis. Two additional experiments with three repetitions each where designed utilizing the same parameters as the midpoint of the parametric investigation. Figure 22 shows an overview of the impact of the needle inner diameter on the fibre diameter, the standard deviation of the diameter distributions and the area of deposition of the electrospun scaffolds. There is the possibility that the needle outer diameter is actually affecting the electrospinning behaviour as opposed to the inner diameter. Shin et al. (2001) have shown that under certain spinning conditions the Taylor cone encompasses the whole diameter of the needle[282]. There is no study available that investigates the influence of the outer diameter however so all the data given here is in terms of the needle inner diameter. The needle outer diameter changes from 0.7 mm to 0.9 mm to 1.7 mm for an inner diameter of 0.4 mm, 0.6 mm and 1.2 mm respectively.

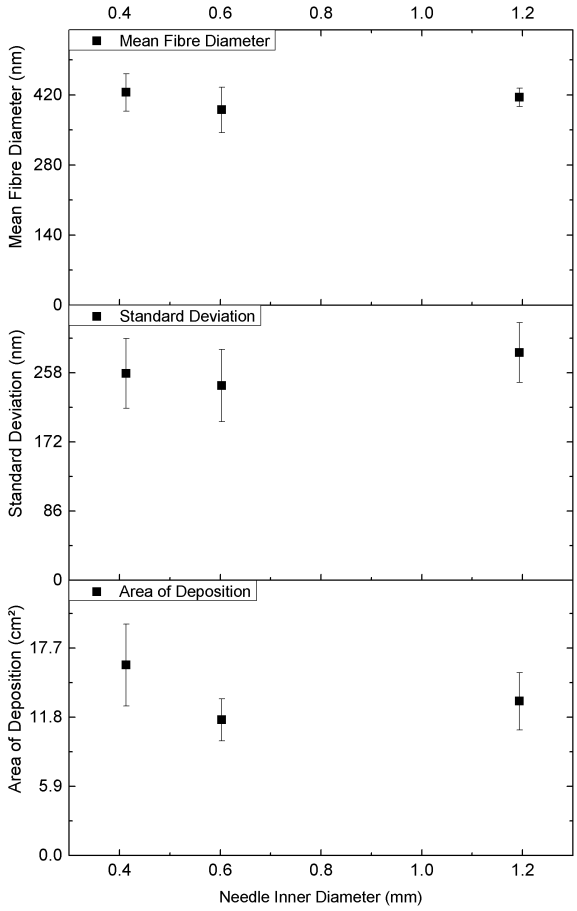

Figure 22: Comparison of the influence of the needle inner diameter on the mean fibre diameter, standard deviation of fibre diameters and area of deposition of the scaffolds for the PCL experimental series.

The needle inner diameter had no significant influence on either the mean diameter of the fibres or the standard deviation. A small decrease in area of deposition was from ~ 16 cm² to ~12 cm² was found with an increase in needle inner diameter.

3.3.2. Summary of PCL Study

In this study, advanced experimental design was used to achieve a facile and thorough characterisation and understanding of the influence of the processing conditions on the morphology and production of PCL electrospun scaffolds on an in-house built electrospinning rig. A two-level central-composite-design was used to investigate what impact the spinning voltage, needle-to-collector distance, solution feed rate and the solution concentration had on the mean fibre diameter, the standard deviation of the fibre diameters and the area-of-deposition of the scaffold. The impacts of the processing variables on these parameters were examined and physical explanations of the findings in conjunction with the

literature were given. Mathematical models were successfully developed and employed to predict morphological properties of electrospun scaffolds with great precision.

3.3.3. PMMA Parameter Study

Similar to the PCL work the main investigation was focused on the average fibre diameter, the standard deviation of the diameter distributions and the area of deposition for each experiment. A higher molecular weight was used for PMMA as a literature survey showed that smoot nanofibres could be produced from PMMA at a M_w of 350000 in HFIP[283]. The processing parameters involved are, spinning voltage, needle-to-collector distance, polymer concentration, solution feed rate and needle inner diameter. Each experimental run was repeated three times. An overview of the experimental runs can be found in Table 9.

Sample No.	Voltage (kV)	Distance (cm)	Feed Rate (mL/h)	Concentration (wt%)	Needle Size (mm)
1	15	15	0.55	4	0.6
Midpoint	20	15	0.55	4	0.6
2	25	15	0.55	4	0.6
3	20	12	0.55	4	0.6
4	20	18	0.55	4	0.6
5	20	15	0.1	4	0.6
6	20	15	1	4	0.6
7	20	15	0.55	3	0.6
8	20	15	0.55	5	0.6
9	20	15	0.55	4	1.2
10	20	15	0.55	4	0.4

Table 9: Overview of the processing parameters and experimental set-up for the PMMA experimental series.

The average fibre diameter is found to vary from 234 nm to 1105 nm with the midpoint of the series exhibiting an average fibre diameter of 574 nm ± 10 nm and showing an excellent reproducibility at standard conditions. At the midpoint of this series the fibres are larger than the fibre distributions seen for PCL scaffolds. The standard deviation of the fibre distribution shows a range from 72 nm to 501 nm while the midpoint had a standard deviation of 228 nm ± 75 nm. This is in the same range as the PCL scaffolds. The area of deposition varied from 1.4 cm² to 21 cm² with the midpoint having an average

area of deposition of 13.6 cm^2 ± 3 cm^2. Parallel to the PCL investigation it was found that the area of deposition showed the largest variance in the dataset. Figure 23 shows an overview of the range of scaffolds obtained with PMMA.

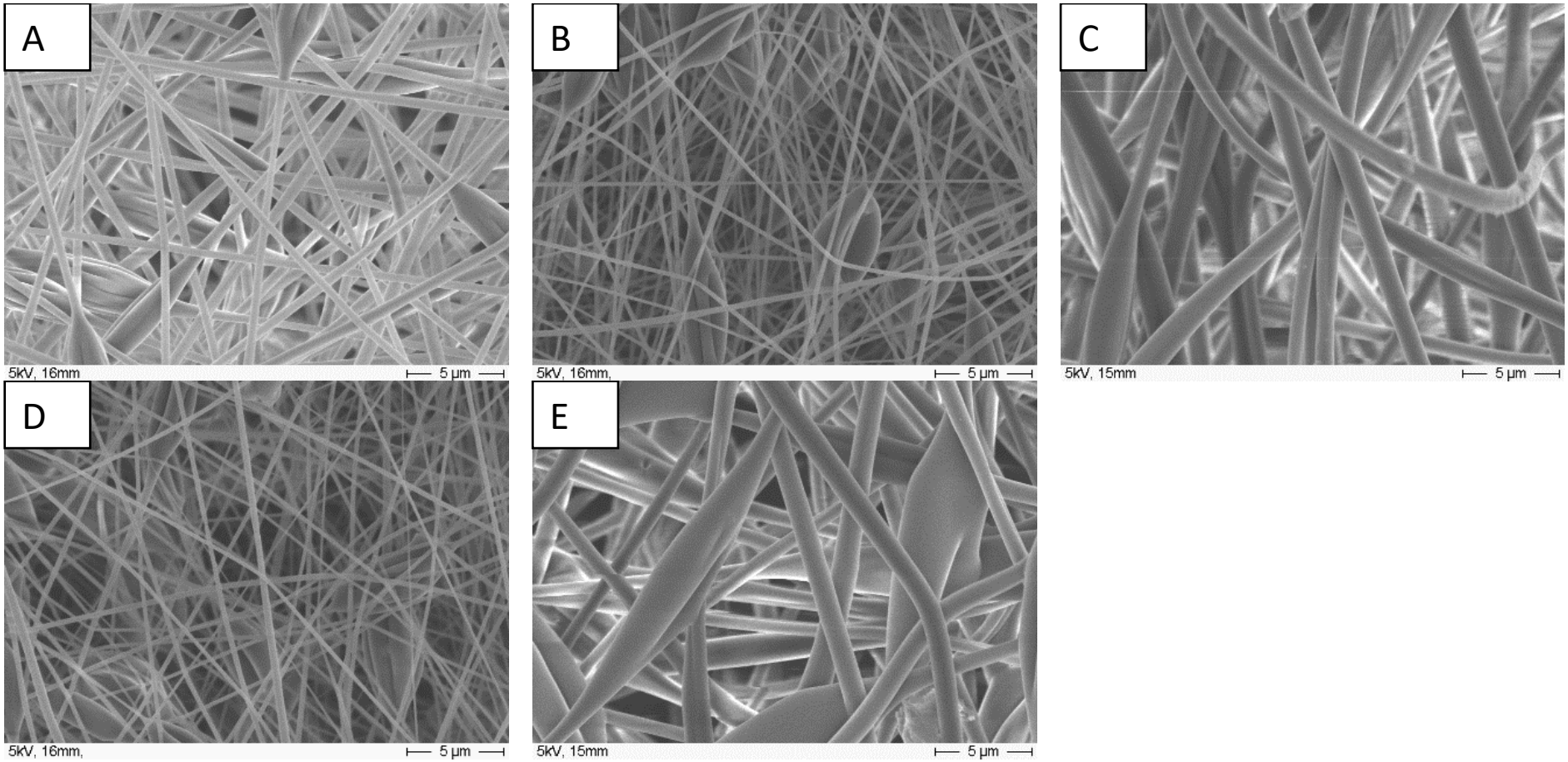

Figure 23: Overview of various types of PMMA scaffolds produced. Scaffolds that exhibited the smallest fibre diameters (A), a standard midpoint sample (B). the largest average fibre diameter found (C), scaffolds with the smallest standard deviation of the fibre distribution (D) and the largest standard deviation found (E). All scale bars are 5 µm.

Contrary to the PCL experimental series it is found that almost every sample exhibits a small amount of beading. Samples with a smaller average fibre diameter show a more pronounced beading than larger fibres. The size and shape of the beads are not affected by the fibre size as they are consistent throughout all samples. The shape of the beads can be described as a biconcave disk with a flattened centre (similar to red blood cells). This type of beading morphology has been observed in the literature before with certain solvents and is found to be dependent on the polymer concentration in the solution, where a higher concentration leads to less beading[284]. However given the very strong correlation between polymer concentration and average fibre diameter it is not possible to obtain sub-micron sized fibres with higher concentrations for the PMMA/HFIP system used here.

Figure 24 shows an overview of the one-parameter at a time design and parametric influence on the investigated morphological properties. The concentration has the biggest impact on the average fibre diameter, changing it from 309 nm ± 32 nm to at 3 wt% to 956 nm ±154 nm at 5 wt%. This is in good agreement with the previous work on PCL and the literature at large where the solution concentration was identified as the most important parameter affecting the mean fibre diameter[257–259]. There is a small drop in the fibre diameter with an increased voltage. The flow rate shows a small but statistically significant positive influence on the mean fibre diameter of the PMMA fibres produced. Finally, the needle inner diameter was found to have a measurable effect on the size of the fibres produced. This is in contrast to the PCL study as there was no significant change observed when the inner diameter was changed from 0.4 mm to 1.2 mm. There is no difference in the average size of fibres when changing from 0.4 mm to 0.8 mm but an increase from 574 nm ± 8 nm at 0.8 mm to 959 nm ± 81 nm at 1.2 mm can be seen. Macossay et al. (2007) found no correlation between the needle inner diameter and the average fibre diameter of PMMA scaffolds[281]. However the largest needle diameter investigated in that study was 0.83 mm at which point the results presented there are in agreement with this study. The distance was found to be statistically insignificant and appears to have no measurable effect on the fibre size.

With regards to the standard deviation of the fibre diameters, both the concentration and the needle size are found to have the most significant impacts on the spread in the fibre diameters produced. There is a clear increase from a low concentration to a high concentration with a concurrent increase in the spread of the standard deviations found. The needle inner diameter only shows an effect on the standard deviation at its high level of 1.2 mm. At both 0.4 mm and 0.8 mm there is no difference between the standard deviation of the fibre distributions whereas at a 1.2 mm inner diameter the largest average increase in standard deviation seen. Both the distance and the flow rate had a small positive influence on the standard deviation albeit with large errors associated with them. The voltage has a negative effect on the standard deviation at its high value of 25 kV whereas no change was observed at 15 kV and 20 kV. Both the magnitude and the direction of the individual parameters on the standard deviation are very similar to their behaviour observed for the mean diameter above. These results are in agreement with the PCL study with regards to the impact of the concentration and the applied voltage.

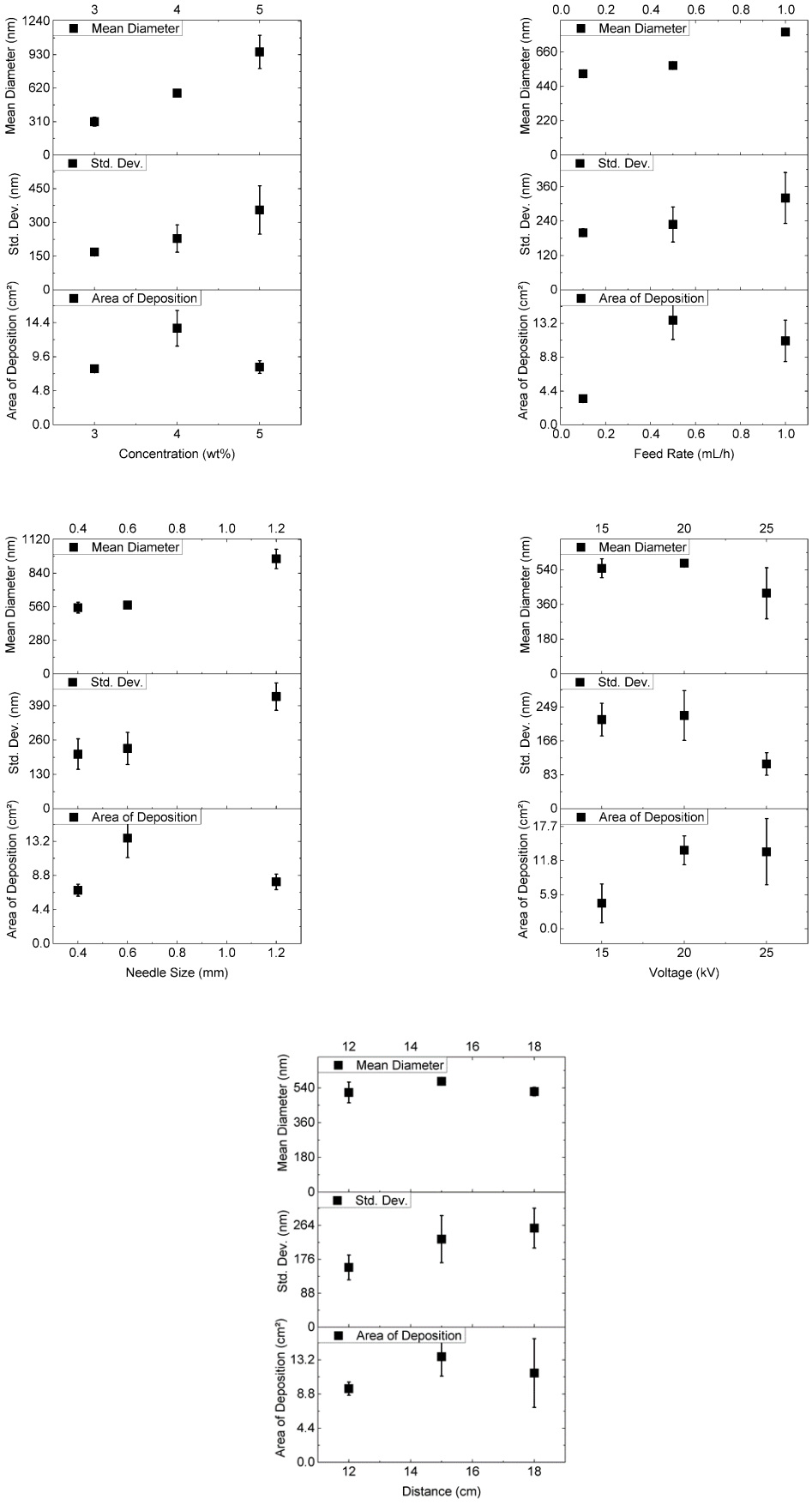

Figure 24: Overview of the individual influence of the processing parameters on the average fibre diameter, the standard deviation of diameters and the area of deposition of PMMA scaffolds.

As with the results for PCL a large variance in the area-of-deposition data is seen. The applied voltage has the strongest impact on the area of deposition with an almost 3-fold increase from 15 kV to 25 kV. The flow rate used has the second largest impact on the area of deposition with a comparable increase to the voltage but a significantly lower variance in the values found. The needle-to-collector distance had no discernible effect on the size of the deposited scaffold other than a higher variance found at the maximum distance used. Both the results for the influence of the concentration or the needle size on the deposition area appear to indicate a parabolic behaviour where an increase followed by a decrease is observed.

Similarly to the PCL study a linear regression was carried out to establish a mathematical model of the correlation between the investigated processing parameters and the average fibre diameter, the spread of fibre diameters found in the scaffolds and the area of deposition. The R^2 values for the developed models based on Equation 5 are shown in Table 10.

Precision of the Established Models		
Average Diameter	Standard Deviation	Area of Deposition
R^2 = ~0.88	R^2 = ~0.71	R^2 = ~0.58

Table 10: Overview of the r^2 values of the models constructed for the average fibre diameter, the standard deviation of the fibre diameters and the area of deposition of the PMMA scaffolds.

The three models show a decreasing level of precisions in terms of their R^2 values. A very good agreement is seen with the average diameter whereas the model for the area of deposition shows the worst fit. In comparison to the PCL study the PMMA regression models follow the same trend in their precision and appear to be similarly good fits for the data presented. In order to test the predictive capabilities of the established models three experiments are carried out in triplicates with random processing parameter choices. The needle inner diameter is kept at 0.6 mm in order to offer a better comparability with the PCL study. The parameters used for the test samples are shown in Table 11.

Experimental Run	Voltage	Distance	Feed Rate	Concentration
1	17	18	0.3	3
2	22	15	0.7	4
3	25	15	0.75	5

Table 11: Overview of the randomly chosen processing parameters for the test experimental series.

In a similar fashion to the PCL study the values predicted of the test samples based on the regression models are compared with the actual measured values for the three investigated parameters (Table 12). The predicted values show a very poor match with the actual measured values. The model for the fibre diameter consistently underestimates the actual values and shows an average difference of 40% ± 10% across the three test samples. The fit of the regression model for the standard deviation of the fibre diameters follows a similar trend where all predicted values underestimate the measured ones. It shows a slightly better fit with an average deviation from the measured values of 28% ± 12% across the three test samples.

Experimental Run	Predicted Value	Measured Value
Fibre Diameter		
1	223 nm ± 242 nm	479 nm ± 11 nm
2	600 nm ± 92 nm	856 nm ± 76 nm
3	887 nm ± 202 nm	1423 nm ± 59 nm
Standard Deviation		
1	187 nm ± 189 nm	209 nm ± 72 nm
2	226 nm ± 72 nm	360 nm ± 8 nm
3	275 nm ± 157 nm	438 nm ± 37 nm
Area of Deposition		
1	-2.3 cm^2 ± 9 cm^2	7.4 cm^2± 3.8 cm^2
2	15.6 cm^2 ±3.4 cm^2	14.5 cm^2 ± 1.5 cm^2
3	8.7 cm^2 ±7.5 cm^2	12.3 cm^2 ± 1.7 cm^2

Table 12: Comparison of the predicted and measured values for the average fibre diameter, standard deviation of fibre diameters and area of deposition of the PMMA scaffolds for the validation experiments.

Finally the accuracy of the regression model for the area of deposition with the measured values is found to be the worst with an average deviation of 49% ± 20%. It should be noted that for the first test experiment the predicted value is negative, which is physically impossible. All three developed regression models for PMMA fail to successfully predict the properties of the experimental test series in contrast to the PCL models. This is despite the similarity in the R^2 values found for both cases. These results highlight the shortcomings of the one-parameter-at-a-time approach. While it is possible to determine the individual impact of processing parameters on the investigated morphological qualities of the scaffolds, the lack of inclusion of second-order interaction parameters in the experimental design leads to the development of inaccurate regression models. In terms of the average fibre diameter

advanced experimental design has been shown to be powerful tools to develop highly accurate mathematical models to predict experimental values[257–259].

3.4. Conclusion

In this chapter the relationship between the processing and solution parameters of an in-house built electrospinning rig and the morphological properties, as measured by the mean fibre diameter, the standard deviation of the diameter distributions and the area of deposition of the scaffolds, was investigated. An extensive two-level central-composite design was devised and successfully employed to explore the empirical correlations of the processing parameters with the scaffold properties of electrospun PCL nanofibres and to elucidate the physical background of the nature of these interactions.

The average fibre diameter was found to be strongly, positively correlated with the solution concentration and the solution flow rate. The applied voltage was shown to reduce the fibre diameter with an increase in voltage. Additionally it was seen that the second-order interactions between the flow rate and the concentration (positive impact) and the voltage and concentration (negative impact) are statistically significant. To the best of the author's knowledge this represents the most in-depth study on the dependency of the variance found in the fibre distributions of electrospun PCL scaffolds to date. There exists very limited information on the behaviour of the deposition area with electrospinning parameters. This study currently represents the most systematic analysis of the area of deposition in electrospinning. Based on the results of the experimental investigation it was possible to create regression models for all three morphological parameters which were shown to exhibit excellent predictive capabilities in validation experiments. The influence of the needle inner diameter was also studied and was shown to have no statistically significant impact on any of the three parameters.

In addition to the PCL series a comparison study was carried out with PMMA, where a standard one-parameter-at-a-time approach was utilized. PMMA was chosen due to the existing understanding and body of literature on the impact of various processing parameters on the fibre diameter. The experimental series was able to reproduce basic results found in the literature and the same interactions as established in the PCL work for the first order interactions with the notable exception of the needle inner diameter. Regression models built on the dataset however failed to replicate a satisfactory level of

precision in predicting results in validation experiments. These results highlight the importance and usefulness of advanced experimental design.

In conclusion it was shown that the in-house built electrospinning set-up is capable of reliably producing PCL and PMMA nanofibrous scaffolds. Advanced experimental design was shown to be a powerful tool to understand correlations between processing parameters and the morphology of the produced scaffolds. The design of experiments employed in the PCL study is superior in its predictive capability over a standard one-parameter-at-a-time approach. Based on the regression models developed it is possible to tailor and design PCL scaffolds with desired morphological properties, eliminating the need to individually check samples due their high precision.

4. The Crystalline Properties of Electrospun PCL Fibres

4.1. Introduction

The crystallinity of a semi-crystalline polymer is a fundamental property that influences various physical characteristics, specifically the mechanical strength[285], which has been shown to be important in determining cell growth fate[120]. The two most commonly employed techniques to measure to characterise the crystalline structure of polymers are x-ray diffraction (XRD) and differential scanning calorimetry (DSC)[286]. Due to the aforementioned importance of the mechanical properties for tissue engineering and other applications, considerable work has been carried out on the tensile properties of electrospun scaffolds[287]. The emerging consensus from the existing body of literature is that the average fibre diameter as determined by the polymer solution concentration is an important indicator of the mechanical performance of nanofibrous scaffolds, where a decrease in the fibre diameter was found to result in an increase in tensile properties[288–290].

Polycaprolactone (PCL) (Figure 25) is a biodegradable, semi-crystalline, linear aliphatic polyester with an orthorhombic crystal structure of the $P2_12_12_1$ space group[291]. It is one of the most commonly used polymers for a biomedical applications because of its excellent biocompatibility[262].

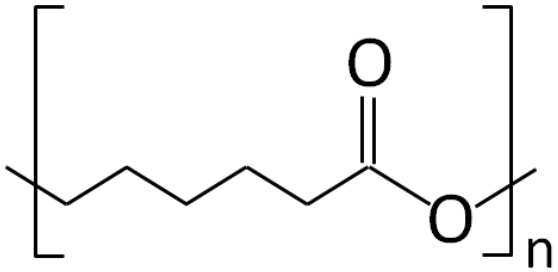

Figure 25: Molecular structure of polycaprolactone.

This chapter examines the relationship between the fibre diameter, the crystalline properties and the mechanical properties of electrospun PCL scaffolds. An additional focus is the nature and reliability of the aforementioned techniques in accurately measuring the crystalline properties of electrospun nanofibres. A significant discrepancy is found for the measured values of the degree of crystallinity between the two techniques and an explanation for the findings if given. Furthermore the results from

this study show that the correlation between fibre morphology and tensile properties is not as straightforward as previously thought and that the crystallinity is an important factor that needs to be considered.

4.2. Methods

4.2.1. Electrospinning

Electrospinning was carried out with the protocol described in [2.1]. PCL was dissolved in HFIP at fixed weight percents of 3 wt%, 4 wt%, 5 wt%, 6 wt% and 7 wt% with respect to the solvent. The spinning time was 20 minutes for all experiments. Two sets of experiments were carried out, one concentration series and one feed rate series. An overview of the processing parameters are found in Table 13. All experimental runs were done in triplicates in order to assess variability.

Experimental Run	Voltage (kV)	Distance (cm)	Feed Rate (mL/h)	Concentration (wt%)
Concentration Series	25	15	0.55	3, 4, 5, 6, 7
Feed Rate Series	25	15	0.1, 0.55, 1	5

Table 13: Overview of the processing parameters for the electrospinning of PCL scaffolds from the two experimental series.

4.3. Mechanical Testing of Whole Scaffolds

In this and subsequent chapters the mechanical properties of different kinds of electrospun scaffolds are investigated. As described in [2.8] the method utilized in this work is a simple tensile testing of cut-outs of whole scaffolds. Due to the unavailability of the specialized equipment necessary to measure the properties of individual fibres it was only possible to evaluate the tensile properties of whole scaffolds. In this sub-chapter the relationship between the mechanical properties of a single electrospun fibre and the mechanical properties of a whole scaffolds are investigated from a theoretical point of view.

It has been established that single fibres made by electrospinning generally have weaker mechanical properties as compared to other fabrication methods[77]. Additionally, the modulus and strength was found to increase for PCL with a decrease in fibre diameter due to chain alignment and potential confinement

at very small diameters[288–290]. While morphological and microstructural influences on single fibres can be measured directly, it becomes more difficult when considering a full electrospun scaffold. All the membranes used in this work are randomly aligned and non-woven with a high degree of porosity. The mechanical properties are then not just dictated by the properties of single fibres but also by the interaction between fibres and their movement with respect to each other. Koh et al. (2013) showed that there are two distinct failure mechanisms with electrospun mats, depending on the brittleness of the polymer used[292]. They found that brittle, fibrous gelatin scaffolds maintained their random, non-woven structure as cracks propagated during tensile testing. More ductile PCL scaffolds on the other hand exhibit a strong fibre alignment and hence morphology change during mechanical testing. This means that – when corrected for porosity – scaffolds made from brittle fibres are tested, the expected mechanical properties should deviate further from their bulk properties.

Additionally there is a body of work in the literature that tries to establish some theoretical models on how to predict the mechanical properties of whole scaffolds from the properties of individual fibres coupled with the overall scaffold morphology. Mohammadzadehmoghadam et al. (2016) provide a good overview of the existing literature which attempts to reconcile theoretical models with empirical results[293]. In order to understand the relationship between the mechanical properties of single fibres and the mechanical properties of nanofibre meshes it is important to consider the overall morphology of the scaffold in addition the materials properties. In conjunction with the materials properties, morphological parameters such as fibre alignment[294–296], scaffold porosity[294,295], number of fibre fusion points[296,297] and curvature of fibres[294]. It is beyond the scope of this work to fully investigate the interaction between all of these parameters and their individual influence on the mechanical properties of the various scaffolds produced. Because of the aforementioned influence of the morphological structure of the scaffolds and the difference between brittle and ductile polymers it is difficult to assess and compare different types of polymers and scaffold and their mechanical properties. Hence all the values given in this work for the tensile data of different scaffolds are not to be taken as reference data for this type of polymer but rather for the combination of materials properties and morphology. However within the datasets – given that parameters such as alignment, porosity and curvature of fibres do not change significantly with fibre diameter – it is possible to obtain comparative information that can be traced to microstructural changes

with the fibres. The number of fibre fusion points – which can be approximated by the number of fibre intersections per unit area – is dependent on fibre diameter. Smaller fibres will exhibit more intersections per unit area. Hence when comparing scaffolds of the same material with large differences in fibre diameters there will be a small contribution to the mechanical properties due to more fibre fusion points. Nevertheless, within the same datasets a change in the measured tensile properties will be indicative of a change the tensile properties of the fibres albeit potentially in non-linear and more complex way. All scaffolds in this work are randomly aligned and are sufficiently similar (sometimes almost identical) morphologically that any significant change in membrane tensile properties can be attributed to a change in mechanical properties at the individual fibre level. This hypothesis is implicitly assumed in every instance of analysis of the mechanical properties in this work.

4.4. Results and Discussion

All experimental processing conditions produced smooth, defect-free, nanofibrous scaffolds [3.3.1]. The average diameter of the fibres was determined by SEM [2.3] and it was found that all were monotonically increasing with both investigated parameters, as evidenced by Figure 26. These results are in accordance with previous observations on the effect of various processing conditions on the fibre diameter [3.3.1]. Within the investigated processing conditions the average fibre diameter changes from ~250 nm – ~980 nm and from ~290 nm to ~1140 nm for the concentration or the feed rate respectively. Hence it is possible to control the average size of the fibres via a change in these two parameters by roughly an order of magnitude (Figure 26).

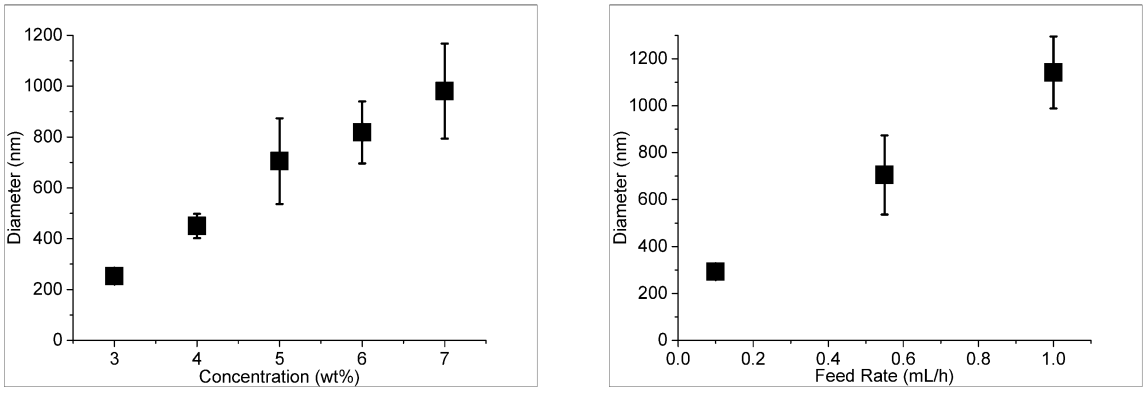

Figure 26: Relationship between the average fibre diameters with respect to a change in either concentration or feed rate.

The crystallinity of the fibres from this solution concentration series was measured using both XRD and DSC techniques [2.6] and [2.9] respectively. The crystallinity of the as-received PCL pellets was found to be 44% or 46% as determined by XRD and DSC respectively. The XRD analysis of the concentration series showed a decreasing trend in the measured degree of crystallinity with solution concentration. Starting at 55.3% ±1.9% at a 3 wt% concentration down to 48% ± 0.9% at 7 wt% (as shown in Figure 27). Concurrently the degree of crystallinity measured by DSC for the concentration series exhibits an increasing trend with solution concentration, from 39.7% ± 2.5% at 3 wt% to 45.7% ±1.9% for the 7 wt% solutions. A direct comparison of these two techniques reveals a significant difference in the measured values of the degree of crystallinity at the lower solution concentrations or smaller fibre diameters. A change in the feed rate elicits a similar behaviour. The degree of crystallinity was found to decrease from 63.3% ± 2% at 0.1 mL/h down to 44% ± 1.6% at 1 mL/h with an increase in flow rate as measured by XRD. The measured values for the degree of crystallinity by DSC showed a strong, increasing trend with an average of 18% ± 4.5% at a flow rate of 0.1 mL/h, up to 48% ± 4.5% at 1 mL/h. The observed difference between the two techniques is greater when the feed rate is lowered which also coincides with a decrease in the average fibre diameter. The difference in the measured values for the degree of crystallinity between XRD and DSC at the lowest feed rate is ~3.5. A small difference in the absolute values of crystallinity measured by these two techniques was observed in bulk materials before[298] but normally the values obtained by the different techniques are in agreement with each other[299].

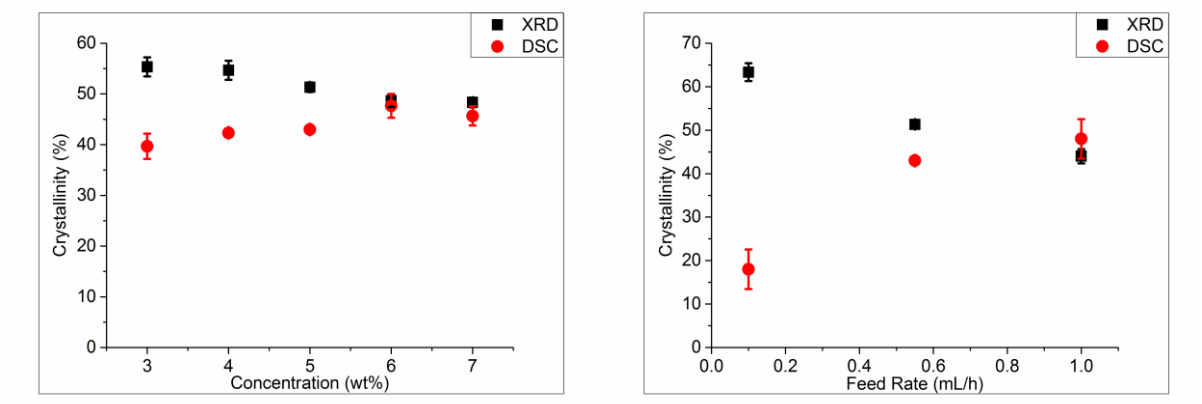

Figure 27: Relationship between the degree of crystallinity as measured by DSC and XRD with respect to a change in the concentration or the feed rate.

The difference in the measured crystallinity, both in absolute values as well as the general trend has not previously been reported for electrospun scaffolds. Some studies on various electrospun polymers, as well as PCL report that the electrospinning process reduced the overall crystallinity[300,301,302] as judged only from DSC measurements.. The results from the XRD measurements in this work are in agreement with the literature concerning the influence of fibre diameter on crystallinity[290,303]. The apparent discrepancy amongst studies of the influence of electrospinning on the crystalline structure in the literature and the results presented in this work point towards a previously unreported phenomenon. XRD measures the degree of crystallinity by directly comparing the amount of crystalline material with the amount of amorphous polymer present[304]. DSC on the other hand relies on thermodynamic assumptions to calculate the crystallinity using the melting behaviour of the material[305].

The average size of the crystallites was investigated in order to draw conclusions between the internal crystalline structure found in the nanofibres and the processing conditions as shown in Figure 28. A change in the solution concentration did not result in any significant change in crystallite size for either the (110) or the (200) reflection. The crystallite size derived from the (110) feature was 29 nm ± 0.3 nm at 3 wt% and 29.8 nm ± 0.8 nm at 7 wt%. The size derived from the (200) feature was similarly unaffected by a change in solution concentration with a size of 22.5 nm ± 0.6 nm for the 3 wt% solution and a size of 21.2 nm ± 0.8 nm for the 7 wt% solution. A change in the solution feed rate was found to have a significant effect on the crystallite size. For the (110) reflection the size was found to be 21.2 nm ±0.5 nm for a feed rate of 0.1 mL/h which increased to 25.6 nm ± 0.7 nm at 1 mL/h. This was found to be still slightly lower than all the measured values at 0.55 mL/h. Similarly the size derived from the (200) reflection crystallites decreased to 16.8 nm ± 0.7 nm at 0.1 mL/h and increased to 21 nm ± 0.3 nm at 1 mL/h, changing the ratio of (110)/(200) which remained practically constant for all other measurements. These measurements show that the solution feed rate has a more significant influence on the internal crystalline structure of the fibres than the solution concentration.

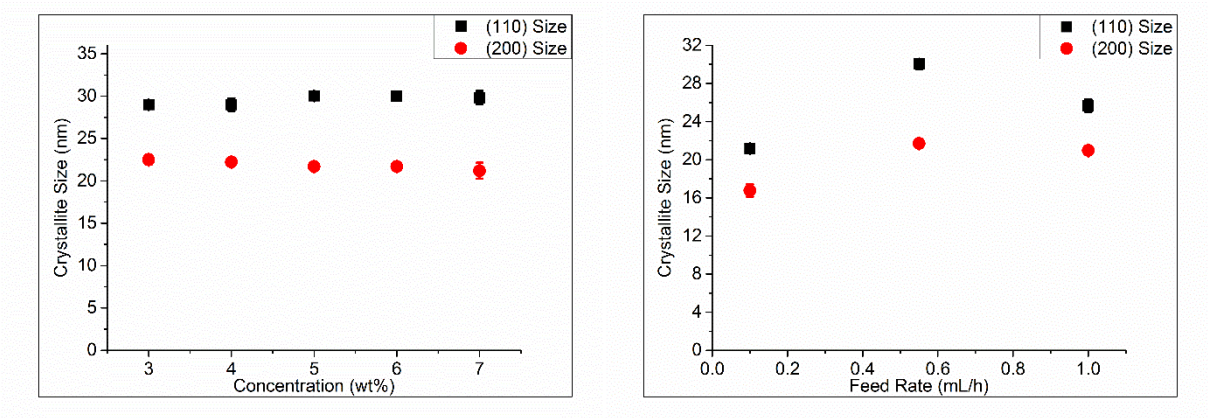

Figure 28: Comparison of the relationship with the (110) and (200) crystallite size as measured by XRD with a change in concentration or feed rate.

Figure 29 shows an overview of typical thermograms obtained from scaffolds made from a 5 wt% solution, a 3 wt% solution and a 5 wt% solution with a feed rate of 0.1 mL/h. The determination of the degree of crystallinity in DSC relies on the melting behaviour of the materials involved. It is assumed that the ratio of the measured melting enthalpy to that of a 100% crystalline bulk sample is equivalent to the degree of crystallinity. Electrospun scaffolds typically exhibit porosities of up to ~90%[137] and very large surface areas in the range of 10 – 20 m^2/g[306]. These factors lead to known issues with DSC measurements with regards to thermal lag and phase transitions[298,307]. The results presented in this work suggest that there is a size effect leading to a reduction in melting enthalpy. A reduction in the polymer solution concentration only leads to a change in the average fibre diameter, whereas the internal crystalline morphology remains unchanged as evidenced by the crystallite size measurements. Smaller fibres exhibit a poorer heat conduction due to smaller fibre-fibre connections and a significantly increased surface area for the same weight. During melting the reduction in surface area releases energy which suppresses the measured melting enthalpy. Hence the observed difference in degree of crystallinity at small fibre diameters between DSC and XRD, whereas at large fibre diameters or in bulk the measured values are converging.

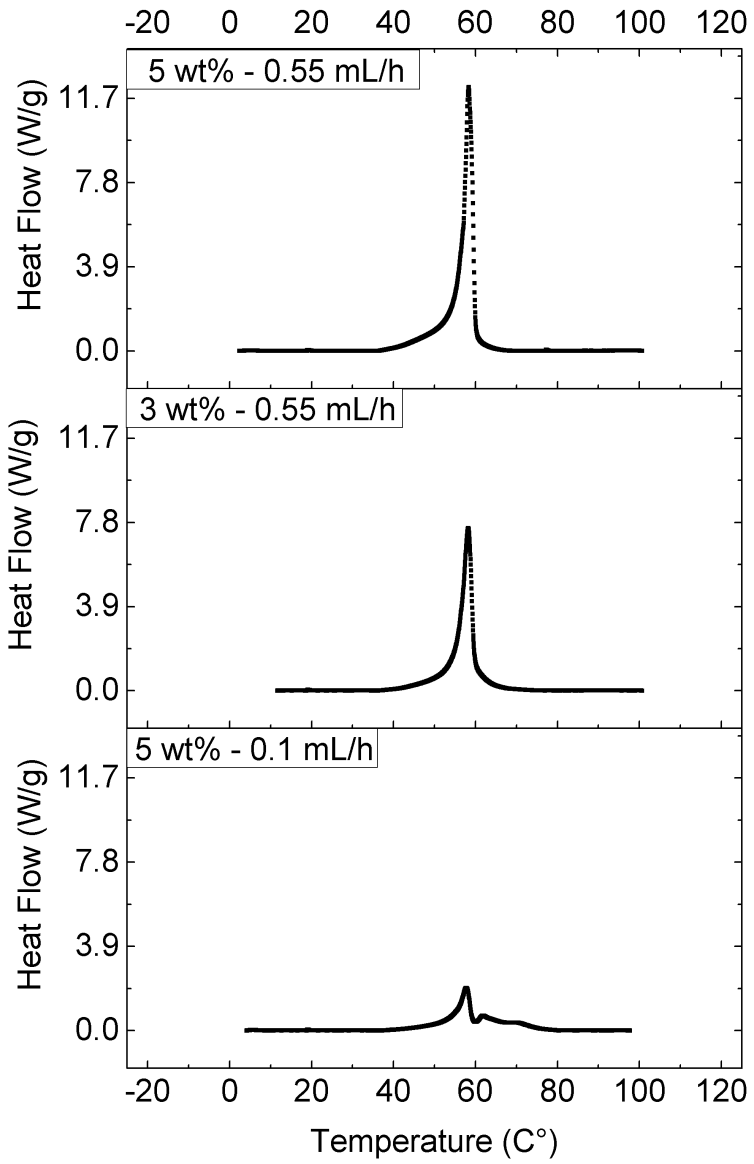

Figure 29: DSC thermograms taken of PCL scaffolds made with a 5 wt% solution at 0.55 mL/h (top), a 3 wt% solution at 0.55 mL/h (middle) and 5 wt% solution at 0.1 mL/h (bottom).

By lowering the feed rate not only is the average fibre diameter decreased but the size of the crystallites is lowered significantly. Van Dooren et al. (1982) have observed that the particle size of various materials can have a significant impact on the enthalpy of melting and thermograms obtained by DSC[308]. The DSC thermogram at 0.1 mL/h exhibits a largely reduced peak and shows a small second peak at ~61°C. This is indicative of recrystallization and remelting[309] which can be avoided using specialized, high heating rate equipment (which was unavailable for this work). The presence of smaller crystallites in larger numbers is conducive to recrystallization, whereby during melting smaller crystallites fuse

together to form larger crystals and then subsequently melt. This process releases energy which further suppresses the measured melting enthalpy and results in the large difference observed between the degree of crystallinity measured by XRD and DSC.

The mechanical properties of the whole scaffolds of the two series are summarised in Figure 30. There were three mechanical properties measured for each of the investigated processing parameters, namely, the modulus, the ultimate tensile strength and the strain at break. For a change in concentration it was found that both the modulus and the ultimate tensile strength decreased as the solution concentration was increased. The modulus was found to decrease from 8 MPa ± 1.6 MPa at 3 wt% to 4 MPa ± 0.3 MPa at 7 wt%. The ultimate tensile strength followed a similar trend, decreasing from 0.18 MPa ± 0.05 MPa at 3 wt% to 0.15 MPa ± 0.03 MPa at 7 wt%. The strain at break was found to increase with solution concentration, from 108 ± 9 at 3 wt% to 246 ± 27 at 7 wt%. The results for the feed rate series follow the same trends in a more pronounced way. The modulus was found to decrease with an increase in feed rate, from 18 MPa ± 1.1 MPa at 0.1 mL/h to 8.1 MPa ± 0.8 MPa at 1 mL/h. The ultimate tensile strength decreased from 0.28 MPa ± 0.04 MPa at 0.1 mL/h to 0.18 MPa ± 0.01 MPa at 1 mL/h. Similarly to the concentration series an increase in the strain at break was found with an increase in feed rate, with a strain at break of 135 ± 34 at 0.1 mL/h to 246 ± 27 at 1 mL/h. The measured mechanical properties are within the range of values found in the literature for electrospun PCL scaffolds[86,310–312].

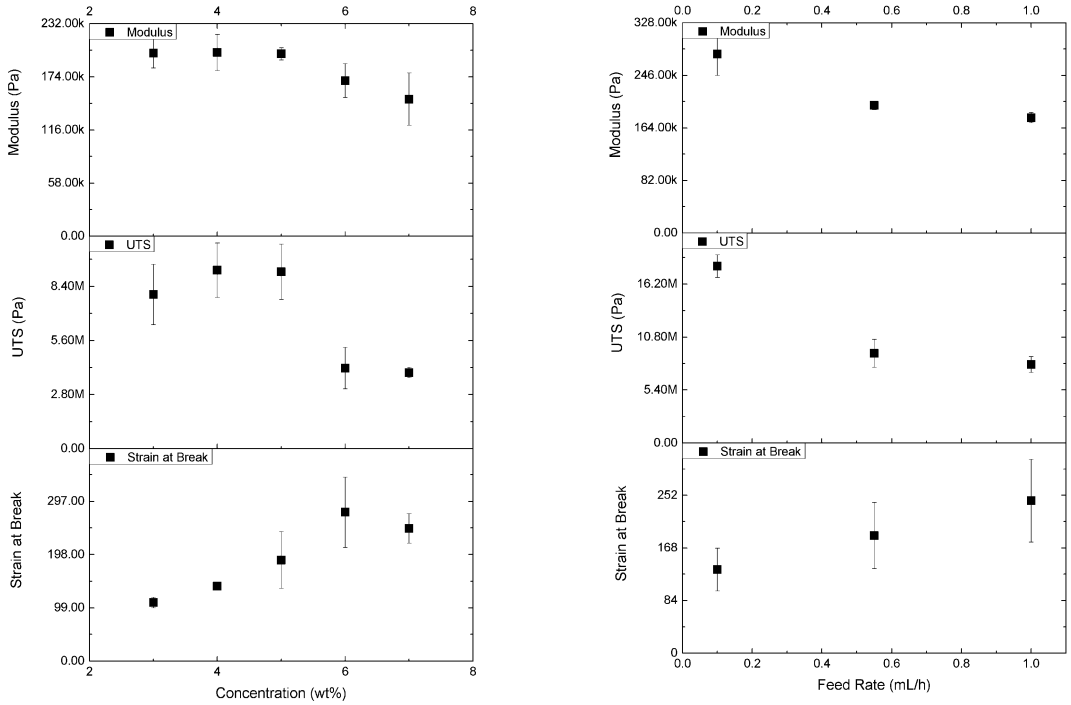

Figure 30: Relationship of the modulus, UTS and strain at break of the PCL scaffolds with respect to a change in concentration or solution feed rate.

These results show a clear dependency of the mechanical properties on the investigated parameter, namely the solution the concentration and the feed rate. Previous studies have establish a correlation between the size of the fibres and their mechanical properties[288–290]. Figure 31 gives an overview of all the mechanical testing data with respect to the diameters of the particular scaffold. As can be seen there is no strong trend emerging with either the UTS or the modulus. The strain at break of the scaffolds does exhibit a correlation with the mean fibre diameter, where an increase in diameter is accompanied with an increase in the strain at failure. From these results it becomes evident that it is possible to have very different tensile strengths and tensile moduli of electrospun membranes while exhibiting similar average fibre diameters. These results suggest that the mechanical properties of electrospun PCL scaffolds need to be understood as the interplay between fibre morphology and the internal crystalline structures. It is possible to produce fibres in similar diameter ranges and tailor the whole-scaffold mechanical properties through a change in the internal crystalline structure.

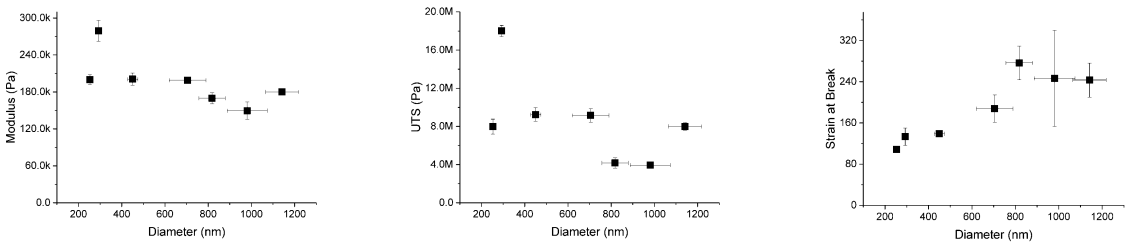

Figure 31: Overview of the modulus, UTS and strain at break for PCL scaffolds with respect to the average fibre diameter of the scaffold.

Building on the above observations a simple model can be constructed to explain the difference in mechanical properties found for scaffolds containing fibres of similar average diameters. The mechanical properties of electrospun PCL membranes must be understood not solely as a function of average fibre diameter but rather as the relationship between average fibre diameter and internal fibre microstructure. While it is understood that size effects at smaller diameters come into effect in tensile testing, mainly due to surface energy contributions[313], the effects measured in this study go beyond that contribution. The overall degree of crystallinity as well as the crystallite size needs to be taken into account. Figure 32 shows a conceptual overview of the internal crystalline structure of two fibres with similar diameters but made under different processing conditions in conjunction with their stress/strain curves. At this point the reader is reminded of the discussion in [4.3] where the mechanical properties of a whole scaffold can be understood as a product of scaffold morphology and individual fibre properties. Given the condition of identical morphology and fibre diameter the observed large difference in mechanical properties can be attributed to the change in tensile properties of individual fibres. Lim et al. (2008) proposed a similar model based on AFM phase imaging of single nanofibres[288] They were able to show that fibres with different diameters have different internal structures and smaller fibres have more densely packed and smaller crystalline areas. In this study the properties of the overall scaffold is considered and it is demonstrated that through a change in processing conditions, especially the solution flow rate, it is possible to produce scaffolds with similar mean diameters but very different crystalline morphologies.

A good overview of the existing literature and correlation between fibre diameter and tensile properties was established by Yao, Bastiaansen and Peijs, (2014)[77]. The general consensus is that confinement effects play an important role in the observed increase in mechanical properties with a decrease in fibre

diameters, as the polymer coils are forced to align with the nanofibre axis. In order to achieve stronger mechanical properties the polymer chain orientation needs to align with the nanofibre axis. Based on the work from the aforementioned review these confinement effects can be excluded for the length-scales achieved in this work. The observed increase in mechanical properties for the PCL fibres used here can hence better be explained by the measured increase in crystallinity and crystallite size.

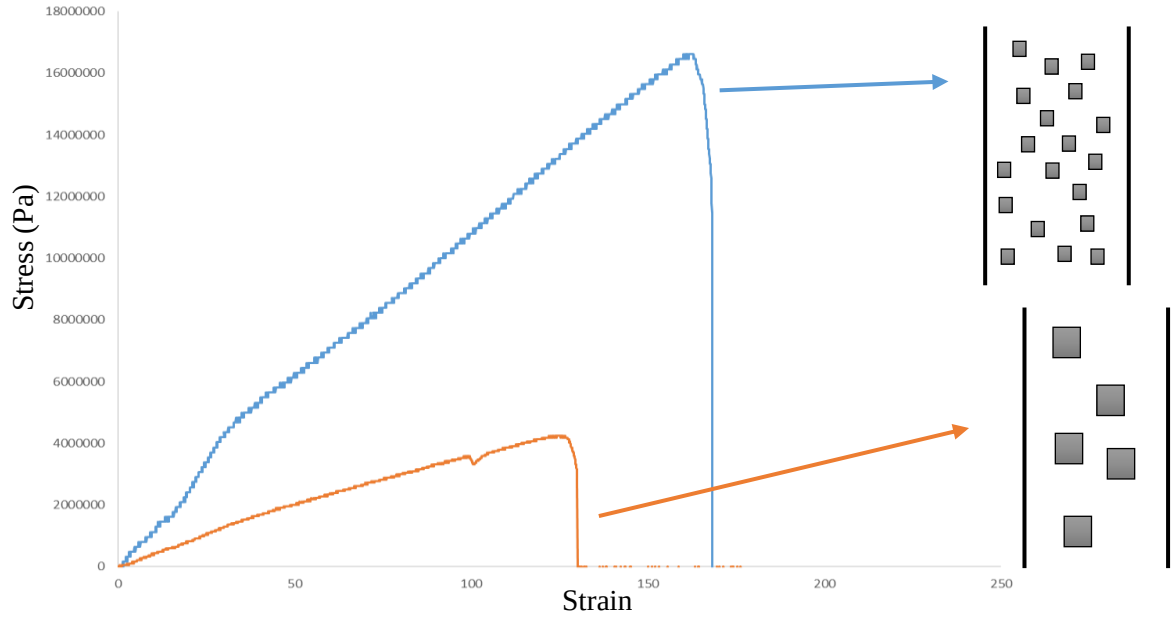

Figure 32: Comparison of two stress-strain curves of PCL scaffolds with similar average diameters. The scaffold with a higher degree of crystallinity and smaller crystallite sizes (blue) has a significantly higher modulus, UTS and strain at break than the scaffold with a similar diameter (orange) but a lower degree of crystallinity and larger average crystallite sizes.

It is well established that the degree of crystallinity is a defining parameter for the mechanical properties of polymers, with the crystallites acting as a hard phase, leading to a classical thermoplastic deformation behaviour and the amorphous phase acting as a soft phase[314]. This offers an explanation for the difference seen in the mechanical properties between fibres which have different degrees of crystallinity.

Greenfield et al. (2012) carried out an extensive study on the impact of the processing parameters on the evolution of the diameter of the jet radius and the ratio of solvent to polymer during the linear portion of the electrospinning jet[315]. They found that both the initial solution concentration and the feed rate had significant effects. An increase in both parameters lead to thicker jets and larger remaining polymer concentrations in the electrospinning jet. These observations in turn were shown to result in lower

evaporation rates and lower strain rates. Additionally it is known that both the evaporation rate[316] and the strain rate[317] during crystallization have a significant impact on the crystalline properties of semi-crystalline polymers – such as degree of crystallinity and crystallite size – as well as the orientation of crystallites[318]. Based on the existing literature and the presented results it is strongly suggested that lower solution concentrations as well as lower flow rates during electrospinning increase the degree of crystallinity through strain and evaporation induced crystallization.

4.5. Conclusion

In this chapter the degree of crystallinity of electrospun PCL fibres was measured with XRD and DSC, the two methods were compared with regards to their accuracy to determine the crystallinity of these fibres and a relationship was established between the average fibre diameter, the crystalline structure and the mechanical properties of the scaffolds. In two experimental series the influence of a change in polymer solution concentration and spinning feed rate were investigated with respect to the aforementioned properties. It was found that the two methods vary greatly in the values given for the degree of crystallinity. While XRD measurements showed a decrease in degree of crystallinity with larger fibres, DSC measurements exhibited the opposite. It was demonstrated that the DSC thermograms were influenced by the size effects at small fibre diameters, where recrystallization and remelting was observed. It is hence strongly advised that future investigations in the degree of crystallinity in PCL nanofibres should rely on XRD techniques rather than DSC measurements. Differences as large as ~40 percent points were found in samples with small fibre diameters and reduced crystallite sizes. No comparative studies are available for different polymers but it is likely that this discrepancy might translate to other systems commonly used in electrospinning and should be investigated.

A change in the PCL solution concentration had no impact on the average crystallite size as determined by XRD whereas it was found that a low spinning flow rate reduced the sizes derived from both the (110) and the (200) reflections. This can be attributed to the increased strain of the electrospinning jet experienced under these conditions and faster solidification rates that prevent the crystallites from growing larger during fibre formation.

The tensile properties of the scaffolds were measured and a strong correlation for both the ultimate tensile strength and the elastic modulus were found with a change in spinning parameters. Increased concentrations or feed rates resulted in weakened mechanical properties whereas the opposite trend was observed for the strain at failure for these scaffolds. Additionally it was shown that it is possible to produce scaffolds with similar, small fibre diameters but distinctly different tensile properties through a control of the processing conditions. The crystalline properties of the PCL scaffolds were established as the most important factor determining the mechanical properties over the fibre morphology.

In conclusion the crystalline properties of electrospun PCL scaffolds determine the tensile strength and modulus. To the best of the author´s knowledge the work in this chapter represents the first demonstration of a large discrepancy found in the measured degree of crystallinity between XRD and DSC. It is possible to tailor those properties through a control of the processing conditions, specifically the solution concentration and the feed rate. The measurement of the degree of crystallinity is dependent on the technique used and DSC can give false results at small fibre diameters due to size effects during melting.

5. Reinforcement of PCL Nanofibres with Carbon Nanotubes

5.1. Introduction

Multiwalled carbon nanotubes exhibit extraordinary physical properties, such as superior mechanical properties to most known materials[180], excellent electrical conductivity[189] and extremely large aspect ratios[319]. They are an ideal candidate for the use as a reinforcement in composite materials. In this chapter CNT's are chemically bound to a polymer to produce highly homogeneous composites. I show that electrospun polymer-functionalised CNTs form scaffolds with superior mechanical properties as compared to neat polymer fibres. Using the optimised electrospinning parameters developed in [3.3] the link between the physical and microstructural properties of these scaffolds are understood and subsequently used for cell growth experiments in [7].

The first published work of electrospun CNT-polymer fibres were produced by Seoul et al. (2003)[206] who successfully added SWCNTs into PVDF fibres which resulted in a five-fold increase in the electrical conductivity of the electrospun mat. There is an existing body of literature exploring how CNTs affect the physical properties, such as electrical[149,226,320], thermal[320,321] and optical[148] of the as-spun scaffolds. A number of authors have found that as the CNT concentration increases the tensile strength is also increased until it peaks and then decreases. The concentration at which the highest increase in tensile strength is observed varies between studies and seems to be dependent on many factors, such as the polymer used, type of CNT, CNT functionalization, solvent and the spinning parameters that are employed. It is understood that the relationship between the amounts of CNTs added the final degree of reinforcement for polymer/CNT composites does not follow a *rule-of-mixtures* behaviour[322]. The rule-of-mixtures can adequately describe macroscopic fibre composites[323] but often fails for nanocomposites. In some cases it was possible to use a modified Halpin-Tsai[324] equation to model the measured mechanical properties of the CNT-reinforced nanofibre mats[210,325–327]. The motivation behind an investigation of CNT-containing electrospun scaffolds for cell growth is such scaffolds were shown to outperform neat polymer scaffolds in terms of biocompatibility and cell proliferation[142,144,220,237].

5.2. Materials and Method

5.2.1. CNT Synthesis

Multiwalled carbon nanotubes (MWCNTs) were produced using an aerosol-assisted chemical vapour deposition (AACVD) technique consisting of a piezo-driven aerosol generator (RBI Pyrosol 7901), a quartz tube (2.2 cm inner diameter) and a 50 cm long horizontal electrical furnace, equipped with a gas flow controller and a gas trap filled with acetone. A solution of 5 wt% Ferrocene ($Fe(C_5H_5)_2$, 98%) was dissolved in toluene ($C_6H_5CH_3$, Fluka 99.7%) and prepared in an ultrasonic bath for 30 min. For the carbon nanotube growth the Ferrocene-containing toluene solution was fed into the piezo-driven aerosol generator. The generator (located as near as possible to the furnace in order to avoid the coalescence of droplets) was then connected to the quartz tube located in the horizontal tube furnace. Once the system was set-up, the aerosol generator and the quartz tube were flushed with 100 sccm argon while the furnace was heated to a temperature of 850°C in order to remove any unwanted oxygen from the reactor. When the desired temperature was reached the aerosol generator was switched on and the argon flow was increased to 2500 sccm for the duration of the experiment (30 minutes). Subsequently, the flow rate was reduced again to 100 sccm and the piezo-driven aerosol generator was switched off while the furnace was left to cool to room temperature[328]. The CNTs were synthesised by Dr. Shayan Meysami (Department of Materials, University of Oxford).

5.2.2. CNT Functionalization

The functionalization of the CNTs consisted of a three step process. At first, one gram of the as-produced MWCNTs was chemically modified by an acid-reflux in a 3:1 (v/v) mixture of concentrated H_2SO_4 (Concentrated, Sigma-Aldrich) and HNO_3 (60%, Sigma-Aldrich) for four hours and then filtered until the pH normalised to a pH of 7. In the second step 100mg of the acid-functionalized CNTs were mixed with 5g of N,N'-Dicyclohexylcarbodiimide (DCC, Sigma-Aldrich) and 5mL of Ethylenediamine (EDA, Sigma-Aldrich) into 100 mL of Dimethylformamide (DMF, Sigma-Aldrich) in a 20 mL round bottom-flask. The mixture was heated up to 120°C and reacted under magnetic stirring for 48h resulting in a -NH_2 functionalization. After the reaction was finished the mixtures were washed, filtered and vacuum dried. In the third step 100mg of the NH_2 functionalized CNTs were mixed with 2g of DCC and 1g of

PCL into 10 mL of DMF in a 20 mL round bottom-flask. The mixture was then refluxed and magnetically stirred at 120°C for 60 hours. After the reaction was finished the mixture was washed with warm ethanol at 50°C three times to remove excess PCL, filtered and vacuum dried overnight.

5.2.3. FT-IR Spectroscopy

Fourier transform infrared spectroscopy was performed using a Varian Excalibur FT-IR microscope (Varian Inc.). A small amount of the respective functionalized CNTs as well as the pristine CNTs were used to obtain the spectra.

5.2.4. Incorporation of CNTs into PCL Nanofibres

Functionalized CNTs were suspended in various concentrations in HFIP solutions overnight. PCL was added subsequently at a fixed weight percentage of 4 wt% with respect to the solvent and left to dissolve overnight again. Prior to the addition of PCL the CNT/HFIP solution were sonicated for 1h to ensure a good dispersion of the CNTs. The resulting solutions were electrospun at the fixed spinning parameters found in Table 14. Each experimental run was carried out in triplicate in order to address variability.

Experimental Run	Voltage (kV)	Distance (cm)	Feed Rate (mL/h)	CNT Concentration (wt%)
MWCNT-OH	25	15	0.55	0, 1, 2.5
MWCNT-PCL	25	15	0.55	0, 1, 2.5

Table 14: Overview of the processing conditions used for PCL scaffolds containing –OH functionalized and PCL-grafted CNTs.

5.2.5. Streaming Potential Measurements

Surface charge measurements could not be carried out in-house as no such equipment was available. Anton Paar GmbH offered kindly to perform a small number of measurements with their specialized equipment in Austria. Four electrospun scaffolds were sent for measurements made with different PCL and –OH functionalized CNT concentrations (Table 15).

Sample No.	Voltage (kV)	Distance (cm)	Feed Rate (mL/h)	PCL Concentration (wt%)	CNT Concentration (wt%)
1	25	15	0.55	2.5	0
2	25	15	0.55	4	0
3	25	15	0.55	4	5
4	25	15	0.55	7	0

Table 15: Overview of the processing parameters used for the scaffolds used for the streaming potential measurements.

The streaming current and streaming potential measurements were performed on an Anton Paar SurPASS using an Adjustable Gap. The samples were soaked in water for >24 h prior to measurement. For each measurement a pair of scaffold samples of the same composition was fixed on the sample holders (with a cross section of 20 x 10 mm^2) using double-sided adhesive tape. The sample holders were inserted in the Adjustable Gap Cell such that the surface of the samples were exactly facing each other. A gap of approx. 100 µm was adjusted between the sample surfaces. Before starting the measurement, the samples were carefully rinsed with the measuring electrolyte. A 10^{-3} M KCl solution is used as the background electrolyte and the pH of this aqueous solution is adjusted with 0.05 M HCl.

The zeta potential ζ is calculated from streaming current measurements according to:

$$\zeta = \frac{dl}{dp} * \frac{\eta}{\varepsilon * \varepsilon_0} * \frac{L}{A}$$

Equation 6: Calculation of the zeta potential where, dl/dp = slope of streaming current vs. differential pressure, η = electrolyte viscosity, ε_0 = permittivity, ε = dielectric coefficient of electrolyte, L/A cross section of the streaming channel.

5.3. Results and Discussion

CNTs are often functionalized prior to their incorporation into electrospun fibres in order to improve their dispersion properties[209,211,221,222] and to ensure a more homogenous distribution within the scaffold. Preliminary experiments with pristine CNTs showed that solutions of CNTs in HFIP did not produce stable suspensions and hence could not be spun into homogenous composites. FTIR spectroscopy and XPS were used to confirm the successful functionalization of the CNTs.

The successive functionalization of the CNTs was confirmed using FTIR. Figure 33 A shows a comparison of absorbance spectra collected from untreated CNTs, -OH functionalized CNTs and Amino functionalized CNTs. It was generally found difficult to obtain clear spectra of CNTs as they showed a tendency of high absorbance, especially at lower wavenumbers below 1500 cm^{-1}. No significant difference in the FTIR spectra was found between pristine CNTs and –OH functionalized CNTS. Amino functionalized CNTs showed an appearance of peaks, specifically at 2917cm^{-1} and 2848 cm^{-1} which can be assigned to CH_2 stretching. The peaks at 1250 cm^{-1} and 1100 cm^{-1} are attributed to C-N stretching which demonstrate the successful grafting of amino groups onto the CNTs.

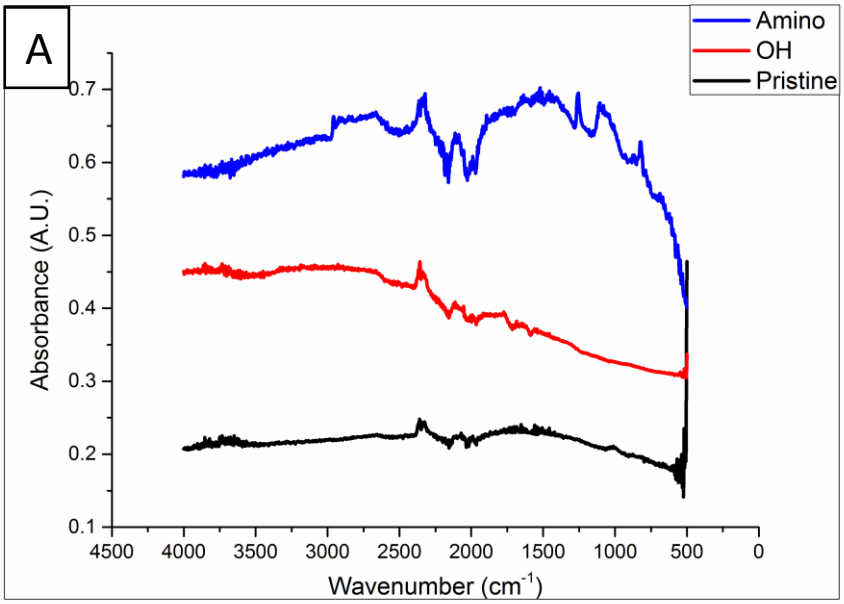

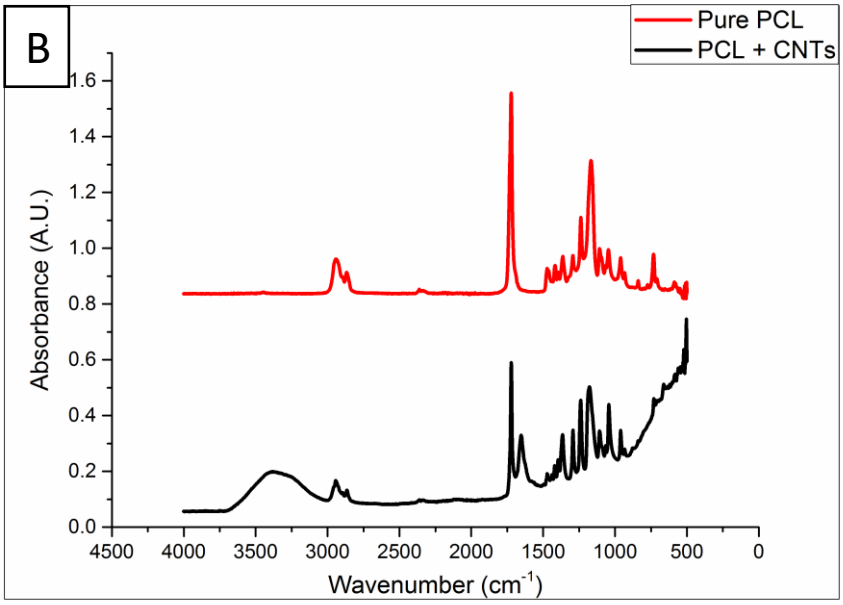

Figure 33: A: Comparison of FT-IR spectra for pure CNTs (black, -OH functionalized CNTs (red) and amino-functionalized CNTs (red). B: Comparison of FT-IT spectra for electrospun pure PCL scaffolds (red) and PCL-grafted CNTs containing PCL scaffolds (black).

Figure 33 b) shows the comparison of FTIR spectra of pure PCL and CNTs with chemically grafted PCL after washing. The spectrum of the PCL-CNTs displays a good match with the pure PCL spectrum, indicating the presence of the polymer while still exhibiting the aforementioned absorbance at lower wavelengths due to the presence of CNTs.

As the FTIR analysis for the –OH functionalization was inconclusive, XPS was carried out for pristine and –OH functionalized CNTs using the protocol described in [2.10]. Figure 34 shows a comparison between pristine and –OH functionalized CNTs. The pure CNTs are found to contain carbon (97.65 at%) with some oxygen (2.26 at%). The remaining 0.09 at% are within the level of error for the instrument used (±0.1%). The –OH functionalized CNTs show a substantial increase in oxygen at 15.08 at% with a concurrent reduction of carbon to 82.56 at%. Traces of sulphur (0.95 at%), nitrogen (0.72 at%), silicon (0.45 at%) and phosphorus (0.24 at%) were also detected. The large increase in oxygen found in the CNTs is strongly indicative of molecular bound oxygen in the CNTs. Since there was no change in sample preparation and transport the possibility of sample contamination can be excluded as the source of the additional oxygen for the functionalized sample.

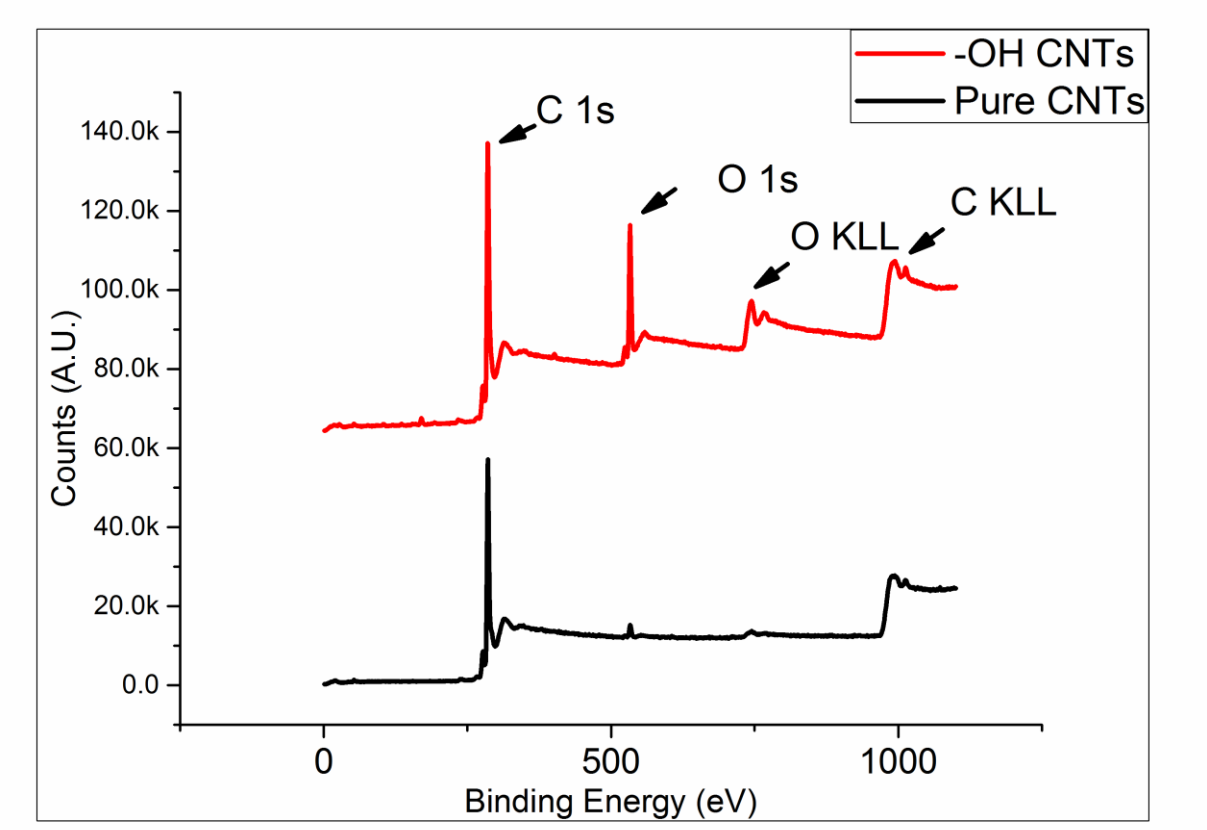

Figure 34: Comparison of XPS spectra of pure CNTs (black) and –OH functionalized CNTs (red). The peaks for carbon and oxygen are highlighted.

All experimental runs with CNT containing solutions produced smooth, defect-free fibres as with pure PCL. Figure 35 shows an overview of the influence of the CNT content on the average fibre diameter for MWCNT-OH and MWCNT-PCL incorporation into the scaffolds.

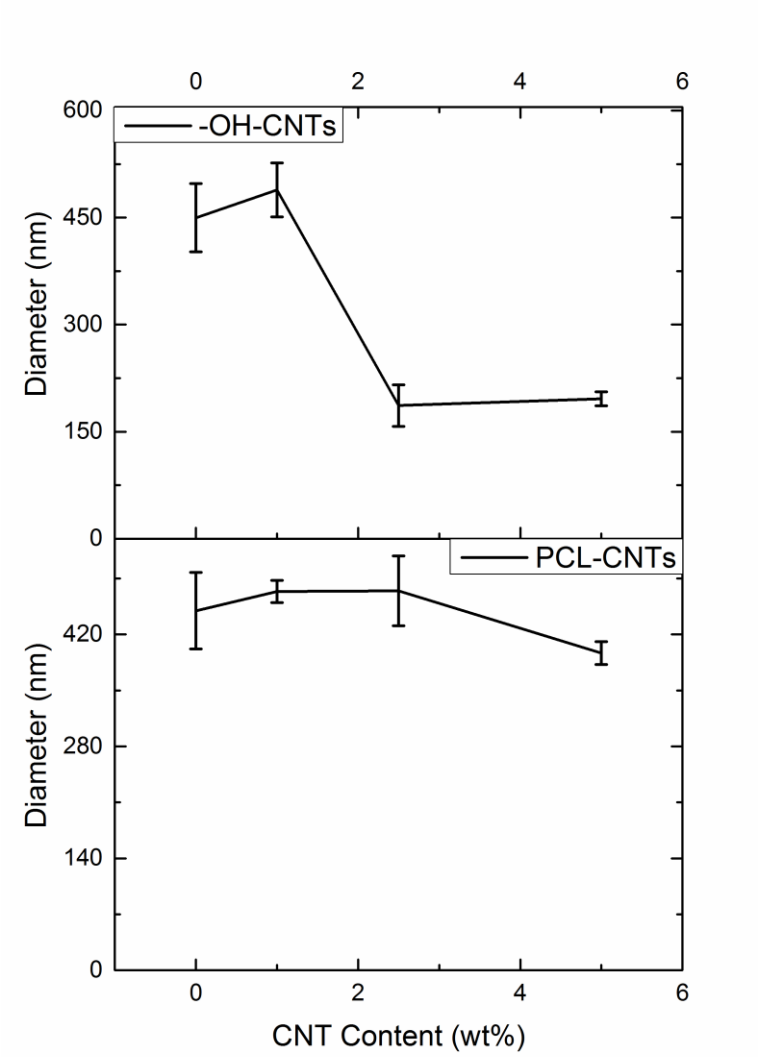

Figure 35: Comparison of the change in average fibre diameter with respect to CNT content in PCL scaffolds. Top: -OH functionalized CNTs. Bottom: PCl-grafted CNTs.

These results show that the influence of the CNTs on the composite fibres differs significantly between the types of functionalization used. The simple –OH addition resulted in a substantial reduction in the average fibre diameter for concentrations higher than 1 wt%. The PCL-grafted CNTs on the other hand only showed a minor impact on the diameter with a slight reduction at 5 wt%. Upon closer inspection it was found that the scaffolds with –OH functionalized CNTs exhibit a bimodal distribution of diameters whereas the PCL-grafted CNTs did not change the fibre distribution as compared to neat PCL fibres (Figure 36).

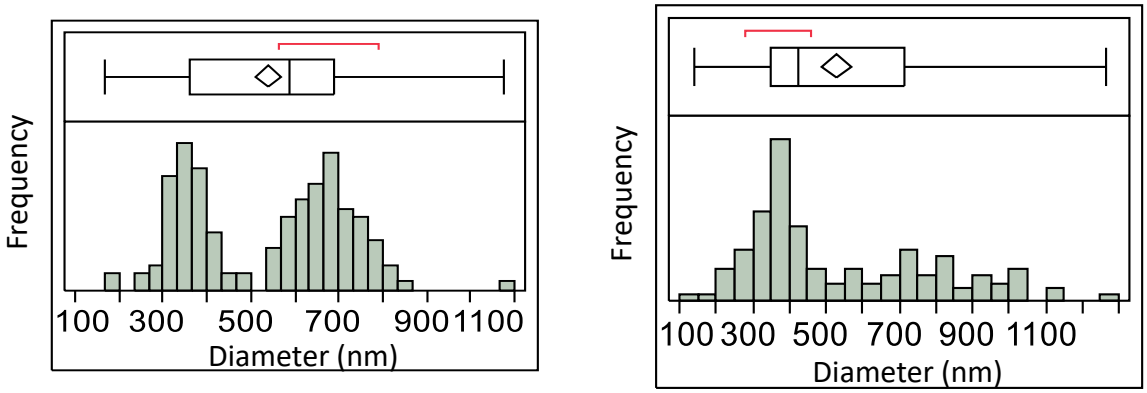

Figure 36: Examples of diameter distributions of fibre distributions found for –OH functionalized CNT containing scaffolds (left) and PCL-grafted CNT containing scffolds (right) with outlier box plots.

Bimodal fibre distributions have been observed before in a PEO/Water system[306] at high polymer weight concentrations in the solvent and through the addition of graphene oxide in nylon-6 fibres[329]. In the first case the smaller fibre population was found to have diameters of about one third of the larger ones whereas in the second case the smaller fibre population was significantly smaller and produced a spider-web like morphology. In the case of the –OH functionalized CNT containing fibres presented here the smaller fibre population has a diameter of roughly half of the larger fibres (Figure 37).

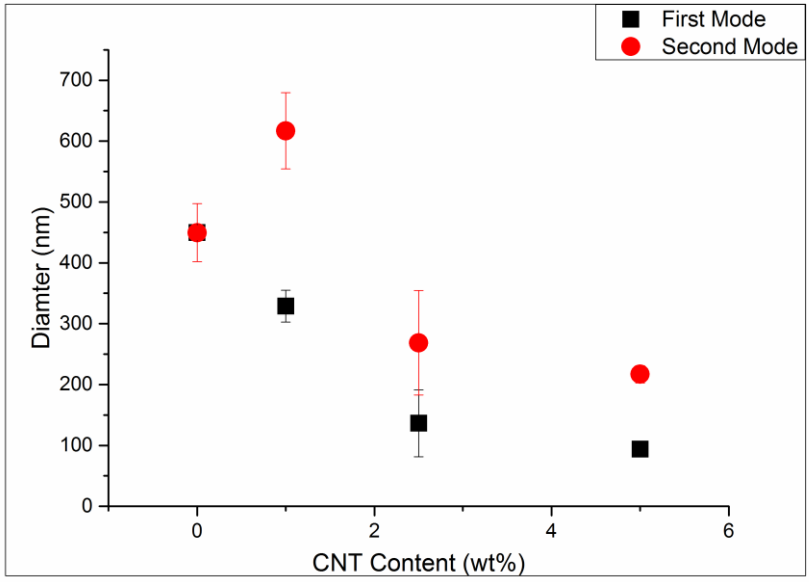

Figure 37: Change in the two modes of the fibre distributions for –OH functionalized CNT containing scaffolds with CNT content.

The ratios of the diameter of the second/first mode are 0.53, 0.5 and 0.43 for 1 wt%, 2.5 wt% and 5 wt% -OH-CNT addition respectively. The presence of the two fibre populations is a strong indication that the CNTs are not homogenously distributed within the fibres, indicating that CNTs are accumulated in the

larger fibres. These results might appear counter-intuitive at first as the addition of CNTs into a polymer solvent system has been shown to increase the viscosity slightly (albeit not to the same extent as a simple increase in polymer concentration)[206]. The reduction in average fibre diameter for the –OH-CNTs as well as the fact that the addition of PCL-grafted had no influence on the average fibre diameter have to be explained with an increase of solution viscosity in mind. The increase in viscosity stems from the inclusion of the CNTs and not an increase in chain entanglement and overall volume of polymer, which are the main reasons for the increase in average fibre diameter when the polymer concentration is increased. The reduction in fibre diameter with the inclusion of electrically conductive CNTs can be attributed in a similar fashion as to the addition of salts in electrospinning, whereas the change in the charge density of the polymer jet during fibre spinning is induced[330]. Additionally large agglomerates of CNTs (as a result of inhomogeneous mixing) will experience a higher acceleration in the electric field during fibre formation and lead to more shear thinning and hence thinner fibres.

TEM was employed to further confirm the incorporation of CNTs into the fibrous scaffolds. Due to the limitations of TEM (“good” images are normally acquired using samples with a thickness lower than ~100 nm) only CNTs in very thin fibres could be imaged appropriately. No CNTs were found in small fibres in the –OH functionalized CNT series, but clusters of CNTs can be seen in larger fibres (Figure 38).

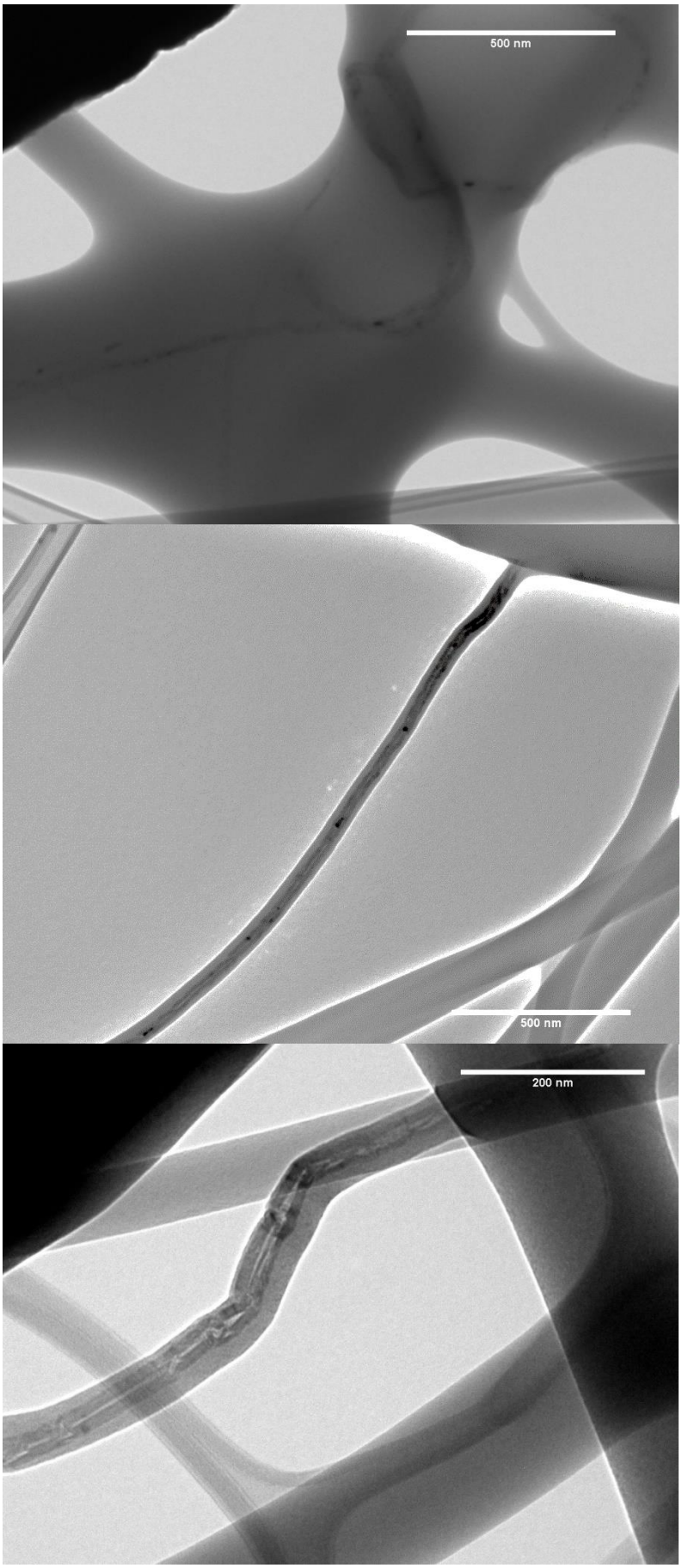

Figure 38: TEM images of CNT containing PCL fibres. Top: Cluster of –OH functionalized CNTs. Middle and bottom: Aligned PCL-grafted CNTs in PCL fibres.

Individual CNTs were found to be well-aligned within smaller fibres for the PCL-grafted experimental series.

The mechanical properties of scaffolds with various loadings of –OH-CNTs and PCL-grafted CNTs were evaluated using tensile testing according to the protocol described in [2.8]. It was found that the incorporation of –OH functionalized CNTs monotonically increases the ultimate tensile strength of the scaffolds from 9.2 MPa ± 1.4MPa for the neat PCL scaffolds to 11.4 MPa ± 1.8 MPa at 5 wt% addition of CNTs (Figure 39). The Young´s modulus of the scaffolds increase from 0.21 MPa ± 21 kPa for the pure PCL fibres to 0.31 MPa ± 57 kPa at a concentration of 1 wt% after which it decreases again to 0.21 MPa ± 22 kPa at the highest concentration used here of 5 wt%. The incorporation of –OH-CNTs is found to significantly reduce the strain at break at every level of CNT-concentration. Neat PCL scaffolds exhibit a strain at break of 139 ± 3 which reduces down to 32 ± 9 at a CNT concentration of 5 wt%.

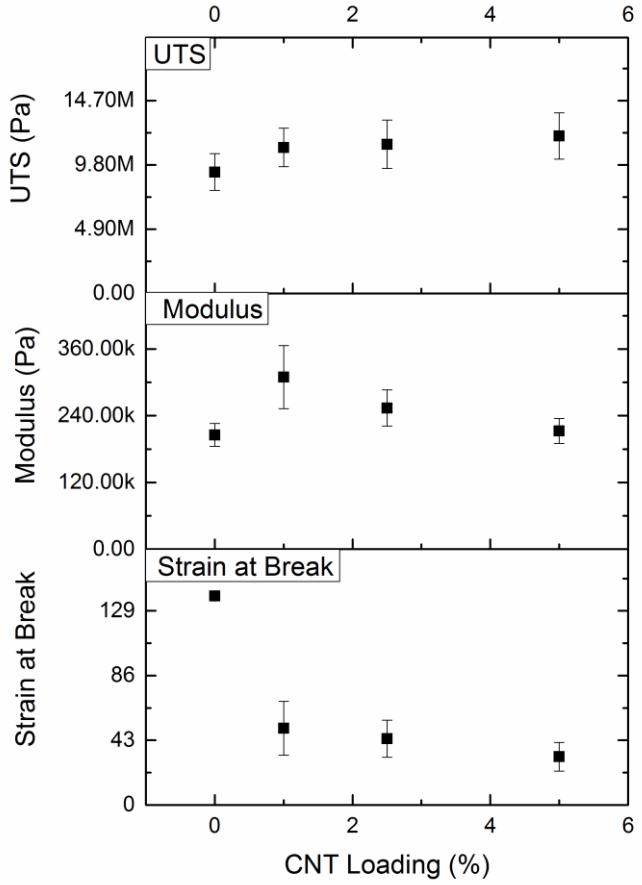

Figure 39: Overview of UTS, modulus and strain at break of –OH functionalized CNT containing PCL scaffolds.

The mechanical properties for the addition of PCL-grafted CNTs into nanofibrous scaffolds were characterized in the same way as the –OH-functionalized CNT containing fibres. The PCL-grafted CNTs were found to increase the ultimate tensile strength by a factor of ~1.8x, from 9.2 MPa ± 1.4MPa for the neat PCL scaffolds to 17 MPa ± 1.7 MPa at 5 wt% addition of CNTs (Figure 40). The Young´s modulus was found increase substantially by a factor of ~3 from 0.21 MPa ± 21 kPa for the pure PCL fibres to 0.64 MPa ± 177 kPa at a concentration of 1 wt% after which it decreases again to 0.24 MPa ± 18 kPa for a concentration of 5 wt%. Similar to the inclusion of –OH-CNTs, the incorporation of PCL-grafted CNTs results in a lower strain at break. The lowest values was found at a 1 wt% concentration of CNTs with a strain at break of 62 ± 18 which increased slightly to 71 ± 13 at a 5 wt% concentration of CNTs.

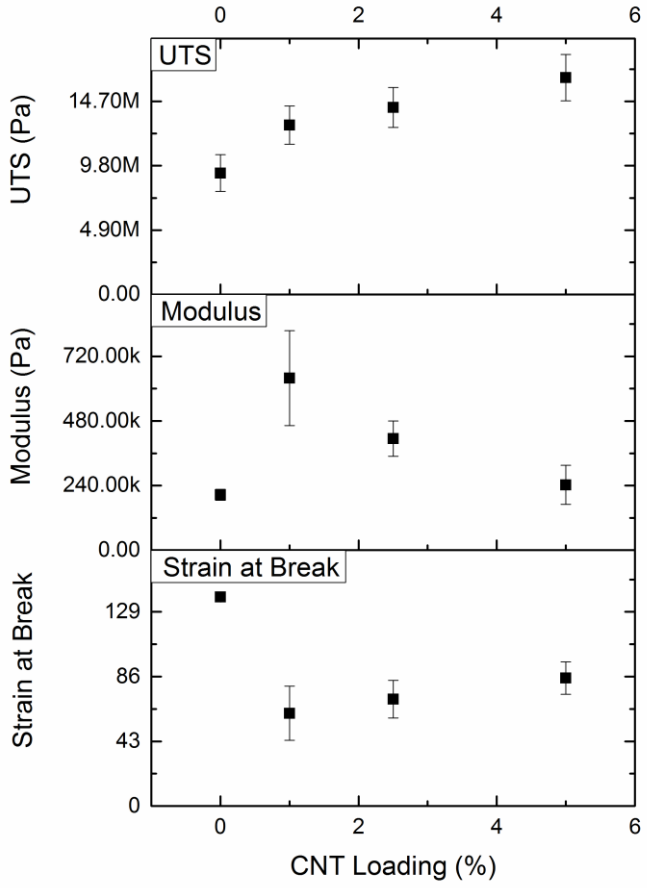

Figure 40: Overview of UTS, modulus and strain at break of PCL-grafted CNT containing PCL scaffolds.

These results show that the addition of CNTs into electrospun PCL fibres has a beneficial effect on the tensile properties of the fibrous scaffolds in terms of the ultimate tensile strength and the Young´s

modulus. However the scaffolds do become more brittle as evidenced by a reduced strain at break. The chemical grafting of PCL onto the functionalized CNTs has a significant effect on the mechanical properties of the scaffolds as the level of reinforcement surpasses the impact of the simple –OH functionalized CNTs substantially. The observed decrease in both UTS and Young´s modulus for both types of CNTs used is an indication for a less homogeneous distribution of CNTs at higher concentrations in the fibres.

A simple analysis based on the rule of mixtures shows that the produced composite scaffolds are below the level of mechanical reinforcement that would be expected from such a calculation.

$$E_c = fE_f + (1 - f)E_m$$

Equation 7: Equation used for the estimation of reinforcement from a rule of mixture. E_c = Composite property, f = volume fraction of CNTs, E_f = CNT property (modulus or yield strength, E_m = bulk matrix property.

The mechanical properties for the MWCNTs were taken as 0.3 TPa for the modulus and 50 GPa for the yield strength respectively[331], whereas the bulk properties for PCl were taken as 350 MPa for the modulus and 13 MPa for the yield strength respectively[332]. Taking into account a reduction in cross-section due to porposity of ~90% the values for the expected modulus and yield strength according to the rule of mixture are 334 MPa and 51 MPa respectively at a CNT loading of 1 wt%. The differences between the theoretical values for the rule of mixture and the measured values can be explained by both the complex fibre geometry and orientation within the scaffolds and a potential overestimation of the mechanical properties of the MWCNTs.

There is some data available in the literature on the mechanical properties of electrospun CNT/PCL scaffolds. Meng et al. (2010) found that the addition of –OH functionalized CNTs increased the tensile strength of electrospun PCL scaffolds by a factor of ~1.4 from ~1 MPa for pure PCL fibres to 1.42 MPa with the addition of 0.5 wt% CNTs[137]. No data was given for the modulus of the scaffolds and the strain at break was not found to be significantly affected. Shao et al. (2011) utilized malic anhydride functionalized CNTs in their scaffolds and measured the tensile properties of these. They found that the addition of 3 wt% CNTs increased the ultimate tensile strength from 7 MPa to 9.6 MPa, the Young´s modulus from 8.5 MPa to 18 MPa and reduced the strain at break from 435 down to 151. Crowder et al.

(2013) observed an increase in the Young´s modulus for untreated CNT-reinforced PCl scaffolds from 15 MPa for pure PCL fibres to 23 MPa at a loading of 10 wt% CNTs[333]. Finally, Wickham et al. (2014) incorporated thiophene-conjugated CNTs into electrospun PCL scaffolds and observed an increase in the tensile strength from 0.9 MPa for neat PCL fibres to 1.3 MPa for a 20 wt% addition of CNTs, an increase in the Young´s modulus from 8.4 MPa to 11 MPa for the Young´s modulus[334].

A comparison of the available data on the reinforcement of PCL with the current work shows that the chemical grafting of PCL onto CNTs results in superior tensile strengths and moduli for the electrospun scaffolds (Figure 41). To the best of the authors' knowledge this work demonstrates the largest recorded increase in both UTS and Young´s modulus through the incorporation of CNTs into electrospun, nanofibrous scaffolds as compared to the neat PCL fibres.

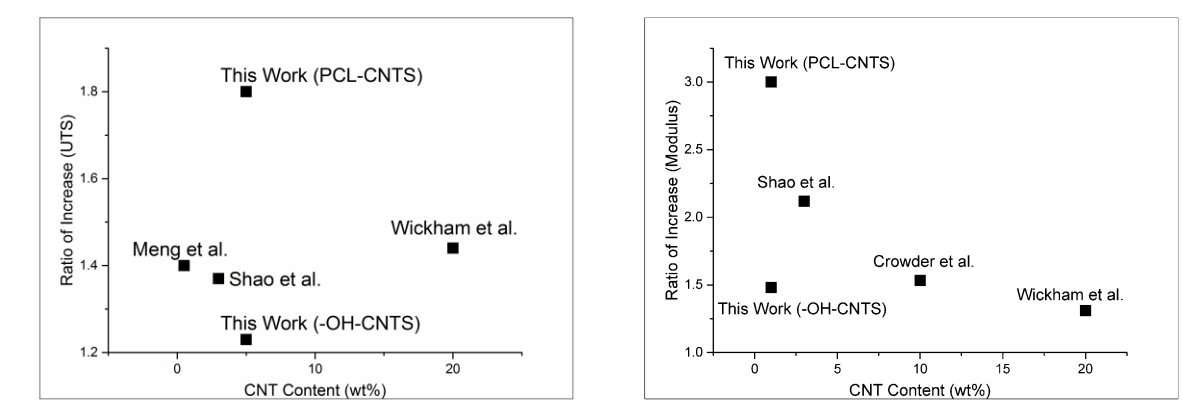

Figure 41: Comparison of the ratios for the increase in UTS (left) and modulus (right) of the literature. The ratios were created by taking the largest increase found with respect to pure PCL scaffolds.

To further understand the effect of the addition of CNTs into PCL nanofibres, the crystalline properties of PCL-grafted-CNT-containing scaffolds were investigated. The crystallinity of samples containing 1 wt%, 2.5 wt% and 5 wt% CNTs were evaluated using XRD, employing the protocol described in [2.6]. The degree of crystallinity increases with the CNT content from 55% ± 1.9% for neat PCL fibres to 66% ± 4.6%, 69% ± 5.1% and 63% ± 4.2% for 1 wt%, 2.5 wt% and 5 wt% CNTs respectively (Figure 42). In another extensive study it was found that the addition of MWCNTs into bulk PCL composites did not affect the overall degree of crystallinity[335]. However that work did not study electrospun nanofibres but slow-cooled bulk samples. Crystallization times in electrospinning are several orders of magnitude

faster[336] and the difficulty in measuring the degree of crystallinity using DSC [4.4], as employed in the above mentioned study, could explain that discrepancy.

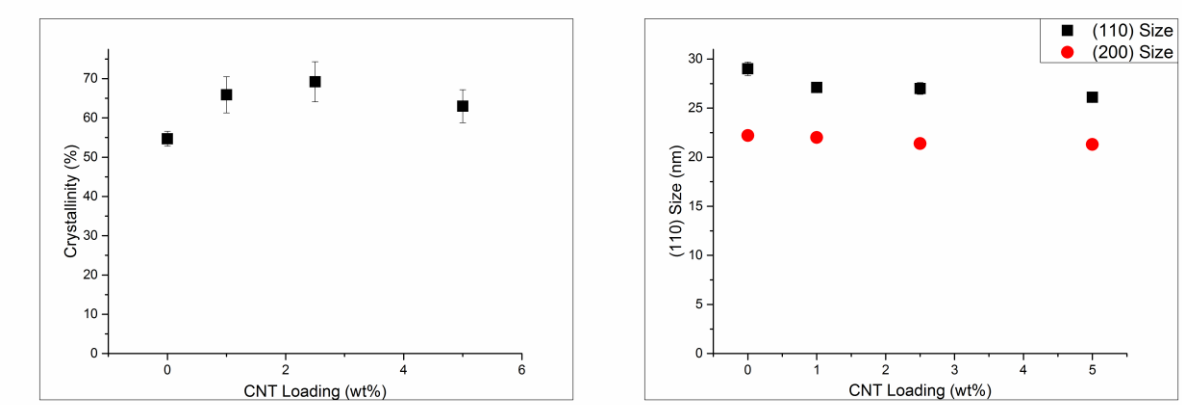

Figure 42: Change in degree of crystallinity (left) and crystallite size (right) with PCL-grafted CNT loading as measured by XRD.

The average crystallite size was estimated using the method described in [2.6]. A small change in the average crystallite size for the (110) reflection can be seen with an increase in CNT loading from 29 nm ± 0.7 nm for pure PCL scaffolds down to 26.1 nm ± 0.4nm at 5 wt% CNTs. The change in the size from the (200) feature is almost negligible with a very small decrease in average size from 22.2 nm ± 0.19 nm to 21.3 nm ± 0.24 nm at a 5 wt% CNT loading. The increase in crystallinity is of a similar scale as the increase observed in [4.4] due to the reduction in flow rate. A similar increase in UTS was observed in that case, to 18 MPa ± 1.1 MPa at 0.1mL/h to 9.2 MPa ± 1.4MPa at standard spinning conditions. It is therefore not possible to discern whether the increase in UTS found here is due to the increase in crystallinity or the addition of CNTs. The increase in Young´s modulus with the incorporation of 1 wt% PCL-grafted CNTs is significantly higher than what was found due to the reduction in flow rate (and hence increase in crystallinity). The change in crystallite size observed for the addition of CNTs is too small to explain the large differences in mechanical properties. Therefore it can be concluded that the introduction of CNTs into electrospun PCL nanofibres has a reinforcement effect on the elastic modulus of the whole scaffold beyond the positive influence of the increased degree of crystallinity.

The thermal properties of PCL-grafted-CNTs containing scaffolds were investigated with DSC, using the protocol described in [2.9]. The incorporation of CNTs into electrospun PCL nanofibres is found to increase the melting temperature of the scaffold from 58.4 °C for pure PCL fibres to 63.7 °C, 63.8 °C and 63.9 °C for 1 wt%, 2.5 wt% and 5 wt% of CNTs added respectively (Figure 43). These results show

that the incorporation of the CNTs used in this study increase the melting temperature of electrospun PCL scaffolds by ~5°. [4.4]. The inclusion of CNTs into polymer nanofibres have been shown to both slightly increase the melting temperature in some systems[337] whereas in other it leads to a small decrease in the melting temperature[338] which suggests that the effect of CNT addition has a complex interaction that depends on the polymer system used.

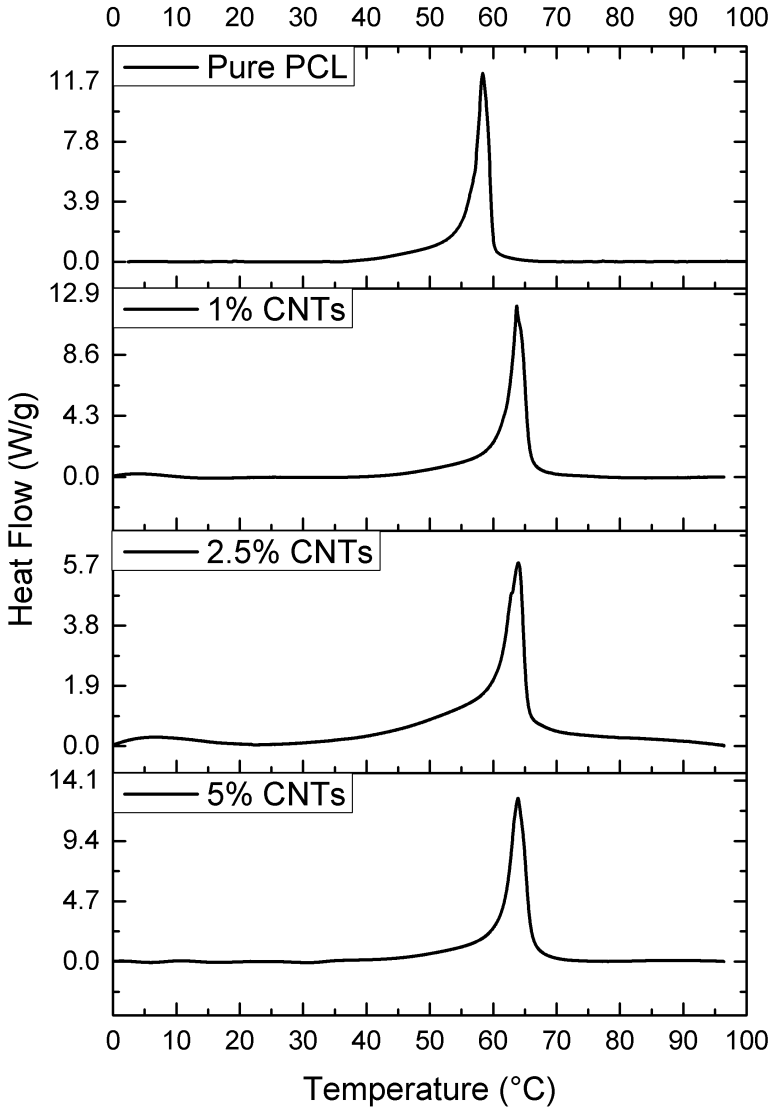

Figure 43: DSC thermograms for PCL scaffolds with different PCL-grafted CNT loadings.

It was shown that the incorporation of MWCNTs into bulk PCL polymers results in the presence of a binary melting endotherm[335]. Upon closer inspection the DSC thermograms obtained in this study show the emergence of a secondary peak, prior to the melting point (Figure 44).

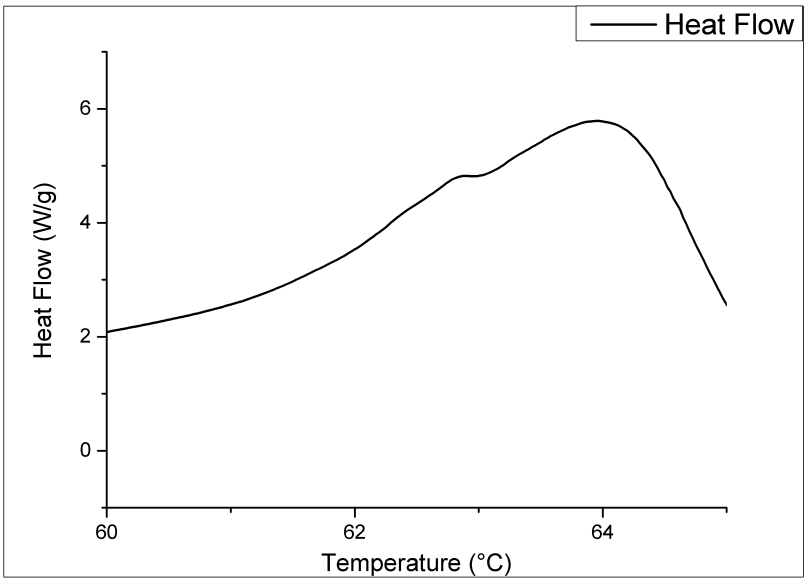

Figure 44: Close-up of a DSC thermogram of a PCL scaffold containing 5 wt% of PCL-grafted CNTs. Two distinct melting peaks are visible.

The variation in the position and magnitude of the secondary melting peak compared to bulk PCL/CNT composites can be explained by the aforementioned difference in crystallization times due to the fast evaporation rates encountered during electrospinning. The degree of crystallinity was not evaluated from the DSC thermograms as it was demonstrated in [4.4] that this method can be unsuitable for electrospun PCL nanofibres.

The surface charge as measured by the zeta potential of any functional material used in tissue engineering is one of the most important parameters influencing cell growth and differentiation[339]. The surface charge of pure PCL scaffolds made from solutions with different PCL content was measured and compared with the surface charge of a CNT containing PCL scaffold at different pH values. Due to the unavailability of any suitable equipment the samples could not be measured in-house and only a limited set of scaffolds could be sent to Anton Paar. These preliminary results show that the zeta-potential of electrospun PCL scaffolds (Figure 45) is dependent on the average fibre diameter (a change in solution concentration leads to a change in fibre diameter [3.3]).

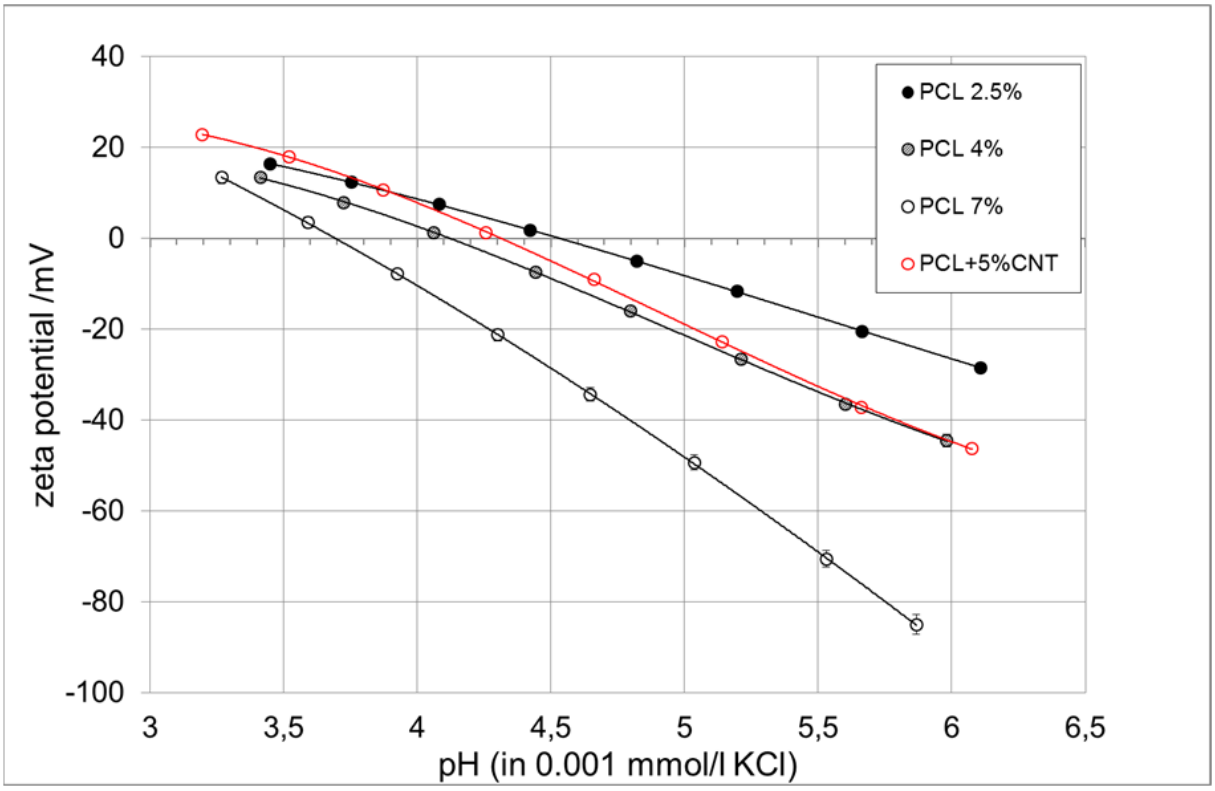

Figure 45: Change in zeta potential of PCL scaffolds made from different solution concentrations and a CNT containing scaffolds with solution pH.

There is only one available reference for the zeta-potential of electrospun scaffolds by Vaquette et al. (2008)[340]. It was found that at a pH of 5.1 the zeta-potential of scaffolds made from 16 wt% PCL in dichloromethane was -28mV ± 1mV. This compares well with the results presented here. The zeta-potential is negative for all scaffolds below a pH of ~4.5 with significant difference in the magnitude of the zeta-potential with PCL solution concentration. The higher the PCL concentration is, the more negative the zeta-potential is. The incorporation of CNTs into does not seem to affect the zeta-potential significantly as the measured values are very close to those of the pure, 4 wt% PCL sample. The zeta-potentials of human cells have been found to be in the range of -19 mV - -31 mV *in vivo*[341]. The measured values here are in a similar range which should be beneficial in mimicking the biological environment these cells experience. These results suggest that the introduction of CNTs into electrospun PCL fibres does not alter the electrokinetic properties of the scaffolds. This is an important results with the use of such scaffolds for tissue engineering applications in mind as changes in the zeta potential are known to affect cell growth[342] and would hence make it more difficult to understand in what capacity incorporated CNTs might affect cell behaviour.

5.4. Conclusion

. In this chapter CNTs were successfully functionalized with –OH-groups followed by the addition of amine groups and a final chemical grafting of PCL in a three-step process. –OH functionalized and PCL-grafted CNTs were then incorporated into electrospun nanofibres and their morphology was assessed. The –OH-CNT containing scaffolds were found to exhibit a bimodal fibre distribution with a substantial overall lowering of the average fibre diameter indicating an inhomogeneous distribution of the CNTs within the scaffold which was further confirmed by TEM imaging. The PCL-grafted CNTs resulted in scaffolds with diameter distributions akin to pure PCL fibres and did not affect the average fibre diameter significantly as compared to neat PCL scaffolds. This is further supported by the TEM analysis of the fibres. The mechanical properties of the two types of scaffolds with varying concentrations of CNTs were investigated using tensile testing. The addition of both types of functionalized CNTs was seen to significantly increase the ultimate tensile strength and the elastic modulus of the scaffolds, with the PCL-grafted-CNT containing scaffolds outperforming the –OH functionalized CNTs substantially. The highest recorded increase in both UTS and Young´s modulus was found for the PCL-grafted CNTs with an increase of ~1.8x and ~3x respectively. In both cases the strain at break was reduced after the CNT reinforcement. XRD analysis revealed that the introduction of CNTs considerably increases the degree of crystallinity in electrospun PCL fibres and slightly lowers the crystallite size. The thermal properties of the composite scaffolds were explored using DSC. It was found that CNTs increase the melting temperature of the by around ~5 °C. Finally in a preliminary experiment the surface charge of electrospun PCL scaffolds was not found to be affected by the addition of CNTs.

In conclusion the chemical grafting of the matrix polymer onto CNTs – in this case PCL – for electrospun scaffolds has a beneficial influence on the mechanical and thermal properties and offers another way of tailoring the scaffolds without changing the morphology or surface charge significantly. To the best of the author´s knowledge this work shows the highest reported percentual increase in mechanical properties of CNT-containing PCL scaffolds through the use of targeted chemical grafting. This will be shown to be beneficial for the application of electrospun nanofibres as scaffolds for tissue engineering in [7].

6. Electrospinning of Gelatin and CNT/Gelatin Nanofibres

6.1. Introduction

Electrospinning offers a fast and facile method to create three dimensional, nanofibrous scaffolds with morphologies and physical properties mimicking the extracellular matrix[268]. The use of various synthetic biodegradable and bioinert polymers has been well documented and favoured in the past due to the ease of production and materials handling, as well as low material cost[343]. Recently the possibility of using biopolymers in the electrospinning process has been explored[344]. Natural polymers offer the obvious advantage of a non-toxic degradation and superior biocompatibility but come with a difficulty of batch-to-batch variation[343] and inferior control over their physical properties as comparted to synthetic polymers[345]. Examples of natural polymers used in electrospinning are collagen[19,128,346,347], gelatin[124,348–352], chitosan[22,353–357], fibrinogen[26], chitin, silk fibroin[18,127,128,358], cellulose[125,126,359], alginate[20,360] and hyaluronic acid[361–366]. The choice of what material to use is usually based on considerations of availability, cost and final application. Building on the knowledge gained from [3] this chapter describes a systematic approach to electrospin gelatin nanofibrous scaffolds in a controlled fashion. Based on the results from [5] carbon nanotubes are then for, the first time, introduced into gelatin scaffolds in order to improve their mechanical properties.

6.2. Materials and Method

6.2.1. Electrospinning of Pure Gelatin Nanofibres

Powdered Gelatin from Porcine skin was purchased from Sigma Aldrich (300g bloom) and dissolved in HFIP at concentrations of 3 wt%, 4 wt% and 5 wt%. The solutions were magnetically stirred overnight at 500RPM at room temperature. Electrospinning was carried out with the equipment described in [2.1I] using the above solutions.

Voltage (kV)	Distance (cm)	Flow Rate (mL/h)	Concentration (wt%)	Solution Age (days)
25	15	0.55	3,4,5	1,3,5

Table 16: Overview of solution and processing parameters for the electrospinning of gelatin scaffolds.

Solution were spun using the parameters shown in Table 16. In addition to investigating the influence of the solution concentration on the properties of gelatin scaffolds, the age of the solution was employed as an additional parameter in order to evaluate possible degradation effects. The viscosity of the solutions with various ages after preparation were measured using the protocol described in [2.7]. Each experimental run was repeated in triplicates to assess variability in the system.

6.2.2. Incorporation of Carbon Nanotubes into Gelatin Nanofibres

PCL-grafted CNTs were prepared using the method described in [5.2.4]. Functionalized CNTs were suspended in various concentrations in HFIP solutions overnight. Gelatin was added subsequently at a fixed weight percentage of 4 wt% with respect to the solvent and left to dissolve overnight again. Prior to the addition of Gelatin the CNT/HFIP solution were sonicated for 1h to ensure a good dispersion of the CNTs. Electrospinning was carried out with CNT/Gelatin solutions using the parameters shown in Table 17.

Voltage (kV)	Distance (cm)	Flow Rate (mL/h)	Gelatin Content (wt%)	CNT Concentration (wt)
25	15	0.55	4	1,2.5,5

Table 17: Overview of solution and processing parameters for the electrospinning of PCL-grafted CNT containing gelatin scaffolds.

Each experimental run was repeated three times.

6.3. Results and Discussion

The use of natural polymer, specifically collagen type I has been well documented as an attractive route to design and produce biomimetic scaffolds for tissue engineering[367]. Fluorinated solvents, particularly HFIP yields the most reproducible and consistent results but comes with the drawbacks of the costs of pure collagen and the possible denaturation due to solvent – polymer interaction[130]. An experimental series was constructed to investigate the spinnability of gelatin/HFIP solutions and solvent – polymer

interactions with time, after initial experiments with collagen have shown significant changes to the morphology of the scaffolds with solution age [10.2].

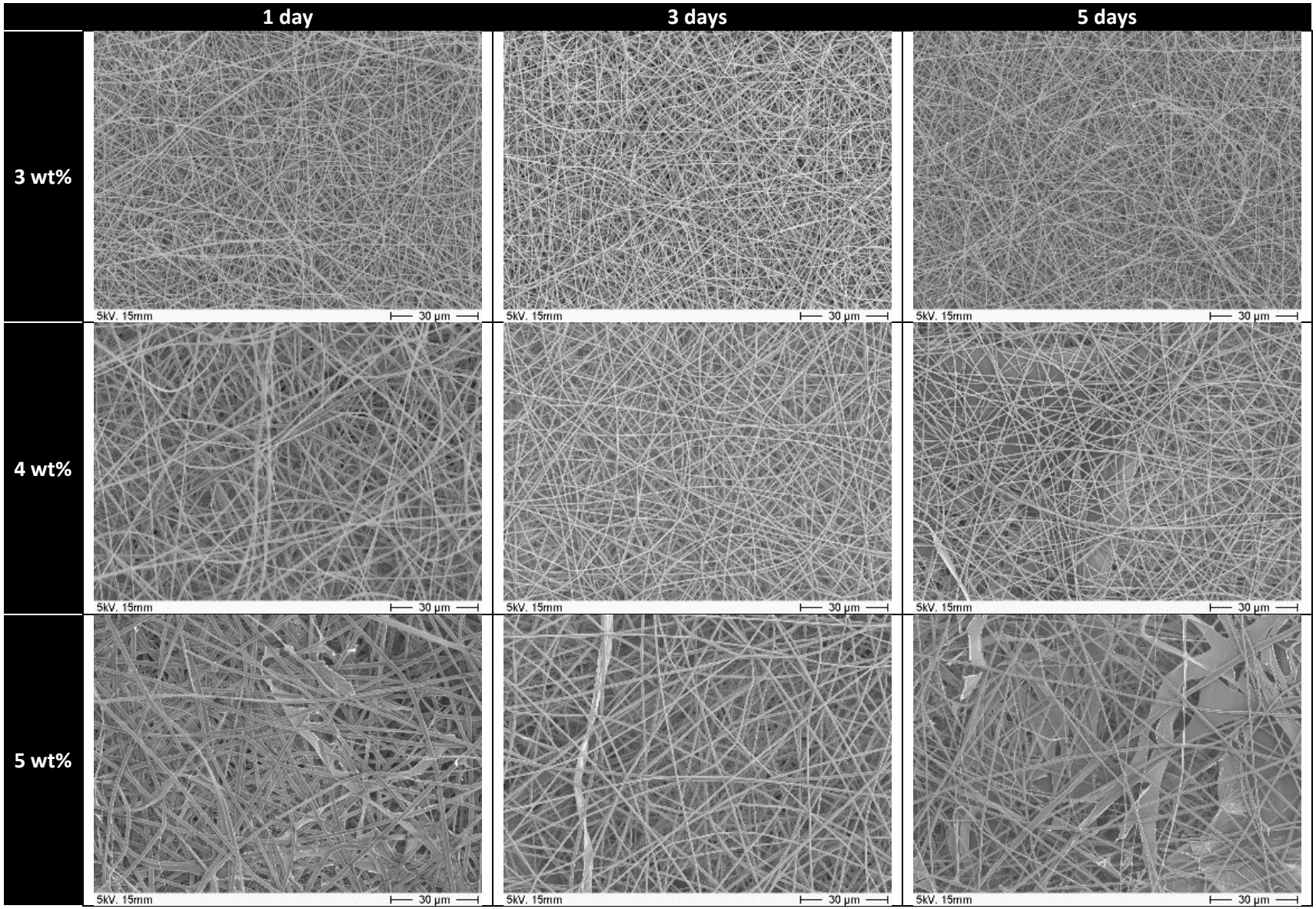

Figure 46: SEM images of electrospun gelatin scaffolds made from solutions with different ages and different gelatin solution concentrations. All scale bars are 30 µm.

Figure 46 shows SEM images [2.3] of scaffolds made with varying solution concentrations of gelatin at different solution ages. All experimental parameters produced smooth, fibrous scaffolds. With an increase in solution age scaffolds at 5 wt% exhibit the appearance of large defects which look similar to electrospun flat ribbons that were observed elsewhere[253]. An analysis of the fibre diameters from the various scaffolds reveals clear trends with respect to both concentration and solution age (Figure 47).

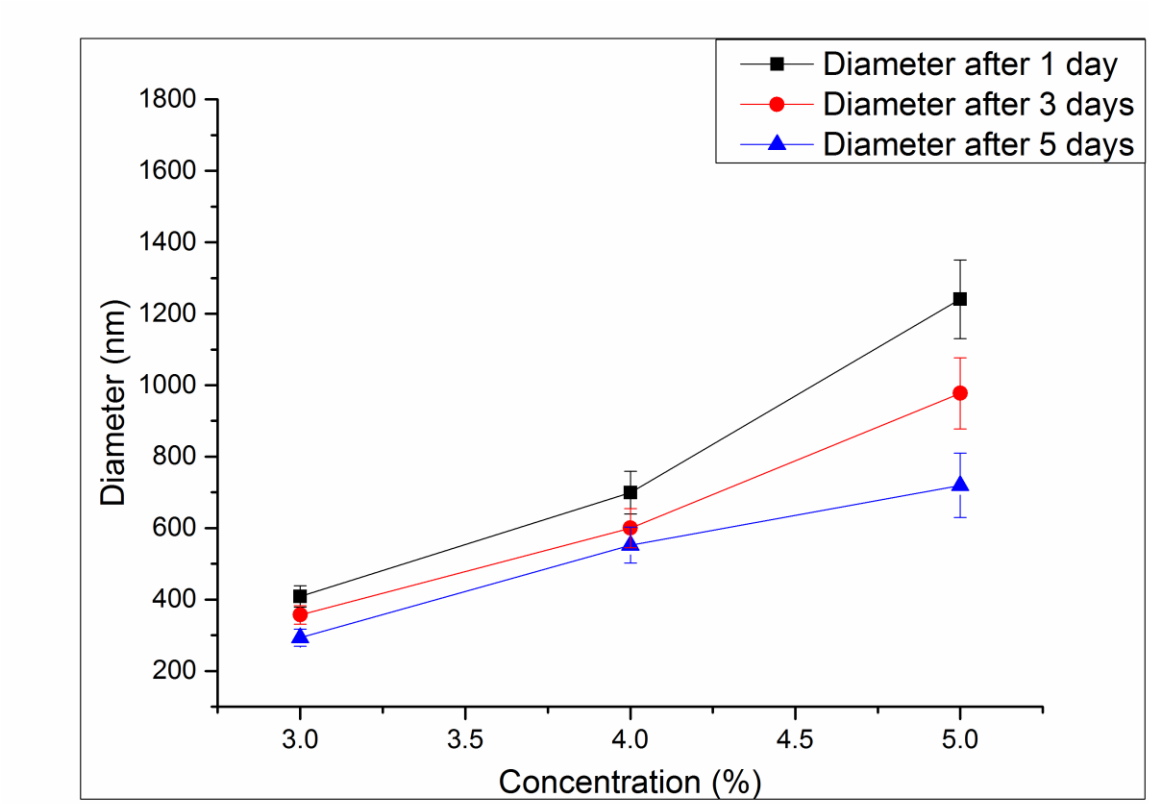

Figure 47: Overview of the change in average fibre diameter with gelatin solution concentrations and solution age.

An increase in the gelatin solution concentration at for one day old solutions leads to an average increase in mean fibre diameter from 409 nm ± 31 nm at 3 wt% to 699 nm ± 5 9 nm at 4 wt% to 1241 nm ± 109 nm at 5 wt%. The observed trend with concentration is in agreement with previous observations for PCL [3.3.1] and the literature[352]. The age of the solution has a significant impact on the average diameter, reducing it for all concentrations used. The average fibre diameter was reduced by 28%, 21% and 41% with a solution age of five days for 3 wt%, 4 wt% and 5 wt% respectively. The large change in fibre diameter with solution age is a strong indication for an interaction between the solvent used and the gelatin. For the PCL/HFIP system there was no interaction observed for the age of the solution and the

fibre morphology. It has been shown that fluorinated solvents, such as HFIP destroy the typical triple-α-helix found in collagen and lower the denaturation temperature substantially[130] although the timescale over which this process occurs was not investigated. Gelatin is not a single chemical substance but rather a large collection of polypeptide molecules with varying molecular weight distributions, based on the parent collagen used, while maintaining part of the α-helix structure found in collagen[368]. It is therefore plausible that HFIP will have a denaturising effect on gelatin, similar to collagen. This is further supported by the measurement of the solution viscosity, both with gelatin concentration and solution age (Figure 48).

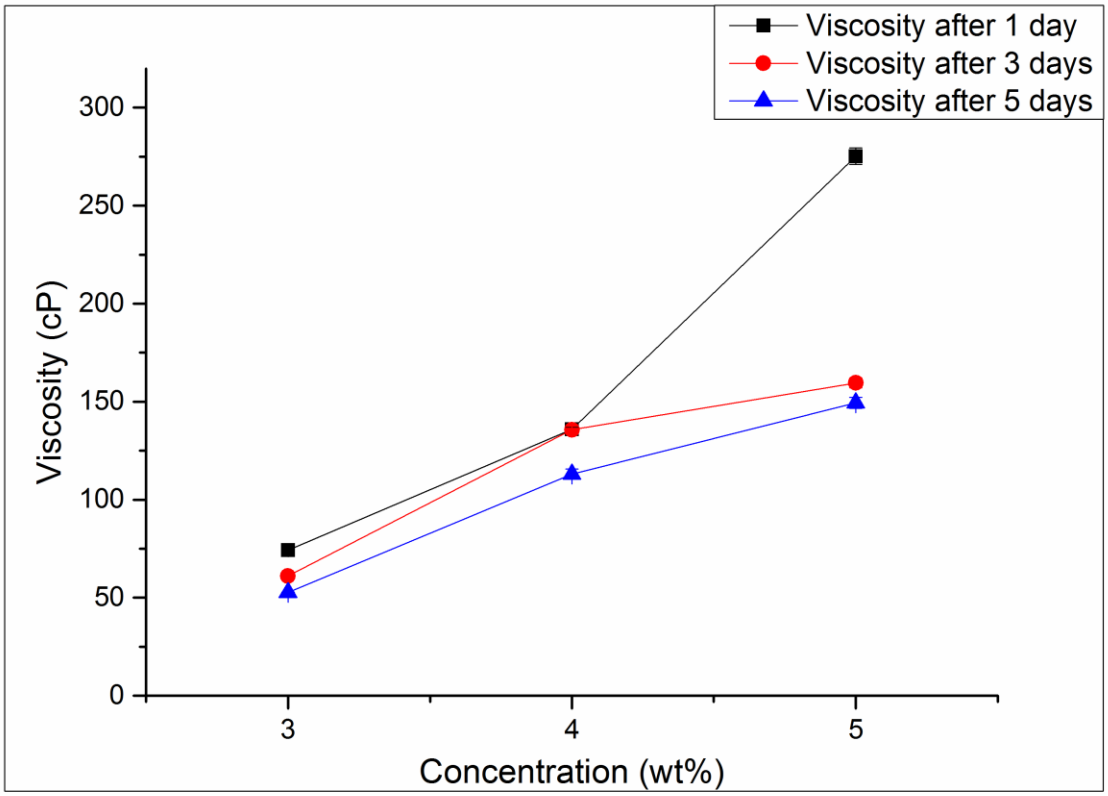

Figure 48: Change in solution viscosity with both gelatin concentration and solution age.

The change in viscosity with solution concentration follows a linear relationship, as is expected for a solution in the low concentration regime[369], except for the 5 wt% after one day as it is entering a higher concentration regime[370]. The solution age has the same effect on the viscosity as it does on the fibre diameter (Figure 47), reducing it significantly for all concentrations investigated, with the 5 wt% solution experiencing the largest reduction in solution viscosity. The relationship between the solution viscosity and the fibre diameter is well established[249] and the gelatin/HFIP system presented here is

following that empirical trend. The viscosity of a collagen or gelatin solution is a factor that can be used to determine the structural state of the polymer. A loss or reduction in helical structure and crosslinking will result in a decrease in viscosity which can therefore be used as a measure of the state of progressing denaturation[371,372], similar to a reduction in crosslinking for conventional polymers[373]. Given the current understanding on the impact of fluorinated solvents on the secondary and tertiary structure of collagen[374] the change in solution viscosity with time presented here is a strong indication for the time-dependent denaturation of gelatin in the HFIP solution. It is well established by Shenoy et al. (2005) that the facility of the electrospinning process – in terms of solution properties – to produce smooth, defect-free fibres is dependent on the chain entanglement factor of the polymer in the solution[375]. The solution viscosity and concurrently the average fibre diameter of a variety of polymer/solvent systems can be understood as a function of the polymer concentration, the average molecular weight of the polymer and the conformation of the polymer molecules[376]. Since neither the concentration nor the molecular weight of gelatin will be affected by the dissolution in HFIP the results for the reduction in viscosity and fibre diameter here should be understood as a loss of helicity or secondary as well as tertiary structure. The time-dependency of this denaturation process has not been reported elsewhere and it is strongly suggested that future work which involves the use of fluorinated solvents and biopolymers for the use in electrospinning should carefully control and monitor the age of solutions in order to ensure reproducibility and consistency.

The mechanical properties of electrospun, nanofibrous gelatin scaffolds made from one day old solutions was investigated through tensile testing using the protocol described in [2.8]. Concurrent with the findings in [4.4] both the ultimate tensile strength and the elastic modulus decrease as the gelatin solution concentration is increased (Figure 49). The tensile strength decreases from 2.54 MPa to 1.82 MPa to 1.66 MPa for scaffolds made from 3 wt%, 4 wt% and 5 wt% respectively.

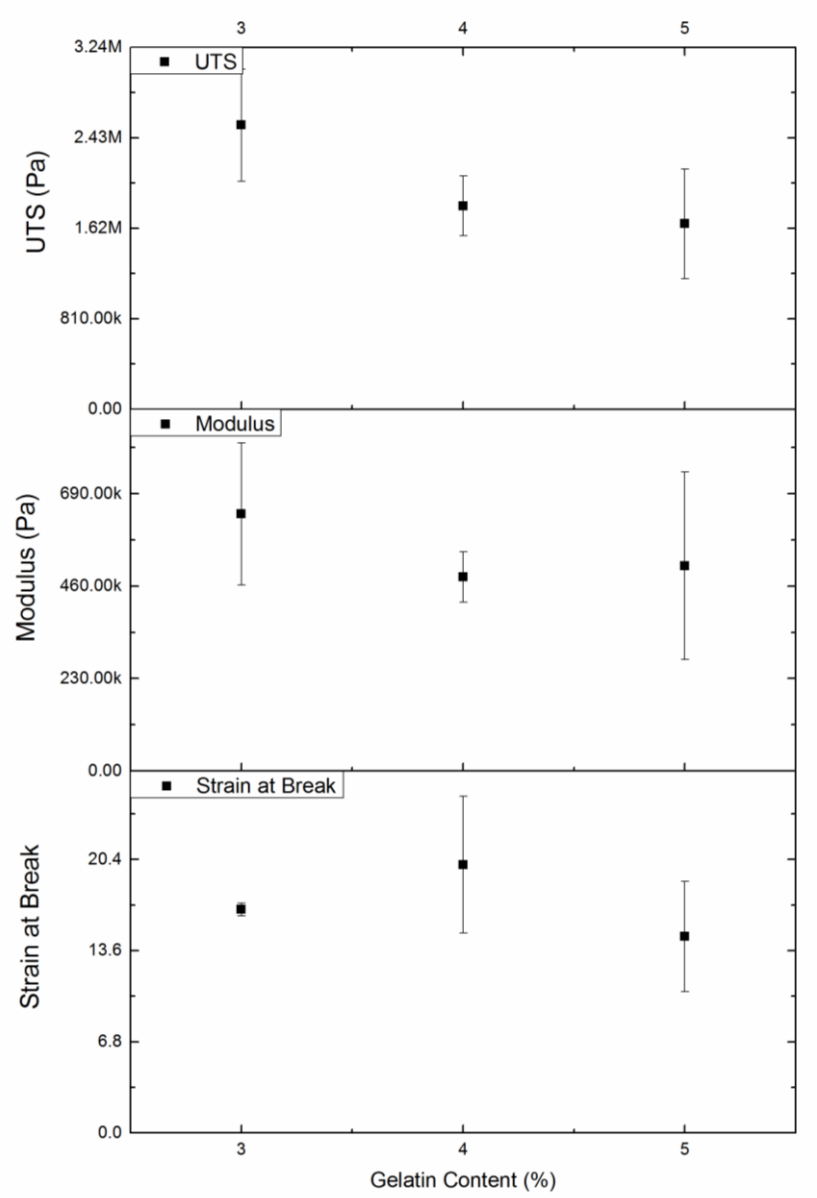

Figure 49: Comparison of the change in UTS, modulus and strain at break of electrospun gelatin scaffolds with gelatin solution concentration.

The Young´s modulus is following a similar trend as the tensile strength, where a slight reduction is observed with an increase in solution concentration. The elastic modulus was found to decrease from 639 kPA ± 177 kPa to 483 kPa ± 63 kPa to 511 kPa ± 233 kPa for scaffolds made from 3 wt%, 4 wt% and 5 wt% solutions. The strain at break of gelatin is low compared to electrospun scaffolds made from PCL. A change in solution concentration does not appear to have a significant impact on the strain at break where the range of the strains at break are found from 14.7 to 20. No trend is apparent as the standard deviation is too large to make statistically significant statements about the correlation between solution concentration and the strain at break. The brittle nature of electrospun gelatin scaffolds in random alignments (such as the ones presented here) has been described before and was attributed by

Koh et al. (2013) to a failure of realignment of fibres during stretching[292]. The observed trends for the tensile strength and the elastic modulus here are in agreement with the findings described in and [4.4] where an increase in fibre diameter was found to be to the detriment of the mechanical properties. Available mechanical data on pure gelatin scaffolds is sparse. The work by Huang et al. (2004)[352] shows a negative correlation with solution concentration in terms of ultimate tensile strengths and modulus, however with the use of 2,2,2-trifluoroethanol instead of HFIP as the solvent of choice. Carlisle et al. (2010) demonstrated that single, electrospun collagen fibres follow the same trend observed[377]. Based on the observations presented in this study it can be concluded that the solution concentration and hence the average fibre diameter of gelatin nanofibres has an important effect on the mechanical properties of scaffolds made from these fibres. The change in fibre diameter does not affect the strain at break for gelatin scaffolds unlike the change found for PCL scaffolds [4.4].

PCL-grafted carbon nanotubes were incorporated into electrospun gelatin scaffolds made from solutions containing 4 wt% gelatin. CNTs were added in concentrations of 1 wt%, 2.5 wt% and 5 wt% with respect to gelatin. Each experimental run produced, smooth, defect-free nanofibrous scaffolds as seen in Figure 50.

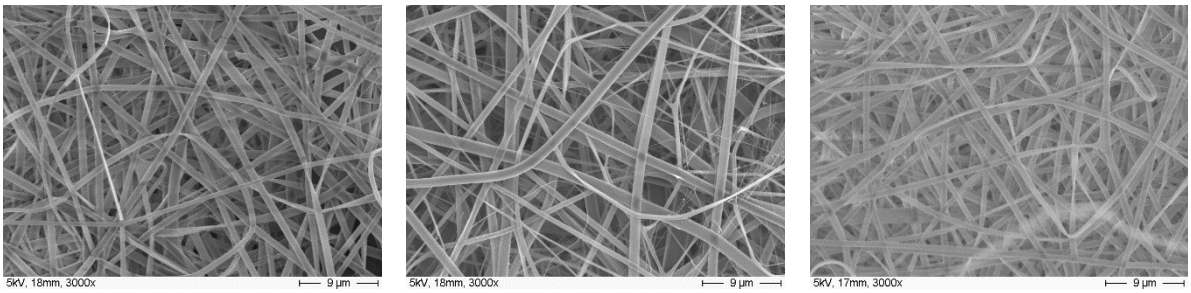

Figure 50: SEM images of electrospun gelatin scaffolds containing 1 wt% (left), 2.5 wt% (middle) and 5 wt% (right) PCL-grafted CNTs. All scale bars are 9 µm.

SEM analysis reveals no observable difference in the morphology of scaffolds containing different amounts of CNTs. No large particles were found anywhere in the scaffolds, indicating that there are no sizeable agglomerates of CNTs but rather a homogenous distribution of CNTs present in the scaffolds. TEM imaging was carried out using the protocol described in [2.5]. Individual, dispersed CNTs were found to be present in every type of scaffold made (Figure 51). It has to be noted that lacey carbon TEM grids were used for this study. The interconnected structures in figure 51 are the lacey carbon and not

the electrospun fibres. No small agglomerates of CNTs could be found in any of the fibres, suggesting a good dispersion of CNTs within the fibres.

A statistical analysis of the fibre diameter distributions of CNT-containing gelatin scaffolds was carried out according to the protocol described in [2.4]. The addition of PCL-grafted CNTs has a minor effect on the average fibre diameter of electrospun gelatin scaffolds as seen in figure 7. At a 1 wt% concentration of CNTs there is a small increase from 700 nm ± 61 nm to 812 nm ± 32 nm in average fibre diameter as compared to pure gelatin scaffolds. The increase in mean diameter is then diminishing from 809 nm ± 87 nm to 738 nm ± 3 nm for 2.5 wt% and 5 wt% added PCL-grafted CNTs respectively. All distributions were near-Gaussian as no bimodal distributions were found as was the case for –OH-functionalized CNTs in PCL fibres [5.3].

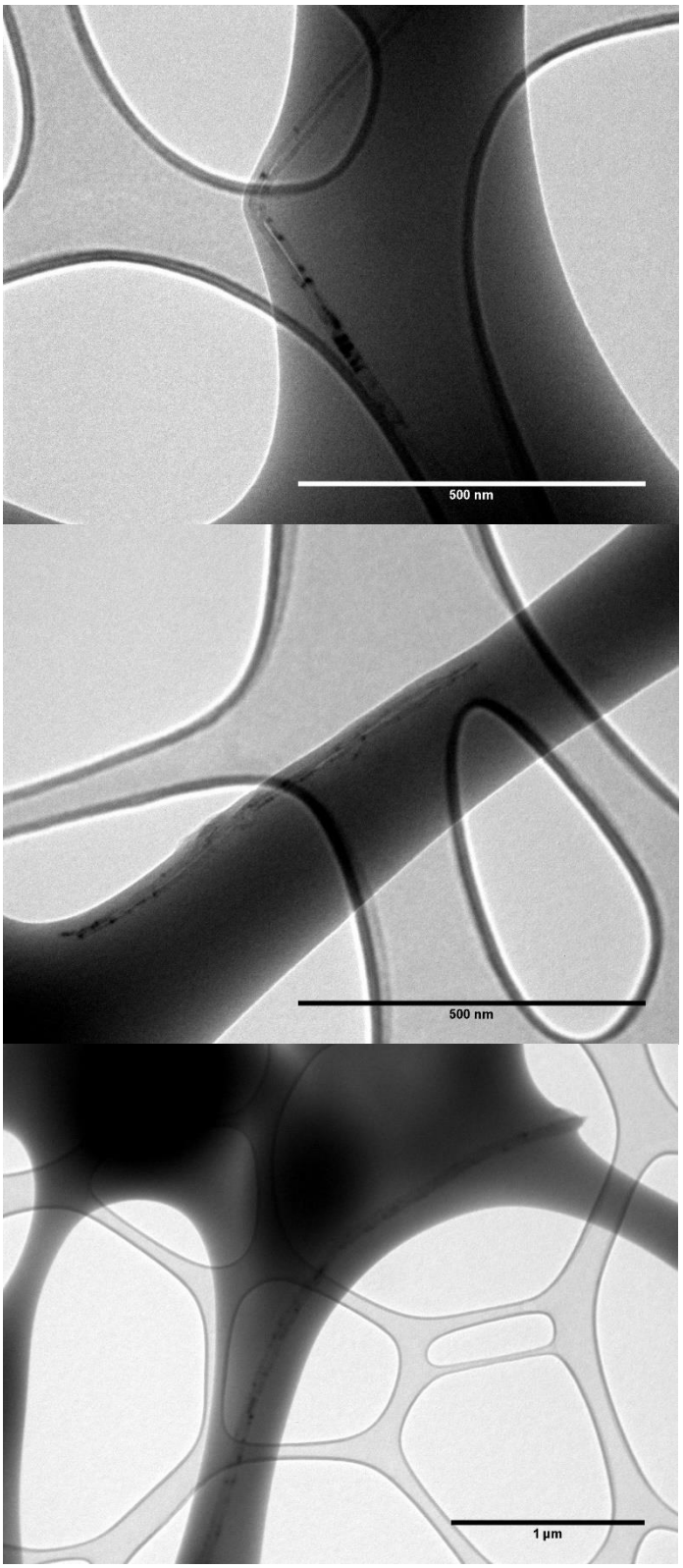

Figure 51: TEM images of PCL-grafted CNTs incorporated into gelatin nanofibres.

The results presented for the influence of the concentration of PCL-grafted CNTs in the gelatin fibres on the average fibre diameter further support the hypothesis that a homogenous distribution of the CNTs was achieved, as a larger impact on the fibre diameter would be expected otherwise [5.3].

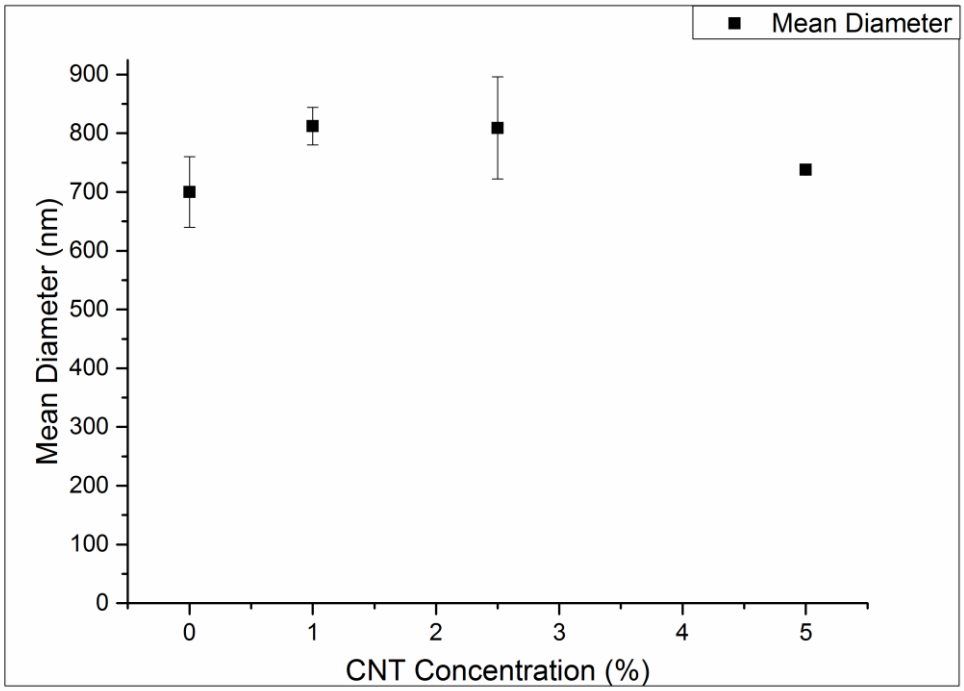

Figure 52: Change in average fibre diameter in electrospun gelatin scaffolds with increased PCL-grafted CNT loading.

The tensile properties of PCL-grafted CNT containing gelatin scaffolds were measured using the protocol described in [2.8]. While the above-mentioned influence on the fibre morphology was minimal, a substantial impact on the mechanical properties can be found, as seen in Figure 53. The tensile strength of the scaffolds increased from 2.54 MPa ± 0.5 MPa for pure gelatin scaffolds to 5.58 MPa ± 0.18 MPa for an addition of 1 wt% CNTs after which it decreased again to 3.97 MPa ± 1.4 MPa and 3 MPa ± 0.13 MPa for 2.5 wt% and 5 wt% of added CNTs respectively. A similar behaviour is found for the elastic modulus. An addition of 1 wt% increases the Young's modulus from 0.64 MPa ± 0.18 MPa for pure gelatin scaffolds to 2.03 MPa ± 0.29 MPa after which a reduction to 1.4 MPa ± 0.27 MPa and 0.69 MPa ± 0.19 MPa for 2.5 wt% and 5 wt% of added CNTs respectively occurs.

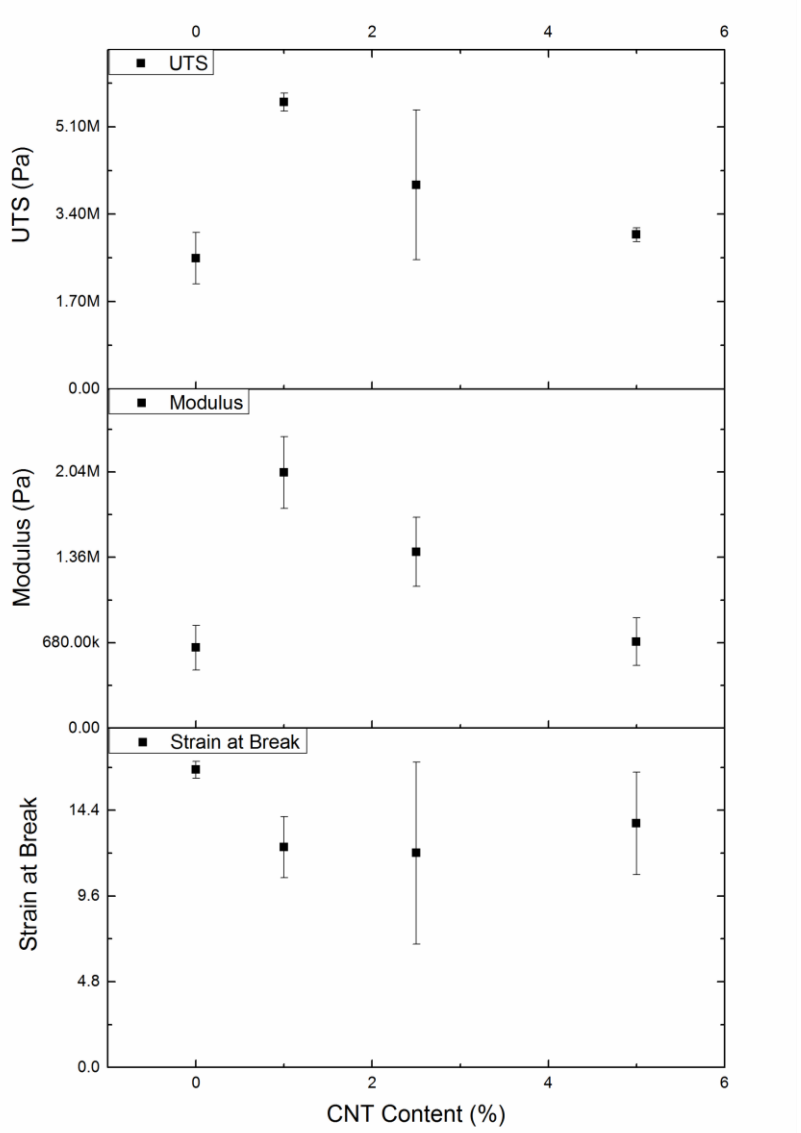

Figure 53: Overview of UTS, modulus and strain at break of electrospun gelatin scaffolds with a change in PCL-grafted CNT content.

The addition of CNTs is found to result in a slight overall reduction in the strain at break. The strain at break is reduced from 16.7 ± 0.5 for a pure gelatin scaffold made from a 4 wt% solution to 12.3 ± 1.7, 12 ± 5 and 13.7 ± 2.9 for an addition of 1 wt%, 2.5 wt% and 5 wt% of CNTs respectively. The reduction for the strain of break is similar to what was observed for the incorporation of CNTs into PCL scaffolds [5.3]. To the best of the author´s knowledge the work presented here the first reported instance of the incorporation of CNTs into electrospun gelatin fibres. The addition of CNTs into gelatin nanofibres proves to have a strong reinforcement effect on the mechanical properties of the scaffolds, greatly increasing the tensile strength and modulus (Figure 54) while a small reduction in the elongation at break is observed.

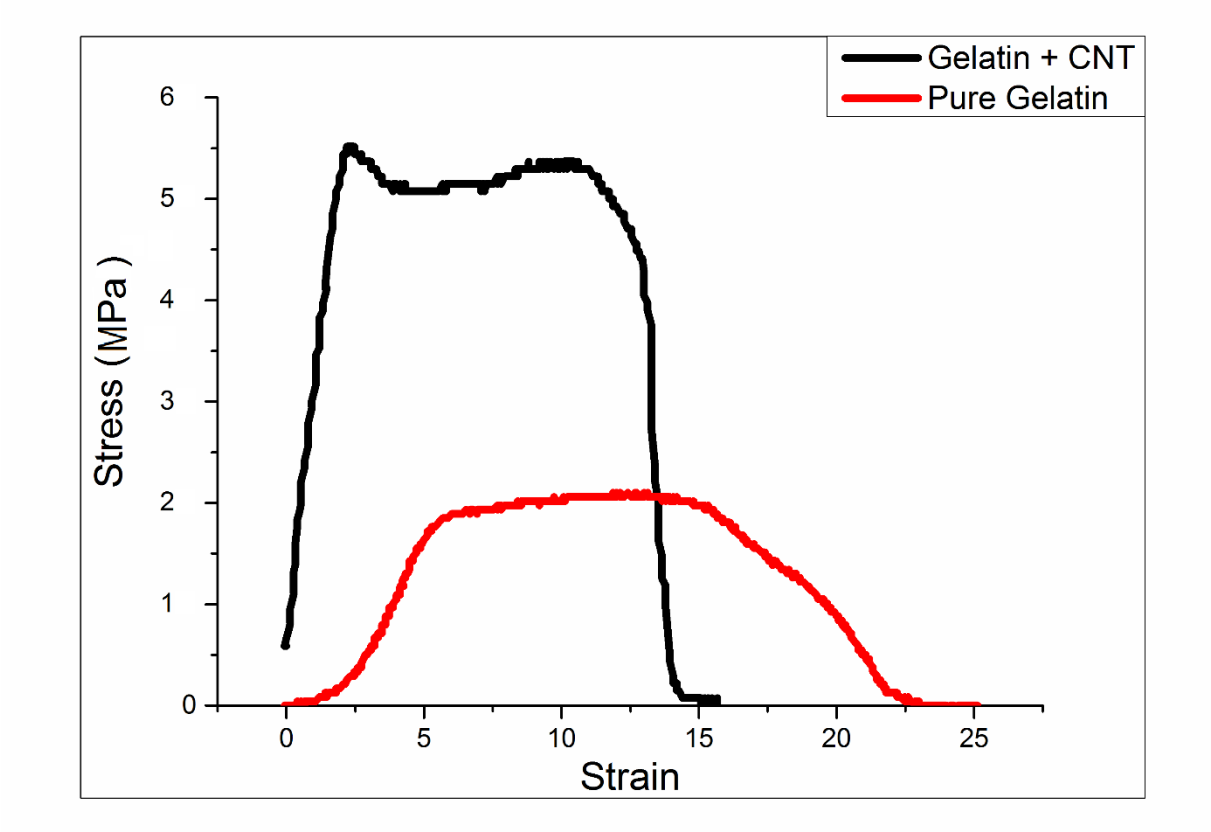

Figure 54: Comparison of stress-strain curves for a pure electrospun gelatin scaffold (red) and a PCL-grafted CNT containing gelatin scaffold.

The addition of 1 wt% PCL-grafted CNTs resulted in the largest increase observed for both tensile strength and Young´s modulus of the scaffolds, where an increase of ~220% and ~317% respectively were found as compared to pure gelatin fibres. This substantial increase in strength and elastic modulus in conjunction with the negligible impact on the mean fibre diameter makes PCL-grafted CNTs a good candidate to tailor the mechanical properties of electrospun gelatin scaffolds without altering the scaffold morphology. There is very limited data available on the mechanical properties of electrospun biological polymers containing CNTs. Ayutsede et al. (2006) found a similar reinforcement behaviour of *Bombyx mori* silk nanofibres with the addition of CNTs[127] in terms of elastic modulus and elongation at break. An addition of 1 wt% single-walled CNTs (SWCNTs) resulted in a large increase in Young´s modulus. However there was a large reduction in tensile strength and the Young´s modulus was found to decrease with any other amount of SWCNTs added in their study. The strain at break was found to be decrease for all additions of SWCNTs. It is generally understood that the incorporation of CNTs into electrospun nanofibres of synthetic polymers follows a similar pattern as described in this study. For the tensile strength there is an optimal level of CNT addition at which a highest increase is found, after

which the strength will then be reduced. This has been observed for fibres made from polyimide[219], polyacrilonitrile[321,326,378], polyvinyl alcohol[150], polystyrene[379] and polyethylene oxide[380]. The elastic modulus was found to follow a similar behaviour in most cases with some exceptions where the tensile strength showed a peak and the modulus monotonically increased with the CNT concentration[219,320,380]. A similar behaviour can be observed for polymer/CNT composites produced by other processing techniques[381]. CNTs have a mechanical percolation threshold in every matrix they are incorporated in that will depend on their aspect ratio, their agglomeration and the homogeneity of their dispersion[382]. The concentration dependency of the reinforcement of any given polymer/CNT system will depend on those factors, as any addition of a material with the same aspect ratio beyond the percolation threshold will add to the agglomeration or a more inhomogeneous distribution within the matrix. Given the large differences in mechanical properties between a thermoplastic polymer and CNTs – which are very brittle in comparison with the polymer – agglomerates of CNTs will act as stress initiation points and their beneficial reinforcement effects will consequently be diminished and in some cases the overall mechanical properties of the composite can be lower than those of the pure matrix[150].

The brittle nature of electrospun gelatin scaffolds is a drawback for their subsequent use in various applications which has led many researchers to create fibre blends which exhibit superior mechanical properties[345]. The results presented here offer another possibility to augment the physical properties of electrospun gelatin scaffolds without changing their morphology or chemical composition which could aid a more widespread use of such scaffolds for biomedical applications.

6.4. Conclusion

In this chapter pure gelatin nanofibres were successfully electrospun into nanofibrous scaffolds using HFIP as a solvent. A consistent correlation was established between the solution properties and the morphology of the resulting scaffolds. The average fibre diameter is found to monotonically increase with an increase in the weight percentage of gelatin in the solutions. Additionally it was shown, through the use of viscosity measurements and changes in final fibre morphology, that HFIP has a time-dependent, denaturising influence on the gelatin used. The age of the solution was identified as an important parameter which determines the mean fibre diameter of scaffolds produced. With a

progressing age of the solution the fibre diameter is significantly reduced and the effect was found to be more pronounced for solutions containing a larger amount of gelatin. It is suggested that future work on the electrospinning of gelatin (and by extension collagen) with fluorinated solvents control the solution age carefully. The mechanical properties of pure gelatin scaffolds were investigated using tensile testing. A clear correlation between the solution concentration and hence the average fibre diameter was found. Scaffolds containing a larger average fibre diameter were found to have reduced ultimate tensile strengths and elastic moduli, similar to the findings in [4.5] whereas the elongation at break was not statistically significantly influenced by the fibre diameter. PCL-grafted CNTs were successfully incorporated into gelatin nanofibres. The addition of CNTs into the gelatin scaffolds had a minimal influence on the average fibre diameter. The CNTs were found to be homogenously distributed inside the nanofibres. The mechanical properties of the scaffolds were greatly increased by the inclusion of the PCL-grafted CNTs. The tensile strength and the Young´s modulus were found to be increased as by a factor of 2.2 and 3.17 respectively with the addition of 1 wt% CNTs whereas the elongation at break was slightly reduced. Larger amounts of CNTs still had a beneficial effect on the UTS and the elastic modulus but with diminishing increases.

In conclusion it is possible to electrospin gelatin into nanofibrous scaffolds using HFIP and the solution concentration can be used as a means of tailoring the morphology and mechanical properties of those scaffolds. The age of the solution was identified as a crucial parameter in terms of reproducibility and morphology. The incorporation of CNTs can be used as at technique to significantly augment and improve the mechanical properties of gelatin scaffolds which may facilitate their use in tissue engineering application. To the best of the author´s knowledge the work carried out in this chapter demonstrates the first, successful incorporation of CNTs into electrospun gelatin nanofibres and their characterisation.

7. Neuronal Cell Growth on Electrospun PCL Scaffolds

7.1. Introduction

The utilization of biodegradable nanofibrous scaffolds for the use in neuronal tissue engineering is particularly attractive due to the morphological similarities with the extracellular matrix[383]. Polycaprolactone (PCL) is an synthetic biodegradable polymer with a long degradation time compared to other polymers[384] which allows neuronal cells enough time to grow and form networks. The *in vivo* degradation of PCL is non-toxic and occurs through the breakup of ester linkage by a non-enzymatic, random hydrolysis[385]. *In vivo* rat studies have shown that the degradation manifests itself via a reduction in the average molecular weight and does not accumulate in the body but is excreted out safely[386], further justifying the attractiveness for the use of PCL in tissue engineering applications.

The use of carbon nanotubes as filler materials in tissues engineering composites has recently seen a rise in early-stage research[387]. With the introduction of any new material into tissues their toxicity needs to be understood and controlled. The cytotoxicity of pure CNTs is a topic of ongoing debate and appears to be dependent on the various factors such as production method, length, diameter, method of purification and concentration[388,389] Furthermore it has been shown that certain types of CNTs can be carcinogenic, again depending on their specific morphology[390]. There is very little data available on the toxicity of in vivo implants of composites containing CNTs. Chua et al. (2015) successfully managed to implant artificial trachea implants made of CNTs and poly-di-methyl-siloxane in porcine models with no adverse side effects or breathing difficulties[391].

The incorporation of CNTs in electrospun fibres and their effect on cell growth was explored by Meng et al. (2010) who found that the addition of CNTs into electrospun PCL fibres showed no cytotoxic effect on the mouse fibroblast cells L-929 and NIH3T3 as compared to pure PCL fibres after 3 days of cell growth[137]. Another study on the bioinert polymer polyurethane by Meng et al. (2009) demonstrated that the addition of CNTs "*significantly enhance the cell adhesion, proliferation, migration and aggregation, and secretion*" of 3T3-L1 mouse fibroblasts[392]. It was concluded that the CNTs provided a suitable microenvironment for cells to migrate and aggregate. Similarly, Zomer Volapto et al. (2010) found an enhanced proliferation and activation of human osteogenic sarcoma osteoblasts (MG63 cell

line) with the addition of CNTs into polyamide 6[393]. The beneficial effect of the CNTs was attributed to a change in surface morphology of the fibres, effectively "nanopatterning" the polyamide 6 fibres.

While these results are encouraging with regards to the use of CNTs in tissue engineering, more work is required to gain a better understanding on the impact and performance of CNT-containing composites for tissue engineering applications. Building on the findings from [4.4] and [5.3] this chapter compares and contrasts the performance of different electrospun PCL and PCL-grafted CNTs containing PCL scaffolds for the growth of human neurons and astrocytes derived from human progenitor cells. Due to financial constraints of the project it was only possible carry out a smaller pilot study where cell growth was investigated for a 7 day time period. A more reduced experimental design was also used with fewer samples employed than would be in a typical study. The results presented here show a strong enough effect to promote further work to be carried out.

7.2. Materials and Method

7.2.1. Electrospinning

Electrospinning of scaffolds was carried out using the equipment described in [2.1]. Five different types of electrospun PCL fibres – using the processing parameters shown in Table 18– were electrospun, with three types of pure PCL scaffolds and two types of PCL-grafted CNT containing scaffolds [2.1].

Sample	Voltage (kV)	Distance (cm)	Flow Rate (mL/h)	PCL Content (wt%)	CNT Conc. (wt%)
1	25	15	0.55	3	0
2	25	15	0.55	5	0
3	25	15	0.55	7	0
4	25	15	0.55	4	1
5	25	15	0.55	4	5

Table 18: Overview of the processing and solution parameters used for the electrospinning of the cell study scaffolds.

The as-produced scaffolds were cut into circular samples with a diameter of ~1 cm² (dry), placed in a 24-well plate and held in place with a rubber ring on top. The average fibre diameter of the different scaffolds were measured with SEM using the protocol described in [2.3]. Each type of scaffold was made in triplicates, where two were used for normal cell growth experiments and one was subjected to an oxygen plasma treatment prior to the cell seeding.

7.2.2. Cell Line

The cell used in this study were human neurons and astrocytes derived from human progenitor cells purchased from Axol Bioscience (Cambridge, UK). The Axol 13 cell line was used, which are derived from induced pluripotent stem cell (iPSC). The cell line was maintained by Dr. Julian George at the Institute of Biomedical Engineering (University of Oxford). Cell seeding, sterilisation, coating and fixation was also kindly carried out by Dr. Julian George.

7.2.3. Sterilisation and Coating

The scaffolds were sterilised by ethanol submersion for one hour prior to coating and dried in a fume hood. Samples were coated in Poly-L-Ornithine (Sigma-Aldrich) (10ug/ml) in PBS for one hour at 37 C° and then subsequently coated in Laminin (20ug/ml Sigma-Aldrich) in PBS for one hour at 37 C°. Electrospun scaffolds were coated in laminin prior to cell growth to improve cell attachment and neuronal cell growth[394] as uncoated samples exhibited poor cell attachment in previous experiments.

7.2.4. Seeding

Cells were seeded onto the scaffolds through enzymatic digestions of the cells to the well plates using accutase (Sigma-Aldrich). For this, cells were washed in a phosphate-buffered saline (PBS) solution and 1 mL accutase was added to each 6-well plate, incubated for five minutes at 37 C°. 2 mL of fresh culture medium Neural Basal Medium (Axol, Cambridge) was then added to stop the accutase action. A pipette is used to wash and mechanically separate the cells from the surface to form a single cell suspension. Cell pellets are then generated by centrifuging the cells at 300x gravity for 5 minutes after which the pellets are resuspended in 10 mL of fresh medium. Cells are counted using a haemocytometer and seeded at 1000 cells/mm². Cells are left to attach for 40 minutes at 37C (5%CO_2, 100% humidity) and then a further 500µl of medium is added slowly to each well to not disturb the attached cells. Media is then changed every 2-3 days, and after 7 days the attached cells were fixed.

7.2.5. Fixation

Prior to fixation, all scaffolds with attached cultured cells were removed from wells and gently washed in PBS. Scaffolds were fixed through incubation with 4% paraformaldehyde (PFA; Sigma-Aldrich, UK) in PBS at 4°C overnight. Fixed scaffolds were washed three times in PBS and stored for up to one week in PBS at 4°C.

7.2.6. Staining

Neurites were imaged after immunostaining of β-III tubulin. Before staining cells were blocked and permeablised at room temperature for 1 hour in PBS containing 10% bovine serum albumin (BSA; Sigma-Aldrich, UK) and 1% Triton X-100 (Sigma-Aldrich, UK). Neurons were stained where the scaffolds were placed into wells of a 24-well plate and incubated overnight at 4°C with mouse monoclonal anti-βIII tubulin antibody (TuJ-1 staining: R&D, UK) diluted 1:1000 in staining buffer (1% BSA and 0.1% Triton X-100 in PBS). After incubation, scaffolds were washed three times in staining buffer, and incubated at room temperature for 1 hour with Alexa Fluor 488 goat anti-mouse IgG (Life Technologies, UK) diluted 1:500 in staining buffer. Scaffolds were gently washed three times in PBS and mounted onto slides with mounting medium (Vectashield, Vector, UK) containing the blue fluorescent nuclear dye 4',6-diamidino-2-phenylindole (DAPI).

7.2.7. Image Acquisition

Fluorescently stained and fluorescent protein expressing cells were imaged using a cooled CCD camera (EXI blue; QImaging, UK) attached to an inverted microscope (Eclipse Ti, Nikon) with stable LED illumination (pE-2; CoolLED, UK).

7.2.8. Image Analysis

Cell Counting was performed using the ImageJ software (National Institutes of Health, USA) from three random locations on the scaffolds. Prior to the analysis, the background was removed using the "Remove Background" command after which the "Enhance Local Contrast" command was used with the settings "Blocksize" at 127, "Histogram Bins" at 256 and "Maximum Slope" at 3. The tool "Find Maxima" was then used with a noise tolerance of 36 to calculate the number of cells present in each image. Three random images from each of the batches were used to determine average number of cells.

The number of dendrites were determined by manual counting and the average dendrite length was estimated by manual measurement of 20 randomly selected dendrites from images that contained dendrites.

7.2.9. Control Samples

A set of flat control samples were made by coating 1 cm^2 glass slides with Laminin using the above-mentioned coating protocol. The same protocols as for the electrospun scaffolds were used for cell seeding, fixation, staining, image acquisition and image analysis.

7.3. Results and Discussion

Previous studies by Lowery et al. (2010)[395] and Badami et al. (2006)[396] strongly indicate that cell growth and proliferation – as determined by cell counting – is significantly enhanced on scaffolds which exhibit larger average fibre diameters. The electrospinning parameters of this chapter were designed to produce PCL scaffolds with varying mean fibre diameters. Figure 53 shows an overview of the average fibre diameter of the five types of scaffolds produced. As observed before [3.3.1] the mean fibre diameter is found to increase with the PCL solution concentration from 252 nm ± 23 nm to 705 nm ± 169 nm and 987 nm ± 187 nm for 3 wt%, 5 wt% and 7 wt% PCL solutions respectively. The incorporation of CNTs

into the scaffolds resulted in a decreased average fibre diameter – as discussed in [5.3] – with diameters of 407 nm ± 56 nm and 319 nm ± 16 nm for an addition of 1 wt% and 5 wt% CNTs respectively. The scaffolds produced exhibit a variety of fibre diameters with the pure PCL samples being sufficiently different in order to attribute changes in cell growth to their morphology.

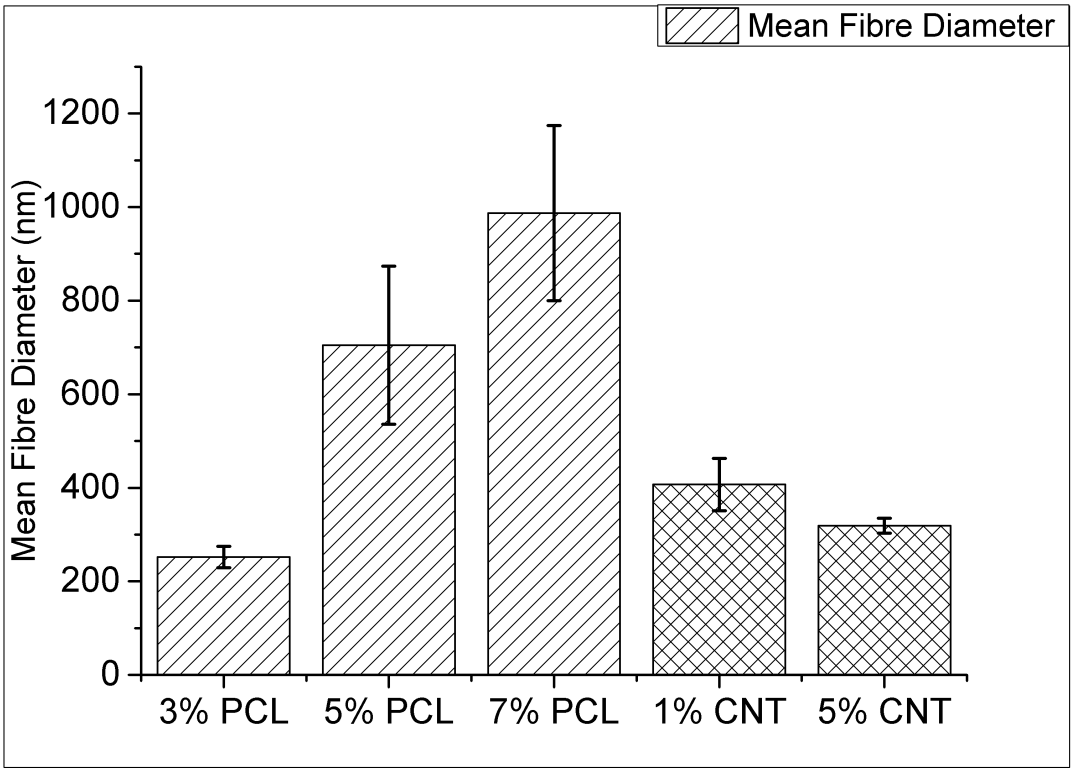

Figure 55: Comparison of the average fibre diameter of the different types of scaffolds used for the cell study.

Human iPSC-derived cells are seeded onto flat control samples as a control group. An additional O_2 plasma treatment was carried out on a set of samples but cell growth experiments resulted in no neuronal cell development. The O_2 plasma was initially used as a comparison as some studies have shown better cell attachment for plasma treated, electrospun scaffolds[397]. Flat glass slides generally show a good cell attachment and growth but these are two dimensional scaffolds and hence limited for the use in any more advanced tissue engineering applications. DAPI staining is used to image cell nuclei as it binds to DNA which then emits blue fluorescent light at a wavelength ~450 nm when excited with ultraviolet light[398]. TuJ-1 staining is a popular method of identifying neurons in immunocytochemistry[399]. TuJ-1 staining uses antibodies to bind to β-III tubulin which is a protein almost exclusively found in neurons[400]. B-III tubulin is an element of the cytoskeleton of neurons and thus present in axons and dendrites. For

the TuJ-1 staining in this work a green fluorescent dye was used. Figure 56 shows a representative image of developed neurons after 7 days of growth on a flat control sample.

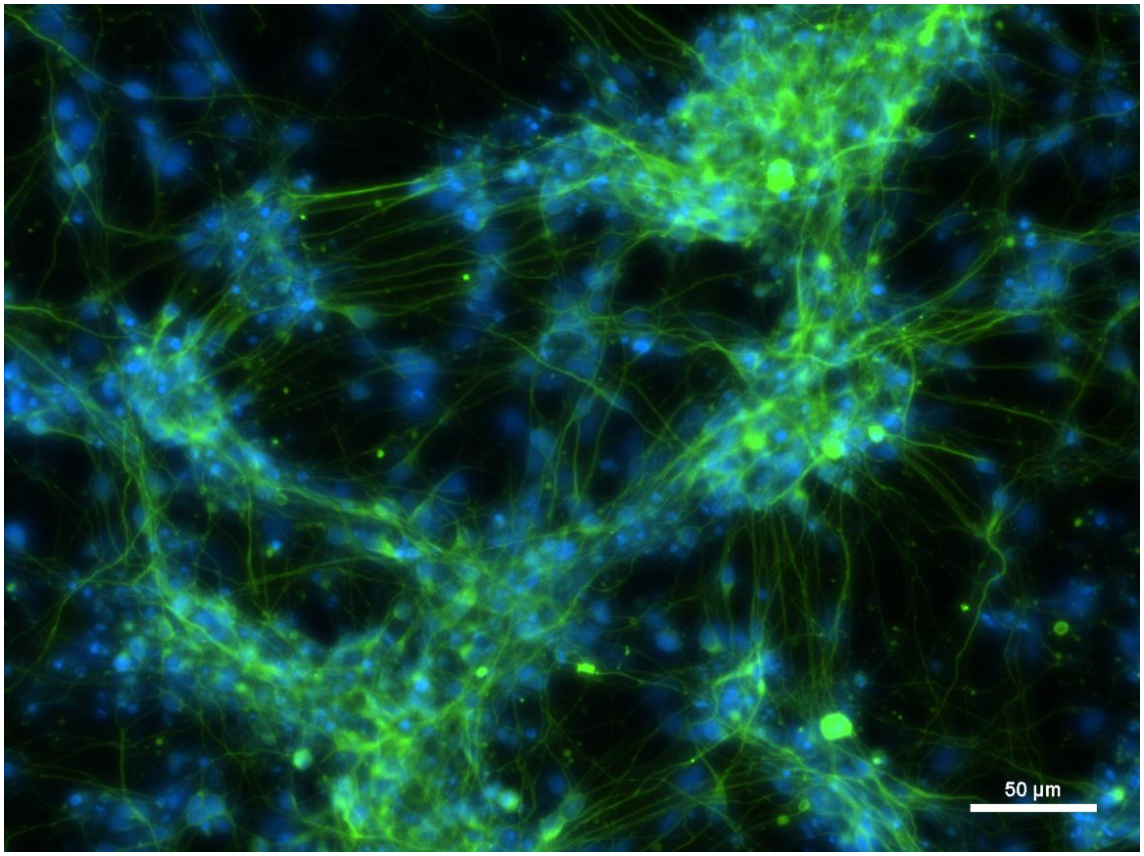

Figure 56: Fluorescence microscopy image of neurons grown on a flat substrate after 7 days of cell growth.

A large number of cells are seen with an interconnected network of axons and dendrites present. All the control samples showed good growth and differentiation into neurons.

Cell growth on electrospun scaffolds was carried out with two batches of cells using two different cell pellets. Both batches resulted in cell growth and proliferation on all electrospun scaffolds. Figure 57 and Figure 58 illustrate representative images of cells on the electrospun scaffolds after 7 days of growth for batch 1 and batch 2 respectively. Visual inspection of the images of the images show a clear presence of cell nuclei (blue) and the presence of neurons (green). No dendritic structures are found for pure PCL scaffolds in batch 1 whereas PCL-grafted CNT containing scaffolds do show the presence of dendrites. Batch 2 exhibits the presence of dendrites for all samples investigated. This suggests that the cells in batch 1 developed less favourably which is a common occurrence when working with cells, where a large variance in cell growth behaviour is expected.

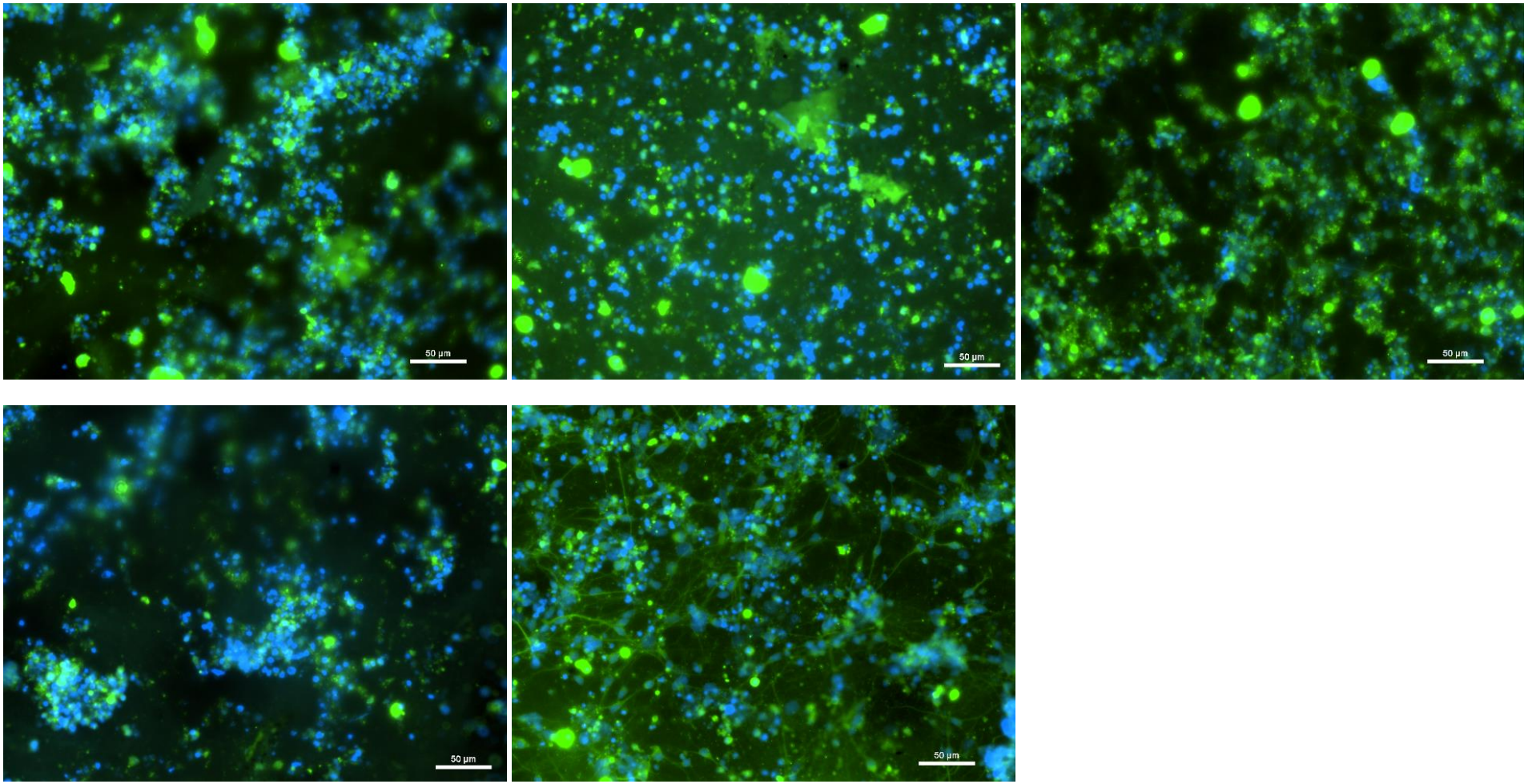

Figure 57: Fluorescence microscopy images of cells from the first batch grown for 7 days on the different scaffolds used. Top left: 3 wt% PCL. Top center: 5 wt% PCL. Top right: 7 wt% PCL. Bottom left: 1 wt% CNTs. Bottom right: 5 wt% CNTs.

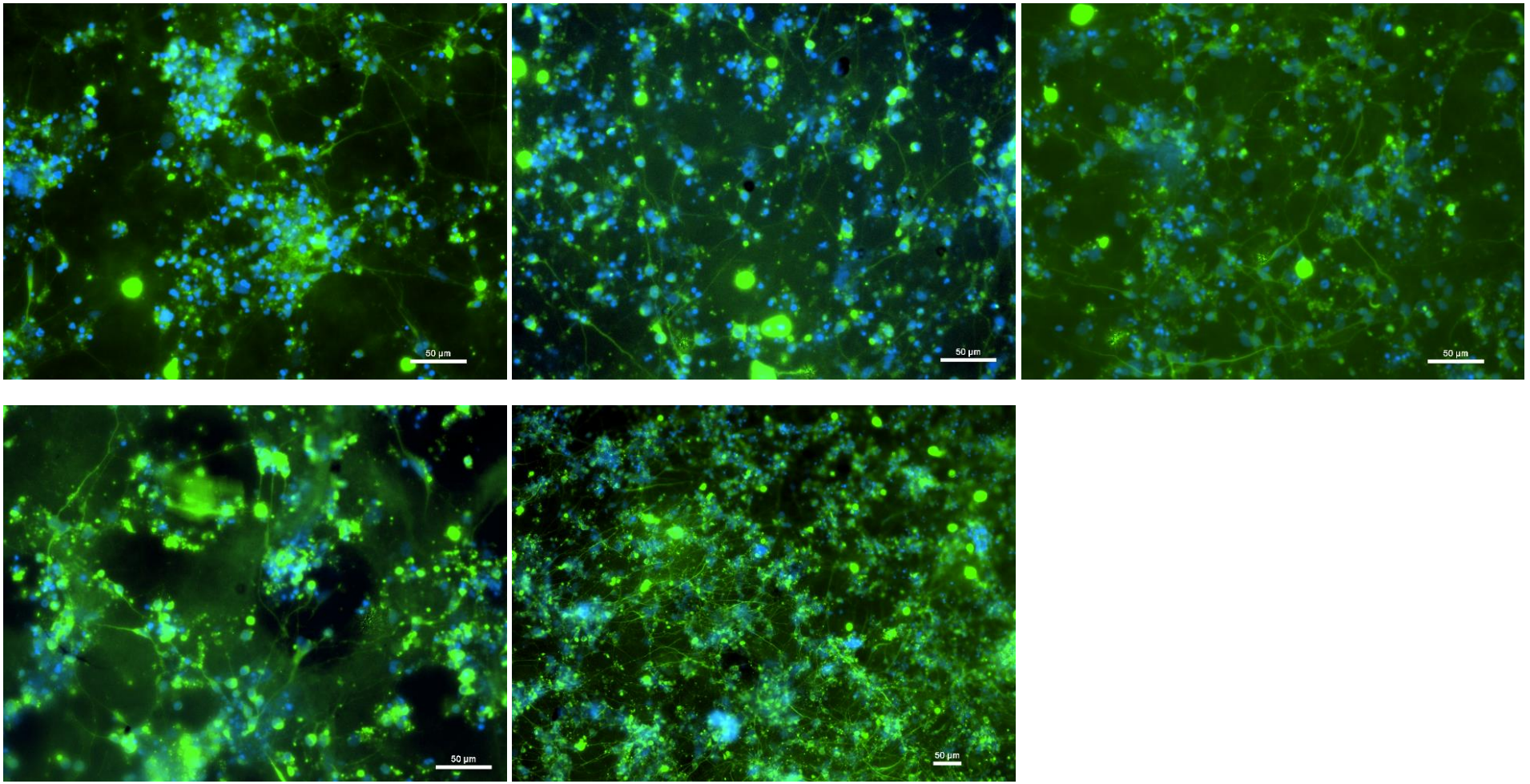

Figure 58: Fluorescence microscopy images of cells from the second batch grown for 7 days on the different scaffolds used. Top left: 3 wt% PCL. Top center: 5 wt% PCL. Top right: 7 wt% PCL. Bottom left: 1 wt% CNTs. Bottom right: 5 wt% CNTs.

Figure 59 displays a comparison of the average number of cells found on the scaffolds. A clear trend emerges with respect to the pure PCL fibres. As the weight percentage of PCL increases – and hence the average fibre diameter – the average number of cells increases. The cell count increases from ~3300 cells/mm² ± 750 cells/mm² to ~3400 cells/mm² ± 830 cells/mm² to ~4000 cells/mm² ± 750 cells/mm² for 3 wt%, 5 wt% and 7 wt% scaffolds respectively. The CNT containing scaffolds show an increase in the average number of cells with the CNT content, increasing from ~2800 cells/mm² ± 540 cells/mm² to ~4000 cells/mm² ± 900 cells/mm² for 1 wt% and 5 wt% added CNTs respectively. The control samples have the highest cell count with ~4200 cells/mm² ± 780 cells/mm² by a small margin. All samples exhibit an increase in the number of cells as compared to the 1000 cells/mm² that were initially seeded onto the samples, confirming significant cell proliferation.

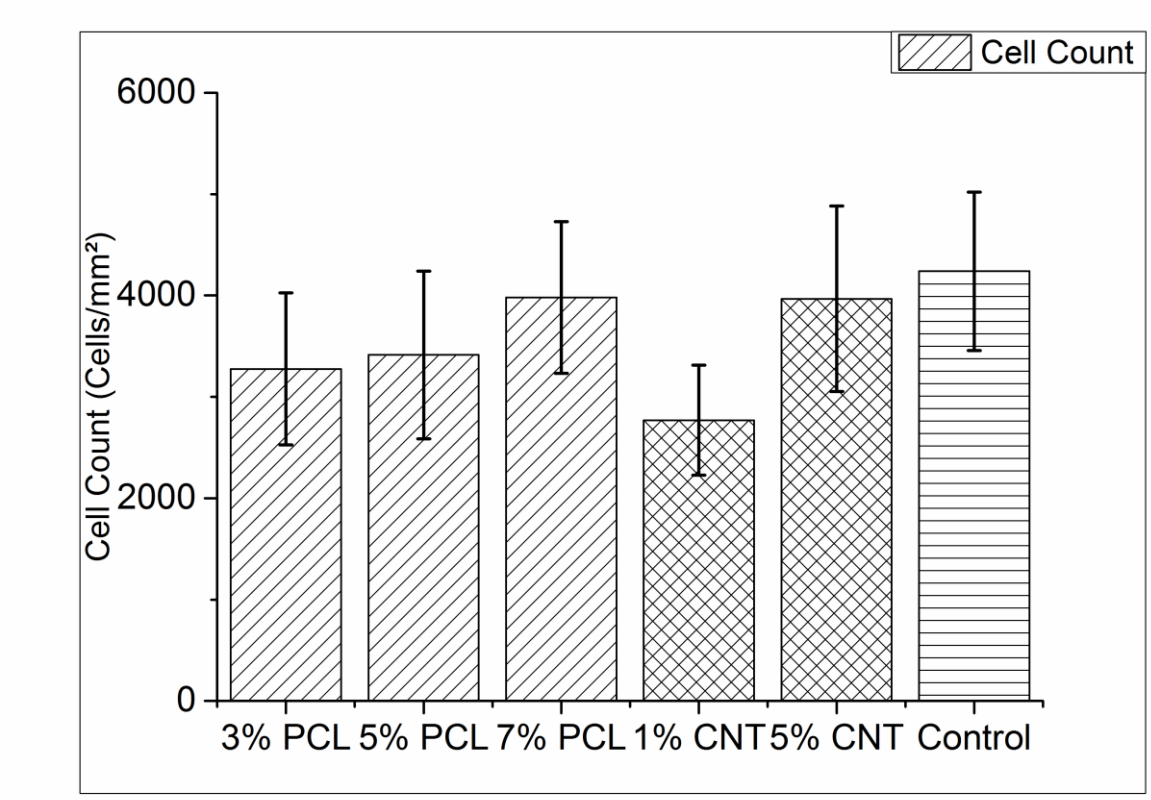

Figure 59: Comparison of the average cell count found on the different types of scaffolds and the control substrate after 7 days of cell growth.

A higher cell count on flat control samples has been observed before to varying degrees[396,401,402]. An explanation that was put forward for this is that cell attachment occurs faster on flat substrates as compared to nanofibrous scaffolds. When a longer culturing time was taken into account, the cell count on electrospun scaffolds was found to surpass that of flat controls in some cases[396,401]. The porous

morphology of electrospun scaffolds presents an initial barrier to the spreading of cells and thus it will take a slightly longer time for the cells to proliferate. Nonetheless the observed difference in this work is minimal compared to what is found in the literature.

The aim of any type of scaffold in tissue engineering is to mimic the natural environment of the cells so that their growth and development occurs naturally[12]. The number of synapses in the human neocortex is a staggering ~1.5 * 10^{16}, which indicates an extremely high interconnectivity of the human brain[403]. Hence any scaffold which promotes dendritic growth and density – and therefore interconnectivity – can be considered superior in its usefulness for neuronal tissue engineering relative to other scaffolds. The cell count is a good measure to investigate the performance of a given scaffold in terms of cell proliferation and cytotoxicity. The average number of cells however does not take into account the capability of the scaffold to induce cell differentiation, as all cells are counted regardless of their cell type. Since the cells used in this study develop into neurons it was of a particular interest to investigate the capacity of a given scaffold to support a neural network. In order to quantify that effect the density of neuronal dendrites was investigated.

The dendrite density of the five different scaffolds and the control sample were measured and the results are summarized in Figure 60. The control sample exhibits the highest dendrite density of 2074 dendrites/mm² ± 525 dendrites/mm². A positive correlation can be found within the electrospun, pure PCL scaffolds, where an increase in the density from 305 dendrites/mm² ± 40 dendrites/mm², to 580 dendrites/mm² ± 41 dendrites/mm², to 852 dendrites/mm² ± 45 dendrites/mm² is seen for 3 wt%, 5 wt% and 7 wt% samples respectively. In this case it can be concluded that the larger fibre diameters, as a result of the change in solution concentration, are beneficial for cell functionality and promote a higher interconnectivity. The addition of CNTs has a significant influence on the dendrite density. The dendrite density is found to increase from 598 dendrites/mm² ± 66 dendrites/mm² at 1 wt% of added CNTs to 1841 dendrites/mm² ± 467 dendrites/mm² at a 5 wt% loading of CNTs. The 5 wt% CNT fibres outperform the pure PCL fibres from the 7 wt% solutions by a factor of ~2.2.

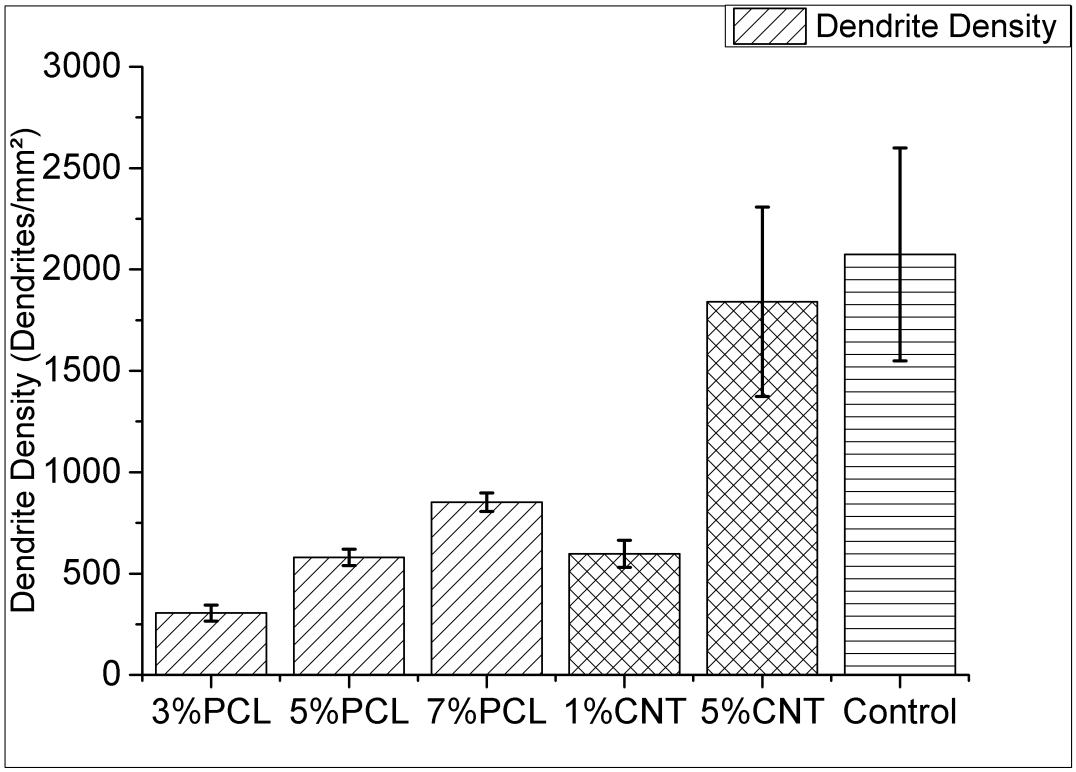

Figure 60: Comparison of the dendritic density found on the different types of scaffolds and the control substrate after 7 days of cell growth.

This large increase in inter-neuron connections is observed despite the significant difference in average fibre diameter. The effect of the incorporation of CNTs into the fibres – specifically at the 5 wt% level – must be understood beyond the morphological implications, as the fibre diameter is substantially smaller than the best performing, pure PCL scaffold. It was shown in [5.3] that the addition of CNTs does not alter the electrokinetic properties of the scaffolds and similarly TEM imaging [5.3] revealed that CNTs are encapsulated by the PCL fibres and do not penetrate the fibre walls. The positive impact of the CNTs on neuronal cell development as indicated by the promotion of dendrite growth and outreach is therefore a product of the altered physical properties of the overall scaffold rather than individual interactions with CNTs on the surface of the fibres. In this case it is a result of either the mechanical reinforcement as evidenced in [5.3] or the increase in electric conductivity expected by the incorporation of CNTs into electrospun polymer scaffolds[404] or a combination of the two. It was shown that cell stem fate is highly controlled by the physical interactions with the extracellular matrix, specifically the mechanical properties[120]. Roach et al. (2010) have speculated that in order to understand the influence of a substrate on neuronal tissue growth a "triangle of factors (chemistry – topography –

stiffness)" need to be considered[405]. Previous characterisations of CNT containing scaffolds in this thesis have shown that surface chemistry and overall fibre topography is not significantly altered through the incorporation of CNTs. This points towards the change stiffness and/or resistivity being responsible for the enhanced neurite growth. Jeong et al (2008) showed that nanofibrous scaffolds with enhanced conductivity outperformed less-conductive scaffolds in terms of in-vitro cellular activity of human dermal fibroblasts[406]. However because the increased conductivity was caused by blending, surface chemistry effects could not be fully excluded. Additionally Gleixner et al. (2006) found that the electric resistivity of the ECM for rat neurons is ~12.6 MΩ[236]. To the best of the author´s knowledge there is no data available on the bulk resistivity of PCL, however assuming a similar resistivity to polyethylene (~10^{15}Ω) the ECM is several orders of magnitude more conductive than pure PCL. Based on these considerations the incorporation of CNTs into electrospun PCL scaffolds results in more beneficial mechanical properties as well as electric properties that are closer to the conditions that neurons experience *in-vivo*. Due to the limitations in scope of this study it is not possible to conclusively elucidate and separate the nature of mechanisms responsible for the enhanced neurite growth.

An additional assessment of the quality of the scaffolds for use as neuronal cell substrates is carried out by the measurement of the average length of the dendrites. The rationale behind this is that a longer average dendrite length is indicative of a more complete and long-range network formed between the neurons. The average dendrite length in the control samples is found to be 143 µm ± 11 µm. The average length for the pure PCL samples is found to vary from 77 µm ± 1 µm, to 103 µm ± 9 µm, to 102 µm ± 3 µm for 3 wt%, 5 wt% and 7 wt % samples respectively (Figure 61].

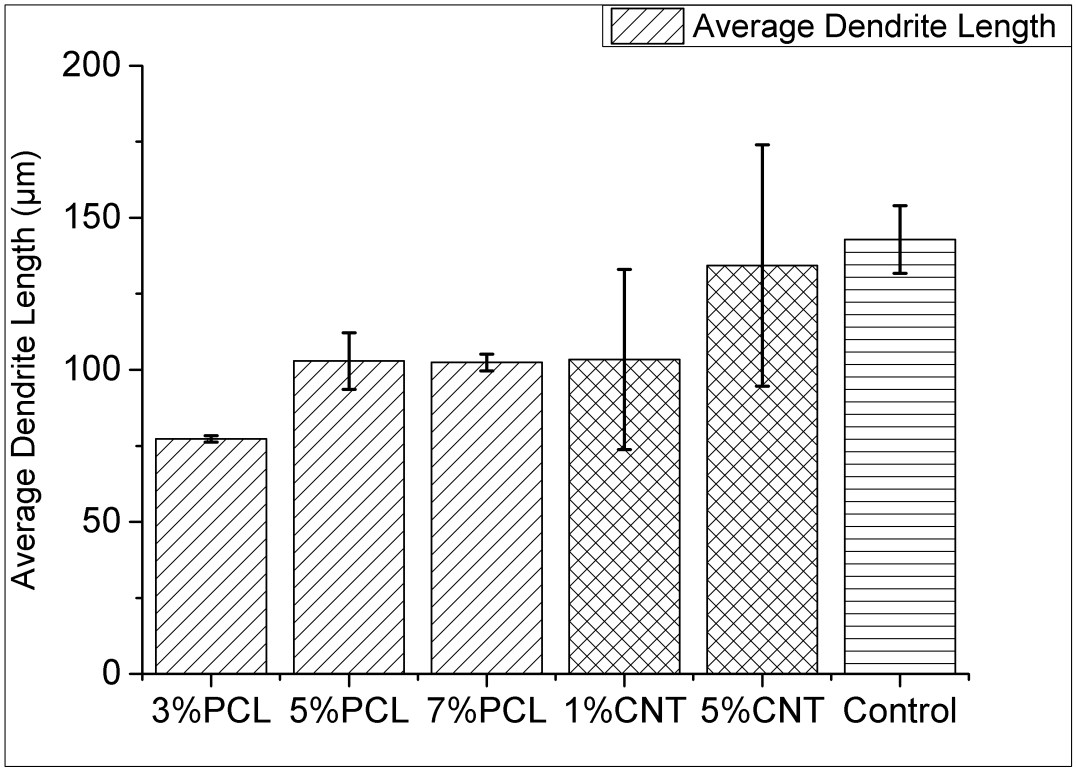

Figure 61: Comparison of the average dendrite length found on the different types of scaffolds and the control substrate after 7 days of cell growth.

The 3 wt% samples – which exhibit the smallest average fibre diameter observed for the scaffolds used here – seem to inhibit the outreach of dendrites as compared to the larger 5 wt% and 7 wt% samples. There was no statistically significant difference in average dendrite length found between the 5 wt% and 7 wt% samples, suggesting a cut-off average fibre diameter for the dendrite lengths due to fibre morphology. The scaffolds with 1 wt% added CNTs shows a similar mean dendrite length of 103 µm ± 30 µm as the 5 wt% PCL and 7 wt% samples. The scaffolds with 5 wt% added PCL-grafted CNTs exhibits a longer average dendrite length of 134 µm ± 40 µm, which is the same range as the control samples. As with the above-mentioned cell count and dendrite density the 5 wt% CNT containing scaffolds are a positive outlier with respect to the dendrite length. For the other electrospun scaffolds used in this study there is a clear correlation between the average fibre diameter and the average dendrite length, which is indicative of a minimum average fibre diameter after which no additional gain in dendrite length is observed. The increase in dendritic length for the 5 wt% CNT scaffolds must then be influenced – as mentioned before – by the change in physical properties of the PCL fibres.

The results from the cell count, the dendrite density and the average dendrite length indicate that, in the absence of other influencing factors, the average fibre diameter is a good indicator of the performance of electrospun PCL scaffolds with respect to neuronal tissue engineering. The addition of 5 wt% has a significant, positive effect on all three factors, despite possessing a smaller average fibre diameter whereas the addition of only 1 wt% CNTs does not appear to have any benefit. These results strongly suggest that the addition of CNTs above a certain threshold are significantly enhancing the capability of electrospun PCL scaffolds to perform as neuronal tissue engineering scaffolds.

Electrospun scaffolds with added 5 wt% of CNTs exhibit the largest level of interconnectivity between neurons as compared to any other non-control sample. Qualitative analysis of fluorescence micrographs shows individual dendrites with a length of up to ~700 µm connecting different neurons (Figure 62). Imaging of the electrospun samples was comparatively more difficult to carry out than on the flat control samples as evidenced by relative difference in sharpness between images of the control sample and images of cells on electrospun scaffolds.

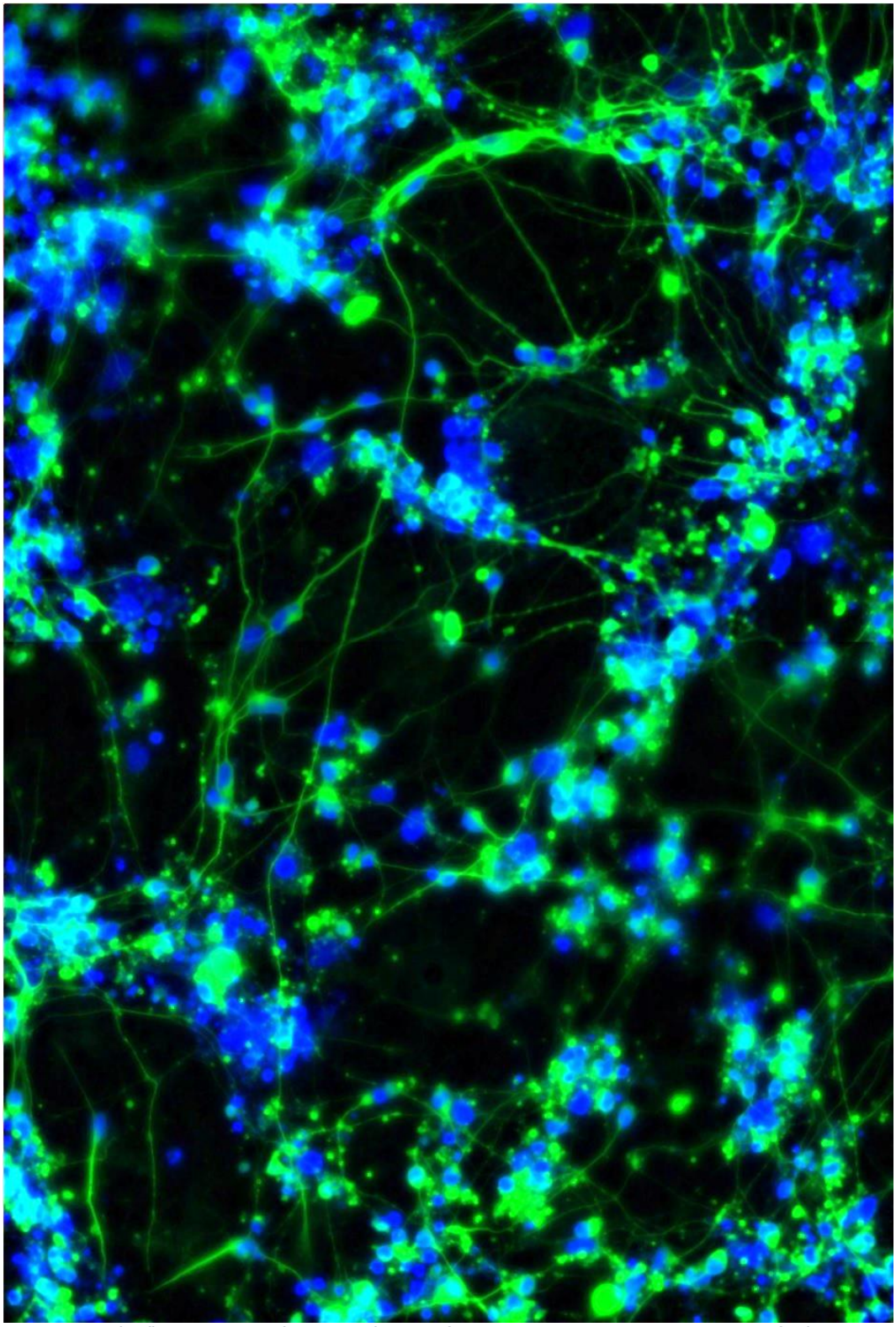

Figure 62: Composite fluorescence microscopy image of neurons grown on a 5 wt% PCL-grafted CNT containing PCL scaffold exhibiting good interconnectivity and long dendrite outgrowth.

The differences in the image quality are due to the fact that it was not possible to capture all feature in one focal plane on the electrospun scaffolds. Out of focus nuclei and dendrites are seen between in-focus features. This is a strong indication that the cells have infiltrated the nanofibrous scaffolds and form a

three dimensional network. Cells seeded onto the flat control samples are more easily imaged due to their two dimensional nature.

The use of electrospun scaffolds is particularly attractive for tissue engineering applications because of their ECM-like structure[268,407]. The results presented here show that electrospun PCL scaffolds can be used for neuronal tissue engineering purposes of iPSC-derived human neurons. Cell proliferate and differentiate to varying degrees, depending on the fibre morphology and the addition of CNTs and are able to infiltrate the scaffolds to a certain degree, forming a three-dimensional neuronal network.

7.4. Conclusion

A small scale, proof-of-concept study was carried out to investigate the cell growth performance of nanofibrous, electrospun, PCL scaffolds on iPSC-derived human neuronal cells. It was possible to investigate cell proliferation and differentiation at one time point after seven days. It was shown that all electrospun scaffolds support cell growth and a significant increase in the cell count – as compared to the original number of cells seeded onto the scaffolds – was found on every sample. The average cell density of pure PCL scaffolds made from 3 wt%, 5 wt% and 7 wt% solutions as well as the 1 wt% addition of CNTs were found to follow a diameter dependent behaviour. Larger average fibre diameters exhibited a slightly higher cell count then smaller ones. Scaffolds made with the addition of 5 wt% CNTs supported a similar amount of cells as the most efficient pure PCL scaffolds despite a ~3.1 times reduction in average fibre diameter.

The capability in supporting and maintaining cell differentiation into neurons as well as the capacity to form interconnected neuronal networks was investigated by a quantitative analysis of the dendritic network and the average dendrite length. Pure PCL scaffolds and the 1 wt% CNT containing scaffolds exhibited a simple, linear correlation in terms of dendrite density with fibre morphology. An increase in the average fibre diameter lead to an increase in the dendrite density. The 5 wt% CNT containing scaffolds significantly outperformed all electrospun samples in terms of dendrite density by a factor of ~2.2 with respect to the 7 wt% pure PCL scaffolds in spite of their smaller mean fibre diameter.

A similar trend was observed for the average dendrite lengths found in the samples. The pure PCL scaffolds as well as the 1 wt% CNT containing samples exhibited a maximum average diameter after

which no change in dendrite lengths was seen. Neurons seeded on scaffolds with the smallest mean fibre diameter showed a ~30% reduction in average dendrite length compared to the other samples. The incorporation of 5 wt% CNTs resulted in a ~30% increase in dendritic length despite the significant reduction in fibre diameter as compared to the best performing pure PCL scaffolds.

The novelty of this chapter is the demonstrations of a diameter dependency of the efficacy of electrospun PCL scaffolds in the proliferation, differentiation and network formation of iPSC-derived human neurons. The incorporation of CNTs into the scaffolds shows a substantial improvement of the scaffold cell-supporting performance at higher levels of CNT addition (5 wt%) significantly deviating from the diameter trend, whereas small additions (1 wt%) exhibit no such effect. By incorporating results from the previous chapters it can be concluded that the beneficial effect of the CNTs is not due morphological changes in the scaffold structure but rather through a change in physical properties of the scaffold as a whole. It was shown that the CNTs do not alter the electrokinetic properties of the nanofibres and that there is not direct interaction between CNTs and cells, as the CNTs are fully encapsulated by the polymer matrix. The incorporation of CNTs offer the possibility of enhanced neuronal cell growth and network formation while allowing the opportunity to maintain a smaller, more ECM-like[408] scaffold morphology.

8. Conclusion

In this thesis three major themes of investigation were pursued. The first was the study of the processing and solution conditions during electrospinning on the morphology, microstructure and mechanical properties of electrospun scaffolds and possible interactions between those properties. The second was an examination of the effect that an incorporation of carbon nanotubes had on those properties of the aforementioned scaffolds. The literature discussions in this thesis as well as the experimental work undertaken were tailored with a tissue engineering application in mind for the nanofibrous scaffolds. The last theme was an exploration of the performance of the different kinds of scaffolds, described above, as substrates for neuronal cell growth.

8.1. Understanding of the Electrospinning Process and Nanofibrous Structures

Electrospinning is a fast and facile method to create three dimensional, nanofibrous scaffolds. The nature of the technique allows for a large variety of natural and synthetic polymers to be utilized as the scaffold material. With a view to an optimized growth and differentiation of cells the use of three dimensional scaffolds holds significant benefits over regular, flat substrates[409–412]. Additionally it has been shown that nanosized features of a potential scaffold – in the range accessible by electrospinning – can interact with cells in a synergistic way[413,414]. It is hence imperative for the use of any electrospinning rig to gain an understanding of how the processing parameters effect the morphology of the nanofibrous scaffolds in order to be able to tailor and optimize that morphology.

As an initial investigation in this work the capability of an in-house built electrospinning kit to produce consistent scaffolds was examined. It was possible to consistently produce fibrous mats from both PCL and PMMA solutions. An advanced two-level central composite experimental design was employed for scaffolds made from PCL and compared to a standard one-parameter-at-a-time approach which was used for PMMA samples. The advanced experimental design was found to be significantly superior in its capability to be used to construct a mathematical model to predict scaffold morphology. Based on these two series a physical explanation was given for the impact of various processing parameters on

the morphological properties of the nanofibrous scaffolds. A change in the solution concentration and the solution feed rate during spinning had the greatest effect on the average fibre diameter and the spread of fibre diameters found in the scaffolds.

Building on the knowledge gained from the morphological investigation the effect of the mean fibre size and the internal crystallinity of PCL scaffolds on their mechanical properties was explored. By controlling the processing parameters it was possible to significantly change the tensile strengths and moduli of the scaffolds. Where previous studies showed correlations of the mechanical properties with either fibre diameter or crystallinity this study examined the interplay between those two parameters on the tensile properties. It was found that it is possible to control the two parameters independently to some degree, producing fibres with similar diameter ranges but markedly different strengths and elasticities. Additionally it was shown that one of the most widely used technique to measure the degree of crystallinity, namely DSC, produced results differing greatly from measurements taken with XRD. The difference was explained in terms of a hitherto unreported size effect that alters the obtained thermograms for PCL nanofibres at small sizes.

8.2. Multi-Walled Carbon Nanotubes as Reinforcement Material in Nanofibres

A large proportion of the work done towards the thesis has been the incorporation of CNTs into electrospun fibres and the investigation of the change in scaffold properties and morphology as a result thereof. Two different types of CNTs with different chemical functionalizations were utilized in this study. The effect of the use of a standard –OH functionalization and a matrix-tailored PCL-grafted CNT functionalization on PCL nanofibres was compared. The –OH CNTs were found have a significant effect on the average fibre size – where an increase in CNT loading lead to a decrease in mean fibre diameter – and resulted in bimodal fibre distributions. At small loading levels the –OH CNTs slightly improved the tensile strength and modulus of the scaffolds. A tailored chemical grafting of PCL onto CNTs did not alter the fibre morphology and exhibited a much greater improvement on the mechanical properties of the scaffolds. These results suggest that the surface chemistry of CNTs plays an important role in the

successful reinforcement of electrospun composites and a matrix-specific functionalization offers significant benefits in mechanical properties while not affecting the scaffold morphology.

The electrospinning of natural polymers is decidedly more difficult than synthetic polymers. Gelatin nanofibres were electrospun from gelatin/HFIP solutions. It emerged that the age of those solutions were an important and overlooked parameter that influenced the fibre morphology noticeably. Older solutions resulted in fibres with smaller diameters which could be attributed to gelatin denaturation due to the fluorinated solvent. As a further demonstration of the effectiveness of electrospun CNT composites, PCL-grafted CNTs were successfully incorporated into gelatin nanofibres for the first time. The addition of CNTs resulted in a ~2 fold increase in tensile strength and a ~3 fold increase in the elastic modulus of gelatin scaffolds. It is advantageous to use natural polymers over synthetic, biodegradable polymers as scaffolds for tissue engineering applications. However electrospinning of natural polymers such as collage, gelatin or chitin results in scaffolds with very weak mechanical properties which are difficult to handle. In this work it was shown that CNTs could be used to address these issues.

8.3. Electrospun Scaffolds for Neuronal Tissue Engineering

Based on the processing optimisation, the morphological and physical characterisation and the successful incorporation of CNTs into electrospun PCL scaffolds a pilot study was carried out in this thesis to explore the capabilities' of different types of scaffolds as substrates for neuronal tissue growth. iPSC-derived human neuronal cells were seeded onto PCL scaffolds with different average fibre diameters and different contents of incorporated PCL-grafted CNTs as well as on flat control samples. Amongst the pure PCL scaffolds a clear diameter dependency could be seen with regards to cell proliferation after seven days of growth. Scaffolds with larger average fibre diameters supported more cells than scaffolds with smaller diameters. Concurrently scaffolds with larger fibres exhibited a higher dendritic density, indicating the formation of a more developed neuronal network. The addition of CNTs had no measurable effect at small quantities as compared to fibres of a similar size. At a loading of 5 wt% however a substantial improvement was seen for the overall cell count, the network density as well as the average length of dendrites found. The scaffolds containing 5 wt% CNTs showed comparable results to the control samples which outperformed all other electrospun substrates.

9. Future Work

The avenues of research pursued in this thesis represent a small cross section of the interdisciplinary work that is being carried out in the field of tissue engineering. Due to resource and time constraints there are several suggestions for future work to be carried out in order to improve and build upon the results presented in this research.

9.1. Mechanical Testing

There is a great interest in the mechanical properties of electrospun scaffolds in the literature and it has been a focus of this work in particular as well. Accounts in the literature for whole scaffolds value drastically even when similar processing conditions and polymers are concerned. There is more robust and reproducible mechanical data available for the tensile properties of single electrospun fibres, however it is the strength and modulus of the overall scaffold that is of interest usually. The reason for the variance in the data found is due to non-standardised measuring protocols and particularly because of the simplification that is being used for tensile testing of scaffolds. The cross-sectional area of the electrospun fibre mats are taken as a solid, whereas it is known that these scaffolds exhibit very large amounts of porosity. Depending on the exact spinning set-up and the post-processing conditions as well as the measuring protocol that porosity will vary between samples and labs. A more precise method would be to obtain clear cross-sectional areas and investigate those in an SEM to measure those. A possibility for that would be focussed ion-beam microscopy. This technique would allow for representative cross-sectional measurements and a better estimation of the void space between the fibres. An attempt to acquire such data was undertaken but could not be fully carried out due to limited time and training available for the equipment [10.4].

9.2. Electric Conductivity of CNT Containing Scaffolds

The electric conductivity of CNT containing scaffolds is an important metric to judge successful incorporation of CNTs. In this study it was found that the addition of tailored CNTs into PCL and gelatin nanofibres can have a beneficial impact on the mechanical properties and cell growth behaviour of such scaffolds without affecting the surface charges on those fibres. An attempt was made to measure the

electric conductivity of CNT containing scaffolds from this work using a voltmeter and a four-point-probe. No change in the conductivity was measured however. There are several studies available on the incorporation of CNTs into electrospun PCL fibres however only Crowder et al. (2013) measured the electric conductivity using electrochemical impedance spectroscopy, where a clear increase was found through the addition of CNTs[333]. A systematic investigation into the effect of loading levels of both –OH functionalized CNTs and PCL-grafted CNTs on PCL and gelatin using electrochemical impedance spectroscopy would be greatly beneficial for a deeper understanding of the impact of the electrical conductivity on cell growth.

9.3. Gelatin Molecular Weight Reduction

It was found that the age of gelatin/HFIP solutions have a great effect on the morphology of electrospun gelatin scaffolds. It was argued that, through rheological observations, the reduction in fibre diameter with solution age must be a result of gelatin denaturation, possibly through a reduction in the average molecular weight of the gelatin. However the evidence provided in this is indicative only, as the molecular weight could not be measured directly. An experimental series using sodium dodecyl sulfate polyacrylamide gel electrophoresis (SDS-PAGE) on gelatin solutions with varying ages would provide direct measurements of the molecular weights and their changes with time of the gelatin used.

9.4. Cell Study

The neuronal cell research undertaken in this thesis represents a pilot study that shows promising effects with regards to the advantageous capabilities of CNT-containing, PCL scaffolds. A more thorough study is needed in order to obtain a complete picture of the impact of morphology and physical properties of those scaffolds on neuronal cell growth. Ideally such a study would incorporate several growth times for the cells, such as 3, 7, 14 and 28 days to see how scaffolds perform over time. It is entirely possible that CNT containing scaffolds only accelerate cell growth and differentiation rather than promote them, which could not be picked up with the data available. Moreover the iPSC-derived human neuronal cells have the ability to differentiate into either astrocytes or neurocytes. Using additional staining it would be possible to quantify the presence of astrocytes as well – as only neurocytes were considered in the work undertaken – and to examine potential differences between those two populations as a result of

differences in the scaffolds. Ultimately a comparison in the use of PCL and gelatin scaffolds would complete such a study with the work carried out in this thesis. Given the results from this thesis such an extended study would allow to reach conclusions on the impact of physical and morphological parameters of scaffolds on neuronal cell growth and would show whether PCL or gelatin are better suited for such purposes.

10. Appendix

10.1. Residual Solvent Analysis of PCL Scaffolds

FT-IR spectra of as-received, pure PCL, HFIP and an electrospun PCL scaffold made under the midpoint conditions [3.2.1.2] were collected using the protocol described in [5.2.3]. The spectra of the pure PCL and the electrospun PCL scaffold show a good agreement and no significant change (Figure 63). Upon closer inspection it becomes evident that no peaks from the HFIP are visible in the electrospun sample, indicating that there is no residual solvent in the electrospun scaffolds.

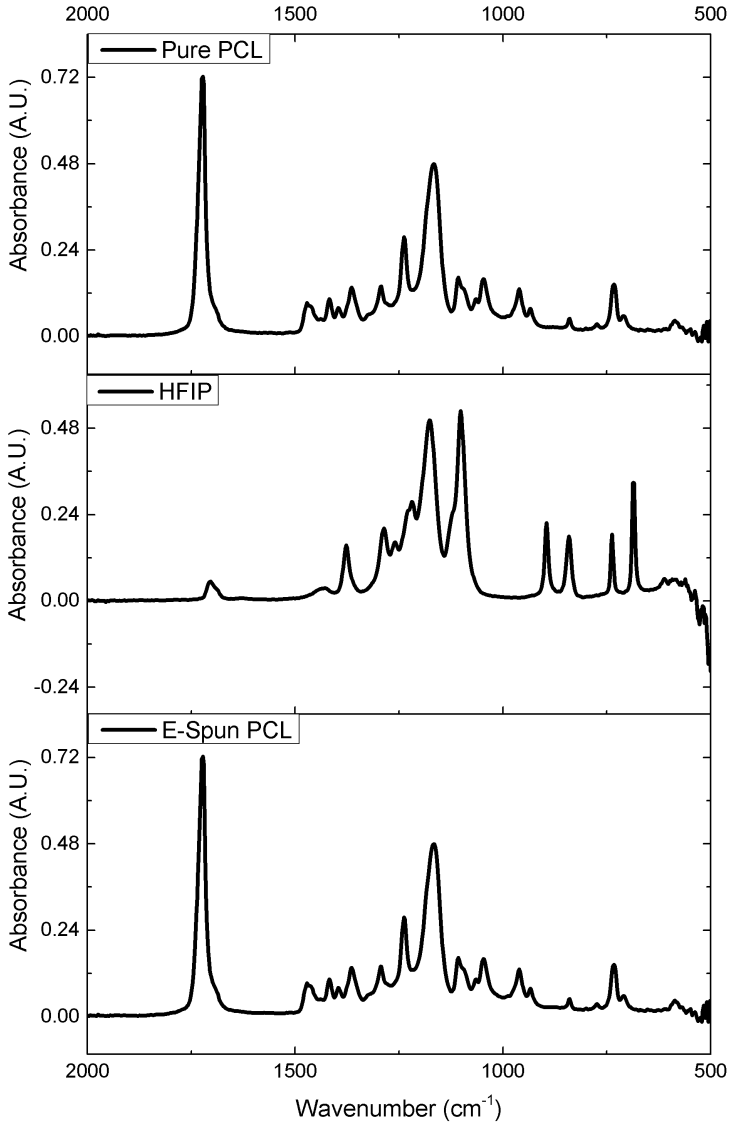

Figure 63: FT-IR spectra of pure PCL (top), HFIP (middle) and an electrospun PCL scaffold (bottom).

10.2. Electrospinning of Type 1 Collagen and Degradation Analysis

Acid soluble, lyophilized collagen type I from calf skin was purchased from Sigma-Aldrich UK. The collagen was dissolved in 1,1,1,3,3,3 hexafluoro-2-propanol (HFIP), purchased from Sigma-Aldrich UK. The electrospinning was carried out using the protocol described in [2.1]. An overview of the processing parameters are shown in Table 19. Spinning time was 5 minutes for all samples.

Sample	Voltage (kV)	Distance (cm)	Flow Rate (mL/h)	Collagen Content (wt%)
1	20	15	0.55	3
2	20	15	0.55	4
3	20	15	0.55	5

Table 19: Overview of processing parameters for the electrospinning of collagen nanofibres.

Fibres were imaged in an SEM using the protocol described in [2.3]. All processing conditions produced smooth, nanofibrous scaffolds (Figure 64). An increase in collagen solution concentration results in an increase in beading of the fibres.

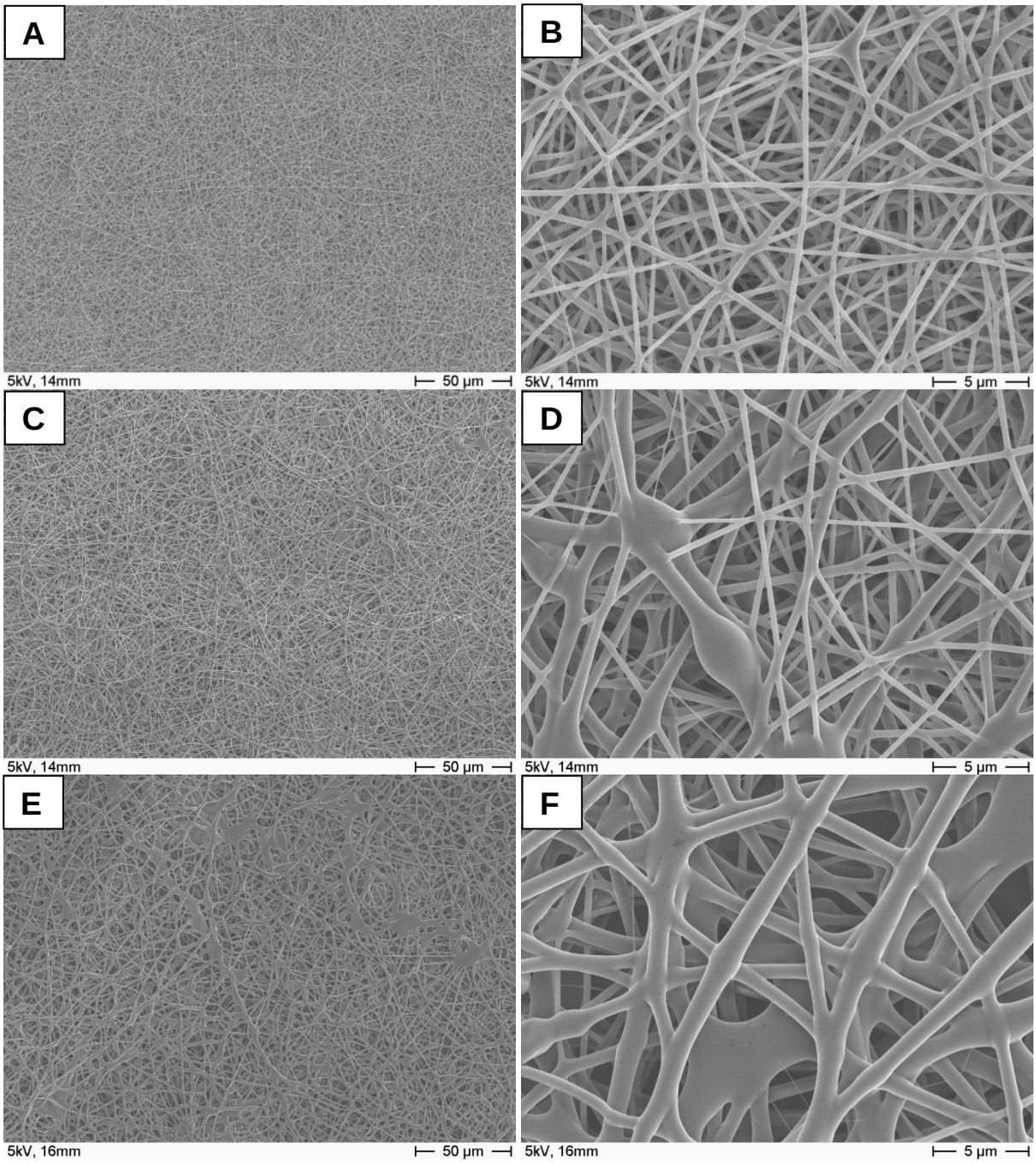

Figure 64: Low and high magnification SEM images of 3 wt% collagen (A and B respectively), 4 wt% collagen (C and D respectively) and 5 wt% collagen (E and F respectively). Scale bars are 50 µm for the left column and 5 µm for the right column of images.

Diameter distribution were calculated using the protocol in [2.4]. An increase in collagen solution concentration results in an increase in average fibre diameter as previously observed with PCL [3.3.1], PMMA [3.3.3] and gelatin [6.3] (Figure 65).

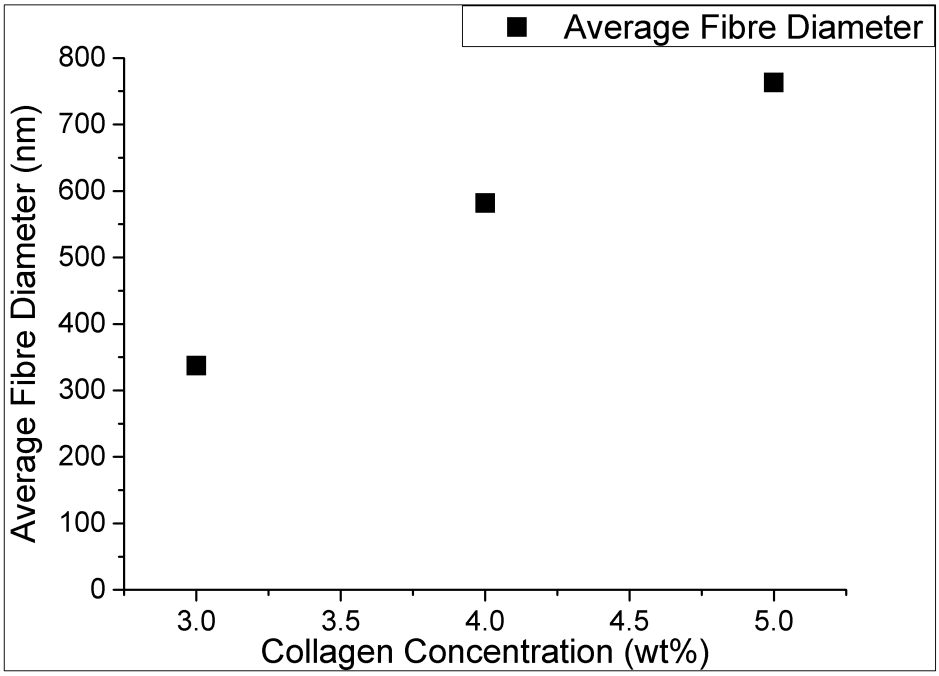

Figure 65. Change in average fibre diameter of electrospun collagen scaffolds as a function of collagen solution concentration.

While the electrospinning of one day old solutions produced smooth fibrous scaffolds it was found that with an increase in solution age the spinnability decreased significantly. It is found that seven day old solutions do not produce homogenous fibrous scaffolds (Figure 66).

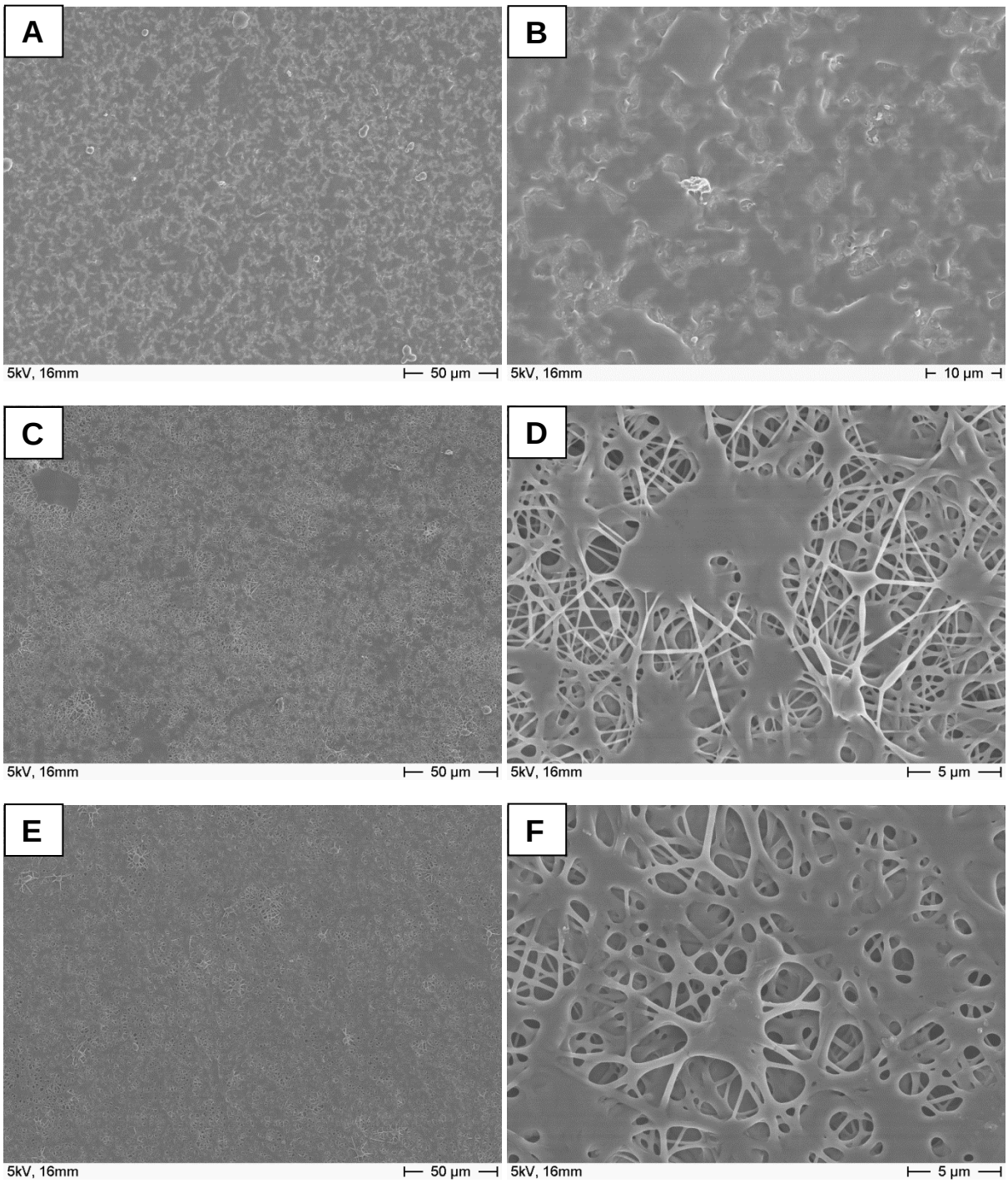

Figure 66: Low and high magnification SEM images of seven day old electrospun 3 wt% collagen (A and B respectively), 4 wt% collagen (C and D respectively) and 5wt% collagen (E and F respectively) solutions. Scale bars are 50 µm for the left column and 5 µm for the right column of images.

At collagen solution concentrations of 3 wt% no fibre were detected and it is suggested that the samples were electrosprayed rather than electrospun. At concentrations of 4 wt% and 5 wt% a mix of fibres and patches of collagen can be seen. These results suggest an interaction of the fluorinated solvent (HFIP) with the collagen. Due to the high price of collagen type I and limited resources available for the project

the focus was shifted from collagen to gelatin in this thesis in order to be able to produce more samples to better investigate these findings.

10.3. Residual Solvent Analysis of Collagen Scaffolds

FTIR spectra of as-received, pure collagen powder, HFIP and electrospun collagen scaffolds were taken using the protocol described in [5.2.3]. The spectrum for the electrospun collagen is markedly different than that for pure collagen (Figure 67).

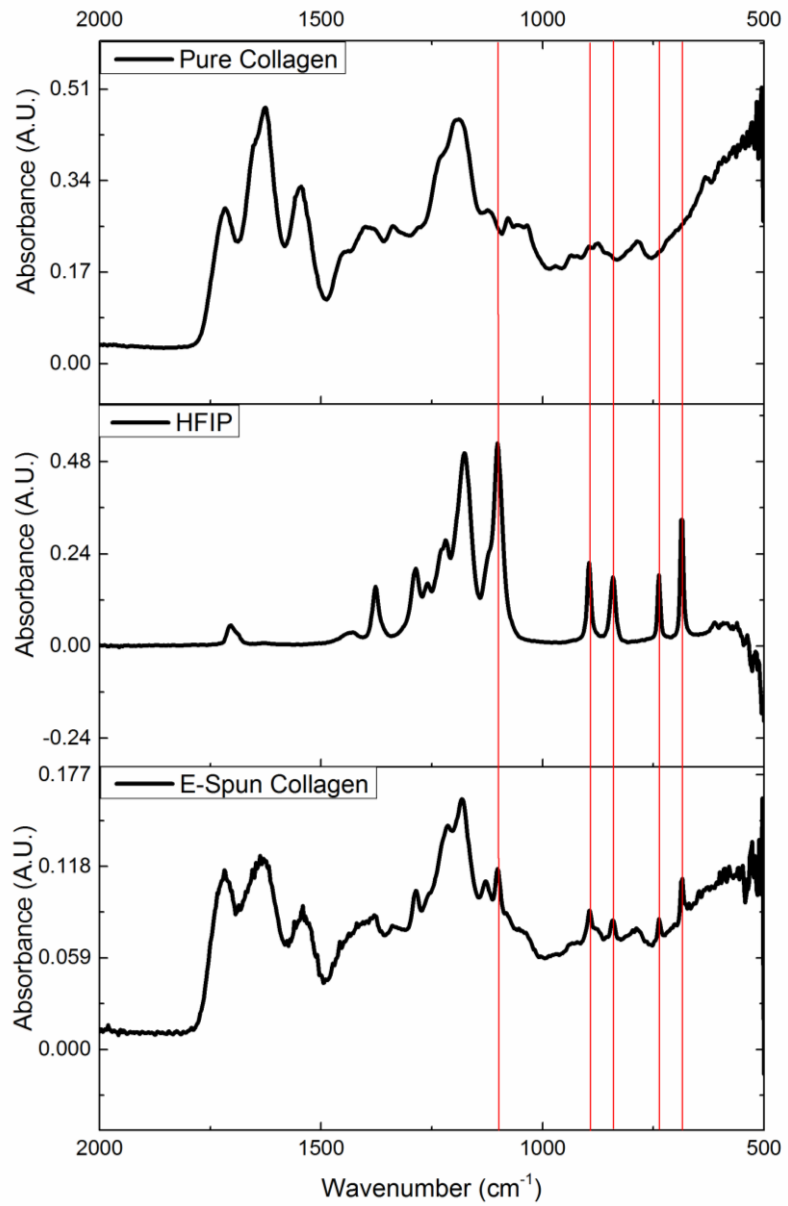

Figure 67: Comparison of FT-IR spectra for pure collagen powder (top), HFIP (middle) and an electrospun collagen scaffold (bottom). Five prominent peaks found in HFIP are marked with red lines.

Additionally the peaks at 1100 cm^{-1}, 895 cm^{-1}, 842 cm^{-1} 737 cm^{-1} and 685 cm^{-1} found in the spectrum for HFIP are visible in the electrospun collagen scaffold and absent in the pure collagen spectrum. In

contrast to the electrospun PCL scaffolds which exhibited none of the HFIP peaks these results strongly suggest that there is residual solvent present in the collagen scaffolds. This supports the proposed theory of time-dependent denaturation of collagen and gelatin due to the use of fluorinated solvents [6.3].

10.4. SEM Imaging of PCL Scaffold Cross-Section

Cross-sections of electrospun PCL scaffolds produced using the midpoint processing parameters described in [3.2.1.2] were made using a Zeiss NVision 40 FIB-SEM. Images were taken by Ms. Nataliia Stepina. Scaffolds were coated in carbon prior to the focussed ion-beam milling using the carbon source in the equipment. A small line was cut out first and then expanded after which the samples were tilted and imaged at an angle (Figure 68). It is possible with that technique to create and image a cross-section of electrospun scaffolds which could be used to analyse the void space between the fibres and to improve mechanical testing. Due to limited access to the equipment it was not possible to expand on this technique and optimize the milling and imaging conditions for the work carried out in this thesis.

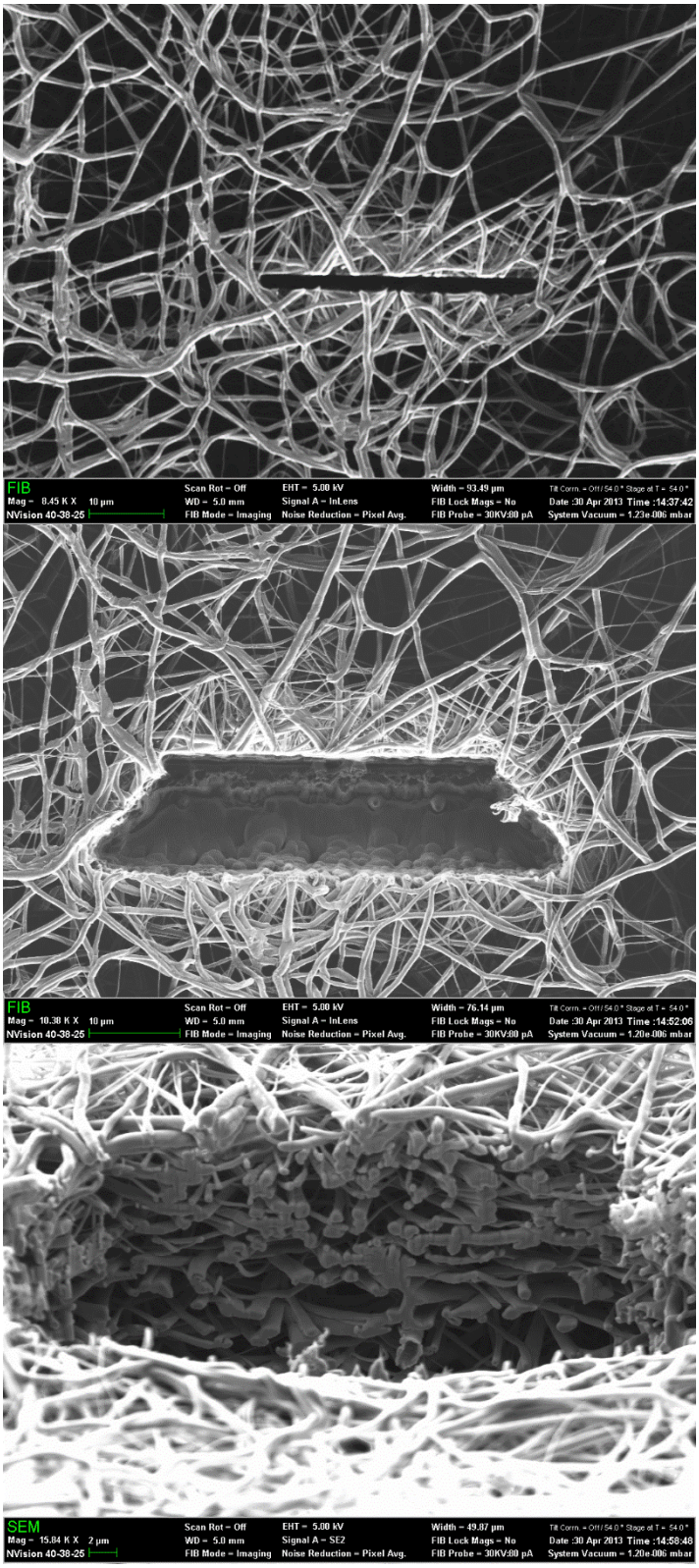

Figure 68: SEM images of the process of creating a cross-section in a FIB-SEM. Top: First cut perpendicular to the surface. Middle: Expansion of the area in front of the cut. Bottom: Tilted image of the created cross-section.

11. Bibliography

1. Miles, D. Modelling the impact of demographic change upon the economy. *Econ. J.* **109,** 1–36 (1999).
2. Oeppen, J. & Vaupel, J. W. Demography. Broken limits to life expectancy. *Science* **296,** 1029–31 (2002).
3. Madsen, J., Serup-Hansen, N. & Kristiansen, I. S. Future health care costs--do health care costs during the last year of life matter? *Health Policy* **62,** 161–72 (2002).
4. Vellas, B. J., Albarede, J. L. & Garry, P. J. Diseases and aging: patterns of morbidity with age; relationship between aging and age-associated diseases. *Am. J. Clin. Nutr.* **55,** 1225S–1230S (1992).
5. Abbott, L. F. & Nelson, S. B. Synaptic plasticity: taming the beast. *Nat. Neurosci.* **3 Suppl,** 1178–83 (2000).
6. Jakel, R. J., Schneider, B. L. & Svendsen, C. N. Using human neural stem cells to model neurological disease. *Nat. Rev. Genet.* **5,** 136–44 (2004).
7. American Liver Foundation. Vital Statistics of the United States. **II,** (1988).
8. George, J. H. S. Engineering of Fibrous Scaffolds for use in Regenerative Medicine Department of Materials. (Imperial College London, 2004).
9. Mason, C. & Dunnill, P. A brief definition of regenerative medicine. *Regen. Med.* **3,** 1–6 (2008).
10. Ikada, Y. Challenges in tissue engineering. *J. R. Soc. Interface* **3,** 589–601 (2006).
11. Greenwood, H. L. H. L. <sup></sup. *et al.* Regenerative medicine: new opportunities for developing countries. *Int. J. Biotechnol.* **8,** 60–77 (2006).
12. Langer, R. & Vacanti, J. Tissue engineering. *Science (80-.).* **260,** 920–926 (1993).
13. Zhang, J. *et al.* Engineering of vascular grafts with genetically modified bone marrow mesenchymal stem cells on poly (propylene carbonate) graft. *Artif. Organs* **30,** 898–905 (2006).
14. Sakai, S., Yamada, Y., Yamaguchi, T. & Kawakami, K. Prospective use of electrospun ultra-fine silicate fibers for bone tissue engineering. *Biotechnol. J.* **1,** 958–62 (2006).
15. Dalton, P. D., Lleixà Calvet, J., Mourran, A., Klee, D. & Möller, M. Melt electrospinning of poly-(ethylene glycol-block-epsilon-caprolactone). *Biotechnol. J.* **1,** 998–1006 (2006).
16. Teo, W.-E., He, W. & Ramakrishna, S. Electrospun scaffold tailored for tissue-specific extracellular matrix. *Biotechnol. J.* **1,** 918–29 (2006).
17. Sui, G. *et al.* Poly- L -lactic acid / hydroxyapatite hybrid membrane for bone tissue regeneration. *Energy* (2007). doi:10.1002/jbm.a
18. Li, C., Vepari, C., Jin, H.-J., Kim, H. J. & Kaplan, D. L. Electrospun silk-BMP-2 scaffolds for bone tissue engineering. *Biomaterials* **27,** 3115–24 (2006).
19. Matthews, J. A., Wnek, G. E., Simpson, D. G. & Bowlin, G. L. Electrospinning of collagen nanofibers. *Biomacromolecules* **3,** 232–238 (2002).
20. Nie, H. *et al.* Effects of Chain Conformation and Entanglement on the Electrospinning of Pure Alginate. *Biomacromolecules* **9,** 1362–1365 (2008).
21. Schneider, O. D. *et al.* Cotton Wool-Like Nanocomposite Biomaterials Prepared by Electrospinning : In vitro Bioactivity and Osteogenic Differentiation of Human Mesenchymal Stem Cells. *J. Biomed. Mater. Res.* 350–362 (2007). doi:10.1002/jbmb
22. Matsuda, A., Kagata, G., Kino, R. & Tanaka, J. Preparation of Chitosan Nanofiber Tube by

Electrospinning. *J. Nanosci. Nanotechnol.* **7,** 852–855 (2007).

23. Huang, L., Nagapudi, K., PApkarian, R. & Chaikof, E. L. Engineered collagenPEO nanofibers and fabrics. *J. Biomater. Sci. Polym. Ed.* **12,** 979–993 (2001).
24. Taepaiboon, P., Rungsardthong, U. & Supaphol, P. Vitamin-loaded electrospun cellulose acetate nanofiber mats as transdermal and dermal therapeutic agents of vitamin A acid and vitamin E. *Eur. J. Pharm. Biopharm.* **67,** 387–97 (2007).
25. Telemeco, T. a *et al.* Regulation of cellular infiltration into tissue engineering scaffolds composed of submicron diameter fibrils produced by electrospinning. *Acta Biomater.* **1,** 377–85 (2005).
26. McManus, M. C., Boland, E. D., Simpson, D. G., Barnes, C. P. & Bowlin, G. L. Electrospun fibrinogen: feasibility as a tissue engineering scaffold in a rat cell culture model. *J. Biomed. Mater. Res. A* **81,** 299–309 (2007).
27. Yang, S., Leong, K. F., Du, Z. & Chua, C. K. The design of scaffolds for use in tissue engineering. Part I. Traditional factors. *Tissue Eng.* **7,** 679–89 (2001).
28. Perin, L., Da Sacco, S. & De Filippo, R. E. Regenerative medicine of the kidney. *Adv. Drug Deliv. Rev.* **63,** 379–87 (2011).
29. MacDonald, R. a, Laurenzi, B. F., Viswanathan, G., Ajayan, P. M. & Stegemann, J. P. Collagen-carbon nanotube composite materials as scaffolds in tissue engineering. *J. Biomed. Mater. Res. A* **74,** 489–96 (2005).
30. Kumar, V. a., Brewster, L. P., Caves, J. M. & Chaikof, E. L. Tissue Engineering of Blood Vessels: Functional Requirements, Progress, and Future Challenges. *Cardiovasc. Eng. Technol.* **2,** 137–148 (2011).
31. Harvard Bioscience, Inc. - Photo Release -- Harvard Bioscience's Bioreactor Grows a Synthetic Tissue-Engineered Trachea Used in World's First Successful Human Transplantation. Available at: http://www.harvardbioscience.com/releasedetail.cfm?ReleaseID=589734. (Accessed: 29th September 2011)
32. Bhat, Z. F. & Fayaz, H. Prospectus of cultured meat—advancing meat alternatives. *J. Food Sci. Technol.* **48,** 125–140 (2010).
33. Tuomisto, H. L. & de Mattos, M. J. T. Environmental impacts of cultured meat production. *Environ. Sci. Technol.* **45,** 6117–23 (2011).
34. Lab-grown meat could ease food shortage - opinion - 09 July 2008 - New Scientist. Available at: http://www.newscientist.com/article/mg19926635.600-labgrown-meat-could-ease-food-shortage.html. (Accessed: 27th September 2011)
35. Wallner, E. I., Yang, Q., Peterson, D. R., Wada, J. & Kanwar, Y. S. Relevance of extracellular matrix, its receptors, and cell adhesion molecules in mammalian nephrogenesis. *Am. J. Physiol.* **275,** F467-77 (1998).
36. Scott, J. E. Extracellular matrix, supramolecular organisation and shape. *J. Anat.* **187 (Pt 2,** 259–69 (1995).
37. Aumailley, M. & Gayraud, B. Structure and biological activity of the extracellular matrix. *J. Mol. Med.* **76,** 253–265 (1998).
38. Zagris, N. Extracellular matrix in development of the early embryo. *Micron* **32,** 427–38 (2001).
39. Stevens, M. M. & George, J. H. S. Exploring and engineering the cell surface interface. *Science* **310,** 1135–8 (2005).
40. Anderson, D. G., Burdick, J. a & Langer, R. Materials science. Smart biomaterials. *Science* **305,** 1923–4 (2004).

41. Lutolf, M. P. & Hubbell, J. a. Synthetic biomaterials as instructive extracellular microenvironments for morphogenesis in tissue engineering. *Nat. Biotechnol.* **23,** 47–55 (2005).

42. Hench, L. L. & Polak, J. M. Third-generation biomedical materials. *Science* **295,** 1014–7 (2002).

43. Zhang, S. Fabrication of novel biomaterials through molecular self-assembly. *Nat. Biotechnol.* **21,** 1171–8 (2003).

44. Shin, H., Jo, S. & Mikos, A. G. Biomimetic materials for tissue engineering. *Biomaterials* **24,** 4353–4364 (2003).

45. Rosso, F. *et al.* Smart materials as scaffolds for tissue engineering. *J. Cell. Physiol.* **203,** 465–70 (2005).

46. Ratner, B. D. & Bryant, S. J. Biomaterials: where we have been and where we are going. *Annu. Rev. Biomed. Eng.* **6,** 41–75 (2004).

47. Adams, J. C. & Watt, F. M. Regulation of development and differentiation by the extracellular matrix. *Development* **117,** 1183–98 (1993).

48. Mecham, R. P. *The Extracellular Matrix: An Overview*. (Springer, 2011).

49. Hallmann, A. Extracellular matrix and sex-inducing pheromone in Volvox. *Int. Rev. Cytol.* **227,** 131–182 (2003).

50. Curtis, A. & Wilkinson, C. New depths in cell behaviour: reactions of cells to nanotopography. *Biochem. Soc. Symp.* **65,** 15–26 (1999).

51. Yim, E. K. F., Darling, E. M., Kulangara, K., Guilak, F. & Leong, K. W. Nanotopography-induced changes in focal adhesions, cytoskeletal organization, and mechanical properties of human mesenchymal stem cells. *Biomaterials* **31,** 1299–306 (2010).

52. Webster, T. J., Schadler, L. S., Siegel, R. W. & Bizios, R. Mechanisms of enhanced osteoblast adhesion on nanophase alumina involve vitronectin. *Tissue Eng.* **7,** 291–301 (2001).

53. Zinger, O. *et al.* Differential regulation of osteoblasts by substrate microstructural features. *Biomaterials* **26,** 1837–47 (2005).

54. Andersson, A.-S. *et al.* Nanoscale features influence epithelial cell morphology and cytokine production. *Biomaterials* **24,** 3427–3436 (2003).

55. Price, R. L., Ellison, K., Haberstroh, K. M. & Webster, T. J. Nanometer surface roughness increases select osteoblast adhesion on carbon nanofiber compacts. *J. Biomed. Mater. Res. A* **70,** 129–38 (2004).

56. Curtis, a S. G. *et al.* Cells react to nanoscale order and symmetry in their surroundings. *IEEE Trans. Nanobioscience* **3,** 61–5 (2004).

57. Teixeira, A. I., Nealey, P. F. & Murphy, C. J. Responses of human keratocytes to micro- and nanostructured substrates. *J. Biomed. Mater. Res. A* **71,** 369–76 (2004).

58. Frenot, A. & Chronakis, I. S. Polymer nanofibers assembled by electrospinning. *Curr. Opin. Colloid \& Interface Sci.* **8,** 64–75 (2003).

59. Morton, W. J. Method of Dispersing Fluid. 4 (1902).

60. Lukáš, D. *et al.* Physical principles of electrospinning (Electrospinning as a nano-scale technology of the twenty-first century). *Text. Prog.* **41,** 59–140 (2009).

61. Gilbert, W. *De magnete, magneticisque corporibus, et de magno magnete tellure*. (Petrus Short, 1600).

62. Nollet, J. A. *Recherches sur les causes particulieres des phenomenes electriques (Google eBook)*. (1754).

63. Norris, I. Electrostatic fabrication of ultrafine conducting fibers: polyaniline/polyethylene oxide

blends. *Synth. Met.* **114,** 109–114 (2000).

64. Bhardwaj, N. & Kundu, S. C. Electrospinning: a fascinating fiber fabrication technique. *Biotechnol. Adv.* **28,** 325–47 (2010).

65. Tan, S.-H., Inai, R., Kotaki, M. & Ramakrishna, S. Systematic parameter study for ultra-fine fiber fabrication via electrospinning process. *Polymer (Guildf).* **46,** 6128–6134 (2005).

66. Kwon, I. K., Kidoaki, S. & Matsuda, T. Electrospun nano- to microfiber fabrics made of biodegradable copolyesters: structural characteristics, mechanical properties and cell adhesion potential. *Biomaterials* **26,** 3929–39 (2005).

67. Publishing, S. *Jmp 9 Design of Experiments Guide*. (SAS Publishing, 2010).

68. Tong, H. W. & Wang, M. An investigation into the influence of electrospinning parameters on the diameter and alignment of poly (hydroxybutyrate-co-hydroxyvalerate) fibers. *J. Appl. Polym. Sci.* (2011). doi:10.1002/app

69. Reneker, D. H. & Yarin, A. L. Electrospinning jets and polymer nanofibers. *Polymer (Guildf).* **49,** 2387–2425 (2008).

70. electrospinning_diagram. Available at: http://upload.wikimedia.org/wikipedia/commons/c/ca/Electrospinning_Diagram.jpg. (Accessed: 17th April 2011)

71. Ramakrishna, S. *An introduction to electrospinning and nanofibers*. (World Scientific, 2005).

72. Feng, J. Stretching of a straight electrically charged viscoelastic jet. *J. Nonnewton. Fluid Mech.* **116,** 55–70 (2003).

73. Spivak, A., Dzenis, Y. & Reneker, D. H. A model of steady state jet in the electrospinning process. *Mech. Res. Commun.* **27,** 37–42 (2000).

74. Yu, J., Fridrikh, S. & Rutledge, G. The role of elasticity in the formation of electrospun fibers. *Polymer (Guildf).* **47,** 4789–4797 (2006).

75. He, J. & Liu, H. Variational approach to nonlinear problems and a review on mathematical model of electrospinning. *Nonlinear Anal.* **63,** e919–e929 (2005).

76. Reneker, D. H., Yarin, A. L., Fong, H. & Koombhongse, S. Bending instability of electrically charged liquid jets of polymer solutions in electrospinning. *J. Appl. Phys.* **87,** 4531 (2000).

77. Yao, J., Bastiaansen, C. & Peijs, T. High Strength and High Modulus Electrospun Nanofibers. *Fibers* **2,** 158–186 (2014).

78. The Electrospinning Company. Available at: http://www.electrospinning.co.uk/.

79. Kumbar, S. G., James, R., Nukavarapu, S. P. & Laurencin, C. T. Electrospun nanofiber scaffolds: engineering soft tissues. *Biomed. Mater.* **3,** 34002 (2008).

80. Ramakrishna, S. *et al.* Electrospun nanofibers: solving global issues. *Mater. Today* **9,** 40–50 (2006).

81. Holzwarth, J. M. & Ma, P. X. 3D nanofibrous scaffolds for tissue engineering. *J. Mater. Chem.* **21,** 10243 (2011).

82. Huber, A., Pickett, A. & Shakesheff, K. M. Reconstruction of spatially orientated myotubes in vitro using electrospun, parallel microfibre arrays. *Eur. Cell. Mater.* **14,** 56–63 (2007).

83. Murugan, R. & Ramakrishna, S. Design strategies of tissue engineering scaffolds with controlled fiber orientation. *Tissue Eng.* **13,** 1845–66 (2007).

84. Ayres, C. E. *et al.* Incremental changes in anisotropy induce incremental changes in the material properties of electrospun scaffolds. *Acta Biomater.* **3,** 651–61 (2007).

85. Thomas, V. *et al.* Mechano-morphological studies of aligned nanofibrous scaffolds of

polycaprolactone fabricated by electrospinning. *J. Biomater. Sci. Polym. Ed.* **17,** 969–84 (2006).

86. Li, W.-J., Mauck, R. L., Cooper, J. a, Yuan, X. & Tuan, R. S. Engineering controllable anisotropy in electrospun biodegradable nanofibrous scaffolds for musculoskeletal tissue engineering. *J. Biomech.* **40,** 1686–93 (2007).

87. Zhong, S. *et al.* An aligned nanofibrous collagen scaffold by electrospinning and its effects on in vitro fibroblast culture. *J. Biomed. Mater. Res. Part A* (2006). doi:10.1002/jbm.a

88. Lala, N. L. *et al.* Fabrication of nanofibers with antimicrobial functionality used as filters: protection against bacterial contaminants. *Biotechnol. Bioeng.* **97,** 1357–65 (2007).

89. Wang, X. *et al.* Electrostatic Assembly of Conjugated Polymer Thin Layers on Electrospun Nanofibrous Membranes for Biosensors. *Nano Lett.* **4,** 331–334 (2004).

90. Jianrong, C., Yuqing, M., Nongyue, H., Xiaohua, W. & Sijiao, L. Nanotechnology and biosensors. *Biotechnol. Adv.* **22,** 505–18 (2004).

91. Ye, H., Cui, Z. F., Ellis, M. J., Macedo, H. & Mantalaris, A. *Comprehensive Membrane Science and Engineering*. (Elsevier, 2010). doi:10.1016/B978-0-08-093250-7.00014-1

92. Kattamuri, N. *et al.* Development and surface characterization of positively charged filters. *J. Mater. Sci.* **40,** 4531–4539 (2005).

93. Ahn, Y. *et al.* Development of high efficiency nanofilters made of nanofibers. *Curr. Appl. Phys.* **6,** 1030–1035 (2006).

94. Burger, C., Hsiao, B. S. & Chu, B. Nanofibrous Materials and Their Applications. *Annu. Rev. Mater. Res.* **36,** 333–368 (2006).

95. Jeong, E. H., Yang, J. & Youk, J. H. Preparation of polyurethane cationomer nanofiber mats for use in antimicrobial nanofilter applications. *Mater. Lett.* **61,** 3991–3994 (2007).

96. Ma, Z. & Ramakrishna, S. Electrospun regenerated cellulose nanofiber affinity membrane functionalized with protein A/G for IgG purification. *J. Memb. Sci.* **319,** 23–28 (2008).

97. Kim, B.-H., Yang, K. S., Woo, H.-G. & Oshida, K. Supercapacitor performance of porous carbon nanofiber composites prepared by electrospinning polymethylhydrosiloxane (PMHS)/polyacrylonitrile (PAN) blend solutions. *Synth. Met.* **161,** 1211–1216 (2011).

98. Mu, J. *et al.* Tin oxide (SnO2) nanoparticles/electrospun carbon nanofibers (CNFs) heterostructures: controlled fabrication and high capacitive behavior. *J. Colloid Interface Sci.* **356,** 706–12 (2011).

99. Laforgue, A. All-textile flexible supercapacitors using electrospun poly(3,4-ethylenedioxythiophene) nanofibers. *J. Power Sources* **196,** 559–564 (2011).

100. Laforgue, A. & Robitaille, L. Fabrication of Highly Conductive PEDOT nanofibers. in *MRS 2009 Fall meeting* (2009).

101. Wee, G., Soh, H. Z., Cheah, Y. L., Mhaisalkar, S. G. & Srinivasan, M. Synthesis and electrochemical properties of electrospun V2O5 nanofibers as supercapacitor electrodes. *J. Mater. Chem.* **20,** 6720 (2010).

102. Choi, S. W., Jo, S. M., Lee, W. S. & Kim, Y.-R. An Electrospun Poly(vinylidene fluoride) Nanofibrous Membrane and Its Battery Applications. *Adv. Mater.* **15,** 2027–2032 (2003).

103. Teo, W.-E., Inai, R. & Ramakrishna, S. Technological advances in electrospinning of nanofibers. *Sci. Technol. Adv. Mater.* **12,** 13002 (2011).

104. Zhang, D. & Chang, J. Electrospinning of three-dimensional nanofibrous tubes with controllable architectures. *Nano Lett.* **8,** 3283–7 (2008).

105. Dabirian, F., Hosseini, Y. & Ravandi, S. a. H. Manipulation of the electric field of electrospinning system to produce polyacrylonitrile nanofiber yarn. *J. Text. Inst.* **98,** 237–241 (2007).

106. Smit, E., Buttner, U. & Sanderson, R. Continuous yarns from electrospun fibers. *Polymer (Guildf).* **46,** 2419–2423 (2005).

107. Yao, C., Li, X. & Song, T. Preparation and characterization of zein and zein/poly-L-lactide nanofiber yarns. *J. Appl. Polym. Sci.* **114,** 2079–2086 (2009).

108. Wang, X. *et al.* Continuous polymer nanofiber yarns prepared by self-bundling electrospinning method. *Polymer (Guildf).* **49,** 2755–2761 (2008).

109. Khil, M.-S., Bhattarai, S. R., Kim, H.-Y., Kim, S.-Z. & Lee, K.-H. Novel fabricated matrix via electrospinning for tissue engineering. *J. Biomed. Mater. Res. B. Appl. Biomater.* **72,** 117–24 (2005).

110. Li, X. *et al.* Conjugate electrospinning of continuous nanofiber yarn of poly(L-lactide)/nanotricalcium phosphate nanocomposite. *J. Appl. Polym. Sci.* **107,** 3756–3764 (2008).

111. Teo, W.-E., Gopal, R., Ramaseshan, R., Fujihara, K. & Ramakrishna, S. A dynamic liquid support system for continuous electrospun yarn fabrication. *Polymer (Guildf).* **48,** 3400–3405 (2007).

112. Pan, H., Li, L., Hu, L. & Cui, X. Continuous aligned polymer fibers produced by a modified electrospinning method. *Polymer (Guildf).* **47,** 4901–4904 (2006).

113. Li, D., Wang, Y. & Xia, Y. Electrospinning of Polymeric and Ceramic Nanofibers as Uniaxially Aligned Arrays. *Nano Lett.* **3,** 1167–1171 (2003).

114. Li, D. & Xia, Y. Direct Fabrication of Composite and Ceramic Hollow Nanofibers by Electrospinning. *Nano* (2004).

115. Ding, B. Fabrication of blend biodegradable nanofibrous nonwoven mats via multi-jet electrospinning. *Polymer (Guildf).* **45,** 1895–1902 (2004).

116. Yun, J., Im, J. S., Lee, Y.-S. & Kim, H.-I. Electro-responsive transdermal drug delivery behavior of PVA/PAA/MWCNT nanofibers. *Eur. Polym. J.* **47,** 1893–1902 (2011).

117. Zong, X. *et al.* Structure and process relationship of electrospun bioabsorbable nanofiber membranes. *Polymer (Guildf).* **43,** 4403–4412 (2002).

118. Kim, K. *et al.* Control of degradation rate and hydrophilicity in electrospun non-woven poly(d,l-lactide) nanofiber scaffolds for biomedical applications. *Biomaterials* **24,** 4977–4985 (2003).

119. Hellmann, C. *et al.* High Precision Deposition Electrospinning of nanofibers and nanofiber nonwovens. *Polymer (Guildf).* **50,** 1197–1205 (2009).

120. Guilak, F. *et al.* Control of stem cell fate by physical interactions with the extracellular matrix. *Cell Stem Cell* **5,** 17–26 (2009).

121. S.F., Y. Study on biomimetic artificial bone. (Tsinghua University, China, 1999).

122. Black, J. *Handbook of biomaterial properties*. (Springer, 1998).

123. Feng, W., Wu, Z., Li, Y., Feng, Y. & Yuan, X. The fabrication and electrochemical properties of electrospun nanofibers of a multiwalled carbon nanotube grafted by chitosan. *Nanotechnology* **19,** 105707 (2008).

124. Zhang, Y., Ouyang, H., Lim, C. T., Ramakrishna, S. & Huang, Z.-M. Electrospinning of gelatin fibers and gelatin/PCL composite fibrous scaffolds. *J. Biomed. Mater. Res. B. Appl. Biomater.* **72,** 156–65 (2005).

125. Lu, P. & Hsieh, Y.-L. Multiwalled carbon nanotube (MWCNT) reinforced cellulose fibers by electrospinning. *ACS Appl. Mater. Interfaces* **2,** 2413–20 (2010).

126. Miyauchi, M. *et al.* Conductive cable fibers with insulating surface prepared by coaxial electrospinning of multiwalled nanotubes and cellulose. *Biomacromolecules* **11,** 2440–5 (2010).

127. Ayutsede, J. *et al.* Carbon nanotube reinforced Bombyx mori silk nanofibers by the electrospinning process. *Biomacromolecules* **7,** 208–214 (2006).

128. Zhou, J., Cao, C., Ma, X. & Lin, J. Electrospinning of silk fibroin and collagen for vascular tissue engineering. *Int. J. Biol. Macromol.* **47,** 514–9 (2010).

129. Kang, M., Chen, P. & Jin, H. Preparation of multiwalled carbon nanotubes incorporated silk fibroin nanofibers by electrospinning. *Curr. Appl. Phys.* **9,** S95–S97 (2009).

130. Zeugolis, D. I. *et al.* Electro-spinning of pure collagen nano-fibres - just an expensive way to make gelatin? *Biomaterials* **29,** 2293–305 (2008).

131. Onlinefirst, C. P., Road, R. N. & Province, S. Fabrication and Characterization of Electrospun PLGA/MWNTs/ Hydroxyapatite Biocomposite Scaffolds for Bone Tissue Engineering. *J. Bioact. Compat. Polym.* **25,** 241–259 (2010).

132. Zhang, H. & Chen, Z. Fabrication and Characterization of Electrospun PLGA/MWNTs/ Hydroxyapatite Biocomposite Scaffolds for Bone Tissue Engineering. *J. Bioact. Compat. Polym.* **25,** 241–259 (2010).

133. Zhang, H. *et al.* Biomimetic mineralization of electrospun poly(lactic-co-glycolic acid)/multi-walled carbon nanotubes composite scaffolds in vitro. *Mater. Lett.* **63,** 2313–2316 (2009).

134. Zhang, H. Electrospun poly (lactic-co-glycolic acid)/ multiwalled carbon nanotubes composite scaffolds for guided bone tissue regeneration. *J. Bioact. Compat. Polym.* **26,** 347–362 (2011).

135. Qi, R. *et al.* Electrospun poly(lactic-co-glycolic acid)/halloysite nanotube composite nanofibers for drug encapsulation and sustained release. *J. Mater. Chem.* **20,** 10622 (2010).

136. Meng, Z. X., Zheng, W., Li, L. & Zheng, Y. F. Fabrication and characterization of three-dimensional nanofiber membrance of PCL-MWCNTs by electrospinning. *Mater. Sci. Eng. C* **30,** 1014–1021 (2010).

137. Meng, Z. X., Zheng, W., Li, L. & Zheng, Y. F. Fabrication and characterization of three-dimensional nanofiber membrance of PCL–MWCNTs by electrospinning. *Mater. Sci. Eng. C* **30,** 1014–1021 (2010).

138. Puppi, D. *et al.* Development of electrospun three-arm star poly(ε-caprolactone) meshes for tissue engineering applications. *Macromolecular bioscience* **10,** 887–97 (2010).

139. Saeed, K., Park, S., Lee, H., Baek, J. & Huh, W. Preparation of electrospun nanofibers of carbon nanotube/polycaprolactone nanocomposite. *Polymer (Guildf).* **47,** 8019–8025 (2006).

140. Deng, X. L. *et al.* Electrospun PLLA/MWNTs/HA Hybrid Nanofiber Scaffolds and Their Potential in Dental Tissue Engineering. *Key Eng. Mater.* **330–332,** 393–396 (2007).

141. Rainer, A. *et al.* Electrospun hydroxyapatite-functionalized PLLA scaffold: potential applications in sternal bone healing. *Ann. Biomed. Eng.* **39,** 1882–90 (2011).

142. Mei, F. *et al.* Improved biological characteristics of poly(L-lactic acid) electrospun membrane by incorporation of multiwalled carbon nanotubes/hydroxyapatite nanoparticles. *Biomacromolecules* **8,** 3729–35 (2007).

143. Demir, M. ., Yilgor, I., Yilgor, E. & Erman, B. Electrospinning of polyurethane fibers. *Polymer (Guildf).* **43,** 3303–3309 (2002).

144. Meng, J. *et al.* Electrospun aligned nanofibrous composite of MWCNT/polyurethane to enhance vascular endothelium cells proliferation and function. *J. Biomed. Mater. Res. A* **95,** 312–20 (2010).

145. Hunley, M. T., PÃ¶tschke, P. & Long, T. E. Melt Dispersion and Electrospinning of Non-Functionalized Multiwalled Carbon Nanotubes in Thermoplastic Polyurethane. *Macromol. Rapid Commun.* **30,** 2102–2106 (2009).

146. Sen, R. *et al.* Preparation of Single-Walled Carbon Nanotube Reinforced Polystyrene and Polyurethane Nanofibers and Membranes by Electrospinning. *Nano Lett.* **4,** 459–464 (2004).

147. Zhou, W., Wu, Y., Wei, F., Luo, G. & Qian, W. Elastic deformation of multiwalled carbon nanotubes in electrospun MWCNTs–PEO and MWCNTs–PVA nanofibers. *Polymer (Guildf).* **46,** 12689–12695 (2005).

148. Im, J. S., Kim, J. G., Lee, S.-H. & Lee, Y.-S. Enhanced adhesion and dispersion of carbon nanotube in PANI/PEO electrospun fibers for shielding effectiveness of electromagnetic interference. *Colloids Surfaces A Physicochem. Eng. Asp.* **364,** 151–157 (2010).

149. Shin, M., Kim, Y., Kim, S., Lee, H. & Spinks, G. Enhanced conductivity of aligned PANi/PEO/MWNT nanofibers by electrospinning. *Sensors Actuators B Chem.* **134,** 122–126 (2008).

150. Jeong, J. *et al.* Mechanical properties of electrospun PVA/MWNTs composite nanofibers. *Thin Solid Films* **515,** 5136–5141 (2007).

151. Wang, G. *et al.* Conducting MWNT/poly(vinyl acetate) composite nanofibres by electrospinning. *Nanotechnology* **17,** 5829–5835 (2006).

152. Kim, M. J., Lee, J., Jung, D. & Shim, S. E. Electrospun poly(vinyl alcohol) nanofibers incorporating PEGylated multi-wall carbon nanotube. *Synth. Met.* **160,** 1410–1414 (2010).

153. McCullen, S. D., Ramaswamy, S., Clarke, L. I. & Gorga, R. E. Nanofibrous composites for tissue engineering applications. *Wiley Interdiscip. Rev. Nanomedicine Nanobiotechnology* **1,** 369–390 (2009).

154. Lee, S. J. *et al.* In vitro evaluation of electrospun nanofiber scaffolds for vascular graft application. *Solutions* (2007). doi:10.1002/jbm.a

155. DeQuach, J. A., Yuan, S. H., Goldstein, L. S. B. & Christman, K. L. Decellularized Porcine Brain Matrix for Cell Culture and Tissue Engineering Scaffolds. *Tissue Eng. Part A* **17,** 2583–2592 (2011).

156. Khaing, Z. Z., Thomas, R. C., Geissler, S. A. & Schmidt, C. E. Advanced biomaterials for repairing the nervous system: what can hydrogels do for the brain? *Mater. Today* **17,** 332–340 (2014).

157. Ulrich, T. A., de Juan Pardo, E. M. & Kumar, S. The mechanical rigidity of the extracellular matrix regulates the structure, motility, and proliferation of glioma cells. *Cancer Res.* **69,** 4167–74 (2009).

158. Syková, E. & Nicholson, C. Diffusion in brain extracellular space. *Physiol. Rev.* **88,** 1277–340 (2008).

159. Michel, E., Hernandez, D. & Lee, S. Y. Electrical conductivity and permittivity maps of brain tissues derived from water content based on T_1-weighted acquisition. *Magn. Reson. Med.* n/a-n/a (2016). doi:10.1002/mrm.26193

160. Zhang, B. G. X. *et al.* Recent advances in nerve tissue engineering. *Int. J. Artif. Organs* **37,** 277–91 (2014).

161. Hench, L. L. Bioceramics. *J. Am. Ceram. Soc.* **81,** 1705–1728 (2005).

162. Søballe, K., Hansen, E. S., B-Rasmussen, H., Jørgensen, P. H. & Bünger, C. Tissue ingrowth into titanium and hydroxyapatite-coated implants during stable and unstable mechanical conditions. *J. Orthop. Res.* **10,** 285–99 (1992).

163. Technology, D., Engineering, D. & Medical, T. Mechanical properties of sintered hydroxyapatite for prosthetic applications. *J. Mater.* **16,** 809–812 (1981).

164. Novoselov, K. *et al.* Two-dimensional gas of massless Dirac fermions in graphene. *Arxiv Prepr. cond-mat/0509330* 1–6 (2005).

165. Novoselov, K. S. *et al.* Two-dimensional atomic crystals. *Proc. Natl. Acad. Sci. U. S. A.* **102,** 10451–3 (2005).

166. Iijima, S. Helical microtubules of graphitic carbon. *Nature* **354,** 56–58 (1991).

167. Lv, Radushkevich, O. L. V. M. strukture ugleroda, obrazujucegosja pri termi-ceskom razlozenii okisi ugleroda na zeleznom kontakte. *Zurn Fis. Chim* **26,** 88–95 (1952).

168. Oberlin, A. Filamentous growth of carbon through benzene decomposition. *J. Cryst. Growth* **32,** 335–349 (1976).

169. ABRAHAMSON, J., WILES, P. G. & RHOADES, B. L. Structure of carbon fibres found on carbon arc anodes. *Carbon N. Y.* **37,** 1873–1874 (1999).

170. Kroto, H. W., Heath, J. R., O'Brien, S. C., Curl, R. F. & Smalley, R. E. C60: Buckminsterfullerene. *Nature* **318,** 162–163 (1985).

171. Harris, P. J. F. *Carbon nanotubes and related structures: new materials for the twenty-first century*. (Cambridge University Press, 1999).

172. Xie, S., Li, W., Pan, Z., Chang, B. & Sun, L. Mechanical and physical properties on carbon nanotube. *J. Phys. Chem. Solids* **61,** 1153–1158 (2000).

173. Endo, M. *et al.* The production and structure of pyrolytic carbon nanotubes (PCNTs). *J. Phys. Chem. Solids* **54,** 1841–1848 (1993).

174. Barreiro, a. *et al.* On the effects of solution and reaction parameters for the aerosol-assisted CVD growth of long carbon nanotubes. *Appl. Phys. A* **82,** 719–725 (2005).

175. Ivanov, V. *et al.* The study of carbon nanotubules produced by catalytic method. *Chem. Phys. Lett.* **223,** 329–335 (1994).

176. Deepak, F., Govindaraj, A. & Rao, C. N. R. Synthetic strategies for Y-junction carbon nanotubes. *Chem. Phys. Lett.* **345,** 5–10 (2001).

177. Sinnott, S. B. & Andrews, R. Carbon Nanotubes: Synthesis, Properties, and Applications. *Crit. Rev. Solid State Mater. Sci.* **26,** 145–249 (2001).

178. Tibbetts, G. Why are carbon filaments tubular? *J. Cryst. Growth* **66,** 632–638 (1984).

179. Zhao, X. *et al.* Smallest Carbon Nanotube Is 3 Å in Diameter. *Phys. Rev. Lett.* **92,** 12–14 (2004).

180. Wong, E. W., Sheehan, P. E. & Lieber, C. M. Nanobeam mechanics: elasticity, strength, and toughness of nanorods and nanotubes. *Science (80-.).* **277,** 1971 (1997).

181. Yu, M. F. *et al.* Strength and breaking mechanism of multiwalled carbon nanotubes under tensile load. *Science (80-.).* **287,** 637 (2000).

182. Salvetat, J.-P. *et al.* Elastic Modulus of Ordered and Disordered Multiwalled Carbon Nanotubes. *Adv. Mater.* **11,** 161–165 (1999).

183. Hamada, N., Sawada, S. & Oshiyama, A. New one-dimensional conductor: Graphitic microtubules. *Phys. Rev. Lett.* **68,** 1579–1581 (1992).

184. Fischer, J. *et al.* Metallic resistivity in crystalline ropes of single-wall carbon nanotubes. *Phys. Rev. B* **55,** 4921–4924 (1997).

185. Bockrath, M. *et al.* Single-electron transport in ropes of carbon nanotubes. *Science (80-.).* **275,** 1922 (1997).

186. De Heer, W. A., Chatelain, A. & Ugarte, D. A carbon nanotube field-emission electron source. *Science (80-.).* **270,** 1179 (1995).

187. Dürkop, T., Kim, B. M. & Fuhrer, M. S. Properties and applications of high-mobility semiconducting nanotubes. *J. Phys. Condens. Matter* **16,** R553–R580 (2004).

188. Frank, S., Poncharal, P., Wang, Z. & Heer, W. A. Carbon nanotube quantum resistors. *Science (80-.).* **280,** 1744 (1998).

189. Ebbesen, T. W. *et al.* Electrical conductivity of individual carbon nanotubes. *Nature* **382,** 54–56

(1996).

190. Berber, S., Kwon, Y. & Tomanek, D. Unusually high thermal conductivity of carbon nanotubes. *Phys. Rev. Lett.* **84,** 4613–6 (2000).

191. Tasis, D., Tagmatarchis, N., Bianco, A. & Prato, M. Chemistry of carbon nanotubes. *Chem. Rev* **106,** 1105–1136 (2006).

192. Heller, D. a., Baik, S., Eurell, T. E. & Strano, M. S. Single-Walled Carbon Nanotube Spectroscopy in Live Cells: Towards Long-Term Labels and Optical Sensors. *Adv. Mater.* **17,** 2793–2799 (2005).

193. Sitharaman, B. *et al.* Superparamagnetic gadonanotubes are high-performance MRI contrast agents. *Chem. Commun. (Camb).* 3915–7 (2005). doi:10.1039/b504435a

194. Harrison, B. S. & Atala, A. Carbon nanotube applications for tissue engineering. *Biomaterials* **28,** 344–53 (2007).

195. Radosavljević, M., Freitag, M., Thadani, K. V. & Johnson, A. T. Nonvolatile Molecular Memory Elements Based on Ambipolar Nanotube Field Effect Transistors. *Nano Lett.* **2,** 761–764 (2002).

196. Tan, X., Li, M., Cai, P., Luo, L. & Zou, X. An amperometric cholesterol biosensor based on multiwalled carbon nanotubes and organically modified sol-gel/chitosan hybrid composite film. *Anal. Biochem.* **337,** 111–20 (2005).

197. Xian, Y. *et al.* Nanostructured electrode based on multi-wall carbon nanotubes/Pt microparticles nanocomposite for electrochemical determination of thiols in rat striatum by high performance liquid chromatography separation. *J. Chromatogr. B. Analyt. Technol. Biomed. Life Sci.* **817,** 239–46 (2005).

198. Rochette, J.-F., Sacher, E., Meunier, M. & Luong, J. H. T. A mediatorless biosensor for putrescine using multiwalled carbon nanotubes. *Anal. Biochem.* **336,** 305–11 (2005).

199. Singh, R. *et al.* Binding and condensation of plasmid DNA onto functionalized carbon nanotubes: toward the construction of nanotube-based gene delivery vectors. *J. Am. Chem. Soc.* **127,** 4388–96 (2005).

200. Martin, C. R. & Kohli, P. The emerging field of nanotube biotechnology. *Nat. Rev. Drug Discov.* **2,** 29–37 (2003).

201. Xie, J. & Wang, C.-H. Electrospun micro- and nanofibers for sustained delivery of paclitaxel to treat C6 glioma in vitro. *Pharm. Res.* **23,** 1817–26 (2006).

202. Janát-Amsbury, M. M. *et al.* Combination of local, nonviral IL12 gene therapy and systemic paclitaxel treatment in a metastatic breast cancer model. *Mol. Ther.* **9,** 829–36 (2004).

203. Kam, N. W. S., O'Connell, M., Wisdom, J. a & Dai, H. Carbon nanotubes as multifunctional biological transporters and near-infrared agents for selective cancer cell destruction. *Proc. Natl. Acad. Sci. U. S. A.* **102,** 11600–5 (2005).

204. Tran, P. a, Zhang, L. & Webster, T. J. Carbon nanofibers and carbon nanotubes in regenerative medicine. *Adv. Drug Deliv. Rev.* **61,** 1097–114 (2009).

205. Kamat, P. V., Guldi, D. M., Kadish, K. M., Group, E. S. F. & Meeting, E. S. *Chemistry and physics of fullerenes and carbon nanomaterials: proceedings of the international symposium, Volume 10*. (The Electrochemical Society, 2000).

206. Seoul, C., Kim, Y.-T. & Baek, C.-K. Electrospinning of poly(vinylidene fluoride)/dimethylformamide solutions with carbon nanotubes. *J. Polym. Sci. Part B Polym. Phys.* **41,** 1572–1577 (2003).

207. Lisunova, M., Hildmann, A., Hatting, B., Datsyuk, V. & Reich, S. Nanofibres of CA/PAN with high amount of carbon nanotubes by core–shell electrospinning. *Compos. Sci. Technol.* **70,** 1584–1588 (2010).

208. Jose, M. V. *et al.* Morphology and mechanical properties of Nylon 6/MWNT nanofibers. *Polymer (Guildf).* **48,** 1096–1104 (2007).

209. Choi, J., Park, E. J., Park, D. W. & Shim, S. E. MWCNT–OH adsorbed electrospun nylon 6,6 nanofibers chemiresistor and their application in low molecular weight alcohol vapours sensing. *Synth. Met.* **160,** 2664–2669 (2010).

210. Baji, A., Mai, Y.-W., Wong, S.-C., Abtahi, M. & Du, X. Mechanical behavior of self-assembled carbon nanotube reinforced nylon 6,6 fibers. *Compos. Sci. Technol.* **70,** 1401–1409 (2010).

211. Pan, C., Ge, L. & Gu, Z. Fabrication of multi-walled carbon nanotube reinforced polyelectrolyte hollow nanofibers by electrospinning. *Compos. Sci. Technol.* **67,** 3271–3277 (2007).

212. Hou, X., Yang, X., Zhang, L., Waclawik, E. & Wu, S. Stretching-induced crystallinity and orientation to improve the mechanical properties of electrospun PAN nanocomposites. *Mater. Des.* **31,** 1726–1730 (2010).

213. Sundaray, B., Choi, A. & Park, Y. W. Highly conducting electrospun polyaniline-polyethylene oxide nanofibrous membranes filled with single-walled carbon nanotubes. *Synth. Met.* **160,** 984–988 (2010).

214. Mathew, G., Hong, J., Rhee, J., Lee, H. & Nah, C. Preparation and characterization of properties of electrospun poly(butylene terephthalate) nanofibers filled with carbon nanotubes. *Polym. Test.* **24,** 712–717 (2005).

215. Rein, D. M., Cohen, Y., Lipp, J. & Zussman, E. Elaboration of Ultra-High Molecular Weight Polyethylene/Carbon Nanotubes Electrospun Composite Fibers. *Macromol. Mater. Eng.* **295,** 1003–1008 (2010).

216. Chen, H., Liu, Z. & Cebe, P. Chain confinement in electrospun nanofibers of PET with carbon nanotubes. *Polymer (Guildf).* **50,** 872–880 (2009).

217. Mazinani, S., Ajji, A. & Dubois, C. Fundamental study of crystallization, orientation, and electrical conductivity of electrospun PET/carbon nanotube nanofibers. *J. Polym. Sci. Part B Polym. Phys.* **48,** 2052–2064 (2010).

218. Chan, K. H. K. *et al.* Morphologies and electrical properties of electrospun poly[(R)-3-hydroxybutyrate-co-(R)-3-hydroxyvalerate]/ multiwalled carbon nanotubes fibers. *J. Appl. Polym. Sci.* n/a-n/a (2009). doi:10.1002/app.31572

219. Chen, D., Liu, T., Zhou, X., Tjiu, W. C. & Hou, H. Electrospinning fabrication of high strength and toughness polyimide nanofiber membranes containing multiwalled carbon nanotubes. *J. Phys. Chem. B* **113,** 9741–8 (2009).

220. Shao, S. *et al.* Osteoblast function on electrically conductive electrospun PLA/MWCNTs nanofibers. *Biomaterials* **32,** 2821–33 (2011).

221. Touny, A. H., Lawrence, J. G., Jones, A. D. & Bhaduri, S. B. Effect of electrospinning parameters on the characterization of PLA/HNT nanocomposite fibers. *J. Mater. Res.* **25,** 857–865 (2010).

222. Liu, F. *et al.* Effect of the Porous Microstructures of Poly(lactic-co-glycolic acid)/Carbon Nanotube Composites on the Growth of Fibroblast Cells. *Soft Mater.* **8,** 239–253 (2010).

223. Sui, X.-M., Giordani, S., Prato, M. & Wagner, H. D. Effect of carbon nanotube surface modification on dispersion and structural properties of electrospun fibers. *Appl. Phys. Lett.* **95,** 233113 (2009).

224. Kim, D. O. *et al.* Morphological Characteristics of Electrospun Poly(Methyl Methacrylate) Nanofibers Containing Multi-Walled Carbon Nanotubes. *Mol. Cryst. Liq. Cryst.* **464,** 137–144 (2007).

225. Liu, L.-Q., Tasis, D., Prato, M. & Wagner, H. D. Tensile Mechanics of Electrospun Multiwalled Nanotube/Poly(methyl methacrylate) Nanofibers. *Adv. Mater.* **19,** 1228–1233 (2007).

226. Sundaray, B., Subramanian, V., Natarajan, T. S. & Krishnamurthy, K. Electrical conductivity of a single electrospun fiber of poly(methyl methacrylate) and multiwalled carbon nanotube nanocomposite. *Appl. Phys. Lett.* **88,** 143114 (2006).

227. Mazinani, S. *et al.* Rheological/Morphological Study of PS/CNT Nanocomposite Electrospun Fibers. *AIP Conf. Proc.* **8,** 800–802 (2008).

228. Salalha, W. *et al.* Single-walled carbon nanotubes embedded in oriented polymeric nanofibers by electrospinning. *Langmuir* **20,** 9852–5 (2004).

229. Wu, D. *et al.* Electrospinning of poly(trimethylene terephthalate)/carbon nanotube composites. *Eur. Polym. J.* **47,** 284–293 (2011).

230. Ma, Q. & Cebe, P. Phase structure of electrospun poly(trimethylene terephthalate) composite nanofibers containing carbon nanotubes. *J. Therm. Anal. Calorim.* **102,** 425–434 (2010).

231. Wong, K. K. H. *et al.* The effect of carbon nanotube aspect ratio and loading on the elastic modulus of electrospun poly(vinyl alcohol)-carbon nanotube hybrid fibers. *Carbon N. Y.* **47,** 2571–2578 (2009).

232. Ketpang, K. & Park, J. S. Electrospinning PVDF/PPy/MWCNTs conducting composites. *Synth. Met.* **160,** 1603–1608 (2010).

233. Huang, S. *et al.* Electrospinning of polyvinylidene difluoride with carbon nanotubes: synergistic effects of extensional force and interfacial interaction on crystalline structures. *Langmuir* **24,** 13621–6 (2008).

234. Gandhi, M., Yang, H., Shor, L. & Ko, F. Post-spinning modification of electrospun nanofiber nanocomposite from Bombyx mori silk and carbon nanotubes. *Polymer (Guildf).* **50,** 1918–1924 (2009).

235. Dijkstra, D. J., Cirstea, M. & Nakamura, N. The orientational behavior of multiwall carbon nanotubes in polycarbonate in simple shear flow. *Rheol. Acta* (2010). doi:10.1007/s00397-010-0457-6

236. Gleixner, R. & Fromherz, P. The extracellular electrical resistivity in cell adhesion. *Biophys. J.* **90,** 2600–11 (2006).

237. Han, Z. *et al.* Electrospun Aligned Nanofibrous Scaffold of Carbon Nanotubes-Polyurethane Composite for Endothelial Cells. *J. Nanosci. Nanotechnol.* **9,** 1400–1402 (2009).

238. Yang, L., Liu, H. & Lin, Y. Biomaterial nanotopography-mediated cell responses: experiment and modeling. *Int. J. Smart Nano Mater.* **2014,** (2014).

239. Dalby, M. J., Gadegaard, N. & Oreffo, R. O. C. Harnessing nanotopography and integrin-matrix interactions to influence stem cell fate. *Nat. Mater.* **13,** 558–69 (2014).

240. Wu, C. M. & Chou, M. H. Polymorphism, piezoelectricity and sound absorption of electrospun PVDF membranes with and without carbon nanotubes. *Compos. Sci. Technol.* **127,** 127–133 (2016).

241. Călin, M. A. *et al.* Measuring the Electrical Properties of MWNT-PA6 Reinforced Nanocomposites. *J. Nanomater.* **2015,** 1–9 (2015).

242. Lam, C., James, J. & McCluskey, R. A review of carbon nanotube toxicity and assessment of potential occupational and environmental health risks. *Crit. Rev.* (2006).

243. Maynard A. *et al.* Exposure to Carbon Nanotube Material: Aerosol Release During the Handling of Unrefined Single-Walled Carbon Nanotube Material. *J. Toxicol. Environ. Heal. Part A* **67,** 21 (2004).

244. Takagi, A. *et al.* Induction of mesothelioma in p53+/− mouse by intraperitoneal application of multi-wall carbon nanotube. *J. Toxicol. Sci.* **33,** 105–116 (2008).

245. Kane, A. B. & Hurt, R. H. Nanotoxicology: the asbestos analogy revisited. *Nat. Nanotechnol.* **3,** 378–9 (2008).

246. Shvedova A. *et al.* Exposure to Carbon Nanotube Material: Assessment of Nanotube Cytotoxicity using Human Keratinocyte Cells. *J. Toxicol. Environ. Heal. Part A* **66,** 18 (2003).

247. Castro, C. *et al.* Dynamics of catalyst particle formation and multi-walled carbon nanotube growth in aerosol-assisted catalytic chemical vapor deposition. *Carbon N. Y.* **48,** 3807–3816 (2010).

248. Tripatanasuwan, S., Zhong, Z. & Reneker, D. H. Effect of evaporation and solidification of the charged jet in electrospinning of poly(ethylene oxide) aqueous solution. *Polymer (Guildf).* **48,** 5742–5746 (2007).

249. Gupta, P., Elkins, C., Long, T. E. & Wilkes, G. L. Electrospinning of linear homopolymers of poly(methyl methacrylate): exploring relationships between fiber formation, viscosity, molecular weight and concentration in a good solvent. *Polymer (Guildf).* **46,** 4799–4810 (2005).

250. Crescenzi, V., Manzini, G., Calzolari, G. & Borri, C. Thermodynamics of fusion of poly-β-propiolactone and poly-ϵ-caprolactone. comparative analysis of the melting of aliphatic polylactone and polyester chains. *Eur. Polym. J.* **8,** 449–463 (1972).

251. Li, D. & Xia, Y. Electrospinning of Nanofibers: Reinventing the Wheel? *Adv. Mater.* **16,** 1151–1170 (2004).

252. Kessick, R. & Tepper, G. Microscale polymeric helical structures produced by electrospinning. *Appl. Phys. Lett.* **84,** 4807 (2004).

253. Koombhongse, S., Liu, W. & Reneker, D. H. Flat polymer ribbons and other shapes by electrospinning. *J. Polym. Sci. Part B Polym. Phys.* **39,** 2598–2606 (2001).

254. Tarley, C. R. T. *et al.* Chemometric tools in electroanalytical chemistry: Methods for optimization based on factorial design and response surface methodology. *Microchem. J.* **92,** 58–67 (2009).

255. Bezerra, M. A., Santelli, R. E., Oliveira, E. P., Villar, L. S. & Escaleira, L. A. Response surface methodology (RSM) as a tool for optimization in analytical chemistry. *Talanta* **76,** 965–77 (2008).

256. Box, G. E. P., Hunter, J. S. & Hunter, W. G. *Statistics for experimenters: design, innovation, and discovery*. (Wiley-Interscience, 2005).

257. Mohammad Khanlou, H., Chin Ang, B., Talebian, S., Muhammad Afifi, A. & Andriyana, A. Electrospinning of polymethyl methacrylate nanofibers: optimization of processing parameters using the Taguchi design of experiments. *Text. Res. J.* **85,** 356–368 (2014).

258. Khanlou, H. M. *et al.* Prediction and optimization of electrospinning parameters for polymethyl methacrylate nanofiber fabrication using response surface methodology and artificial neural networks. *Neural Comput. Appl.* **25,** 767–777 (2014).

259. Chen, J.-P., Ho, K.-H., Chiang, Y.-P. & Wu, K.-W. Fabrication of electrospun poly(methyl methacrylate) nanofibrous membranes by statistical approach for application in enzyme immobilization. *J. Memb. Sci.* **340,** 9–15 (2009).

260. Heikkilä, P. & Harlin, A. Parameter study of electrospinning of polyamide-6. *Eur. Polym. J.* **44,** 3067–3079 (2008).

261. Yördem, O. S., Papila, M. & Menceloğlu, Y. Z. Effects of electrospinning parameters on polyacrylonitrile nanofiber diameter: An investigation by response surface methodology. *Mater. Des.* **29,** 34–44 (2008).

262. Cipitria, a., Skelton, A., Dargaville, T. R., Dalton, P. D. & Hutmacher, D. W. Design, fabrication and characterization of PCL electrospun scaffolds—a review. *J. Mater. Chem.* **21,** 9419 (2011).

263. Woodruff, M. A. & Hutmacher, D. W. The return of a forgotten polymer—Polycaprolactone in

the 21st century. *Prog. Polym. Sci.* **35,** 1217–1256 (2010).

264. Nair, L. S. & Laurencin, C. T. Biodegradable polymers as biomaterials. *Prog. Polym. Sci.* **32,** 762–798 (2007).

265. Engelberg, I. & Kohn, J. Physico-mechanical properties of degradable polymers used in medical applications: A comparative study. *Biomaterials* **12,** 292–304 (1991).

266. Lee, K., Kim, H., Khil, M., Ra, Y. & Lee, D. Characterization of nano-structured poly (ε-caprolactone) nonwoven mats via electrospinning. *Polymer (Guildf).* **44,** 1287–1294 (2003).

267. Del Gaudio, C., Bianco, A., Folin, M., Baiguera, S. & Grigioni, M. Structural characterization and cell response evaluation of electrospun PCL membranes: micrometric versus submicrometric fibers. *J. Biomed. Mater. Res. A* **89,** 1028–39 (2009).

268. Srouji, S., Kizhner, T., Suss-Tobi, E., Livne, E. & Zussman, E. 3-D Nanofibrous electrospun multilayered construct is an alternative ECM mimicking scaffold. *J. Mater. Sci. Mater. Med.* **19,** 1249–55 (2008).

269. Theron, S. Experimental investigation of the governing parameters in the electrospinning of polymer solutions. *Polymer (Guildf).* **45,** 2017–2030 (2004).

270. Zheng, Y., Xie, S. & Zeng, Y. Electric field distribution and jet motion in electrospinning process: From needle to hole. *J. Mater. Sci.* **48,** 6647–6655 (2013).

271. Zargham, S., Bazgir, S., Tavakoli, A., Rashidi, A. S. & Damerchely, R. The Effect of Flow Rate on Morphology and Deposition Area of Electrospun Nylon 6 Nanofiber. *J. Eng. Fiber. Fabr.* **7,** 42–49 (2012).

272. Zhang, Y., He, X., Li, J., Miao, Z. & Huang, F. Fabrication and ethanol-sensing properties of micro gas sensor based on electrospun SnO2 nanofibers. *Sensors Actuators B Chem.* **132,** 67–73 (2008).

273. Hsu, C. & Shivkumar, S. Nano-sized beads and porous fiber constructs of Poly(ε-caprolactone) produced by electrospinning. *J. Mater. Sci.* **39,** 3003–3013 (2004).

274. Mit-uppatham, C., Nithitanakul, M. & Supaphol, P. Ultrafine Electrospun Polyamide-6 Fibers: Effect of Solution Conditions on Morphology and Average Fiber Diameter. *Macromol. Chem. Phys.* **205,** 2327–2338 (2004).

275. Fridrikh, S., Yu, J., Brenner, M. & Rutledge, G. Controlling the Fiber Diameter during Electrospinning. *Phys. Rev. Lett.* **90,** 144502 (2003).

276. Beachley, V. & Wen, X. Effect of electrospinning parameters on the nanofiber diameter and length. *Mater. Sci. Eng. C. Mater. Biol. Appl.* **29,** 663–668 (2009).

277. Reneker, D. H. & Chun, I. Nanometre diameter fibres of polymer, produced by electrospinning. *Nanotechnology* **7,** 216–223 (1996).

278. Reneker, D. H., Yarin, A. L., Fong, H. & Koombhongse, S. Bending instability of electrically charged liquid jets of polymer solutions in electrospinning. *J. Appl. Phys.* **87,** 4531 (2000).

279. Mo, X. ., Xu, C. ., Kotaki, M. & Ramakrishna, S. Electrospun P(LLA-CL) nanofiber: a biomimetic extracellular matrix for smooth muscle cell and endothelial cell proliferation. *Biomaterials* **25,** 1883–1890 (2004).

280. Sencadas, V. *et al.* Determination of the parameters affecting electrospun chitosan fiber size distribution and morphology. *Carbohydr. Polym.* **87,** 1295–1301 (2012).

281. Macossay, J., Marruffo, A., Rincon, R., Eubanks, T. & Kuang, A. Effect of needle diameter on nanofiber diameter and thermal properties of electrospun poly(methyl methacrylate). *Polym. Adv. Technol.* **18,** 180–183 (2007).

282. Shin, Y. M., Hohman, M. M., Brenner, M. P. & Rutledge, G. C. Experimental characterization of

electrospinning: the electrically forced jet and instabilities. *Polymer (Guildf).* **42,** 09955–09967 (2001).

283. Qian, Y.-F., Su, Y., Li, X.-Q., Wang, H.-S. & He, C.-L. Electrospinning of Polymethyl Methacrylate Nanofibres in Different Solvents. *Iran. Polym. J.* **19,** 123–129 (2010).

284. Piperno, S., Lozzi, L., Rastelli, R., Passacantando, M. & Santucci, S. PMMA nanofibers production by electrospinning. *Appl. Surf. Sci.* **252,** 5583–5586 (2006).

285. Sobieraj, M. C. & Rimnac, C. M. Ultra high molecular weight polyethylene: mechanics, morphology, and clinical behavior. *J. Mech. Behav. Biomed. Mater.* **2,** 433–43 (2009).

286. Strobl, G. Crystallization and melting of bulk polymers: New observations, conclusions and a thermodynamic scheme. *Prog. Polym. Sci.* **31,** 398–442 (2006).

287. Baji, A., Mai, Y.-W., Wong, S.-C., Abtahi, M. & Chen, P. Electrospinning of polymer nanofibers: Effects on oriented morphology, structures and tensile properties. *Compos. Sci. Technol.* **70,** 703–718 (2010).

288. Lim, C. T., Tan, E. P. S. & Ng, S. Y. Effects of crystalline morphology on the tensile properties of electrospun polymer nanofibers. *Appl. Phys. Lett.* **92,** 141908 (2008).

289. Tan, E. P. S., Ng, S. Y. & Lim, C. T. Tensile testing of a single ultrafine polymeric fiber. *Biomaterials* **26,** 1453–6 (2005).

290. Wong, S.-C., Baji, A. & Leng, S. Effect of fiber diameter on tensile properties of electrospun poly(ε-caprolactone). *Polymer (Guildf).* **49,** 4713–4722 (2008).

291. Bittiger, H., Marchessault, R. H. & Niegisch, W. D. Crystal structure of poly-ε-caprolactone. *Acta Crystallogr. Sect. B Struct. Crystallogr. Cryst. Chem.* **26,** 1923–1927 (1970).

292. Koh, C. T., Strange, D. G. T., Tonsomboon, K. & Oyen, M. L. Failure mechanisms in fibrous scaffolds. *Acta Biomater.* **9,** 7326–34 (2013).

293. Mohammadzadehmoghadam, S., Dong, Y. & Davies, I. J. Modeling electrospun nanofibers: An overview from theoretical, empirical, and numerical approaches. *Int. J. Polym. Mater. Polym. Biomater.* **65,** 901–915 (2016).

294. Pai, C.-L., Boyce, M. C. & Rutledge, G. C. On the importance of fiber curvature to the elastic moduli of electrospun nonwoven fiber meshes. *Polymer (Guildf).* **52,** 6126–6133 (2011).

295. Stylianopoulos, T. *et al.* Tensile mechanical properties and hydraulic permeabilities of electrospun cellulose acetate fiber meshes. *J. Biomed. Mater. Res. Part B Appl. Biomater.* **100B,** 2222–2230 (2012).

296. Rizvi, M. S., Kumar, P., Katti, D. S. & Pal, A. Mathematical model of mechanical behavior of micro/nanofibrous materials designed for extracellular matrix substitutes. *Acta Biomater.* **8,** 4111–4122 (2012).

297. Wei, X., Xia, Z., Wong, S. C. & Baji, A. Modelling of mechanical properties of electrospun nanofibre network. *Int. J. Exp. Comput. Biomech.* **1,** 45 (2009).

298. Kong, Y. & Hay, J. N. The enthalpy of fusion and degree of crystallinity of polymers as measured by DSC. *Eur. Polym. J.* **39,** 1721–1727 (2003).

299. Akovali, G. & Atalay, A. Comparison of crystallinities of high density polyethylene determined by different techniques. *Polym. Test.* **16,** 165–171 (1997).

300. Gao, K., Hu, X., Dai, C. & Yi, T. Crystal structures of electrospun PVDF membranes and its separator application for rechargeable lithium metal cells. *Mater. Sci. Eng. B* **131,** 100–105 (2006).

301. Carrizales, C. *et al.* Thermal and mechanical properties of electrospun PMMA, PVC, Nylon 6, and Nylon 6,6. *Polym. Adv. Technol.* **19,** 124–130 (2008).

302. Kołbuk, D., Sajkiewicz, P. & Kowalewski, T. a. Optical birefringence and molecular orientation of electrospun polycaprolactone fibers by polarizing-interference microscopy. *Eur. Polym. J.* **48,** 275–283 (2012).

303. Wang, X., Zhao, H., Turng, L.-S. & Li, Q. Crystalline Morphology of Electrospun Poly(ε-caprolactone) (PCL) Nanofibers. *Ind. Eng. Chem. Res.* **52,** 4939–4949 (2013).

304. Murthy, N. S. & Minor, H. General procedure for evaluating amorphous scattering and crystallinity from X-ray diffraction scans of semicrystalline polymers. *Polymer (Guildf).* **31,** 996–1002 (1990).

305. Gray, A. P. Polymer crystallinity determinations by DSC. *Thermochim. Acta* **1,** 563–579 (1970).

306. Deitzel, J. ., Kleinmeyer, J., Harris, D. & Beck Tan, N. . The effect of processing variables on the morphology of electrospun nanofibers and textiles. *Polymer (Guildf).* **42,** 261–272 (2001).

307. Kong, Y. & Hay, J. N. The measurement of the crystallinity of polymers by DSC. *Polymer (Guildf).* **43,** 3873–3878 (2002).

308. Dooren, A. Van & Müller, B. Effects of heating rate and particle size on temperatures and specific enthalpies in quantitative differential scanning calorimetry. *Thermochim. Acta* **54,** (1982).

309. Minakov, A. A., Mordvintsev, D. A. & Schick, C. Melting and reorganization of poly(ethylene terephthalate) on fast heating (1000 K/s). *Polymer (Guildf).* **45,** 3755–3763 (2004).

310. Nottelet, B. *et al.* Factorial design optimization and in vivo feasibility of poly(epsilon-caprolactone)-micro- and nanofiber-based small diameter vascular grafts. *J. Biomed. Mater. Res. A* **89,** 865–75 (2009).

311. Jha, B. S. *et al.* Two pole air gap electrospinning: Fabrication of highly aligned, three-dimensional scaffolds for nerve reconstruction. *Acta Biomater.* **7,** 203–15 (2011).

312. Prabhakaran, M. P., Venugopal, J., Chan, C. K. & Ramakrishna, S. Surface modified electrospun nanofibrous scaffolds for nerve tissue engineering. *Nanotechnology* **19,** 455102 (2008).

313. Wu, X.-F. & Dzenis, Y. A. Size effect in polymer nanofibers under tension. *J. Appl. Phys.* **102,** 44306 (2007).

314. Ayoub, G. *et al.* Effects of crystal content on the mechanical behaviour of polyethylene under finite strains: Experiments and constitutive modelling. *Int. J. Plast.* **27,** 492–511 (2011).

315. Greenfeld, I., Fezzaa, K., Rafailovich, M. H. & Zussman, E. Fast X-ray Phase-Contrast Imaging of Electrospinning Polymer Jets: Measurements of Radius, Velocity, and Concentration. *Macromolecules* **45,** 3616–3626 (2012).

316. Giller, C. B., Chase, D. B., Rabolt, J. F. & Snively, C. M. Effect of solvent evaporation rate on the crystalline state of electrospun Nylon 6. *Polymer (Guildf).* **51,** 4225–4230 (2010).

317. Marco, Y., Chevalier, L. & Chaouche, M. WAXD study of induced crystallization and orientation in poly(ethylene terephthalate) during biaxial elongation. *Polymer (Guildf).* **43,** 6569–6574 (2002).

318. Arinstein, A., Burman, M., Gendelman, O. & Zussman, E. Effect of supramolecular structure on polymer nanofibre elasticity. *Nat. Nanotechnol.* **2,** 59–62 (2007).

319. Moniruzzaman, M. & Winey, K. I. Polymer Nanocomposites Containing Carbon Nanotubes. *Macromolecules* **39,** 5194–5205 (2006).

320. Ge, J. J. *et al.* Assembly of well-aligned multiwalled carbon nanotubes in confined polyacrylonitrile environments: electrospun composite nanofiber sheets. *J. Am. Chem. Soc.* **126,** 15754–61 (2004).

321. Hou, H. *et al.* Electrospun Polyacrylonitrile Nanofibers Containing a High Concentration of Well-

Aligned Multiwall Carbon Nanotubes. *Chem. Mater.* **17,** 967–973 (2005).

322. Cadek, M. *et al.* Reinforcement of Polymers with Carbon Nanotubes: The Role of Nanotube Surface Area. *Nano Lett.* **4,** 353–356 (2004).

323. Huang, Z.-M. & Zhou, Y.-X. *Strength of Fibrous Composites*. (Springer Science & Business Media, 2012).

324. Affdl, J. C. H. & Kardos, J. L. The Halpin-Tsai equations: A review. *Polym. Eng. Sci.* **16,** 344–352 (1976).

325. Hong, S. & Kim, G. Fabrication of electrospun polycaprolactone biocomposites reinforced with chitosan for the proliferation of mesenchymal stem cells. *Carbohydr. Polym.* **83,** 940–946 (2011).

326. Ji, J. *et al.* Significant Improvement of Mechanical Properties Observed in Highly Aligned Carbon-Nanotube-Reinforced Nanofibers. *J. Phys. Chem. C* **113,** 4779–4785 (2009).

327. Coleman, J. N., Khan, U., Blau, W. J. & Gun'ko, Y. K. Small but strong: a review of the mechanical properties of carbon nanotube–polymer composites. *Carbon N. Y.* **44,** 1624–1652 (2006).

328. Meysami, S. S., Dillon, F., Koós, A. A., Aslam, Z. & Grobert, N. Aerosol-assisted chemical vapour deposition synthesis of multi-wall carbon nanotubes: I. Mapping the reactor. *Carbon N. Y.* **58,** 151–158 (2013).

329. Pant, H. R. *et al.* Bimodal fiber diameter distributed graphene oxide/nylon-6 composite nanofibrous mats via electrospinning. *Colloids Surfaces A Physicochem. Eng. Asp.* **407,** 121–125 (2012).

330. Luong-Van, E. *et al.* Controlled release of heparin from poly(epsilon-caprolactone) electrospun fibers. *Biomaterials* **27,** 2042–50 (2006).

331. Demczyk, B. *et al.* Direct mechanical measurement of the tensile strength and elastic modulus of multiwalled carbon nanotubes. *Mater. Sci. Eng. A* **334,** 173–178 (2002).

332. Eshraghi, S. & Das, S. Mechanical and microstructural properties of polycaprolactone scaffolds with one-dimensional, two-dimensional, and three-dimensional orthogonally oriented porous architectures produced by selective laser sintering. *Acta Biomater.* **6,** 2467–76 (2010).

333. Crowder, S. W. *et al.* Poly(ε-caprolactone)–carbon nanotube composite scaffolds for enhanced cardiac differentiation of human mesenchymal stem cells. *Nanomedicine* **8,** 1763–1776 (2013).

334. Wickham, A. M. *et al.* Polycaprolactone-thiophene-conjugated carbon nanotube meshes as scaffolds for cardiac progenitor cells. *J. Biomed. Mater. Res. B. Appl. Biomater.* **102,** 1553–61 (2014).

335. Wurm, A. *et al.* Crystallization of poly(ε-caprolactone)/MWCNT composites: A combined SAXS/WAXS, electrical and thermal conductivity study. *Polymer (Guildf).* **55,** 2220–2232 (2014).

336. Bognitzki, M. *et al.* Nanostructured Fibers via Electrospinning. *Adv. Mater.* **13,** 70–72 (2001).

337. Jose, M. V. *et al.* Morphology and mechanical properties of Nylon 6/MWNT nanofibers. *Polymer (Guildf).* **48,** 1096–1104 (2007).

338. Chen, H., Liu, Z. & Cebe, P. Chain confinement in electrospun nanofibers of PET with carbon nanotubes. *Polymer (Guildf).* **50,** 872–880 (2009).

339. Kaivosoja, E. *et al.* Chemical and physical properties of regenerative medicine materials controlling stem cell fate. (2012).

340. Vaquette, C. *et al.* Zeta-potential and morphology of electrospun nano- and microfibers from biopolymers and their blends used as scaffolds in tissue engineering. *Mendeleev Commun.* **18,** 38–41 (2008).

341. Bondar, O. V, Saifullina, D. V, Shakhmaeva, I. I., Mavlyutova, I. I. & Abdullin, T. I. Monitoring of

the Zeta Potential of Human Cells upon Reduction in Their Viability and Interaction with Polymers. *Acta Naturae* **4,** 78–81 (2012).

342. Chen, Y. M. *et al.* Cultivation of endothelial cells on adhesive protein-free synthetic polymer gels. *Biomaterials* **26,** 4588–4596 (2005).

343. Agarwal, S., Wendorff, J. H. & Greiner, A. Use of electrospinning technique for biomedical applications. *Polymer (Guildf).* **49,** 5603–5621 (2008).

344. Sell, S. a, McClure, M. J., Garg, K., Wolfe, P. S. & Bowlin, G. L. Electrospinning of collagen/biopolymers for regenerative medicine and cardiovascular tissue engineering. *Adv. Drug Deliv. Rev.* **61,** 1007–19 (2009).

345. Sill, T. J. & von Recum, H. A. Electrospinning: applications in drug delivery and tissue engineering. *Biomaterials* **29,** 1989–2006 (2008).

346. Bürck, J. *et al.* Resemblance of electrospun collagen nanofibers to their native structure. *Langmuir* **29,** 1562–72 (2013).

347. Meng, L., Arnoult, O., Smith, M. & Wnek, G. E. Electrospinning of in situ crosslinked collagen nanofibers. *J. Mater. Chem.* **22,** (2012).

348. Ayres, C. *et al.* Modulation of anisotropy in electrospun tissue-engineering scaffolds: Analysis of fiber alignment by the fast Fourier transform. *Biomaterials* **27,** 5524–34 (2006).

349. Song, J.-H., Kim, H.-E. & Kim, H.-W. Production of electrospun gelatin nanofiber by water-based co-solvent approach. *J. Mater. Sci. Mater. Med.* **19,** 95–102 (2008).

350. Gautam, S., Dinda, A. K. & Mishra, N. C. Fabrication and characterization of PCL/gelatin composite nanofibrous scaffold for tissue engineering applications by electrospinning method. *Mater. Sci. Eng. C* **33,** 1228–1235 (2013).

351. Thomas, V., Zhang, X., Catledge, S. a & Vohra, Y. K. Functionally graded electrospun scaffolds with tunable mechanical properties for vascular tissue regeneration. *Biomed. Mater.* **2,** 224–32 (2007).

352. Huang, Z., Zhang, Y., Ramakrishna, S. & Lim, C. Electrospinning and mechanical characterization of gelatin nanofibers. *Polymer (Guildf).* **45,** 5361–5368 (2004).

353. Huang, C. *et al.* Electrospun collagen-chitosan-TPU nanofibrous scaffolds for tissue engineered tubular grafts. *Colloids Surf. B. Biointerfaces* **82,** 307–15 (2011).

354. Chen, Z., Mo, X. & Qing, F. Electrospinning of collagen–chitosan complex. *Mater. Lett.* **61,** 3490–3494 (2007).

355. Chen, J.-P., Chang, G.-Y. & Chen, J.-K. Electrospun collagen/chitosan nanofibrous membrane as wound dressing. *Colloids Surfaces A Physicochem. Eng. Asp.* **313–314,** 183–188 (2008).

356. Simşek, M., Capkın, M., Karakeçili, A. & Gümüşderelioğlu, M. Chitosan and polycaprolactone membranes patterned via electrospinning: effect of underlying chemistry and pattern characteristics on epithelial/fibroblastic cell behavior. *J. Biomed. Mater. Res. A* **100,** 3332–43 (2012).

357. Matsuda, A., Kagata, G., Kino, R. & Tanaka, J. Preparation of Chitosan Nanofiber Tube by Electrospinning. *J. Nanosci. Nanotechnol.* **7,** 852–855 (2007).

358. Wang, G., Hu, X., Lin, W., Dong, C. & Wu, H. Electrospun PLGA-silk fibroin-collagen nanofibrous scaffolds for nerve tissue engineering. *In Vitro Cell. Dev. Biol. Anim.* **47,** 234–40 (2011).

359. Luo, Y. *et al.* Carbon nanotube-incorporated multilayered cellulose acetate nanofibers for tissue engineering applications. *Carbohydr. Polym.* **91,** 419–27 (2013).

360. Kong, Q., Yu, Z. & Ji, Q. Electrospinning of Sodium Alginate with Poly (ethylene oxide), Gelatin and Nanometer Silver Colloid. *Mater. Sci. Forum* **610–613,** 1188–1191 (2009).

361. Ji, Y. *et al.* Electrospun three-dimensional hyaluronic acid nanofibrous scaffolds. *Biomaterials* **27,** 3782–92 (2006).

362. Ekaputra, A. K., Prestwich, G. D., Cool, S. M. & Hutmacher, D. W. Combining electrospun scaffolds with electrosprayed hydrogels leads to three-dimensional cellularization of hybrid constructs. *Biomacromolecules* **9,** 2097–103 (2008).

363. Hsu, F.-Y., Hung, Y.-S., Liou, H.-M. & Shen, C.-H. Electrospun hyaluronate-collagen nanofibrous matrix and the effects of varying the concentration of hyaluronate on the characteristics of foreskin fibroblast cells. *Acta Biomater.* **6,** 2140–7 (2010).

364. Kim, T. G., Chung, H. J. & Park, T. G. Macroporous and nanofibrous hyaluronic acid/collagen hybrid scaffold fabricated by concurrent electrospinning and deposition/leaching of salt particles. *Acta Biomater.* **4,** 1611–9 (2008).

365. Ekaputra, A. K., Prestwich, G. D., Cool, S. M. & Hutmacher, D. W. The three-dimensional vascularization of growth factor-releasing hybrid scaffold of poly (epsilon-caprolactone)/collagen fibers and hyaluronic acid hydrogel. *Biomaterials* **32,** 8108–17 (2011).

366. Fischer, R. L., McCoy, M. G. & Grant, S. a. Electrospinning collagen and hyaluronic acid nanofiber meshes. *J. Mater. Sci. Mater. Med.* (2012). doi:10.1007/s10856-012-4641-3

367. Fullana, M. J. & Wnek, G. E. Electrospun collagen and its applications in regenerative medicine. *Drug Deliv. Transl. Res.* **2,** 313–22 (2012).

368. Domb, A. J., Kost, J. & Wiseman, D. *Handbook of Biodegradable Polymers*. (CRC Press, 1998).

369. Einstein, A. Eine neue Bestimmung der Moleküldimensionen. *Ann. Phys.* **324,** 289–306 (1906).

370. Guth, E. & Simha, R. Untersuchungen über die Viskosität von Suspensionen und Lösungen. 3. Über die Viskosität von Kugelsuspensionen. *Kolloid-Zeitschrift* **74,** 266–275 (1936).

371. Miyata, T., Sohde, T., Rubin, A. L. & Stenzel, K. H. Effects of ultraviolet irradiation on native and telopeptide-poor collagen. *Biochim. Biophys. Acta - Protein Struct.* **229,** 672–680 (1971).

372. Stenzel, K. H., Miyata, T. & Rubin, A. L. Collagen as a biomaterial. *Annu. Rev. Biophys. Bioeng.* **3,** 231–53 (1974).

373. Graessley, W. W. *The Entanglement Concept in Polymer Rheology*. **16,** (Springer-Verlag, 1974).

374. Doillon, C. J. *et al.* Chemical inactivators as sterilization agents for bovine collagen materials. *J. Biomed. Mater. Res.* **37,** 212–21 (1997).

375. Shenoy, S., Bates, W., Frisch, H. & Wnek, G. Role of chain entanglements on fiber formation during electrospinning of polymer solutions: good solvent, non-specific polymer-polymer interaction limit. *Polymer (Guildf).* **46,** 3372–3384 (2005).

376. McKee, M. G., Wilkes, G. L., Colby, R. H. & Long, T. E. Correlations of Solution Rheology with Electrospun Fiber Formation of Linear and Branched Polyesters. *Macromolecules* **37,** 1760–1767 (2004).

377. Carlisle, C. R., Coulais, C. & Guthold, M. The mechanical stress-strain properties of single electrospun collagen type I nanofibers. *Acta Biomater.* **6,** 2997–3003 (2010).

378. Saeed, K. & Park, S.-Y. Preparation and characterization of multiwalled carbon nanotubes/polyacrylonitrile nanofibers. *J. Polym. Res.* **17,** 535–540 (2009).

379. Mazinani, S., Ajji, A. & Dubois, C. Morphology, structure and properties of conductive PS/CNT nanocomposite electrospun mat. *Polymer (Guildf).* **50,** 3329–3342 (2009).

380. McCullen, S. D. *et al.* Morphological, Electrical, and Mechanical Characterization of Electrospun Nanofiber Mats Containing Multiwalled Carbon Nanotubes. *Macromolecules* **40,** 997–1003 (2007).

381. Du, J.-H. The present status and key problems of carbon nanotube based polymer composites.

eXPRESS Polym. Lett. **1,** 253–273 (2007).

382. Li, J. *et al.* Correlations between Percolation Threshold, Dispersion State, and Aspect Ratio of Carbon Nanotubes. *Adv. Funct. Mater.* **17,** 3207–3215 (2007).

383. Han, D. & Cheung, K. C. Biodegradable Cell-Seeded Nanofiber Scaffolds for Neural Repair. *Polymers (Basel).* **3,** 1684–1733 (2011).

384. Sung, H.-J., Meredith, C., Johnson, C. & Galis, Z. S. The effect of scaffold degradation rate on three-dimensional cell growth and angiogenesis. *Biomaterials* **25,** 5735–42 (2004).

385. Qian, H., Bei, J. & Wang, S. Synthesis, characterization and degradation of ABA block copolymer of l-lactide and ε-caprolactone. *Polym. Degrad. Stab.* **68,** 423–429 (2000).

386. Sun, H., Mei, L., Song, C., Cui, X. & Wang, P. The in vivo degradation, absorption and excretion of PCL-based implant. *Biomaterials* **27,** 1735–40 (2006).

387. Wang, W., Zhu, Y., Liao, S. & Li, J. Carbon Nanotubes Reinforced Composites for Biomedical Applications. *Biomed Res. Int.* **2014,** 1–14 (2014).

388. Lanone, S., Andujar, P., Kermanizadeh, A. & Boczkowski, J. Determinants of carbon nanotube toxicity. *Adv. Drug Deliv. Rev.* **65,** 2063–9 (2013).

389. Liu, Y., Zhao, Y., Sun, B. & Chen, C. Understanding the Toxicity of Carbon Nanotubes. *Acc. Chem. Res.* **46,** (2012).

390. Toyokuni, S. Genotoxicity and carcinogenicity risk of carbon nanotubes. *Adv. Drug Deliv. Rev.* **65,** 2098–110 (2013).

391. Chua, M., Chui, C.-K., Teo, C. & Lau, D. Patient-specific carbon nanocomposite tracheal prosthesis. *Int. J. Artif. Organs* **38,** 31–8 (2015).

392. Meng, J. *et al.* Enhancement of nanofibrous scaffold of multiwalled carbon nanotubes/polyurethane composite to the fibroblasts growth and biosynthesis. *J. Biomed. Mater. Res. A* **88,** 105–16 (2009).

393. Zomer Volpato, F., Fernandes Ramos, S. L., Motta, A. & Migliaresi, C. Physical and in vitro biological evaluation of a PA 6/MWCNT electrospun composite for biomedical applications. *J. Bioact. Compat. Polym.* **26,** 35–47 (2010).

394. Koh, H. S., Yong, T., Chan, C. K. & Ramakrishna, S. Enhancement of neurite outgrowth using nano-structured scaffolds coupled with laminin. *Biomaterials* **29,** 3574–82 (2008).

395. Lowery, J. L., Datta, N. & Rutledge, G. C. Effect of fiber diameter, pore size and seeding method on growth of human dermal fibroblasts in electrospun poly(epsilon-caprolactone) fibrous mats. *Biomaterials* **31,** 491–504 (2010).

396. Badami, A. S., Kreke, M. R., Thompson, M. S., Riffle, J. S. & Goldstein, A. S. Effect of fiber diameter on spreading, proliferation, and differentiation of osteoblastic cells on electrospun poly(lactic acid) substrates. *Biomaterials* **27,** 596–606 (2006).

397. Chandrasekaran, A. R., Venugopal, J., Sundarrajan, S. & Ramakrishna, S. Fabrication of a nanofibrous scaffold with improved bioactivity for culture of human dermal fibroblasts for skin regeneration. *Biomed. Mater.* **6,** 15001 (2011).

398. Coleman, A. W., Maguire, M. J. & Coleman, J. R. Mithramycin- and 4'-6-diamidino-2-phenylindole (DAPI)-DNA staining for fluorescence microspectrophotometric measurement of DNA in nuclei, plastids, and virus particles. *J. Histochem. Cytochem.* **29,** 959–968 (1981).

399. Lee, M. K., Tuttle, J. B., Rebhun, L. I., Cleveland, D. W. & Frankfurter, A. The expression and posttranslational modification of a neuron-specific beta-tubulin isotype during chick embryogenesis. *Cell Motil. Cytoskeleton* **17,** 118–32 (1990).

400. CUMMING, R., BURGOYNE, R. & LYTTON, N. Differential immunocytochemical localisation of ?-

tubulin and ?-tubulin in cerebellum using monoclonal antibodies. *Cell Biol. Int. Rep.* **6,** 1047–1053 (1982).

401. Subramanian, A., Vu, D., Larsen, G. F. & Lin, H.-Y. Preparation and evaluation of the electrospun chitosan/PEO fibers for potential applications in cartilage tissue engineering. *J. Biomater. Sci. Polym. Ed.* **16,** 861–873 (2005).

402. Kumbar, S. G., Nukavarapu, S. P., James, R., Nair, L. S. & Laurencin, C. T. Electrospun poly(lactic acid-co-glycolic acid) scaffolds for skin tissue engineering. *Biomaterials* **29,** 4100–7 (2008).

403. Pakkenberg, B. Aging and the human neocortex. *Exp. Gerontol.* **38,** 95–99 (2003).

404. Sung, J. H., Kim, H. S., Jin, H.-J., Choi, H. J. & Chin, I.-J. Nanofibrous Membranes Prepared by Multiwalled Carbon Nanotube/Poly(methyl methacrylate) Composites. *Macromolecules* **37,** 9899–9902 (2004).

405. Roach, P., Parker, T., Gadegaard, N. & Alexander, M. R. Surface strategies for control of neuronal cell adhesion: A review. *Surf. Sci. Rep.* **65,** 145–173 (2010).

406. Jeong, S. I. *et al.* Development of electroactive and elastic nanofibers that contain polyaniline and poly(L-lactide-co-epsilon-caprolactone) for the control of cell adhesion. *Macromol. Biosci.* **8,** 627–37 (2008).

407. Asran, A. S., Henning, S. & Michler, G. H. Polyvinyl alcohol–collagen–hydroxyapatite biocomposite nanofibrous scaffold: Mimicking the key features of natural bone at the nanoscale level. *Polymer (Guildf).* **51,** 868–876 (2010).

408. Ma, P. X. & Zhang, R. Synthetic nano-scale fibrous extracellular matrix. *J. Biomed. Mater. Res.* **46,** 60–72 (1999).

409. Cukierman, E., Pankov, R., Stevens, D. R. & Yamada, K. M. Taking cell-matrix adhesions to the third dimension. *Science* **294,** 1708–12 (2001).

410. Wilson, C. J., Clegg, R. E., Leavesley, D. I. & Pearcy, M. J. Mediation of Biomaterial–Cell Interactions by Adsorbed Proteins: A Review. *Tissue Eng.* **11,** 1–18 (2005).

411. Friedl, P., Zänker, K. S. & Bröcker, E. B. Cell migration strategies in 3-D extracellular matrix: differences in morphology, cell matrix interactions, and integrin function. *Microsc. Res. Tech.* **43,** 369–78 (1998).

412. Yamada, K. M., Pankov, R. & Cukierman, E. Dimensions and dynamics in integrin function. *Braz. J. Med. Biol. Res.* **36,** 959–66 (2003).

413. Balasundaram, G. & Webster, T. J. An overview of nano-polymers for orthopedic applications. *Macromol. Biosci.* **7,** 635–42 (2007).

414. Zhang, L. & Webster, T. J. Nanotechnology and nanomaterials: Promises for improved tissue regeneration. *Nano Today* **4,** 66–80 (2009).

415. Nibley, J. S. Health Care and Insurance Schemes and Health Outcomes: A Global Comparative Analysis. *papers.ssrn.com* (2011).

416. Teo, W. E. & Ramakrishna, S. Electrospun fibre bundle made of aligned nanofibres over two fixed points. *Nanotechnology* **16,** 1878–1884 (2005).

417. Teo, W. E. & Ramakrishna, S. A review on electrospinning design and nanofibre assemblies. *Nanotechnology* **17,** R89–R106 (2006).